The Pennsylvania State University

The Graduate School

Department of Electrical Engineering

MULTI-WAVELENGTH DIFFERENTIAL ABSORPTION MEASUREMENTS OF CHEMICAL SPECIES

A Dissertation in

Electrical Engineering

by

David M. Brown

Submitted in Partial Fulfillment
of the Requirements
for the Degree of

Doctor of Philosophy

August 2008

The Dissertation of David M. Brown was reviewed and approved* by the following:

C. Russell Philbrick
Professor of Electrical Engineering
Dissertation Advisor
Chair of Committee

Kultegin Aydin
Professor of Electrical Engineering

Zhiwen Liu
Associate Professor of Electrical Engineering

H. Nels Shirer
Associate Professor of Meteorology

W. Kenneth Jenkins
Professor of Electrical Engineering
Head of the Department of Electrical Engineering

*Signatures are on file in the Graduate School

ABSTRACT

The probability of accurate detection and quantification of airborne species is enhanced when several optical wavelengths are used to measure the differential absorption of molecular spectral features. Characterization of minor atmospheric constituents, biological hazards, and chemical plumes containing multiple species is difficult when using current approaches because of weak signatures and the use of a limited number of wavelengths used for identification. Current broadband systems such as Differential Optical Absorption Spectroscopy (DOAS) have either limitations for long-range propagation, or require transmitter power levels that are unsafe for operation in urban environments. Passive hyperspectral imaging systems that utilize absorption of solar scatter at visible and infrared wavelengths, or use absorption of background thermal emission, have been employed routinely for detection of airborne chemical species. Passive approaches have operational limitations at various ranges, or under adverse atmospheric conditions because the source intensity and spectrum is often an unknown variable.

The work presented here describes a measurement approach that uses a known source of a low transmitted power level for an active system, while retaining the benefits of broadband and extremely long-path absorption operations. An optimized passive imaging system also is described that operates in the 3 to 4 μm window of the mid-infrared. Such active and passive instruments can be configured to optimize the detection of several hydrocarbon gases, as well as many other species of interest.

Measurements have provided the incentive to develop algorithms for the calculations of atmospheric species concentrations using multiple wavelengths.

These algorithms are used to prepare simulations and make comparisons with experimental results from absorption data of a supercontinuum laser source. The MODTRAN^{TM} model is used in preparing the simulations, and also in developing additional algorithms to select filters for use with a MWIR (midwave infrared) imager for detection of plumes of methane, propane, gasoline vapor, and diesel vapor. These simulations were prepared for system designs operating on a down-looking airborne platform. A data analysis algorithm for use with a hydrocarbon imaging system extracts regions of interest from the field-of-view for further analysis.

An error analysis is presented for a scanning DAS (Differential Absorption Spectroscopy) lidar system operating from an airborne platform that uses signals scattered from topographical targets. The analysis is built into a simulation program for testing real-time data processing approaches, and to gauge the effects on measurements of path column concentration due to ground reflectivity variations. An example simulation provides a description of the data expected for methane.

Several accomplishments of this research include:

1) A new lidar technique for detection and measurement of concentrations of atmospheric species is demonstrated that uses a low-power supercontinuum source.
2) A new multi-wavelength algorithm, which demonstrates excellent performance, is applied to processing spectroscopic data collected by a long-path supercontinuum laser absorption instrument.

3) A simulation program for topographical scattering of a scanning DAS system is developed, and it is validated with aircraft data from the ITT Industries ANGEL (Airborne Natural Gas Emission Lidar) 3-λ lidar system.
4) An error analysis procedure for DAS is developed, and is applied to measurements and simulations for an airborne platform.
5) A method for filter selection is developed and tested for use with an infrared imager that optimizes the detection for various hydrocarbons that absorb in the midwave infrared.
6) The development of a Fourier analysis algorithm is described that allows a user to rapidly separate hydrocarbon plumes from the background features in the field of view of an imaging system.

TABLE OF CONTENTS

LIST OF FIGURES

LIST OF TABLES

ACKNOWLEDGMENTS

Completing a dissertation is a multi-person effort. Although my name is on the cover of this work, this dissertation really represents the teamwork of an exceptional group of engineers and scientists led by C. Russell Philbrick, my advisor, my intellectual role model, and my friend. I thank him deeply for his encouragement and guidance throughout my graduate work at Penn State. His attention to detail and love for science, innovation, and learning are truly inspirational. I believe it is this mindset that stimulates the young minds around him. The experience I have gained under his leadership will be highly valued throughout my career – Thanks Dr. Philbrick. I thank my additional dissertation committee members, Dr. Zhiwen Liu, Dr. Kultegin Aydin, and Dr. H. Nels Shirer for their contributions to the work. In particular I would like to thank Dr. Zhiwen Liu for his constant interaction with the work, the use of equipment, and many insightful discussions.

I also must give thanks to all members of the Lidar and Ultrafast Optics Laboratories for constant dialogue on the topics contained within this dissertation. Specifically, I must recognize Adam Willitsford, Perry Edwards, and Joseph Begnoché for their efforts in multiple sections of this work. Thanks to Andrea Wyant for her untiring help in the final stages of this work. Special thanks are also due to Kebin Shi and Qian Xu for their help with the supercontinuum source measurements. The effort of the members of ITT's Space Systems Division is also acknowledged for their support and lidar data.

Finally, I must thank my family for their consistent support throughout the better part of a decade while I have been enrolled at Penn State.

CHAPTER 1
Introduction

Accurate measurements of the concentration of atmospheric species are critical for understanding many important aspects of the Earth's atmospheric chemistry. Analysis of this chemistry on a global perspective provides the framework for studies of air quality, monitoring of industrial pollution, and understanding the optical properties of artic haze, dust storms and volcanic eruptions [ESA, 2004]. Measurement and monitoring of the atmospheric trace species has been and will continue to be important in the efforts to reduce releases of ozone-destroying compounds. Furthermore, advanced monitoring systems can help gauge the effects of atmospheric pollutant levels on the magnitude of the planetary climate changes due to the greenhouse effect. An accurate understanding of atmospheric chemistry will help to determine mankind's effects on the depletion of the polar ice caps and the sea ice area which has decreased on the order of 1 to 3 million km^2, when compared with the area during 1978-87 period [Sreenivasan and Majumdar, 2006].

Simultaneous measurements of many airborne species are extremely important for studies of atmospheric chemistry, and hence current space-based measurements are as spectrally broadband as possible [ESA, 2004]. Newly developing technologies provide several options for the measurements of various species and particularly those atmospheric species of special interest. For example, the SCHIAMACHY system (space-based) is capable of a variety of atmospheric constituent measurements including O_3, NO_2, BrO, SO_2, N_2O, CO, using a passive hyperspectral optical absorption approach [Weber, *et al.*, 2001]. Similar systems utilizing spectrally broadband active or passive techniques further enhance the quality of measurements of atmospheric constituents that aid the development of models, and lead to the understanding of important processes.

The detection of trace levels of various toxic and hazardous chemical species is a primary goal for the Department of Defense (DoD) and the Department of Homeland Security (DHS) for intercepting terrorist activities. New techniques and advanced capabilities are most important for detection and monitoring many different chemicals.

The focus of this work is to advance the techniques that utilize differential absorption for the detection and quantification of atmospheric species using the NIR and MWIR regions of the optical spectrum. We have selected three of the many projects active and completed in this research area to report in this thesis.

1.1 Optical Remote Sensing

With any active remote sensing technique, the wavelength of the outgoing radiation compared with the size of the scattering particle are the primary factors determining scattering cross section, and describing the divergence of the beam of radiation [Bohren and Huffman, 1983]. Hence, when utilizing optical wavelengths, the size of scattering particles at the molecular level can be studied, compared with scattering at radiowave wavelengths, which are useful when studying larger particles ranging from μm to mm in size [Ulaby, 1982]. LIDAR, or LIght Detecting And Ranging, capitalizes on the response due to scattering of optical electromagnetic radiation, therefore using drastically smaller wavelengths compared with RADAR (RAdiowave Detection and Ranging). LIDAR and RADAR systems are complementary, and are typically applied for different size targets. Most designers currently select multi-faceted designs using technologies that span larger ranges of the electromagnetic spectrum, or develop systems that combine the capabilities of both lidar and radar [Hydea, *et al.*, 2007].

During the last couple decades, remote sensing using lasers has been shown to be the premier method to determine characteristics of the Earth's environment [Measures, 1984]. Optical interactions with scattering particles became widely studied following the invention of the laser, and has since spun off many remote sensing devices operating in the optical region of the electromagnetic spectrum.

Lidar measurements began by using single wavelength scattering techniques, which were pioneered by Inaba and Kobayashi in the mid-to-late 1960s [Inaba*, et al.*, 1967], and have continually evolved to expand throughout the optical spectrum. More recent instruments are designed to span spectral regions ranging from the far infrared [Carlisle, *et al.*, 1995] to the deep ultraviolet [Wu, *et al.*, 2000], depending on the requirements of the particular application. A most recent systems has used a spectrally broadband supercontinuum source [Kasparian, *et al.*, 2002] to probe the atmosphere with many wavelength channels. Broadband systems are able to serve as multi-objective remote sensing instruments because they offer a large range of data products that can be determined independently to describe properties and processes as well as characterization of atmospheric species and aerosols.

1.2 Motivation and Path for Continued Research

This study answers questions regarding the viability of environmental monitoring of chemical species through use of broadband and multi-wavelength approaches on a local scale. Measurements of interest in local regions include monitoring of air quality, mapping of industrial pollutants and power plant emissions, detection of leaking hydrocarbon transport pipelines, and emergency preparedness response in the event of a natural disaster or terrorist actions.

Current state-of-the-art lidar systems are typically designed for one application (e.g. tropospheric Raman lidar measurements [Philbrick, 2003; Philbrick, 2005], DIAL (DIfferential Absorption Lidar) measurement of hydrocarbons [Stearns, *et al.*, 2006; Murdock, *et al.*, 2008]). These systems require significant hardware changes if an alternative species is selected, or if a different wavelength range is desired for the investigation. Broadband laser systems can serve as the source of transmitted radiation in an entirely new class of laser remote sensing instruments that can make more flexible use of a wide region of the electromagnetic spectrum. Spectral measurements by the receiver and detector sub-systems can select multiple species within the wavelength ranges of interest for simultaneous measurements. A variety of localized short-range lidar remote sensing applications can be accomplished with a single design concept, which ultimately leads to a single set of hardware and software algorithms. Introducing multi-functional systems, which use similar hardware and detection science, can also mitigate some of the high procurement, overhead, and maintenance costs of lidar systems. For example, the three-wavelength DIAL lidar system operated by ITT's ANGEL (Airborne Natural Gas Emission Lidar) service was originally designed for detection of natural gas leaks by flying above pipeline right-of-ways [Grund, *et al.*, 2004; Murdock, *et.al.*, 2008]. This device is now used for a commercial service that surveys natural gas pipelines throughout the country, and provides leak mapping capabilities for many pipeline companies. Experimental studies with the system have shown the possibility of detecting additional hydrocarbons via DIAL measurements using more than two wavelengths [Stearns, 2006]. This capability would be further enhanced by increasing the number of channels to increase the number of DIAL comparisons possible. A simulation program that carefully models DIAL measurements from an airborne platform provides a useful tool that can be used for development of next-generation systems, similar to ANGEL. Completion of the development of this simulation method is one goal of the present work.

A second goal of this research is to investigate the capability for making rapid measurements of various atmospheric constituents through use of broadband passive spectral techniques. Background Absorption Gas Imaging (BAGI) approaches provide a real-time mechanism to observe hydrocarbon plumes within the field of view of an imager. Various groups have been successful in the real-time imaging of hydrocarbon gas plumes by utilizing absorption spectra and low-power transmitters in the NIR to the LWIR [Cosofret, *et al.*, 2004; Wainner, *et al.*, 2002; Sandsten, *et al.*, 2004]. The detection of large hydrocarbon leaks from an airborne platform can be enhanced by using a passive system, and it has benefits in terms of cost and operational complexity. A passive system using two separate wavelength bands to optimize the detection and imaging of gas plumes has been demonstrated [Cosofret, *et al.*, 2004; Powers, *et al.*, 2000]. A commercial system offered by [FLIR, 2006] supports the close-range detection of a host of hydrocarbons using a purely passive technique, although it is not tunable for specific targets of interest. We have developed and present a solution methodology for individual detection of various hydrocarbon species that absorb in the midwave infrared. An approach is developed for selecting a hydrocarbon-specific band-pass filter, optimizes performance when a passive system is operated on an airborne sensor platform. A data processing technique is also devised that is capable of autonomously detecting pixel regions of suspected hydrocarbon plumes.

A third (and primary) goal of this work is to investigate and demonstrate improved detection of species, and determination of species concentrations using broadband, multi-wavelength approaches. Error calculations from path absorption measurements and simulations are combined with the knowledge developed in this work relative to infrared broadband absorption to create a new multi-wavelength long-path absorption measurement technique. Long-path absorption increases performance by improving both the lower detection limit and the temporal resolution, when compared to differential absorption systems that depend on atmospheric backscattering. One class of systems using long path absorption geometry has been demonstrated by several research groups [Platt and Perner, 1983; Povey, *et al.*, 1998; South, *et al.*, 1998]. These systems employ xenon arc lamps as a source of broadband radiation, and can typically function at ranges of a few hundred meters to kilometers; however, they have limitations in terms of controlling the transmitted beam due to the difficulty of collimating lamp sources [Platt, 1994]. Other approaches [Kasparian, *et al.,* 2002] transmit ultra-high energy pulses (terawatt) into the atmosphere that are then focused to create a plasma that generates a supercontinuum spectra at a remote location. Absorption studies are then performed with a large 1-m telescope at the transmitter location [Méjean, *et al.,* 2003]. The approach that are developing uses a low power fiber optically coupled supercontinuum source to make measurements of atmospheric constituents using long path absorption geometries [Brown, *et al.*, 2008]. Reduction of the transmitted peak power requirement by nearly nine orders of magnitude, in comparison with other supercontinuum source approaches [Méjean, *et al.*, 2003], provides a new technology to use in urban-type applications where eye-safety is a major concern. Until now, the algorithms required to analyze collected data containing one or more absorbing chemical species have not been examined by the research community for robustness, accuracy, and applicability to supercontinuum long path absorption datasets. Such an algorithm has been developed and tested by comparing multiple species measurements with simulations in this dissertation. The Supercontinuum Absorption Spectroscopy (SAS) system developed also uses the algorithm to calculate concentration path length of ambient oxygen and water vapor for experimental test cases.

1.3 Outline of Research Accomplishments and Hypotheses

This section outlines the work which has been undertaken and the hypotheses examined. The primary accomplishments of the research are as follows:

1) An error analysis procedure for Differential Absorption Spectroscopy (DAS) measurements is developed and is shown to be applicable to an airborne platform.
2) An approach for selecting a filter for use with an infrared imager is developed and tested to optimize the detection for various hydrocarbons that absorb in the midwave infrared.

3) An approach to detect and measure the concentration of atmospheric species is demonstrated that uses a low power supercontinuum source.

The main hypotheses that have been investigated are:

1) Laser beam overlap functions and atmospheric background concentrations of interfering species affect the baseline sensitivity for differential absorption spectroscopy, particularly when using topographic targets from an airborne platform.
2) Passive imaging of a scene, with absorbing hydrocarbon vapors present, can be used to detect and characterize the species when solar scatter, atmospheric conditions, and filter selection are properly considered in the analysis.
3) Supercontinuum Absorption Spectroscopy provides new capabilities for rapid, highly accurate, and reliable measurement of atmospheric species.

CHAPTER 2

Scientific Background

The interpretation of signals from electromagnetic radiation scattered by random media of the atmosphere may require analysis procedures associated with Mie particle scattering, Rayleigh scattering, Raman scattering, molecular fluorescence, or absorption. The following chapter describes the processes of scattering and absorption, and reviews the scientific background that supports applications using absorption properties for remote sensing.

2.1 Scattering and Absorption Mechanisms

Rayleigh scattering refers to the regime where the scatterer is much smaller in physical size than the laser wavelength being used for characterization (typically $a<0.1\lambda$); the cross section increases by the sixth power of the size and the fourth power of the frequency for these small particles [Young, 1981]. Rayleigh and Mie scattering processes are referred to as elastic scattering, because the impinging radiation transfers no significant energy during the interaction with the particle.

Mie scattering in particular refers to calculations of scattering from spherical particle with sizes that are comparable or larger the wavelength ($a > \lambda/10$). Calculation of cross-section for these larger particles are generally a more complex function of wavelength and has no closed form solution [Bohren and Huffman, 1983, Mishchenko, *et al.,* 1997].

Raman scattering involves an energy transfer between the radiation field and the particle. The Raman scattered photons provide a unique signature in the spectra of scattered radiation because of a wavelength shift corresponding to the energy states of the molecule, and it uniquely identifies the molecular properties of the scatterer. This well known process is used in Raman lidar systems like the Penn State University LAPS (Lidar Atmospheric Profile Sensor) unit [Philbrick, 2003]. Energy is imparted to or taken from the scattering particles during Raman scattering, and therefore it is classed as an inelastic scattering process.

The process of absorption, as its name implies, is the mechanism that describes the extraction of energy from the radiation field by coupling the energy to a molecule, and results in excitation of molecular and electron energy levels (vibrations rotation, fluorescence, etc.) Consequently, a molecule with many different vibrational modes has the possibility of excitation of vibration to absorb energy at many different frequencies.

Unlike pure rotational spectra where the molecule must have a permanent dipole moment, infrared absorption spectra arises when a changing dipole moment in the molecule is created due to an asymmetrical stretch or vibration. For example, bonds in symmetric N_2 and H_2 molecules are not infrared active because stretching, bending, or other dynamic movement does not change the dipole moment of the molecule. An asymmetric molecule with many dynamical modes widens the possibility of the number of frequencies that may appear in the wavelength response of the absorption spectra. Depending on the type and number of possible intermolecular motions, the response can create widely spaced absorption features like those in methane, or finely structured absorption bands like those in propane that are observed in the 3-5 μm window of the midwave infrared spectrum. The gross selection rule as outlined by Atkins [1990] for infrared activity is that these vibrational motions must correspond to a normal vibrational mode of the molecule. A normal mode is defined as a synchronous motion of atoms or groups of atoms that may be excited without leading to any further excitation. Symmetrical molecular vibrations or “molecular breathing” will not create a changing dipole moment and are thus infrared inactive [Atkins, 1990]. Another example, the symmetrical stretch of CO_2, will not create a changing dipole moment, and hence is not infrared active (Figure 2.1a, left). An asymmetrical stretch (Figure 2.1b, right), however, will generate an unbalanced stretch of the molecule, change the dipole moment, and create spectral components of absorption corresponding to the frequencies of the vibrational stretch. Water will seldom experience a symmetrical stretch due to the permanent dipole moment of the water molecule, and many modes will be infrared active as shown in Figure 2.1(b).

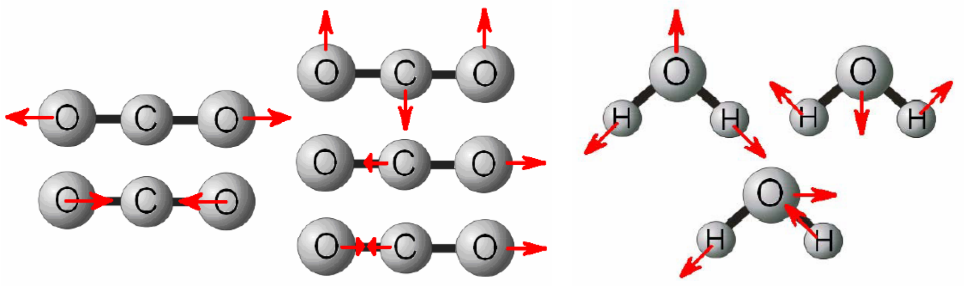

(a) **(b)**

Figure 2.1: (a) Symmetrical (left) and asymmetrical stretches for CO_2 (right), and (b) Possible stretching methods for H_2O, all infrared active [Atkins, 1990].

This simple qualitative reasoning explains the large absorption bands of water vapor throughout the infrared from 2.5 to 20 μm. These bands are so strong that overtones are observed through the near infrared region. Water vapor absorption bands are of particular interest for any remote sensing application in the infrared; the strong absorption bands coupled with the high variability of atmospheric water vapor drastically reduces optical transmission in several wavelength bands. Spectral transmission and radiance models can be used to quantify the effects of water on system operations when water vapor is not the species of interest.

Figure 2.2 depicts some of the most common bonds and associated wavelength regions where covalent bonding (single, double, and triple) common in molecular species yields absorption spectra in midwave infrared (MWIR) and longwave infrared (LWIR).

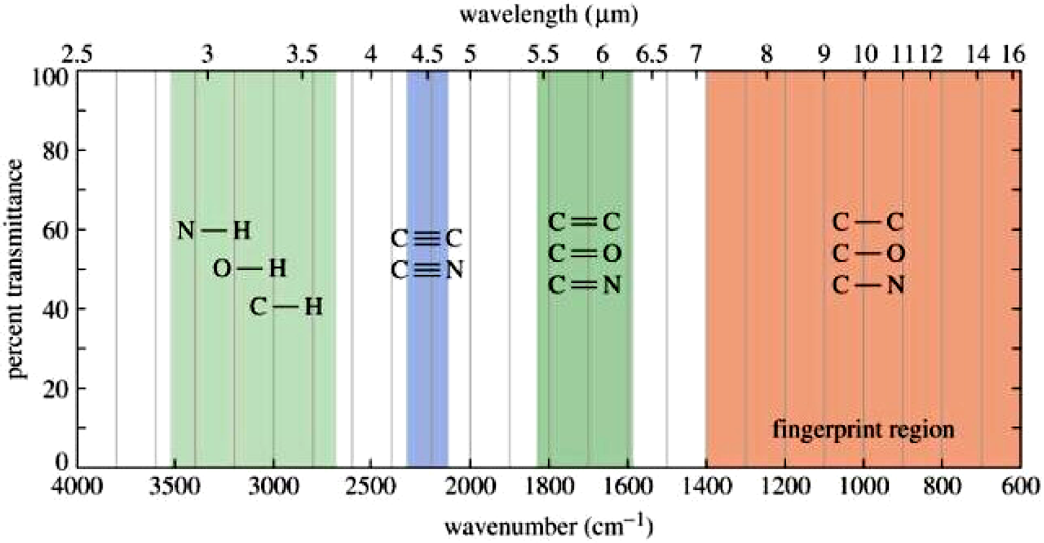

Figure 2.2: Absorption regions of the infrared are indicated for several typical bonding structures. The colors define approximate regions in wavelength and wavenumber that exhibit absorption structure due to the bonds shown [Philbrick, *et al.*, 2006].

All of the primary absorption features occur at energies less than the strongest hydrogen bond at 4160 cm^{-1} (about 2.4 μm) [Weast, *et al.*, 1987]. The chemical uniqueness of various chemical species possessing different types of the single bond structures is recognized in the labeling of the 7 to 16 μm range as the "fingerprint" region. Exploiting the spectral characteristics in this infrared absorption region of the spectrum is a focus for detection of various classes of chemicals that make up dangerous or harmful compounds. The unique energy states of the various molecular species allow sorting in cases where multiple species spectra are overlapped.

2.2 Remote Sensing Using Absorption Properties

There are many techniques that can be used to measure the atmospheric concentrations of gaseous species. Classically, the difference in energy received from atmospheric backscatter at two wavelengths, one online of an absorption feature and one offline, is used in DIAL lidar systems to measure species concentration of a particular atmospheric constituent. Two lasers are normally operated with one wavelength online on an absorption feature and one wavelength offline. Alternatively, a tunable laser may be used to select the specific online and offline wavelengths in a region with minimal background absorption from other species. The atmospheric backscatter signals from pulsed lasers scattered from aerosols and molecules at both wavelengths are used to range-resolve the differential absorption measurements along increments of the beam path. Thus, the range determined from time delay of the signals pinpoints the location along the beam where a chemical species is present. Limitations are imposed on this approach is by necessity of detecting scattering from aerosol particles within each range bin. Because the sensitivity and resolution of technique relies on differentiating the backscatter signals, more integration time is needed for each more distant range bin to attain useable values of signal to noise ratio. The major limits on the accuracy of the DIAL technique are associated with the precision in the matching of the wavelength dependence of the laser and line shape with the absorption feature. Other limitations require that the online and offline wavelengths be close to each other to ensure that atmospheric scatter and the hard target backscatter are similar for both wavelengths. Furthermore, the two wavelengths used to perform the DIAL comparison must interact with the same atmospheric volumes at nearly the same time to freeze atmospheric turbulence effects.

Alternative approaches may use the full path between a laser and a target to measure absorption, with sacrifice of the range resolution property; however this approach has distinct advantages for detecting trace levels of concentrations of species in the atmosphere. A set of path absorption measurements mapped through the atmospheric volume of interest, combined with tomographic data processing routines, can be used to restore a degree of range resolution over a target area [Hashmonay and Yost, 1999]. Hazardous vapor plume mapping, and applications which locate fugitive vapor sources are possible using this technique.

2.2.1 DIAL Systems

Differential Absorption Lidar (DIAL) approaches have been used in the research community for years to detect and measure the concentration of a specific chemical species [Inaba, 1976]. Baumgarter and Byer, for example, were successful in many measurements of atmospheric pollutants in the late 1970's using this approach [Baumgarter and Byer, 1978]. Their work primarily focused on the remote detection of SO_2 and CH_4. They were successful in detecting atmospheric background levels of CH_4 over a 5.4 km path length, and observed SO_2 levels slightly above 100 ppm [Baumgarter and Byer, 1978]. Later research demonstrated measurements of SF_6 in the 1990s, as well as several other species using high energy CO_2 laser technology [Carlisle, *et al.,* 1995]. These systems transmitted a beam horizontally and used scattering from hard target surfaces, or retroreflectors to make column content measurements. Since the 1990s, tunable laser technology has advanced dramatically, leading to investigations using midwave infrared tunable lasers by Weibring *et al.* [2004]. A newly developed fast-switching, frequency-agile optical parametric oscillator (OPO) lidar transmitter was used to measure concentrations in areas of planned releases of methane, ethane, propane, and butane from a distance of 50 m. They demonstrated the idea of a multi-wavelength lidar system with multivariate analyzing techniques can be used for measuring hydrocarbon gas mixtures. Although their system operated as designed, it was difficult to determine individual hydrocarbon concentrations when several species were simultaneously present due to the limited number of wavelength comparisons. This difficulty was further increased in the case of species with significant spectral overlap [Weibring, *et al.,* 2004].

2.2.2 DOAS Systems

Approaches published by Platt *et al*. [1979] and other groups have focused on an alternative type of differential absorption instruments using incoherent sources and are referred to as Differential Optical Absorption Spectroscopy (DOAS). The typical incoherent transmitters in these instruments are Xenon arc lamps, and these DOAS instruments can perform well for monostatic measurements of a range of chemical species. Some of the most interesting experiments with this technology are doubleended measurements carried out by Platt and Perner [1983], where the transmitter and receiver are located at opposite ends of a kilometer length path. The urban measurement example, presented by Platt and Perner [1983], used a collimated high pressure xenon arc lamp (Osram XBO 450 W) coupled with a telescope receiver at opposite ends of the open atmospheric path. At kilometer ranges, the transmitted light was received by a parabolic mirror (30 cm diameter, 60 cm focal length) telescope. The collected signal is focused into a spectrograph with a 550 grooves/mm grating, and the signal is integrated for 2 to 5-minutes. Measurements of O_3, NO_2, HCHO, HONO, H_2O, NO_3, SO_2, BrO, IO, OIO, and several aromatic hydrocarbons were successfully demonstrated using the DOAS technique at concentrations in the ppm to ppt range [Platt and Perner, 1983]. Although it is possible to use this approach over hundreds of meters to a kilometer range, differential absorption measurements over longer ranges require the spatial coherence of the source to form well defined beams. Other issues such as light pollution, optical efficiency, and long detector integration times are additional factors that degrade the system performance when using incoherent sources.

Atmospheric and optical transmission associated with aerosol scattering effects varies relatively smoothly with wavelength in the NIR and MWIR; however, the typical target absorption spectra of the species measured in these regions are highly structured. Therefore, slowly varying characteristics as a function of wavelength due to transmission and scattering effects can be generally compensated for by implementing a high frequency pass filter. Typical DOAS data analysis begins by applying a high pass filter to raw experimental data to create a normalized spectrum of absorption [South, *et al.,* 1998]. To process the broadband spectrum for measurements of one (or multiple species), a weighted sum of squares of the difference between the calculated absorption, σ_i, and observed optical depths is used to determine the best agreement [Patty, *et al.,* 1974]. The general procedure entails the following steps [South, *et al.,* 1998]:

1) Using a high resolution spectrum of the target, calculate the expected transmission, T_i^{FIT},
2) Smooth the T_i^{FIT} spectrum according to the instrument spectral width, w, used to perform the experiment, and arrive at the weighted fit of the differential optical depth (DOD_i^{FIT}) spectrum,
3) Use the resulting spectrum with an initial estimate of the species concentration to determine χ_i^2.
4.) Vary u_i^{FIT}, the concentration of the species, until χ_i^2 has been minimized.

$$T_i^{FIT} = e^{-2u_i^{FIT}\sigma_i} \quad \chi_i^2 = \frac{\sum w\left(DOD_i^{FIT} - DOD_i^{OBS}\right)^2}{\sum w} \quad \text{[Povey, } \textit{et al.}\text{, 1998]} \quad [2.1]$$

Precise adjustment of the wavelength resolution, so that the theoretical spectrum matches the experimental dataset, is important for the analysis, and greatly affects the ultimate conclusion of the least square fitting. Simulating the magnitude and width of the spectral peaks depends upon factors such as the instrument resolution, temperature, and pressure collision broadening effects to calculate the strength of the absorption features expected in the experimental data. All of the parameters influencing the calculated spectra must be included to correctly perform the DOAS analysis technique [South, *et al.,* 1998]. Furthermore, intelligent variation in the concentration of the target species is necessary to ensure that χ_i^2 is fully minimized. Povey has shown, for example, that it is possible to independently detect and measure the concentrations of N_3O and H_2O in their region of slightly overlapping spectra, 650 to 670 nm range, by using a tunable Spectron SL4000B dye chemical laser pumped by the Nd:YAG second harmonic of 1064 nm [Povey, *et al*., 1998]. Additionally, Platt has demonstrated detection of many trace species by using a XeHe lamp as a source of broadband radiation in the UV-VIS range of the spectrum [Platt, 1994].

The techniques developed in the present work expand on path absorption using lamps by employing a supercontinuum laser source for the broadband radiation. Our approach removes the limitations imposed by the wavelength scanning dye laser, and the lack of spatial coherence of the XeHe lamp. Furthermore, the algorithm we developed expands the ability of broadband systems to detect trace species by capitalizing on multiple wavelength maximum likelihood estimation routines.

2.2.3 BAGI Systems

While DIAL and DOAS measurements have demonstrated good performance in identifying gases and measuring their concentrations, the elapsed time between measurement and reporting is typically longer than that required for a real-time data product in many applications. An often adopted alternative approach is a real-time technique, denoted as Backscatter Absorption Gas Imaging (BAGI). Although this method is mostly qualitative in nature and is best suited for close range at high concentrations, the approach permits display of results in a real-time, or a near real-time. This gas visualization method provides a capability for detection that requires less calibration and measurement precision than conventional sensors because it conveys information as a relative contrast among intensities in an image, rather than absolute concentration values [McRae and Kulp, 1993; Cosofret, *et al.*, 2004]. Quantitative measurement of a target gas plume concentrations from imaging can be undertaken, but it requires two parameters:

1) adequate background source (or plume emission) signature (and knowledge of the optical scattering and thermal environment for the region of the plume and the background)
2) infrared camera system with sensitivity and sufficient dynamic range to provide usable contrast for a linear response in the measurement range.

Detection performance depends on using a filter selection that balances the absorbing and non-absorbing contributions to the performance curve. Figure 2.3 shows the addition of bandpass filters to a LWIR camera that include and exclude a major absorption feature in the spectrum of a target species of interest.

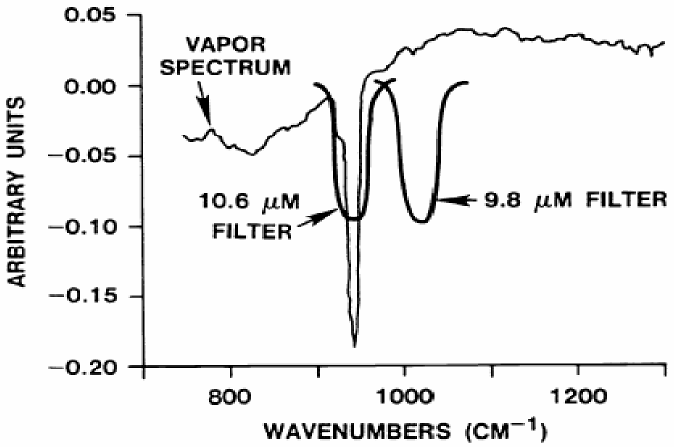

Figure 2.3: Example of filter selection for detection of vapor spectrum for SF_6 via the BAGI technique [Althouse and Chang, 1995].

If a target species is encountered in the field of view, then the absorption will appear as “black smoke” due to less energy being returned to the camera from an emitting warm background. The magnitude of this absorption can describe the approximate concentration of the target gas, based on correctly inferred strength of the emission of the background source.

The work of FLIR Systems Inc. [2006] demonstrates that it is possible to use the surface of the Earth as the backscatter source in detection of hydrocarbon plumes. Simulations via MODTRAN™ have shown, however, that detection probability is highly dependent on atmospheric conditions, particularly at increased ranges. An active BAGI technique, using a laser source, has been demonstrated in various regions of the visible and infrared spectrum to be far more robust for determining the concentration of the target gas species of interest. The tuning ranges of the dye lasers and OPOs available are limited, and the reduced effective ranges of broadband light sources tend to limit the performance. An example of this technique for detection of a large leak in near real-time, is shown in Figure 2.4.

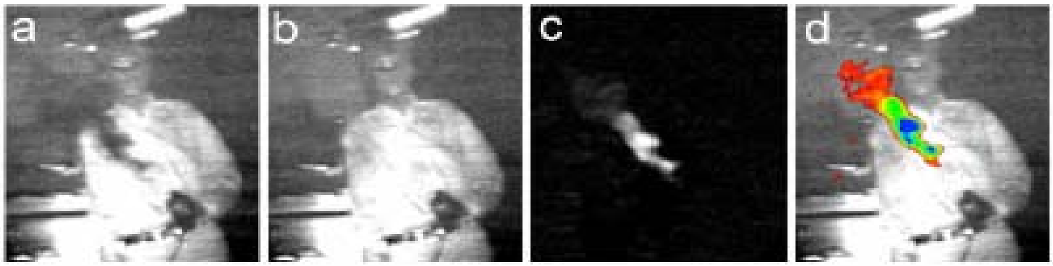

Figure 2.4: Image enhancement by differential absorption; (a) and (b) show images captured with the OPO idler frequency both online and offline of the methane absorption feature. The difference between these images (i.e., the methane plume) is shown in (c). Finally, color is applied to (c) that is then superimposed upon (b) to generate (d) [Stothard, *et al.*, 2004].

Using similar imaging techniques of a purely passive nature, we have developed approaches that enhance leak analysis reporting of the ITT ANGEL service via real time imaging of the larger high concentration hazardous hydrocarbon plumes. The combination of airborne real time imaging of large hydrocarbon plumes with the data from the 3-λ lidar sensor enhances overall performance for a range of species and concentrations when scanning a large spatial area. Although the system will not provide precise measurement of the magnitude of the leak, it will scan the area to find plumes of larger size. This upgrade to the system will assist in identifying targets for more detailed analysis by the ANGEL active remote sensing techniques. The instrument is comparable to the FLIR GasfindIR, although with improved sensitivity and tenability; it is capable of imaging from an airborne platform. The sensor is based on modifications to an existing Merlin MWIR camera, which is used for ANGEL far field beam alignment. Chapters 4 and 5 report on the theoretical study in reference to this work, and suggest a recommended approach for modifying the Merlin MWIR camera. Chapter 6 reports on our calibrations, tests, and data processing algorithms developed to evaluate the performance of the system during a range of tripod tests.

2.2.4 Another Approach: Terawatt Broadband Lasers

A femtosecond lidar system with terawatt intensity was developed in a joint research venture between French, Swiss, and German universities [Méjean, *et al.*, 2003; Wille, *et al.*, 2002]. This system represents another method that uses a totally different lamp source for remote sensing instruments, and still preserves the advantages of broadband operations at long range. This sensor, referred to as "Teramobile," uses ultra-short high energy laser pulses to generate a plasma discharge witch serves as a source to probe the atmosphere for various species and for aerosol studies [Bourayou, *et al.*, 2005]. A supercontinuum is generated from the plasma, created by focusing at a predetermined range; this "white light" source is used to observe the differential absorption of many atmospheric species along a path between the focused region, at several kilometers range, and the detector. The atmospheric white light source, or supercontinuum spectrum, used for the Teramobile absorption approach is generated by focusing high energy laser pulses to extremely high energy density by using a slightly concave exit mirror. The mechanism thus creates very large localized electric fields within the path of the transmitted laser and results in a host of nonlinear effects (four-wave mixing, self-phase modulation, self-steepening, pulse splitting) that cause broadening of the pulse over a wavelength interval. The signals containing the spectrum of the absorption along the path are then collected with a telescope on the ground. This system is fit into a modified cargo trailer, and it features 5 TW of transmitted peak power from pulses at 10 Hz rate are 70 fs in duration at 350 mJ per pulse [Kasparian, *et al.*, 2003]. The useful path for operation of the instrument is adjustable from hundreds of meters, up to several kilometers in altitude, although this requires significant hardware modifications. The mobile laboratory provides the necessary infrastructure for the fieldable laser system, including transmitting and receiving optics, and detection electronics for lidar measurements. The receiving telescope is connected to an Echelle spectrometer that records the spectra over wide spectral regions at a 0.1 Å resolution [Kasparian, *et al.,* 2003]. The system is largely monostatic, and has been used for a variety of demonstrations including a measurement of a broad atmospheric transmission spectrum (bandwidth of 240 nm centered at 808 nm), between the surface and the bottom of a haze layer at 4.5 km altitude. A large wavelength region is available for analysis; it uses the peaks in the spectrum of oxygen and its known concentration to calculate the temperature of the atmosphere, and determine the water vapor concentration. The temperature and water vapor measurements provide a relative humidity value for the atmosphere averaged over the path. This type of analysis demonstrates the importance of simultaneous multi-component measurements for remote sensing applications in the atmosphere.

Disadvantages of this approach stem from the difficulty in controlling the supercontinuum intensity, wavelength stability, location of the source breakdown region, and safety considerations in using such a laser in the open atmosphere. The varying atmospheric nonlinear effects introduced in the focused source region cause the spectrum to change with time during data collection. Additionally, as the name suggests, the transmitted peak power per pulse is at terawatt levels – too dangerous for any type of urban measurement applications.

Other approaches have been able to generate a supercontinuum (via femtosecond lasers) within a cell to perform atmospheric characterizations of aerosols [Galvez, *et al.*, 2002]. Using localized cells to generate a supercontinuum introduces more control into the generation process. These advantages in control are important for making time sequence measurements of atmospheric phenomena, and are similar to those characteristics demonstrated when generating supercontinuum spectra in photonic crystal fibers [Wadsworth, *et al.*, 2002].

2.3 Summary

The extremely broad spectral bandwidth of supercontinuum white light can be used to enhance detection and discrimination of various targets and interferents by proper filtering in various absorption bands. By providing an avenue to compare multiple wavelength ranges on a per pulse (and hence time-step) basis, the resolution of the imaging sequence can be increased. Additionally, the supercontinuum source can be used to take differential images of the scene using a combination of detector and filter technologies similar to the technique outlined by [Stothard, *et al.*, 2004], but with a broader wavelength range than that which has been demonstrated.

CHAPTER 3

Differential Absorption Remote Sensing

To examine multi-wavelength differential absorption approaches, a detailed understanding of the common features of classical differential absorption approaches is necessary. The following sections review various remote detection schemes when employing the differential absorption methodology, and cite parameters that are most important for determining the measurement error. A novel measurement technique described in Chapters 6 and 7 incorporates the error reduction considerations outlined below.

3.1 Remote Measurement of Differential Absorption

The DIAL (DIfferential Absorption Lidar) method utilizes two observation wavelengths, one on the absorption feature of a given molecular species and one slightly off this absorption feature. Originally pioneered by Schotland [1965], DIAL analysis assumes that a pair of DIAL wavelengths are sufficiently close in wavelength that the effects of backscattering are the same at both the online and offline wavelengths. Additionally, it is assumed that the instrument response is relatively constant as a function of wavelength, and hence contributes minimum offset to the measurement [South, *et al.*, 1998]. The two DIAL wavelengths are selected for analysis of a particular absorption feature of a given species, and the ratio of the online to the offline signal measured is in proportion to the number of molecules of the absorbing species.

The DIAL signal attenuation, which is normalized by using the ratio of the online to offline returns and relative power at the two wavelengths, can be used along with the Beer-Lambert law to calculate the concentration of the species number density. In the case of a range resolved system, such as classical DIAL lidar, the change in fraction of the returning energy scattered back from the atmosphere due to the scattering by atmospheric aerosols and molecules in each segment of the path is associated with a time interval. The interaction distance of the beam when signal intensity is measured is defined by the length of this range bin (laser pulse length in time), or the bin width (detector integration time) whichever is larger. Path integrated measurements use Differential Absorption and Spectroscopy (DAS), sometimes called Long Path Absorption (LPA), and use a hard target signal return of the scattered energy back to the receiving lidar telescope [Measures, 1984]. DAS places a less stringent requirement on system design, particularly transmitted power, because topographical targets typically return 10^3 to 10^9 more energy to the detector than DIAL profiles of atmospheric scatter, typically from aerosols [Measures, 1984]. The transmitted power requirements reduce even further when retroreflector targets can be employed at predetermined locations. When a high sensitivity measurement is required, the DAS method is preferred; range resolution and knowledge of target scattering properties are compromised however, because the scattering target is usually at a fixed range from the origin of the transmitted pulse [Measures, 1984]. This technique is often used to observe a plume that only exists over a small range in the laser path, although multiple paths through the same medium can be used to construct plume mapping models [Price, 1999]. Studies suggest that DAS provides the optimum system approach for quick and accurate detection and measurement of a species of interest.

3.2 DIAL and DAS Equations

The following relationships describe the characteristics of path absorption systems operating in both DIAL and DAS configurations. The number density equation useful for both of the differential absorption cases makes use of the basic lidar equation for returned power due to elastic scattering as presented by [Measures, 1984],

$$P_{rec}(\lambda, R) = P_{out}\,\frac{A}{R^2}\,\frac{c\tau_L}{2}\,\xi(\lambda)\xi(R)\beta(\lambda, R)e^{-\int_0^R \kappa_T(R)dR}, \qquad [3.1]$$

where,

P_{out}, P_{rec}	are the respective powers [J] transmitted and received per pulse at wavelength λ,
A	is the area of the receiving telescope [m^2],
c	is the speed of light [m/s],
τ_L	is the pulse duration period [s],
R	is the range to the scattering entity [m],
ξ (λ)	is the total optical efficiency at wavelength λ for all optical elements [unitless],
ξ(R)	is the probability that radiation from range R reaches the detector based on geometrical considerations,
β(λ,R)	is the backscatter cross section per unit volume [m^{-1}] in the volume element for the laser wavelength λ,
κ_T(R)	is the total attenuation coefficient at wavelength λ at range R [m^{-1}].

The DAS measurement for a hard target return begins by expanding the basic lidar equation to characterize differential absorption using two lasers and compare the energies returned. The measured return energy from a pulse transmitted on the absorption feature and slightly off of it for a species of interest can be described via the equations derived from elastic scattering [Measures, 1984],

$$E_{rec,on}(\lambda_{on}, R_T) = E_{out,on}\,\frac{A}{{R_T}^2}\,\xi(\lambda_{on})\xi(R_T)\,\frac{\rho^s \tau_d}{\pi\,\tau_L}\,e^{-2\int_0^{R_T}\left[\kappa(\lambda_{on},R)+N(R)\sigma^A(\lambda_{on})\right]dR} \qquad [3.2]$$

$$E_{rec,off}(\lambda_{off}, R_T) = E_{out,off}\,\frac{A}{{R_T}^2}\,\xi(\lambda_{off})\xi(R_T)\,\frac{\rho^s \tau_d}{\pi\,\tau_L}\,e^{-2\int_0^{R_T}\left[\kappa(\lambda_{off},R)+N(R)\sigma^A(\lambda_{off})\right]dR} \qquad [3.3]$$

where,

$E_{out,on}$, $E_{rec,on}$	are the respective energies transmitted and received per pulse at the online or measurement wavelength [J],
$E_{out,off}$, $E_{rec,off}$	are the respective energies transmitted and received per pulse at the offline or reference wavelength [J],
R_T	is the range to the topographical scattering target [m],
$\xi\,(\lambda_{on})\ \xi\,(\lambda_{off})$	are respectively the total optical efficiency at on and off wavelengths λ_{on} and λ_{off}, for all optical elements [unitless],
$\xi(R_T)$	is the probability that radiation from range R_T reaches the detector based on geometrical considerations,
τ_d	is the detector integration period [s],
τ_L	is the pulse duration period [s],
ρ^s	is the scattering efficiency of the target [unitless],

$\sigma^A(\lambda_{on})$, $\sigma^A(\lambda_{off})$ are the absorption cross sections [m^2] for the species of interest at the online and offline wavelengths λ_{on} and λ_{off},

$\kappa(\lambda_{on},R_T)$, $\kappa(\lambda_{off},R_T)$ are the attenuation coefficients of the atmosphere to the online and offline wavelengths λ_{on} and λ_{off} independent of the absorbing species [m^{-1}],

N(R) is the number density of the absorbing species [# m^{-1}] and,

A is the area of the receiving telescope [m^2].

The term describing the atmospheric backscatter in the normal DIAL case has been replaced with the scattering efficiency of the topographic target. Additionally, there is also a factor of π in the denominator of the equation because the laser reflection is assumed to be diffuse in nature and can be modeled as a Lambertian emitter. The ratio of the detector integration time to the pulse length appears in the equation to normalize measurements, pulse fragments, and appropriately weight the percentage of received energy. Typically, the detector integration time is long enough to capture the entire return pulse, and when this is the case, the detector integration time to pulse length ratio can be set to unity [Measures, 1984]. When the ratio between the online and offline return energies is formed, many of the variables present in both equations can easily be canceled, assuming the transmitted wavelengths are spectrally close to each other. This is also a requirement of the classic DIAL approach. Because the wavelengths are spectrally near each other, they are assumed to have the same fraction of scattered intensity from the target, optical efficiency through the system, and transmission characteristics through the atmosphere. When performing differential absorption measurements using returns from a topographic target, careful consideration must be given to verify that the transmitted online and offline wavelengths have approximately the same target reflectance. Small variations in reflectivity as a function of wavelength can severely bias differential absorption concentration results, particularly for those species that are low in concentration or have large absorption features in the spectra; most surface reflectances vary slowly as a function of wavelength; and it is assumed that the wavelengths used in a DIAL pair are spectrally close [Asner and Heidebrecht, 2003]. The transmitted energy of the two lasers is typically included as a constant ratio in front of the equation [Measures, 1984], and is acquired through energy monitors during laser operation. If both beams are transmitting on the same optical axis and the classical DIAL conditions are met, then the ratio of the offline return energy to the online return energy can be further simplified as,

$$\frac{E_{rec,off}(\lambda_{off},R_T)}{E_{rec,on}(\lambda_{on},R_T)}=\exp\left[2\int_0^{R_T}[N(R)]dR\left[\sigma^A(\lambda_{on})-\sigma^A(\lambda_{off})\right]\right. \\ \left.-\kappa(\lambda_{off},R)+\kappa(\lambda_{on},R)\right] \qquad .[3.4]$$

This ratio can be calculated to find the integrated concentration of the absorbing species along the path of propagation,

$$\int_0^{R_T}N(R)dR=\frac{1}{2\left[\sigma^A(\lambda_{on})-\sigma^A(\lambda_{off})\right]}\left[\ln\left[\frac{E_{rec,off}(\lambda_{off},R_T)}{E_{rec,on}(\lambda_{on},R_T)}\right]+\kappa(\lambda_{off},R)-\kappa(\lambda_{on},R)\right]$$

$$=\frac{1}{2\sigma^A_{diff}}\left[\ln\left[\frac{E_{rec,off}(\lambda_{off},R_T)}{E_{rec,on}(\lambda_{on},R_T)}\right]+\kappa(\lambda_{off},R)-\kappa(\lambda_{on},R)\right], \qquad [3.5]$$

where the differential absorption cross section [Measures, 1984] is,

$$\sigma^A_{diff}=\sigma^A(\lambda_{on})-\sigma^A(\lambda_{off}). \qquad [3.6]$$

The differential absorption cross section is the fundamental quantity in determining the concentration of the target gas species.

The Differential Absorption Spectroscopy (DAS) method uses a hard target return to measure the path integrated species concentration based upon the relative transmission of the two wavelengths along the path to a target and back to the receiving telescope [Measures, 1984]. The typical DAS equation can be applied to the ratio of return energies from the topographic target to determine a species concentration-path-length (CPL),

$$CPL = \int_0^{R_T} N\ (R)dR = \frac{1}{2\sigma_{diff}^{A}}\left(\ln\left[\frac{E_{off}(\lambda_{off}, R_T)}{E_{on}(\lambda_{on}, R_T)} \right]\right). \qquad [3.7]$$

The DIAL/DAS collection geometry assumes that scattering by aerosols, or by the target surface, is essentially the same for both wavelengths; therefore, the difference in transmission through the atmosphere only depends on the difference in molecular absorption between the two wavelengths by the species of interest. Sometimes the measurement will involve measurements of a plume of a gas that is also present in the background atmosphere. Therefore, if there is uniform atmospheric background of the species of interest, the final calculated CPL will be offset by the background CPL. The offset, of course, would depend on the path length and background concentration.

3.3 Atmospheric Background Considerations for DAS

When it is desired to measure the CPL of the column containing a species that also exists in the atmospheric background, the atmospheric absorption of the selected species contribution must be taken into account. Additionally, in the event that the system is configured to detect a molecular species that does not naturally occur in the atmospheric background, then the background atmospheric absorption of any other interfering species must still be considered carefully in selection of the online and offline wavelengths. When other interfering molecules are uniformly distributed in the background atmosphere, the range to topographic target can be reduced to minimize atmospheric signals of the interferent and improve the species CPL measurement. The differential-extinction optical depth of the atmosphere, exclusive of the absorption by the molecular species of interest, can be analyzed to examine the corrections that should be applied for the interfering species. The differential absorption cross section for the interfering species at the chosen wavelengths, and the atmospheric concentration of the interferent CPL are the primary factors influencing the measurement, as indicated in the relation for the interferent species differential absorption optical depth,

$$\xi_e = \int_{R_1}^{R_2} CPL_{bckg.interferent} * \sigma^{A}_{diff,\mathrm{int}erferent} \ , \qquad [3.8]$$

For example, if a DIAL wavelength pair is chosen to detect propane using wavelengths in the MWIR, the optimum selection would avoid the significant methane and water absorption features (interferents) expected in that region. With carefully chosen lines, the contribution of the differential extinction optical depth to the final CPL of propane would be negligible. However, if a DIAL pair is chosen for propane measurements, and the methane absorption is also present on one or both of the lines, then the differential optical depth provides a method calculating the appropriate propane CPL. The final equation for target species CPL (Eq. 3.7) can be modified to include this absorption in the following equation,

$$CPL_{target} = \int_0^{R_T} N_{target}(R)dR = \frac{1}{2\sigma^A_{diff,target}}\left(\ln\left[\frac{E_1(\lambda_1, R_T)}{E_2(\lambda_2, R_T)} \right] - \left[CPL_{bckg.methane} * \sigma^A_{diff,methane} \right] \right), \quad [3.9]$$

and expresses the general form of the DIAL lidar equation, and also can be used for error analysis of DAS measurements.

3.4 Error in DAS Analysis

The previous section shows that the atmospheric effects on the measurement and reference beams, $\kappa(\lambda_{on},R_T)$, $\kappa(\lambda_{off},R_T)$, are principal factors in the final analysis equation. Fluctuations in the atmospheric variables, as well as other error sources, have been well documented by Shell Research Ltd. and SESL through various publications on DIAL lidars [Walmsley and O'Connor, 1998]. Shell Research Ltd. and SESL have together operated an infrared DIAL lidar to measure methane, ethane, and heavier alkanes; also in 1995, they developed and validated their error calculations. The calculations were completed using the classic DIAL analysis for atmospheric backscatter, where minimum return signals drive the key factors in the overall signal-to-noise ratio of the system. Our approach to error calculations appropriate for the DAS geometry are now presented for a case where signal levels are high, and where a different set of factors influence the errors in the measured concentrations.

The limiting factors in DAS system error calculations are due to the fluctuations in the energy of the return signals. Unlike regular DIAL or Raman lidars, DAS systems do not suffer as much from detection limits, but depend primarily on signal-to-noise, or signal-to-background, ratios. DAS systems have smaller errors because they have sufficient signal-to-noise or signal-to-background ratios from the strong backscattering of topographical targets, which are the source of the large return signals. The lower detection limit of the DAS instrument depends on the overall errors in the returned signals. Noise and fluctuation in the returned signals are governed by several parameters that can be grouped into five significant categories:

#1. <u>Uncertainty in Energy Measurements</u> - Two main contributors are:

  a. electronic noise (noise from the transmitted or received signals associated with the control and detector electronics),
  b. statistical error in the collection of return energy measured by the detector system.

#2. <u>Effects of Ground Reflectivity Variations</u> - The effects of variations in ground reflectivity, and systems operating with imperfect far field beam alignment and overlap experience measurement errors.

#3. <u>Uncertainty in the Atmospheric Optical Depth</u> - Uncertainty in the differential extinction optical depth for the atmosphere, **exclusive** of the absorption of the species of interest (i.e. absorption by other species or scattering by aerosols), can influence the accuracy of the analysis.

#4. <u>Match of the Online Laser to the Selected Absorption Feature</u> - Variation in absorption overlap between the transmitter beam spectrum and the spectral absorption structure of the measured species.

#5. Additional Atmospheric Interference – Items such as solar radiance, thermal radiance, transmission scattering from the path, and absorption by other interfering species.

Some additional error sources that are not yet included in the error analysis are laser wavelength jitter, time delay between online and offline measurements (differences caused by changes in scattering properties in regions of higher atmospheric turbulence), system efficiency, and differences in ground reflectivity as a function of wavelength. The noise floor of the actual system detectors (whether they are photon multiplier tubes or solid state) causes some error at the lower end of detection range, but significant signal levels are usually acquired using the DAS method. At higher concentrations, the returned signal may be so highly attenuated that the signal levels approach the noise equivalent power (noise floor) of the system, and cause large errors in CPL to occur.

To determine the minimum detectable limit when using topographic scattering, for either DIAL or DAS lidar, one must first examine the CPL error expected. This error determines the minimum detection limit of the system. The analysis begins with the equation for number density error given by [Measures, 1984] for a DIAL lidar system,

$$\varepsilon_N = \frac{\delta N}{N} = \frac{1}{2 * N * \Delta R * \sigma_{diff}^{A}} \left[\sum_{j=1}^{lasers} \sum_{k=1}^{ranges} \left\{ \left(\frac{hc}{\lambda_j \eta_j \left(\frac{2\Delta R}{c} \right)} \right) \frac{\left(P_{jk}^{signal} + P_j^{skybckg} + P_j^{system} \right)}{m_{jk} * \left(P_{jk}^{signal} \right)^2} + \left(\frac{\delta \beta_{jk}}{\beta_{jk}} \right)^2 \right\} + \xi_e^2 \left(\frac{\delta \xi_e}{\xi_e} \right)^2 \right]^{1/2}$$

[3.10]

where,

ξ_e	is the differential-extinction optical depth exclusive of an atmospheric species of interest,
$\delta\xi_e$	is the variation of the differential-extinction optical depth,
P_{jk}^{signal}	is the signal power returned minus absorption corresponding to wavelength j and range k,
$P_{j}^{skybckg}$	is the power returned due to the sky background radiance, corresponding to wavelength j,
P_{j}^{system}	is the system noise power corresponding to wavelength j,
η_j	is the quantum efficiency at wavelength j of the detector,
m_{jk}	is the number of laser shots used for the calculation for wavelength j, range k,
$\delta\beta_{jk}$	is the uncertainty in the volume backscatter coefficient for wavelength j, range k,
β_{jk}	is the volume backscatter coefficient, for wavelength j, range k,
ΔR	is the range to target,
σ_{diff}^{A}	is the differential absorption cross section,
δN	is the uncertainty in the number density, and
N	is the number density of the species of interest.

The error in the CPL can be calculated using this equation. Examining terms in the equations shows that the first term in the summation describes the total fluctuation in normalized return power due to various measurement errors. The range summation can also be removed in cases when we are only interested in the two-way path attenuation of the transmitted pulse after striking the topographical target. The return from atmospheric backscatter is orders of magnitude less than that from the topographical target. The returns from a pulsed laser are easily found with a simple pulse-finding algorithm. Additionally, if the geometry is properly considered, minimum transmitted power and/or reduced integration time is expected, when compared to atmospheric backscatter lidar systems. For these reasons, it is possible to reduce or eliminate the signal averaging and still have satisfactory performance.

Next, the differential backscattering coefficient is considered for the topographical scattering case. The variations are characterized by the surface reflectivity, $\delta\rho_{topo}$, and the overlap percentage, γ. The variations in ground reflectivity represent the fact that real world measurements are typically collected with a variable topographic reflectivity. Spectral databases can be used to gauge the surface reflectivity for a given target. If the DIAL paradigm is enforced, and wavelengths are chosen to be spectrally “close,” then the error contribution due to reflectivity differences decreases dramatically. The typical surface reflectance variation of topographical targets is a slowly varying function of wavelength; however, it can affect the magnitude of error introduced into the system by the differential backscattering coefficient. If the beams are fully overlapped and strike an unchanging, or slowly changing topographical target, only small errors would be introduced into the observed CPL; whereas, a rapidly changing target with highly variable reflectivity coupled with any beam misalignment will introduce high frequency noise. Variations in wavelength dependence of atmospheric path transmission in the various components in the sensor optical chain can also impart error in CPL. Slowly varying effects can be minimized with proper alignment and calibration, and high frequency effects are typically reduced with integration or by using smoothing algorithms. Depending on the application, sources of error can be reduced; therefore, the following error analysis assumes the DIAL wavelength selection conditions are met. The equation for CPL error fraction using a topographical target at the end of a long absorption path can then be written as,

$$\varepsilon_{CPL} = \frac{\delta CPL}{CPL} = \frac{1}{2 * CPL * \sigma_{diff}^{A}} \left[\sum_{j=1}^{lasers} \left\{ \left(\frac{\delta E_j^{total}}{E_j^{signal}} \right)^2 \right\} + \left(1 - \frac{\gamma}{100} \right) \left(\frac{\delta \rho_{topo}^{s}}{\rho_{topo}^{s}} \right)^2 + \xi_e^2 \left(\frac{\delta \xi_e}{\xi_e} \right)^2 \right]^{1/2} , \tag{3.11}$$

where,

δE_j^{total}	is the uncertainty in the total normalized return energy due to error in energy measurement at wavelength j,
E_j^{signal}	is the signal return energy at wavelength j,
γ	is the overlap percentage,
ρ_{topo}	is the ground reflectivity, and
$\Delta\rho_{topo}$	is the variation in ground reflectivity.

Note that the signal energy, E_j^{signal}, is calculated by removing the dark current response and the sky background noise from the total calculated return energy. Detailed derivations and explanations relative to each of the terms found in Equation 3.11 are included in Appendix A.

3.5 Simulation of Differential Absorption Error Sources

To further examine error in CPL, we simulate a sensor for methane detection using the following logic and the above derivation for DAS. The choices for the online and offline wavelength are the most important as these choices will ultimately determine the sensitivity of the design for small concentrations. The rest of the chosen system parameters are summarized in Table 3.1. Exact wavelengths are not included in this table due to proprietary restrictions. The wavelengths reside in the 3.4 μm region and are separated significantly in wavelength in comparison with classic DIAL cases (roughly 40 nm). Even through they are sufficiently separated, the optical transmission in the selected region of the MWIR is relatively constant as a function of wavelength. Surface reflectivities in the MWIR† vary more significantly, but, the variation is also a minimum for the selected wavelengths. The developed simulation software accounts for a part of these variations in terms of atmospheric differences.

Topographic target spectral variations for wider wavelength bands can be a significant source of error if the DIAL wavelengths are sufficiently separated, and this is not currently included in published versions. As an example of this variation, the NIR reflectivity of a typical topographical target, soil, in the 40 nm wavelength range examined later in this work (Chapter 6) is relatively constant, see Figure 3.1a. Note, however, that the reflectance of other groundcovers over larger wavelength ranges can vary more significantly, see Figure 3.1b.

---

† A full spectral database of ground reflectivity for many groundcovers was created through measurement and is available to Penn State and ITT researchers; it is not yet released in open publication however.

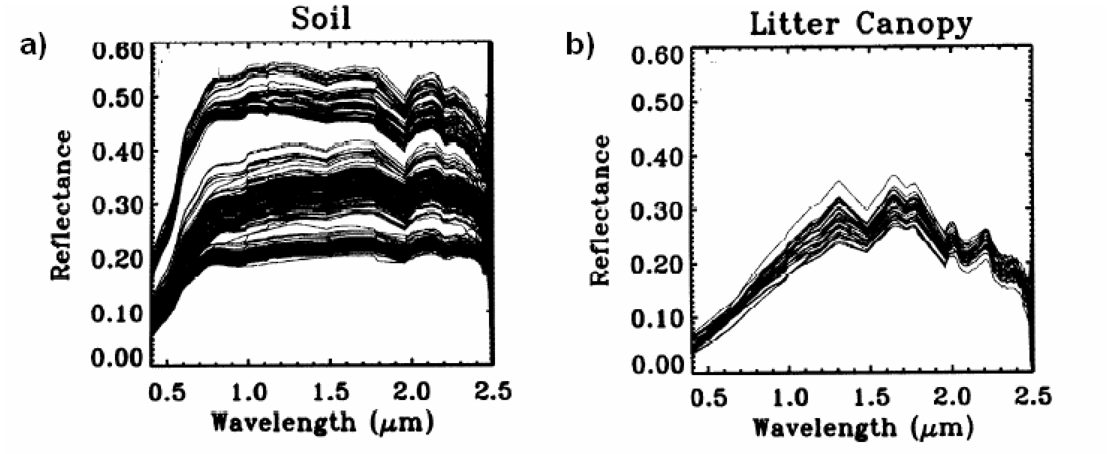

Figure 3.1: Surface reflectivily variation as a function of wavelength for soil (a) and a littered tree canopy (b) for the VIS-NIR [Asner and Heidebrecht, 2003]

Table 3.1: Initial methane detection scheme

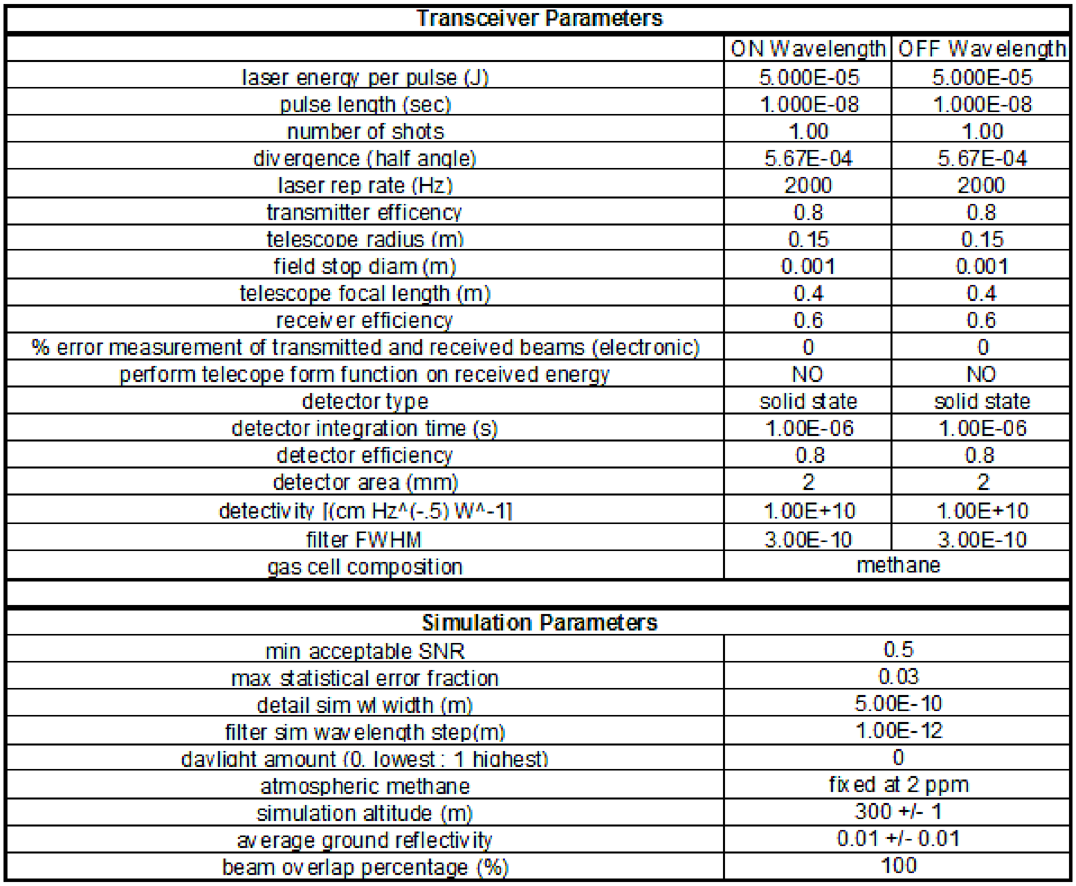

Transceiver Parameters		
	ON Wavelength	OFF Wavelength
laser energy per pulse (J)	5.000E-05	5.000E-05
pulse length (sec)	1.000E-08	1.000E-08
number of shots	1.00	1.00
divergence (half angle)	5.67E-04	5.67E-04
laser rep rate (Hz)	2000	2000
transmitter efficency	0.8	0.8
telescope radius (m)	0.15	0.15
field stop diam (m)	0.001	0.001
telescope focal length (m)	0.4	0.4
receiver efficiency	0.6	0.6
% error measurement of transmitted and received beams (electronic)	0	0
perform telecope form function on received energy	NO	NO
detector type	solid state	solid state
detector integration time (s)	1.00E-06	1.00E-06
detector efficiency	0.8	0.8
detector area (mm)	2	2
detectivity [(cm Hz^(-.5) W^-1]	1.00E+10	1.00E+10
filter FWHM	3.00E-10	3.00E-10
gas cell composition	methane	
Simulation Parameters		
min acceptable SNR	0.5	
max statistical error fraction	0.03	
detail sim wl width (m)	5.00E-10	
filter sim wavelength step(m)	1.00E-12	
daylight amount (0. lowest : 1 highest)	0	
atmospheric methane	fixed at 2 ppm	
simulation altitude (m)	300 +/- 1	
average ground reflectivity	0.01 +/- 0.01	
beam overlap percentage (%)	100	

As explained, typical DAS lidar systems are not as limited as DIAL techniques by the signal-to-noise ratio (SNR) at the low concentrations due to a large fraction of the energy being returned to the detector. Therefore, the minimum useable SNR only makes use of the form factor calculation. This factor is more important for high altitude analysis, or for DIAL lidar calculations where the scattering target is the aerosol background rather than a topographic target at a fixed range. Similar calculations for the statistical error result in low values for small targets at close ranges because of the large energy return from the surface. Consideration of these limits becomes more important for systems where a very small fraction of the transmitted energy is returned (classic DIAL case), because this limitation imposes a cutoff in the system sensitivity. The sensitivity threshold can be used to calculate a SNR, which leads to a value for the signal levels required to properly distinguish the concentration of the selected species. Performance simulations for a DIAL lidar operating similar system parameters with to those shown in Table 3.1 can be found in Appendix B.

3.5.1 DAS Performance Limitations

The DAS performance simulation is used for a variety of tasks including sizing of system components for potential DAS lidar instruments, estimating measurement sensitivity, and troubleshooting existing hardware systems. To demonstrate the capability and importance of the lidar system simulation, we examine a case of methane detection using an air to ground measurement geometry, similar to the ITT ANGEL system [Grund, *et al.*, 2004; Murdock, *et al.*, 2008; Stearns, *et al.*, 2006]. When designing a DAS system similar to the ANGEL, the most important choices are the selection of the online and offline wavelengths, because these will ultimately determine the sensitivity of the sensor for measuring small concentrations. Furthermore, the wavelength selection determines the magnitude of the effects from the clutter signal for random topographic scatterers, which are often not spectrally flat as shown above by Figure 3.1. The error analysis includes the variations due to atmospheric and surface reflectance and introduces appropriate random noise levels to simulate the return signal.

DAS lidar systems are not typically limited by the signal-to-noise ratio at the detection threshold due to the large fraction of the energy scattered back to the detector. Instead, it is the temporal fluctuation in the return signals that severely limits the performance. This type of limitation is particularly important for airborne systems that are looking down at the rapidly varying background of roads, grass, trees, etc. Integration of multiple pulses is not feasible for a fast scanning configuration; hence, CPL calculations are individually performed for each outgoing pulse in such a case. Small temporal fluctuations in the measured signals associated with target reflectivity, and other factors, introduce noise into the calculated CPL, and thus raise the lower detectable limit. The DAS simulations provide the flexibility to simulate both integrating and non-integrating systems, as well as to estimate the magnitude of error sources.

In special cases of highly concentrated plumes, measurement of the species concentration can be difficult if the system is starved for return energy. Furthermore, low signal-to-background in the return energy can occur in a number of cases, particularly if a long absorption path is being used to measure species. Other causes include cases when a background atmospheric concentration of the species being measured is present, or when the end-path topographical target has a low reflectivity. Choosing DIAL online wavelengths that are centered on large absorption features can also severely affect CPL calculations if a species strongly absorbs, and the offline return signal is already small. In this case, it may only be possible to detect that a signature is present qualitatively. These types of measurement conditions cause the error in the CPL result to grow for higher species concentrations of strongly absorbing lines. In summary, important factors include: the wavelength choice, the received energy, and the collection efficiency.

3.5.2 Example DAS Simulation Result

The DAS simulation tools allow a system designer to select configurations, and to size a system to accurately quantify a species at a given range, and for a range of possible concentrations. As an example, we consider a simulation for methane detection. The geometry selected for this system configuration is an aircraft mounted DAS instrument system that uses the ground for a topographical target.

The flight altitude for this simulation is 300 m with a ground reflectivity of 0.01 +/- 0.005. Although this is a case with relatively large fluctuation in reflectivity, we are selecting a case with minimum error in final CPL in this initial example because of choosing a 100% overlap of the beams in the system arrangement. Beam overlap is quite important for DIAL or DAS systems, particularly for those cases where a temporally varying topographic scatterer is expected. If the transmitted beams are not completely overlapped, then variations in the ground reflectivity will dramatically increase the noise in the calculated system CPL. With typical COTS

MWIR hardware parameters as shown by Table 3.1 (i.e. laser transmitter power, detector sensitivity, etc.), and standard atmospheric conditions derived from MODTRAN^{TM} 5, we are able to simulate the signals expected for the online and offline wavelengths as a function of species concentration. The fluctuation in these return energies governs the percent error of measurements obtained by the system. Assuming that we have a case of 100% beam overlap and no electronic noise results in no error in transmitted and return energy measurement. Under these assumptions, we can calculate percentage error as a function of plume size. Simulated return signals for the online and offline wavelengths and percentage error versus target plume CPL can both be found in Appendix C.

Figure 3.2a shows the expected system measured CPL, with the appropriate error bars added, compared with the idealized case. In this example, we have chosen to study methane, and the atmospheric background causes the offset in the system measured plume (blue line). Ideally, we would expect the blue line to overlap the green line with a perfect system, and no atmospheric background absorption. Figure 3.2b describes a simulation of the signal temporal response. The system response is examined for a series of five staged methane leaks with magnitudes of 10, 50, 100, 250, and 500 ppm·m, and each target is probed by the system for a series of five consecutive measurements, then followed by fifty no-plume measurements. This visualization helps us to understand how a sample of raw data would appear, and assists in developing the data processing and temporal averaging algorithms. Note that with 100% overlap and minimal electronic noise, the

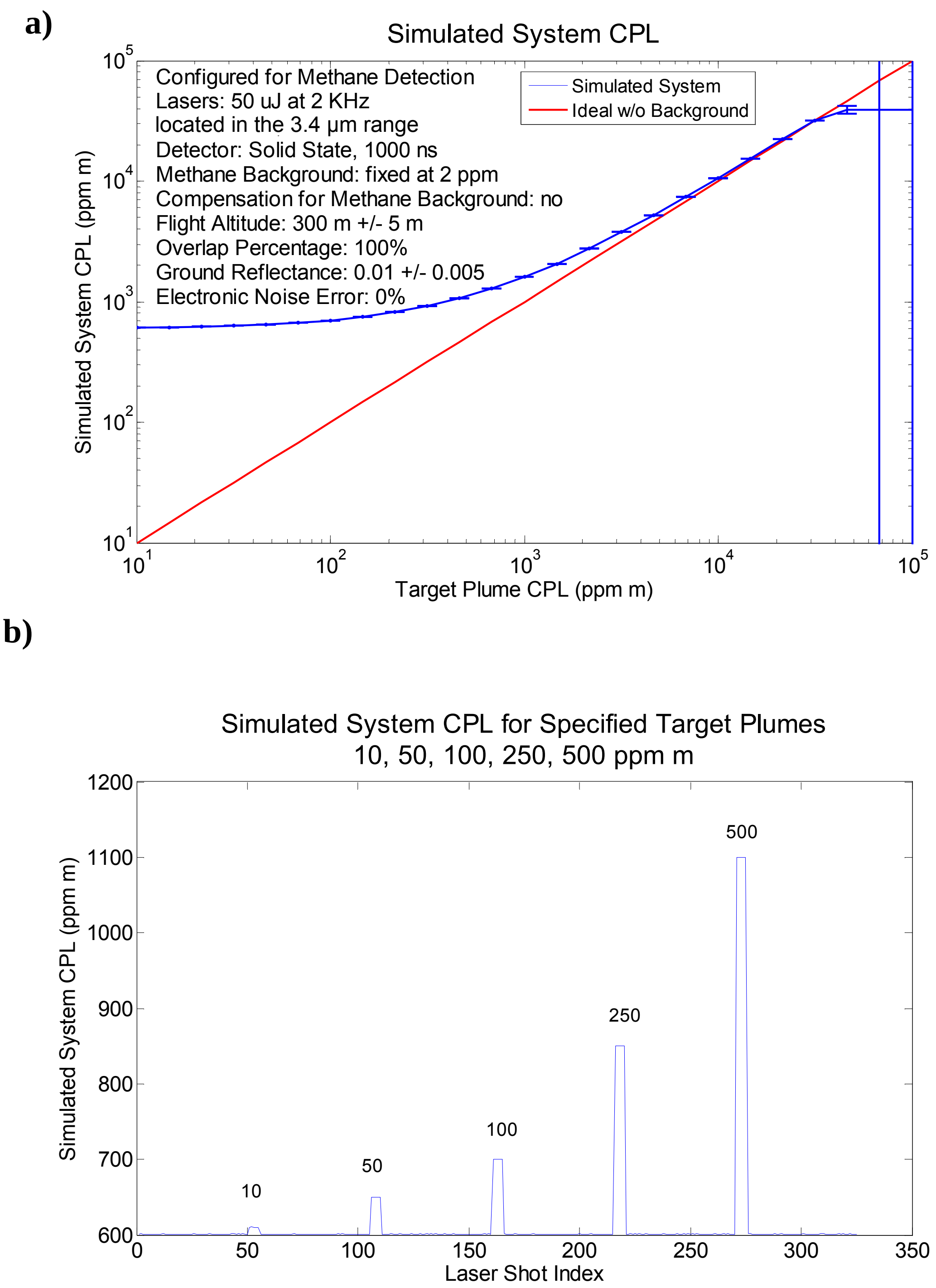

Figure 3.2: Simulation results for methane detection with no transceiver measurement error and 100% overlapping beams. (a) Simulated system CPL as a function of plume size, and (b) Simulated temporal response encountered for a series of five different size plumes.

absorption signature for plumes as small as 50 ppm·m are far enough above the noise floor to be easily observed. If it is assumed that this is the limit of detection for the simulated altitude at 300 m, then the detection limits are expected in the 100s of ppb range for long path absorption, where substantial averaging can be used to improve the SNR, and hence this analysis agrees with predictions of Inaba, *et al.* [1976].

A second example now examines the importance of low noise measurements and careful overlapping of the beams on the system performance, see Figure 3.3. For the same system considered above, we introduce a 5% error due to variations in the transmitted and received energy measurements and in addition we reduce the beam overlap percentage to 80%. The simulated system return signal and percentage error of simulated system CPL can both be found in Appendix C. The simulation shows large errors for small concentrations because the differential absorption is dominated by the noise in the system, see Figure 3.3a. As before, the noise is randomized on a per measurement basis, and can be clearly observed in the simulated CPL output shown in Figure 3.3b.

As Figures 3.3, and 3.3b suggest, the combination of the ground reflectivity variation, non-overlapping beams, and electronic noise cause the once observable small leaks to be lost in noise in the system. Note that this simulation was performed under the assumption that the system is automatically correcting for the methane background offset, hence, the simulated CPL output is centered around zero, and not the original 600 ppm·m. The error introduced in having the system effectively zero out this offset on each measurement also adds to the error associated with each determination of the CPL value.

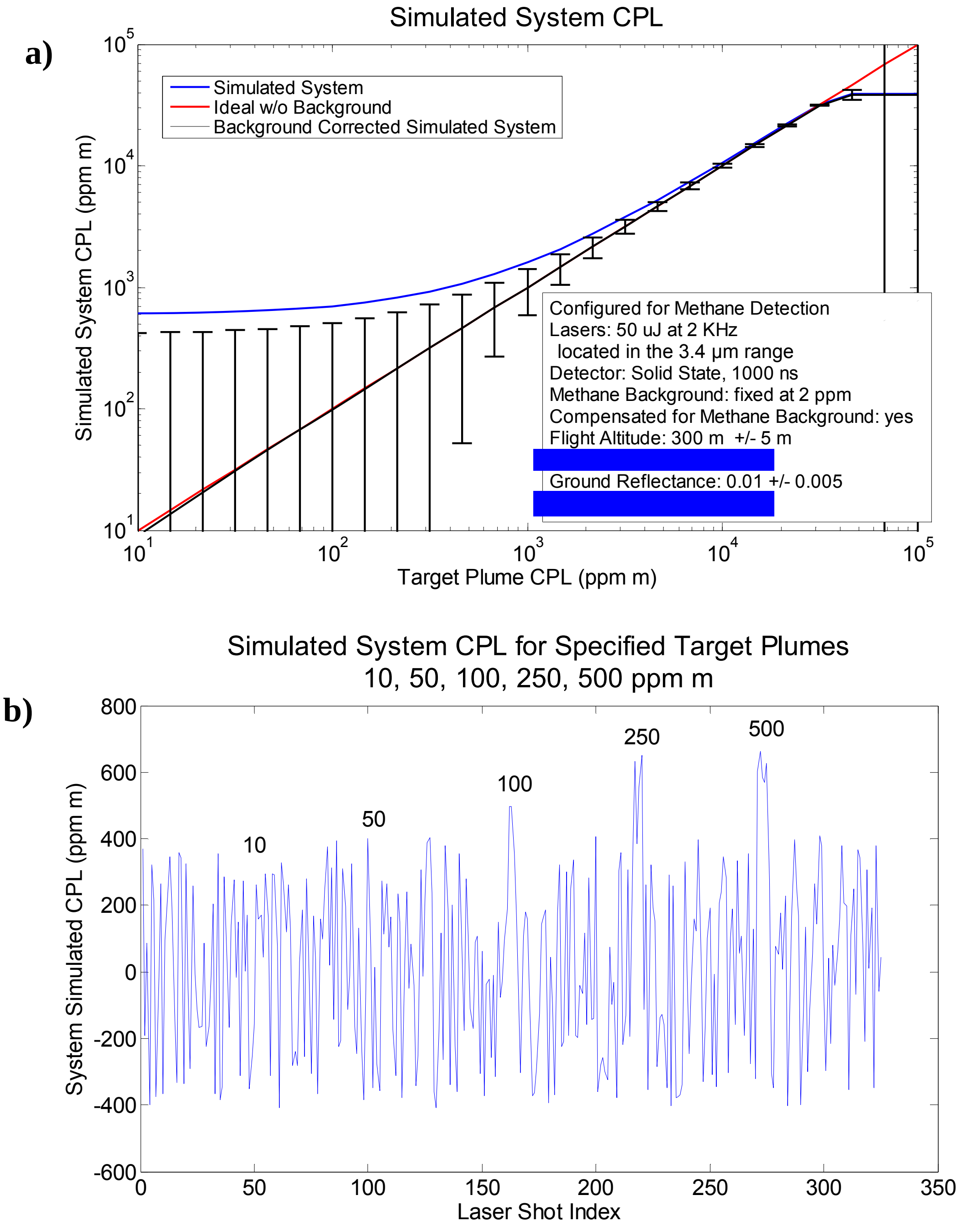

Figure 3.3: Simulation result for methane detection with atmospheric methane background compensation where transceiver measurement and overlap error are introduced. (a) Simulated system CPL as a function of plume size, and (b) Simulated temporal response encountered for a series of five different size plumes.

3.6 Comparing DAS Simulation Results to Experimental Lidar Data

To verify the model, a subset of data from the ITT Industries ANGEL was acquired and used for a comparison. The initial beam alignment of the online and offline lasers was known to be imperfect during integration, and this fact was further confirmed by an overlap test.† A point of reference was chosen in the processed IR camera images to provide the determination of size and center-to-center distance of the online-offline distribution. These overlap measurements provided the information necessary to estimate the methane CPL fluctuation during operation due to misaligned lasers traversing the ground reflectivity variations. While the beam misalignments have since been eliminated from the ANGEL system by and alignment procedure, the data presented below was acquired shortly after the initial aircraft integration and before the final beam alignment procedure. Although there was only a limited amount of data collected when the system was operating in this configuration, a sample flight test over a runway at Buffalo Airport in New York State was sufficient to validate the performance of the model.

3.6.1 Simulation Input and Results

The simulation results shown in Figure 3.4 used proprietary ANGEL system parameters, and therefore are presented with the axes scales removed; the relative comparisons are useful to us in describing the performance however. The results indicate the problem in making a transition across a boundary with different reflection coefficients when the system is misaligned. The CPL trace matches the simulated variations in the measured CPL information relative to the geometry of this case.

---

† Beam overlap tests were administered by Penn State Graduate students Joe Begnoche, Adam Willitsford and myself using a Thermovision 400 Series camera, and a data analysis algorithm [Brown, 2005].

The data set used for comparison was acquired when the ANGEL system was flown over a runway, at a height between 300 and 500 feet with the fast scanning unit deactivated, so the line of the misaligned beams traces across the tarmac on the 7th of October, 2004. The measurement and reference beams scattered from reflectors positioned along the track of the test flight in the middle of the runway. General parameters of the ANGEL system, beam overlap percentage, and topographic reflectivity variation were entered into the DAS simulation model to estimate the magnitude in the variation of the CPL when the system encountered the reflective targets. Overlap percentage was known from a prior overlap test, and reflectivity variations between the tarmac and reflectors were quantified by an infrared reflectivity database developed for use by ITT and Penn State researchers. The simulation was initially run for two cases, when the measurement beam was leading and the other when the reference beam was leading. Although not known at the time of flight, it was determined that the measurement beam was leading the reference beam in the far field distribution.

As distance increases, the leading measurement beam begins to cover the highly reflective paint and the on/off reflectance ratio climbs as shown by Figure 3.4 parts a and b. Concurrently, the system CPL plummets, as shown by Figure 3.4d. The on/off reflectance ratio subsequently falls and returns to the original value as the trailing reference beam moves across the highly reflective target region (Figure 3.4c). The fluctuation in the on/off reflectance ratio causes a decrease and then subsequent increase in concentration path length across the distance of the scan, which can be observed by viewing the full simulation result in Figure 3.4d.

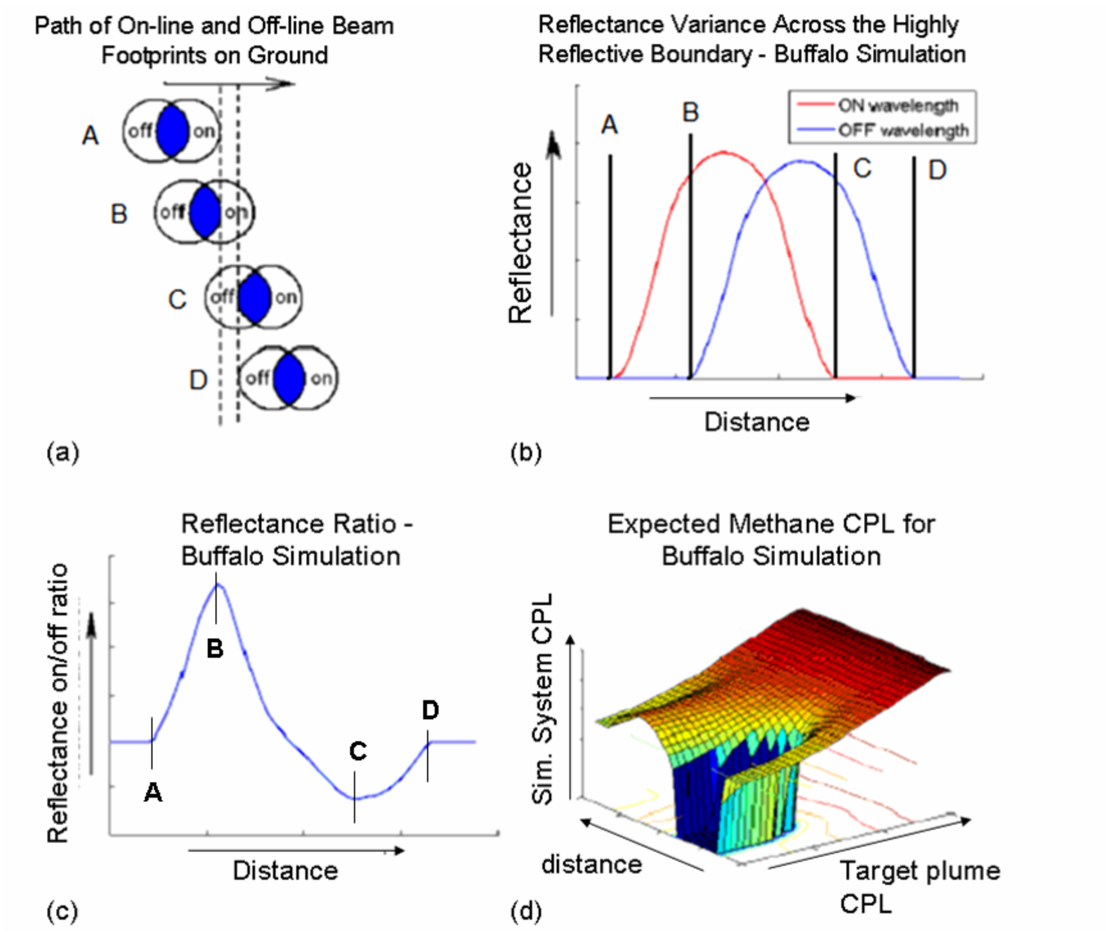

Figure 3.4: Simulation results of the ANGEL System during runway over-flight 10/07/2004. (a) Configuration of far field beam pattern, (b) Variation of reflectance ratio for the online and offline wavelengths, (c) On/off reflectance ratio as the highly reflective boundary is crossed, and (d) Simulated system CPL as a function of target plume CPL and distance as the highly reflective boundary is crossed.

The bottom right axis in Figure 3.4d represents the target plume CPL, while the simulated system CPL is plotted on the vertical axis, analogous to Figures 3.2 and 3.3 above. The depth of the figure (labeled distance) describes the simulated system CPL for many cases as the boundary is crossed. The figure shows that as the target plume CPL increases, the fluctuation in simulated system CPL is less apparent as the boundary is crossed. In contrast, in the case of no methane background, the fluctuation is very dramatic, and even a small amount of reflection variation will affect the CPL reading.

3.6.2 Simulation Results Compared with ANGEL Data

To compare with the ANGEL data taken over the runway on October 7, 2004, we have chosen a section of the simulation to extract in Figure 3.5. Misalignment in the ANGEL system caused periodic deviation in the CPL measurement as the far field distribution of the beams struck the highly reflective paint on the runway as dramatically illustrated in Figure 3.5.

When comparing the ANGEL data with the simulations, we use simulation values described by the region of the 3D plot, Figure 3.4d, in the (Distance, Simulated System CPL) plane where the slope of the graph begins to approach zero, or at the lower edge of the waterfall plot. This trace of the plot corresponds to the case of the system encountering an atmospheric background of methane, and no other absorbing species during the measurement. Although a quantitative assessment of how these apparent CPL readings compare cannot be revealed at this time due to proprietary restrictions, the relative CPL fluctuation for the actual and simulated cases are presented in Figure 3.6.

In general, the actual variation in CPL is closely modeled by the simulation result. The figure also shows that background noise CPL level for the simulation appears to be less than the background noise of the actual data, assuming the constant regions between the passage over the reflectors are averaged. This effect is likely due to the estimated ANGEL system noise parameter values used in the simulation. These values can vary greatly depending on laser stability and beam profile.

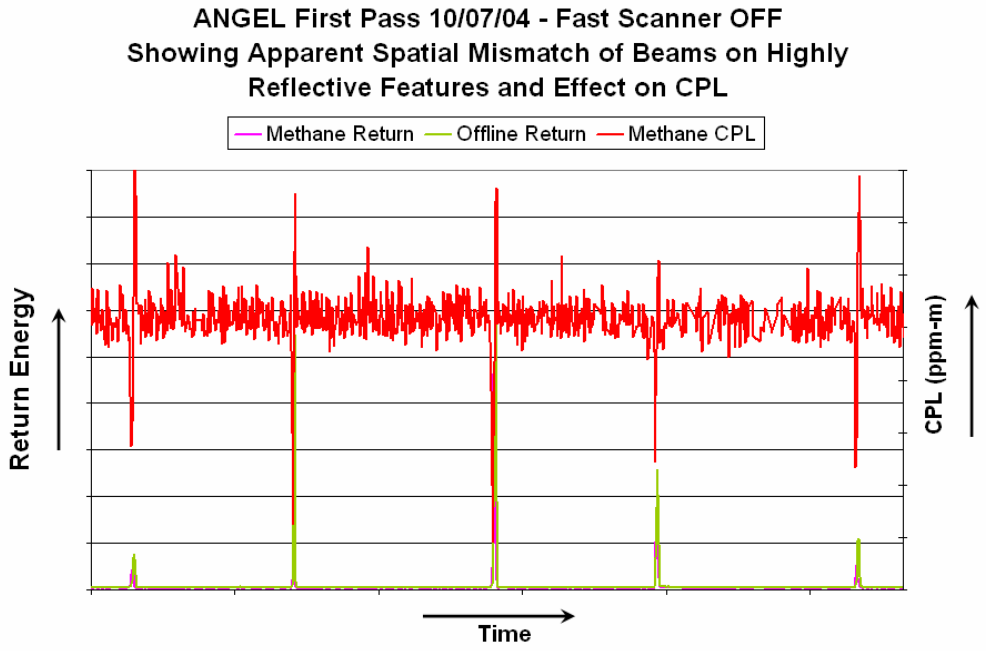

Figure 3.5: CPL fluctuation due to striking of reflective strips in runway.

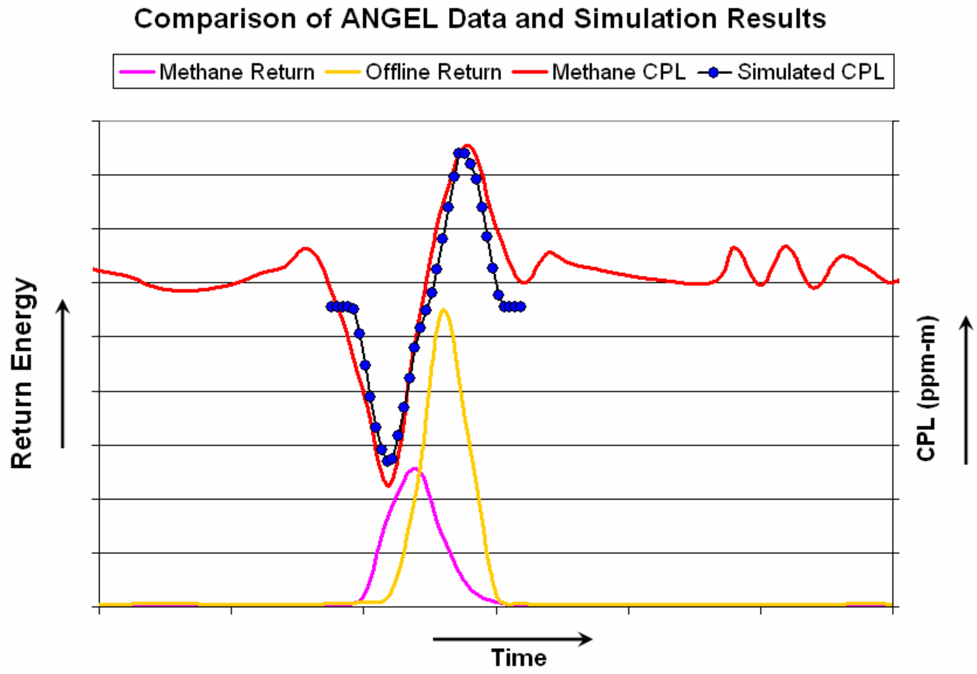

Figure 3.6: Simulated results as compared with actual ANGEL data when striking a single runway reflector.

3.7 Summary

In summary, the error analysis approach has successfully demonstrated the performance changes during various system modifications proposed for use in the ANGEL system for several years. Furthermore, the error analysis and simulations have proven useful for conceptual designs and proof-of-concept studies for following generation DIAL lidar systems using topographical scattering, including the new supercontinuum lidar described in Chapter 7. The DAS simulation program was validated against a controlled set of CPL data from the ANGEL system acquired during a flight test over a runway in Buffalo, NY.

CHAPTER 4

Theory and Simulation of Multi-wavelength Infrared Imaging of Chemical Species

A method for filter selection is developed for a multi-wavelength qualitative detection of hydrocarbon vapor using infrared imaging. The multi-wavelength concepts reported in Chapters 4 and 5 are later combined with classical DAS error reduction concepts reported earlier (Chapter 3) to create a novel measurement scheme (Chapters 7 and 8).

A hydrocarbon plume source within the field of view (FOV) of an imager is investigated to understand how best to effectively image a vapor using a completely passive approach with many wavelengths. Under typical measurement geometry, the source of infrared radiation is the thermal emission from the background being imaged, together with the addition of reflected solar radiation contributions. When an absorbing species is present, the difference in emitted background radiance can be detected by the imager, assuming that absorption removes sufficient intensity to cause a discernable contrast in the image. Additionally, the difference in the images with and without the plume present must be contained within the dynamic range of contrast or sensitivity limit of the camera.

4.1 Characterizing Surfaces with an Imaging Device and Reference Point

Radiometry studies of infrared emission provide the foundation to determine radiant infrared energy from an object of arbitrary shape and size. Classically, the measurement techniques developed to quantify radiant infrared energy are used to measure the temperature of remote objects, or describe temperature differences from a thermal background that indicate heat leaks from a building. Known reference points within the FOV of an image device permit these differences to be used for determining the absolute temperature of remote objects. In the most simple case, it is assumed that objects selected for measurement (humans, stoves, candles, gas plumes) are perfect blackbody radiators where the total isotropic radiated energy can be calculated by use of the Stephan Boltzman law,

$$M = \sigma T^4 \qquad [4.1]$$

where,

M is the isotropic radiative emittance in [W/m^2],
σ is the Stephan Boltzman constant equal to 5.67 x 10^{-8} Wm^{-2}K^{-4},
T is the temperature [K] [Wolfe, 1996].

Isotropic radiators uniformly emit varying amounts of energy in all directions depending on temperature distribution. Figure 4.1 shows several Planck function curves of intensity versus wavelength for different temperatures. The radiant exitance, M_λ in units [W cm^{-2} μm^{-1}], is used to describe the radiant intensity for a given wavelength interval. As the temperature of the blackbody radiator is increased, the entire function will experience a blue shift (to the left), with an increase in the content of shorter wavelengths, while experiencing an increase in magnitude. The Planck distribution can be expressed in terms of wavelength, or as a function of frequency. When expressed as frequency, the radiant energy can be readily observed, as higher frequencies correspond to larger radiant emittance and higher peak values.

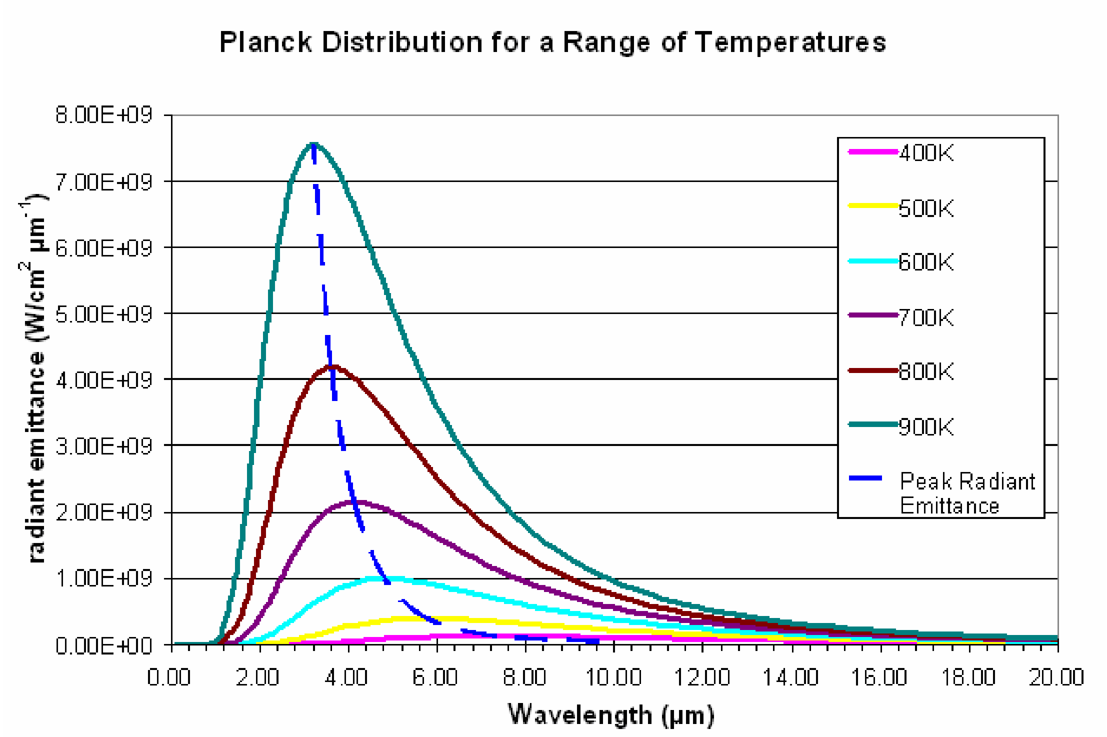

Figure 4.1: Planck functions for different temperatures show the change in peak radiant emittance.

Planck's Law describes the spectral distribution of radiation from a blackbody source with units of watts per square meter per wavelength interval as shown by,

$$M_\lambda = \frac{2\pi c^2 h}{\lambda^5 \left(e^{\frac{hc}{\lambda kT}} - 1 \right)}, \qquad [4.2]$$

where,

c is the speed of light, 3 x 10^8 in [m/s],

h is Planck's constant, 6.626 x 10^{-34} in [J s]

k is Boltzmans constant, 1.38 x 10^{-23} in [J/K], and

M_λ is the radiant exitance emitted [W/cm^2 µm^{-1}] [Wolfe, 1996].

The wavelength of peak radiative emission by a blackbody surface is described by Wiens Displacement Law,

$$\lambda_{max} T = B \, , \qquad [4.3]$$

where,

λ_{max} is the wavelength of maximum radiative energy in meters [m],

B is the constant 2.898 X 10^{-3} meters-Kelvin [m K], and

T is the temperature in Kelvin [K] [Wolfe, 1996].

Isotropic blackbody radiation is useful for characterizing detector systems, because the blackbody source exhibits a broadband and continuous spectrum across a wide range of wavelength. Furthermore, the intensity distribution as a function of wavelength is well known. A simple increase in temperature provides an easy way of increasing the intensity over a range of wavelengths. Isotropic radiation, however, is difficult to measure and therefore it is also difficult to determine the amount of isotropic radiation captured by surfaces.

A Lambertian surface is an important case of radiation transfer occurring when emission is diffuse in nature. The scattering from a Lambertian surface is similar in many respects to a blackbody emitter. When a collimated light source is reflected from a uniform scattering surface, the response is Lambertian. We derive the emitted radiance for this case by starting with the purely spherical isotropic case, as if the radiation is due to a blackbody point source. Instead of allowing the energy to be uniformly disturbed over 4π steradians, however, we choose to allow the energy to be distributed across a half-sphere, corresponding to 2π steradians. To capture the radiant energy, we must then include the area through which the radiant flux passes at range R, as shown by dA_2 in Figure 4.2. The fundamental equation for radiation transfer can be used to calculate the differential element of power projected between two areas shown in Figure 4.2, and described by,

$$d\Phi = L \, \frac{dA_1 \, cos\theta_1 \, dA_2 \, cos\theta_2}{R^2} \qquad [4.4]$$

where,

$d\Phi$	is the differential power element of two areas [W],
dA_1, and dA_2	are respectively the first and second projected areas [m^2],
θ_1, and θ_2	describe the orientation of the first and second projected areas,
R	is the distance between the two projected areas [m], and
L	is the radiance of the Lambertian surface, or the reflected radiance from the incident irradiance [W/m^2 sr] [Wolfe, 1996].

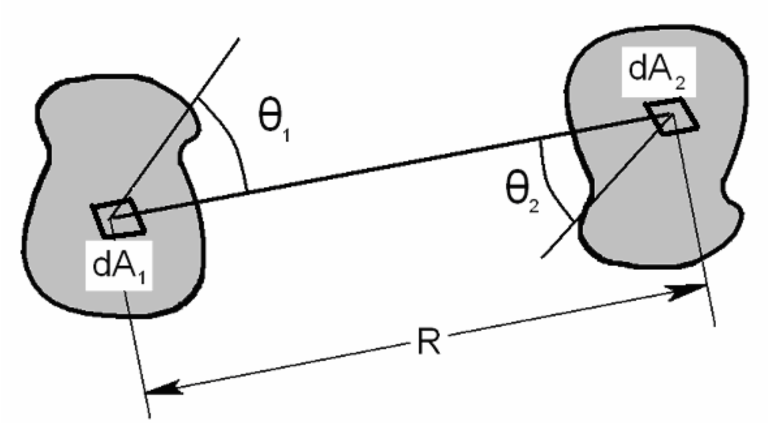

Figure 4.2: Fundamental equation for radiation transfer for two projected areas [Wolfe, 1996].

When one differential element is a Lambertian surface, whether it be an emitter or a reflector, various simplifications can be made to Equation 4.4. By knowing that the emission from the source (the first surface dA_1 radiated over one hemisphere) is received by the second differential area, we can integrate over this region as indicated below using Equation 4.5. The result gives the total emittance in watts per square meter of the Lambertian surface, and can subsequently be simplified to π multiplied by the radiance, L, of the surface [Wolfe, 1996].

$$\begin{aligned} M_{A_1} &= \frac{P}{dA_1} = \frac{\int d\Phi_{A_1}}{dA_1} \\ &= \frac{\int L \frac{dA_1 \, cos\theta_1}{R^2} R^2 \, sin\theta \, d\theta \, d\phi}{dA_1} \qquad [4.5] \\ &= L \int_0^{2\pi} \int_0^{\pi/2} sin\theta \, cos\theta \, d\theta \, d\phi \\ &= L\pi \left[sin^2\theta \right]_0^{\pi/2} = \pi L \left[\frac{W}{m^2} \right], \end{aligned}$$

where,

P is the total power emitted for one half of the total sphere [W],

M_{A_1} is the radiant emittance [W/m^2].

Lambertian emission has also been observed classically in the geometry where a highly collimated light source impinges on a surface. If the reflectivity of the surface and the incident irradiance intensity are known parameters, then the logic of the approach presented above can be used to calculate the radiance from the illuminated surface. Note however, that this assumption is only valid when the reflection is diffuse in nature, as is the case for many real-world topographic targets.

Extending from Equation 4.4 above, we are able to express the radiance from the surface in terms of the incident irradiance,

$$L = \frac{I\, r_{dh}}{\pi} \qquad [4.6]$$

$$M = I\, r_{dh} \qquad [4.7]$$

where,

I is the incident irradiance in watts per square meter [W/m^2], and

r_{dh} is the reflectivity of the surface [unitless] [Wolfe, 1996].

Therefore, Equation 4.7 shows that the radiative emittance, M, from a surface is equal to the reflectivity, r_{dh}, of the surface multiplied by the incident irradiance, I. Noting that the units for radiative emittance, M, and incident irradiance, I, are both [W/m^2] is consistent with these conclusions.

It is possible to make additional calculations that allow description of the emission from remote surfaces by combining knowledge of blackbody radiators and Lambertian surface emission. By measuring the temperature of a blackbody radiator required to match the reflected radiance of a monochromatic light source (typically a laser) scattering from a diffuse reflecting surface, it is also possible to quantify the incident irradiance. In theory, this is relatively easy by numerical methods. The radiant emittance at a range where reflection occurs can be determined using Equation 4.2 and knowing the temperature of the blackbody source. We effectively adjust the radiant emittance at the range by adjusting the temperature of a blackbody source. If the temperature of the blackbody source is adjusted such that the grayscale intensity of the imaged pixels of the blackbody source match the pixels of the reflected laser, then that temperature can be used to calculate an appropriate Planck function. The Planck function found can then be integrated across the wavelength sensitivity range of the imager, thereby defining a radiant emittance of the reflection in terms of [W/m^2]. The incident irradiance can then be easily calculated using Equations 4.6 and 4.7 by knowing the reflectivity of the surface, and assuming it is Lambertian in nature.

Note however, that if this calculation is performed for the typical spectral range of many midwave infrared cameras (3 to 5 μm), then the temperature required to match the reflected radiance of a transmitted laser would be very low. This would then in turn generate a Planck curve that would be out of detectable range and below the sensitivity threshold for most infrared detectors. Therefore, the unmodified measurement technique is best for lasers with high average power. Two simple modifications to this approach provide a mechanism to measure the flux of lower power lasers:

1.) Introduce a notch filter on the imager that straddles the wavelength of the laser radiation under measurement.

2.) Increase the temperature of the blackbody source used to calibrate the measurement.

The notch filter allows only the wavelength of the laser to be transmitted to the focal plane of the imager, thus reducing background effects. The small bandpass of the notch filter, however, limits the region of the Planck curve from the blackbody source observed by the imager. This limitation requires that the radiator be observed at higher temperatures in order to match the reflected flux from the laser.

Any manufactured notch filter will have some amount of spectral width; therefore, accurate transmission characteristics of the filters used in this configuration are required for the calculation of collected energy. In order to account for the emittance spread over a range of wavelengths, every wavelength interval that is allowed to pass must be multiplied by the percent transmittance of the filter function for the interval in question. To express this fact in a familiar form, we modify Equation 4.2 above (Planck's Law) to describe the observed radiative emittance seen through the filter for a given temperature source,

$$M = \sum_{\lambda_1}^{\lambda_1+n(\Delta\lambda)} \frac{2\pi c^2 h}{\lambda^5\left(e^{\frac{hc}{\lambda kT}}-1\right)} \Delta\lambda\, F(\lambda), \tag{4.8}$$

where,

n is the number of wavelength increments [unitless],

Δλ is the width of the wavelength interval in [m],

λ_1 is the beginning of the wavelength range of the filter [m],

M is the total radiant emittance seen through the filter [W/cm^2],

F(λ) is the transmittance for the notch filter at a given wavelength range +/- Δλ/2.

Variations in the distribution of the laser reflection are determined by calculation over a range of temperatures that bound the range of pixel intensities observed in the distribution of the reflection. This intensity scaling of pixel intensities is important for lidar systems when examining beam overlap, clipping, and hot spots in the transmitted beam.

4.2 Directly Characterizing Infrared Imaging Devices

The minimum detectable limit of infrared imagers is determined by integrating under the blackbody radiation curve for the minimum detectable temperature. This integration is bounded in wavelength by the operational wavelength range of the imager. The focal plane arrays (FPA) used in midwave infrared (MWIR) imagers, for example, are sensitive from the NIR to 5 μm in the MWIR. The cold filter placed on the front MWIR imagers typically further reduce the spectral range from 3 to 5 μm.

The method we developed for passive imaging of hydrocarbon plumes depends on an accurate value for the minimum detectable limit of the imager. This limit is governed by lower bound of the measurable temperature range of the imager, in addition to the wavelength sensitivity range. The imager chosen for this study was the Indigo Systems Merlin MWIR. The Merlin camera brochure indicates that the lower bound of the temperature range that can be measured by the Merlin MWIR camera is 0 °C. By searching published results on its core FPA [Hoelter, *et al,* 1999], and reviewing the advanced users manual of the camera [Indigo Systems, 2002], however, we find that the camera is capable of imaging objects of lower temperatures. At the minimum integration time of 2 ms, it is possible to image objects down to temperatures of -20 °C. Furthermore, because the integration time can range from 5 μs to 16 ms, it is feasible to image objects, even below this limit. To retain some flexibility in the system, in terms of integration time and sensitivity, we conclude that the detectable temperature limit of the camera is approximately -20 °C. To determine the minimum detectable limit of the FPA [J s^{-1} m^{-2} μm^{-1} sr^{-1}], we first calculate the irradiance for a -20 °C object, and integrate the area under the curve between 3 and 5 μm. The equations used to remove the μm^{-1} dependence in the total integrated irradiance for the minimum detectable temperature, $I_{\min}$ are,

$$I(\lambda, T) = \frac{2hc^2}{\lambda^5} \frac{1 \times 10^{-6}}{e^{\frac{hc}{\lambda kT}} - 1} \quad \left[\frac{\mathrm{J}}{\mathrm{s}} \frac{1}{\mathrm{m}^2} \frac{1}{\mu\mathrm{m}} \frac{1}{\mathrm{sr}} \right] \qquad [4.9]$$

$$I_{\min} = \int_{\lambda_1}^{\lambda_2} I(\lambda, T) d\lambda \quad \left[\frac{\mathrm{J}}{\mathrm{s}} \frac{1}{\mathrm{m}^2} \frac{1}{\mathrm{sr}} \right], \qquad [4.10]$$

where the units for λ_1 and λ_2 are both in μm, and denote the wavelength range of the bandpass filter associated with the imaging device.

4.3 Capturing Radiant Emittance or Scene Irradiance

The imaging capability of the Merlin camera is modeled on a per pixel basis using published values [Indigo Systems, 2002] for the integration time, optical throughput, and FOV of the camera. We are able to convert the emitted irradiance from a remote surface to radiance collected at the camera, and finally calculate energy captured per pixel in the FPA using these parameters.

4.3.1 Case 1 of Captured Irradiance

The calculation for captured steradiance by an imager depends on the location of the calculated radiance. We define case 1 as an arrangement where the system radiance is calculated at the source, and we define case 2 as an arrangement where the system radiance is calculated at the observer, thus following the approach used in MODTRAN^{TM}. Figure 4.3 depicts the case 1 geometry where radiance is calculated from a surface at elevated temperature. This case can be used to calculate the minimum sensitivity limit of the camera on a per pixel basis.

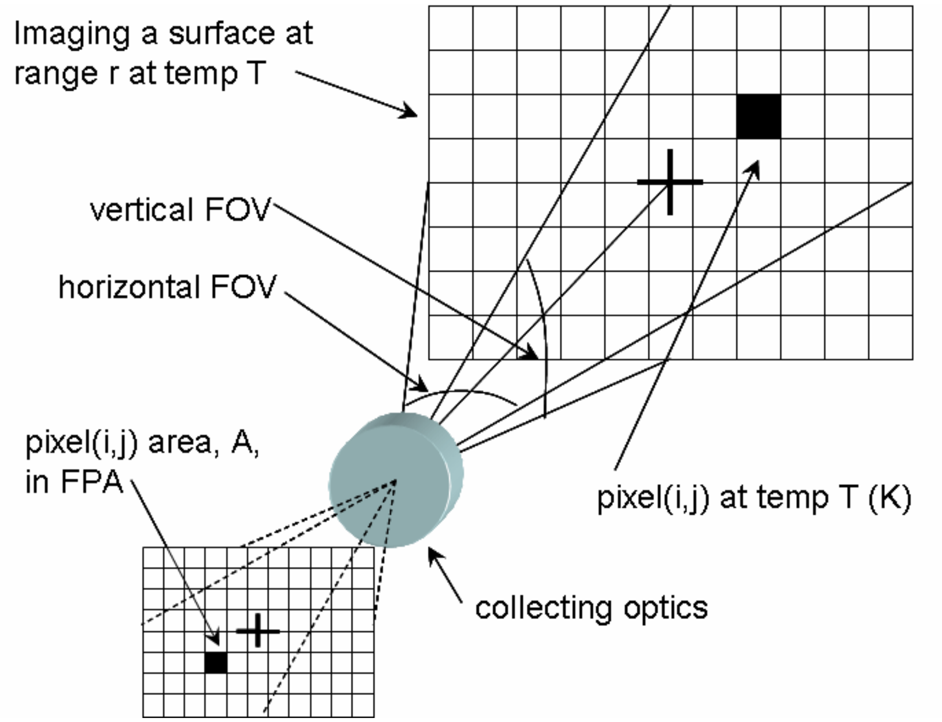

Figure 4.3: Case 1 geometry where a radiating remote surface of constant elevated temperature is used to calculate the energy captured per pixel in the camera FOV.

A well known relationship is used to convert the radiant energy captured by a remote imager on a per pixel basis for simple imaging devices [Mooney, *et al.,* 1989],

$$K_{ij} = \frac{\pi\, A_{ij}\, \tau_0\, t_f\, \cos^4\left(\theta_{ij}\right)}{4\,\left(f\,/\#\right)^2}\,\left[\mathrm{s\ m^2\ sR}\right], \qquad [4.11]$$

where,

i, j index of the pixel $[\text{unitless}]$,

A_{ij} is the area of a pixel in the FPA in $\left[\mathrm{m^2}\right]$,

τ_0 is the optical efficiency of the camera system $[\text{unitless}]$,

t_f is the frame integration time in $[\mathrm{s}]$,

θ_{ij} is the angular location of the pixel of interest in $[\text{degrees}]$,

$f\,/\#$ is the f-number of the imaging device $[\text{unitless}]$.

The camera is characterized in terms of an average performance estimate for the entire FOV through K_{ave},

$$K_{ave} = \frac{1}{N\,M}\sum_{i=1}^{N}\sum_{j=1}^{M} K_{ij}\left[\mathrm{s\ m^2\ sR}\right]. \qquad [4.12]$$

We then combine Equations 4.9 through 4.12 determine the average energy captured per pixel using the following relationship,

$$E_{pixel} = \left(\frac{1}{N\,M}\sum_{i=1}^{N}\sum_{j=1}^{M}\left[\frac{\pi\, A_{ij}\, \tau_0\, t_f\, \cos^4\left(\theta_{ij}\right)}{4\,\left(f\,/\#\right)^2}\right]\right)\int_{\lambda_1}^{\lambda_2}\frac{2hc^2}{\lambda^5}\frac{1\times 10^{-6}}{e^{\frac{hc}{\lambda kT}}-1}d\lambda \quad [\mathrm{J}]. \; [4.13]$$

The parameters N and M in Equations 4.12 and 4.13 correspond to the rows and columns of pixels in the FPA of the imager. E_{pixel} is used as a bottom-rail sensitivity for scene imaging, because below this limit the pixel will appear to be gray or black as minimum photons have been detected by the FPA. The darkening of pixels allows the user to observe absorption plumes in real time. Performance of the system under a variety of atmospheric conditions can be evaluated by calculating this limit prior to selecting a filter for optimum detection performance for the top end of the measurement dynamic range (saturation) by a selected hydrocarbon species (section 4.9).

4.3.2 Case 2 of Captured Irradiance

Case 2 describes the geometry where the total scene radiance is calculated at the observer location, as is done in MODTRAN^{TM}. Classical day-sky and night-sky background models for different look-angles relative to the Sun and Moon are performed in this way to make it easier to determine the interference expected for active remote sensing systems. The passive image formed by absorption of hydrocarbon plume requires adequate contrast between plume-present and plume-absent cases, and relies on sufficient solar or lunar scatter combined with blackbody background emission. It is important to scale radiance calculations to a per pixel basis for comparisons with performance thresholds when attempting to simulate different atmospheric conditions encountered. MODTRAN^{TM} radiance calculations [W m^{-2} μm^{-1} sR^{-1}] are scaled to represent the case of a single pixel in the image space, and provide a basis for selection of an optimum filtering scheme. We perform the calculation in this manner because the object space contains the radiance from the entire path subtended in the solid angle focused onto a single pixel. The technique removes the steradian dependence in the denominator while preserving the per-pixel geometry used previously in the imager characterization study.

Knowing that a single unit of steradian (sr) is defined as the solid angle subtended at the center of a sphere of radius *r* by a portion of the surface of the sphere having an area r^2, we can conclude that the maximum solid angle realized is 4π [sr]. Figure 4.4 depicts these parameters in a graphical representation of total field-of-view for the collection optics on a telescope or imaging device.

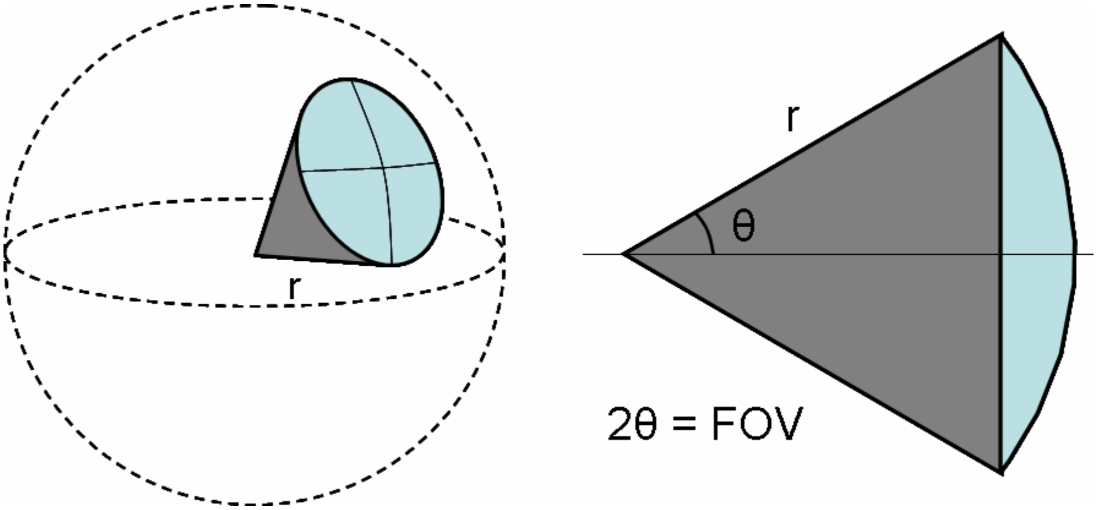

Figure 4.4: Representation of steradian and imaging FOV.

The FOV of a telescope, or imaging device, can be used to calculate the number of steradians observed as a fraction of the total possible (4π sr). Although the steradian is officially a unitless quantity, we choose to keep the units of [sr] at the end of the calculation to emphasize the steradiance dependence on imaging calculations,

$$
sr_{collected} = 4\pi(SA\ ratio) = 4\pi\left(\frac{\int_0^{2\pi}\int_0^{\theta} r^2 \sin\theta'\, d\theta'\, d\varphi}{4\pi r^2}\right)
$$

$$
\begin{aligned}
&= \int_0^{2\pi}\int_0^{\theta} \sin\theta'\, d\theta'\, d\varphi = 2\pi\left(-\cos\theta'\Big|_0^{\theta}\right) \\
&= -2\pi\cos\theta + 2\pi = 2\pi(1-\cos\theta) \\
&= 2\pi\left[1-\cos\left(\frac{FOV}{2}\right)\right] \quad [sr].
\end{aligned}
\qquad [4.14]
$$

The final term to remove the steradian dependence from the radiance calculations is only a function of the telescope or imaging FOV. If the calculation is designed to represent a single pixel in the FOV of an imager, then Equation 4.14 is modified slightly as shown by Equations 4.15 through 4.17,

$$
\begin{aligned}
E_{pixel} = &\left(\frac{1}{N\,M}\sum_{i=1}^{N}\sum_{j=1}^{M}\left[\left(\frac{\pi\, D^2\, \tau_0\, t_f \cos^4(\theta_{ij})}{4}\right)\right.\right. \\
&\left.\left.*\left(2\pi\left[1-\cos\left(\frac{FOV}{2}\right)\right]\right)\right]\right)*\left(\int_{\lambda_1}^{\lambda_2}(MOD5\, rad.)d\lambda\right)
\end{aligned}
\qquad [4.15]
$$

$$
\begin{aligned}
= &\left(\frac{1}{N\,M}\sum_{i=1}^{N}\sum_{j=1}^{M}\left[\left(\frac{\pi\, D^2\, \tau_0\, t_f \cos^4(\theta_{ij})}{4}\right)\right.\right. \\
&\left.\left.*\left(\pi\left[1-\cos\left(\frac{HFOV_{ij}}{2}\right)\right]+\pi\left[1-\cos\left(\frac{VFOV_{ij}}{2}\right)\right]\right)\right]\right)*\left(\int_{\lambda_1}^{\lambda_2}(MOD5\, rad.)d\lambda\right)
\end{aligned}
\qquad [4.16]
$$

$$
\begin{aligned}
= &\left(\frac{1}{N\,M}\sum_{i=1}^{N}\sum_{j=1}^{M}\left[\left(\frac{\pi^2\, D^2\, \tau_0\, t_f \cos^4(\theta_{ij})}{4}\right)\right.\right. \\
&\left.\left.*\left(2-\cos\left(\frac{HFOV_{ij}}{2}\right)-\cos\left(\frac{VFOV_{ij}}{2}\right)\right)\right]\right)*\left(\int_{\lambda_1}^{\lambda_2}(MOD5\, rad.)d\lambda\right)[J].
\end{aligned}
\qquad [4.17]
$$

where,

D is the diameter of the objective lens in meters,

$HFOV_{ij}$	is the horizontal FOV of the pixel in the ith column and the jth row
$VFOV_{ij}$	is the vertical FOV of the pixel in the ith column and the jth row
N and M	are the total number of rows and columns, respectively,
λ_1 λ_2	are the bounds for the wavelength range being examined.

Figure 4.5 describes this case graphically. For general performance calculations, we assume that the efficiency of pixels across the field of view vary as a function of $\cos^4(\theta_{ij})$, similar to Equation 4.11. The final equation (Eq. 4.17) describes an average weighting for all pixels in the FOV of the imaging device that can be applied to MODTRAN^{TM} radiance calculations.

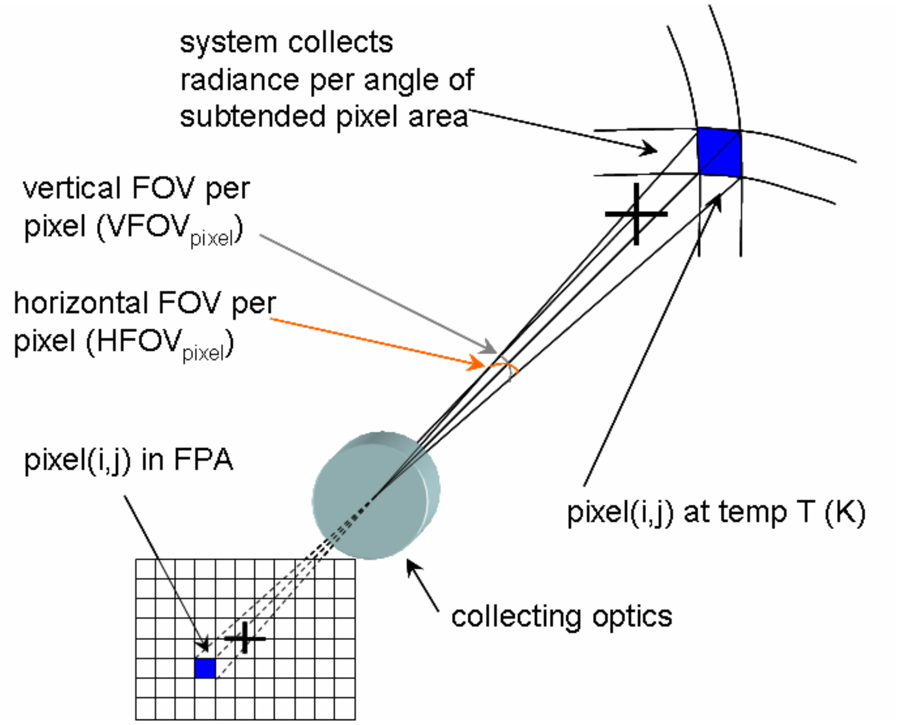

Figure 4.5: Case 2 geometry where a radiance calculation at the observer is used to calculate the energy captured per pixel in the camera FOV.

4.4 Experimental Camera Hardware

The Merlin MWIR camera (Figure 4.6) from FLIR (Indigo Systems) is a research grade device capable of high sensitivity measurements. The camera uses a focal plane array of InSb type detectors to create an IR image with a resolution of 320x256 pixels, which are refreshed at a maximum rate of 60 Hz. The integration time of the camera is selected by the user. The manufacturers technical data report a 0.018 °C sensitivity for temperatures ranging from -20 °C to 2000 °C [Indigo Systems, 2002]. The high sensitivity provided by the Merlin MWIR camera through such a wide range of temperatures is achieved using a sealed Stirling-cycle cooling system integrated with the detector. The Merlin MWIR camera has a built-in cold filter, with a transmission of approximately 98 % in the range of 3 to 5 μm. Its size (14 x 13 x 25 cm) and weight (4.3 kg) are compatible with the small size and low weight requirements for aircraft use. Currently, the 13 mm main objective lens yields a 41 x 31° field of view imaging onto the FPA, see Table 4.1 for a summary of this information.

Figure 4.6: FLIR Merlin MWIR Camera [FLIR, 2008]

Table 4.1: Merlin MWIR camera specifications [Indigo Systems, 2002]

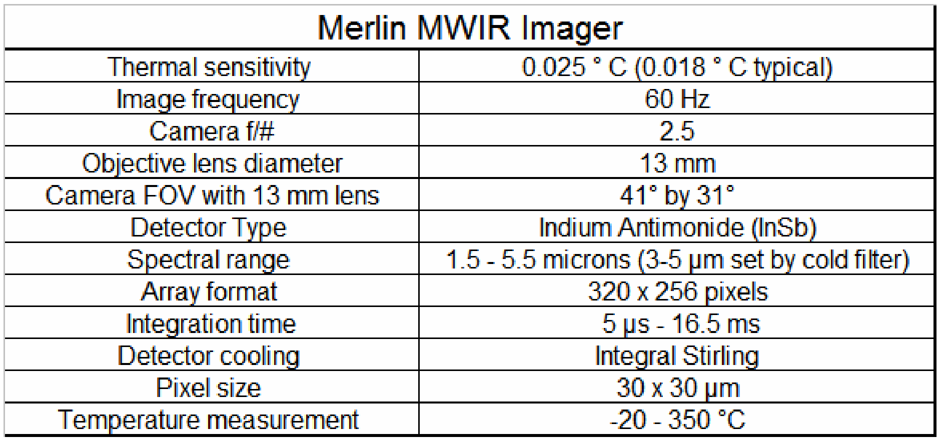

Merlin MWIR Imager	
Thermal sensitivity	0.025 ° C (0.018 ° C typical)
Image frequency	60 Hz
Camera f/#	2.5
Objective lens diameter	13 mm
Camera FOV with 13 mm lens	41° by 31°
Detector Type	Indium Antimonide (InSb)
Spectral range	1.5 - 5.5 microns (3-5 μm set by cold filter)
Array format	320 x 256 pixels
Integration time	5 μs - 16.5 ms
Detector cooling	Integral Stirling
Pixel size	30 x 30 μm
Temperature measurement	-20 - 350 °C

These parameters, in conjunction with previous analyses, allow us to calculate the bottom-rail sensitivity of the FPA in the camera to be roughly 0.005 pJ per pixel given a 2 ms integration time. The bottom-rail sensitivity per pixel is used to determine optimum filter configurations. Another parameter that is important in this analysis is the sensitivity or contrast limit per pixel when the collected energy is above the baseline and within the dynamic range of the camera. Table 4.1 indicates the sensitivity of the Merlin MWIR imager is 0.018 °C, which translates to 4.5×10^{-17} J, when the calculation is performed under worst case conditions of -20 °C for the spectral range covered by the camera.

4.5 Hydrocarbon Absorption Scientific Background

Hydrocarbon vapors have unique absorption spectra throughout the infrared spectrum; however, the spectral region in the 3 to 5 μm range is the most useful for several applications, and this wavelength range corresponds to the active region of the

Merlin MWIR camera. Prior research activities have identified three particular types of materials of interest in this region as, (1) High Volatility hydrocarbons (all gasoline vapors), (2) Low Volatility Hydrocarbons (diesel fuel, kerosene), (3) special gaseous hydrocarbons (propane, methane). Due to the complex nature of these compounds, spectral features associated with the many degrees of freedom yield the broadband and multi-line absorption spectra as shown in Figure 4.7. With proper filtering, these absorption features are detectable in the field of view of the Merlin MWIR camera as "black smoke." Successful imaging of Ethene emissions was reported by Sandsten, *et al.* [2004] using passive techniques. The goal of our study is to design a system that is completely passive, as well as able to detect the several hydrocarbons of interest shown in Figure 4.7 using simple filter changes. Commercial systems (FLIR HAWK, and GasfindIR commercial instruments, see Figure 4.8) have been developed for close range observation of hydrocarbon plumes, but these do not have a capability for wavelength selection. Without an ability to make wavelength selections, the optimum system performance for these hydrocarbons (Fig. 4.8) cannot take advantage of the different spectral features in the MWIR for best contrast. Additionally, the performance of the system at longer ranges must take into account typical atmospheric conditions when choosing a filter to enhance detection probability. The capability of a longer range imaging system is examined by selecting the operating characteristics and modifying the entrance optical configuration to improve performance.

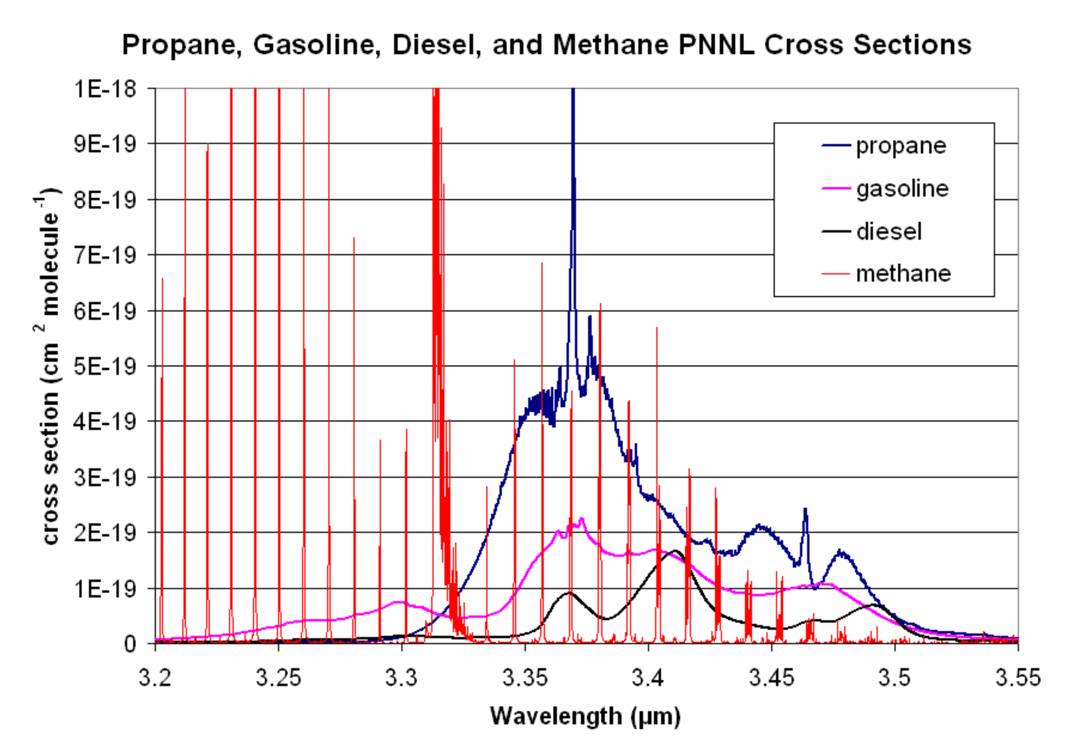

Figure 4.7: Pacific Northwest National Laboratory (PNNL) measured spectrum of propane and methane; reconstructed absorption spectra of gasoline and diesel using weighted PNNL components.

Figure 4.8: Merlin HAWK (left) and GasfindIR (right) detection of hazardous vapors [FLIR, 2008].

4.6 Scene Radiance Considerations

In the airborne down-looking configuration, the planned system utilizes the Earth's surface as a source of broadband infrared radiation, in addition to the solar radiation scatter from the surface. MODTRAN^{TM} was used to simulate the radiance at an altitude of 300 m looking downward at the surface [Berk, *et al.*, 1990] to confirm that the surface of the Earth is an effective generator for the required background radiant energy. Planck curves of ideal blackbody radiators compared with MODTRAN^{TM} simulations show that the Earth emission is represented by a blackbody at a temperature of approximately 15 °C. The deviation from this theoretical value is shown in Figure 4.9, and is due to absorption and scattering included in the MODTRAN^{TM} simulation [Berk, *et al.,* 1990]. In addition, the MODTRAN^{TM} result displays the variations from the ideal blackbody signature in the 3 to 4 μm region. Some departure from the ideal case of a blackbody emitter is due to the Earth's surface not being a perfect radiator, emission by radiating species in the atmosphere, and surface emissivity slightly less than one. Other factors that influence the radiance are primarily associated with absorption by several gas species, and by the absorption/emission process of greenhouse gases.

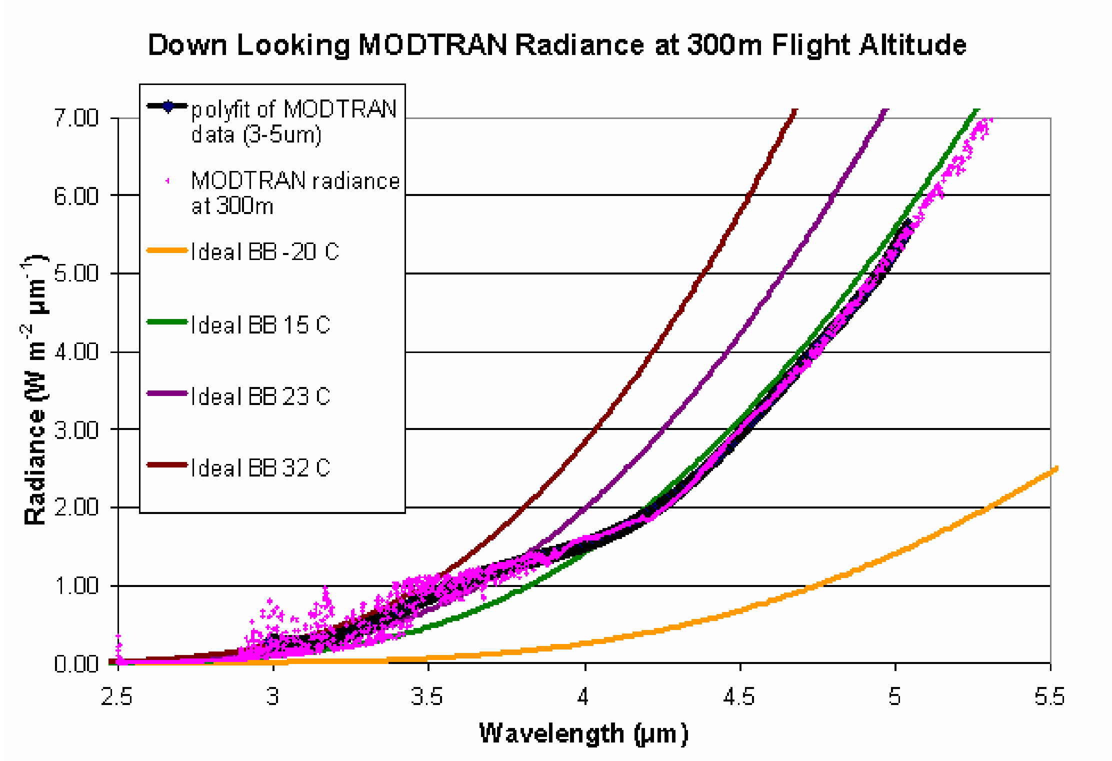

Figure 4.9: Comparison of MODTRAN^{TM} to BB Lambertian emitter at various temperatures, single path radiance collection at night without any solar scatter.

In an attempt to determine the temperature range typically encountered during operation, the typical daily fluctuations of the land surface skin temperature are shown in Figure 4.10 for a day in mid-July at mid-latitudes of 40 to 45° N. The simulation results shown are outputs from the global climatology model of Arizona State University based on GOES-8 and AVHRR land surface satellite observations [Jin and Dickenson, 1999]. These climate data show that the diurnal land surface temperature ranges from approximately 285 to 305 K or 12 to 32 °C. This temperature fluctuation throughout the day will affect the performance of the system because it determines the variation in the background radiance from the surface.

Camera operation without the appropriate filter does not provide real-time analysis of hydrocarbon absorption because the absorption signature of the target hydrocarbon gas cannot be distinguished from the background signature. Conversely, if the surface of the earth is not emitting strongly enough, then the background signature may not exceed the minimum detectable level of the camera, and thus no image will be formed. Initial justifications for the trade-off analysis of filter bandwidth needed to achieve desired performance are provided via the following Figures 4.11 through 4.14. This analysis is performed independent of solar scattering effects. The optimum camera setting will require an active computer intelligent program that auto adjusts the dynamic range and contrast using the real time data.

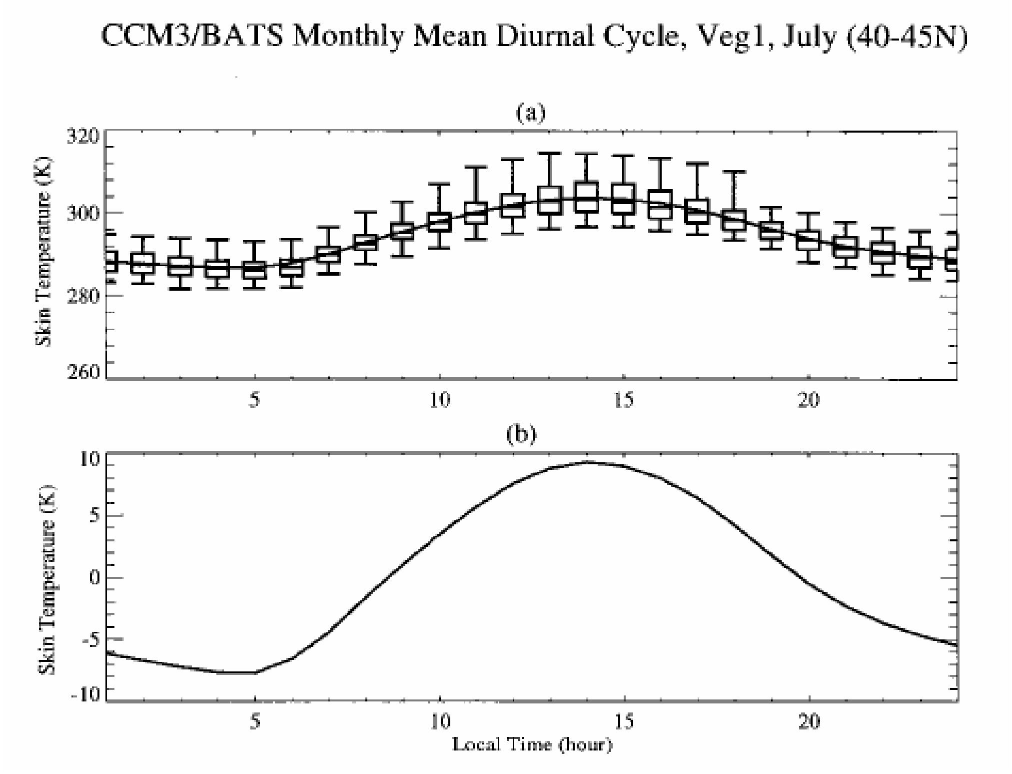

Figure 4.10: Model results for monthly mean skin temperature diurnal cycle for July, clear sky. Ground was vegetated by crop/mixed farming for latitudes of 40-45°N [Jin and Dickinson, 1999] The lower panel is relative to the daily average of 295 K.

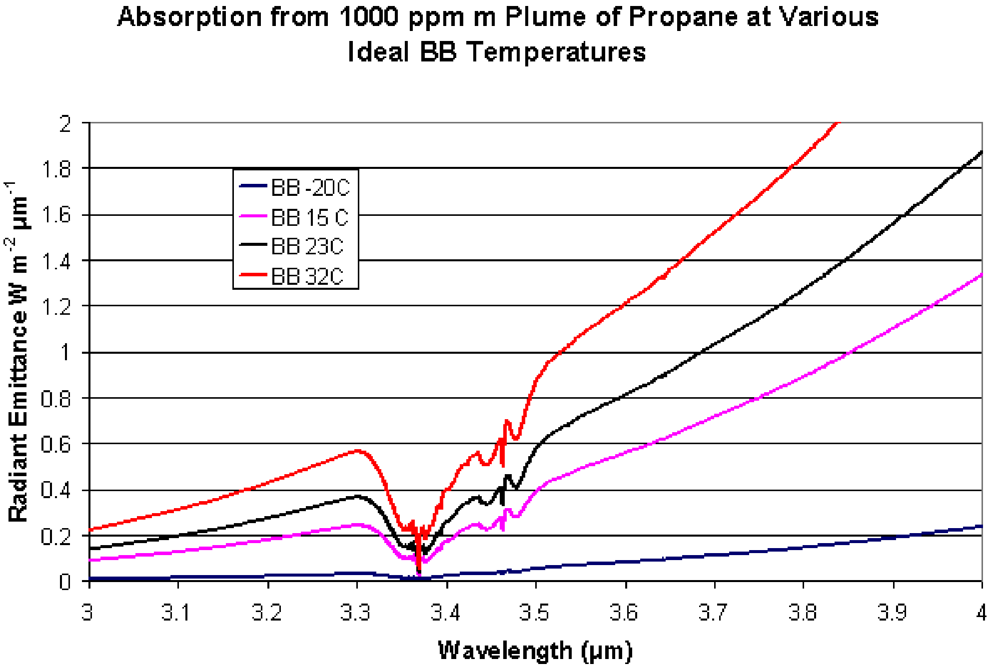

Figure 4.11: Absorption due to a 1000 ppm·m plume of propane at various blackbody temperatures.

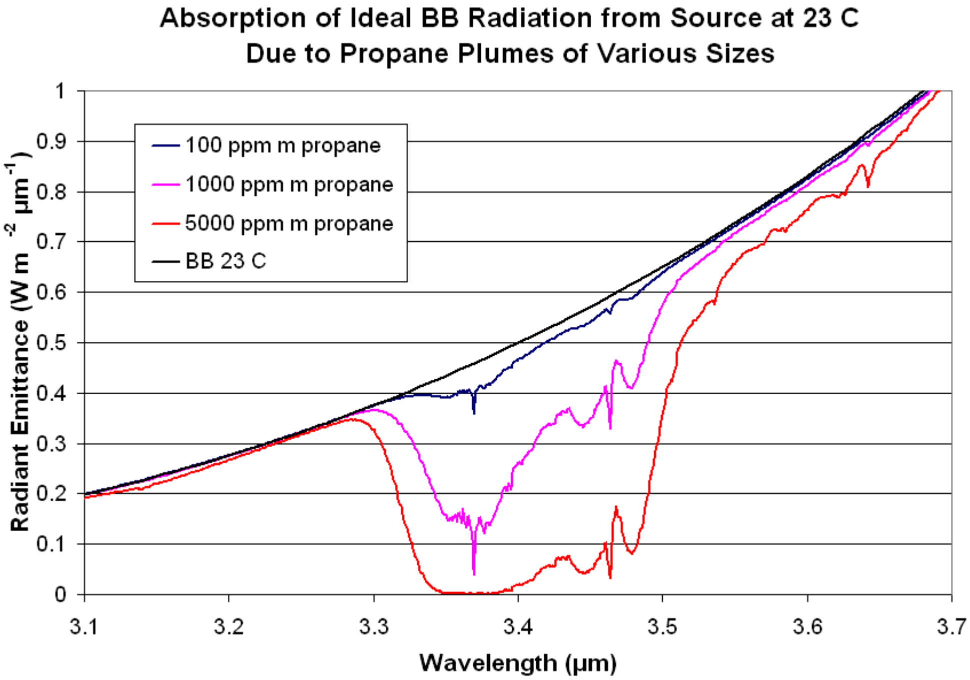

Figure 4.12: Absorption due to various size propane plumes at a blackbody temperature of 23 °C.

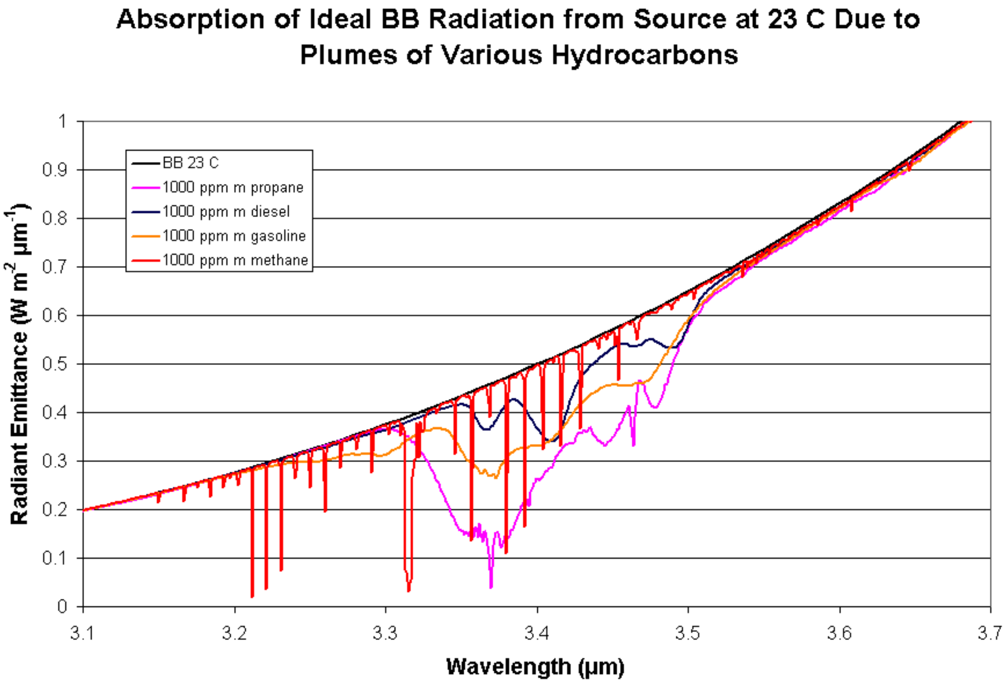

Figure 4.13: **Absorption due to various hydrocarbon plumes at a blackbody temperature of 23 °C.**

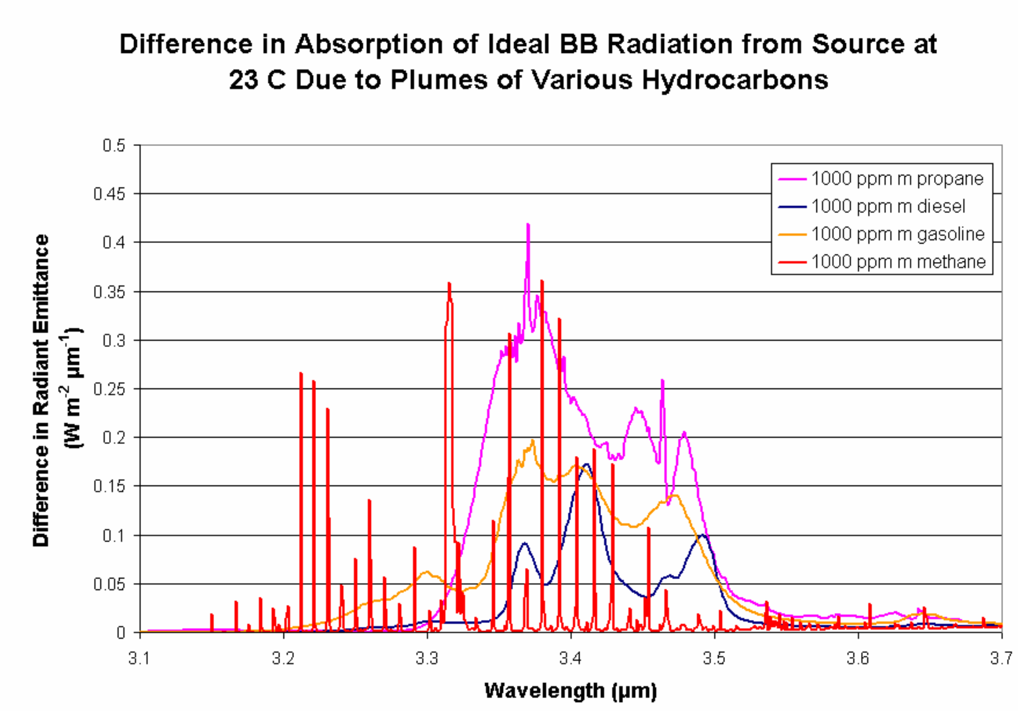

Figure 4.14: **Difference between 1000 ppm·m curve and the appropriate background at a blackbody temperature of 23 °C between the surface and 300 m.**

To expand the explanation of the effect of land surface temperature on the system performance, Figure 4.11 shows the emission at different temperatures observed through a plume of propane at a concentration of 1000 ppm·m. Similar absorption figures have been created for cases of diesel, gasoline, and methane, and these are presented in Appendix D. In an alternative representation, the plume magnitude is modified to represent different size leaks, while the apparent surface temperature is held at a constant 23 °C (Figures 4.12 through 4.14). As shown, the expected plume magnitudes display a range of absorption values in the wavelength band of interest.

Curves from Figures 4.12 through 4.14 show how different leaks can be spectrally discriminated using simple bandpass filters, and they can be compared with the sensitivity parameters of the camera to determine detection probability. Note specifically in Figure 4.14 how the absorption due to methane at longer wavelengths generates more significant differences between the case of a plume present and a plume absent. This increase in absorption is created because the source intensity increases towards longer wavelengths due to the Planck function of the thermal emission, and because the path absorption calculated through the Beer-Lambert law is multiplicative.

4.7 Using MODTRAN^{TM} to Determine Filter Choices

The spectral simulations that are used for optimum filter selection utilize the MODTRAN^{TM} model, and therefore invoke several typical atmospheric conditions expected in real-world situations. Several simulations have been performed using an average surface temperature of 290K (17 °C) with a solar zenith angle (SZA) of 15°

and a surface albedo of 10%. The aerosol conditions set in this simulation correspond to a typical mid-summer day at mid-latitude locations with 23 km visibility (corresponding to very good atmospheric conditions). The standard down-looking radiance observed in this situation is shown by Figure 4.15(a). The structure shown deviates from the typical blackbody curve due to solar scatter, thermal emission, and IR signature from the ground radiating up through the atmosphere to the observer. The effects of absorption and emission of atmospheric species are also included in the radiative transfer calculations built into the MODTRAN^{TM} model. When a 1000 ppm·m size methane plume is introduced at ground level, the simulation shows a significant absorption response as seen in Figure 4.15(b).

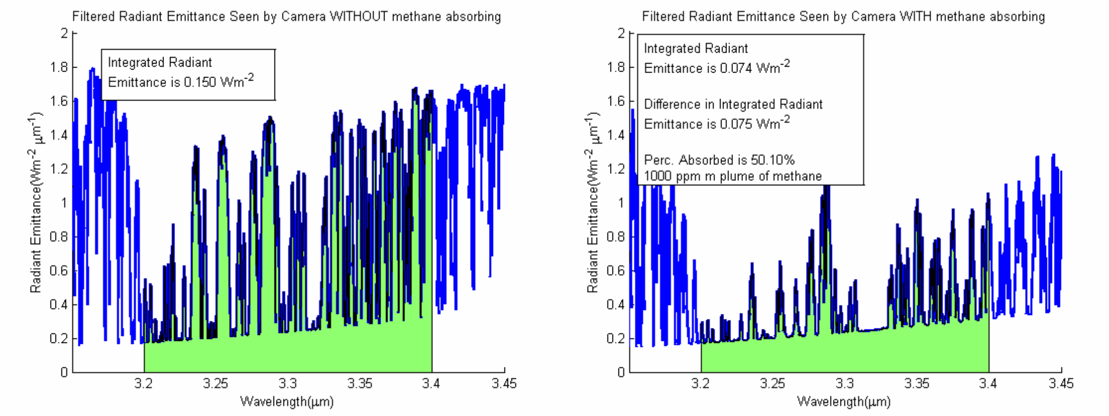

(a) **(b)**

Figure 4.15: MODTRAN^{TM} spectral radiance model result with (b) and without (a) a 1000 ppm·m plume of methane at ground level for a daytime measurement from 150 m.

Although this result is clearly observed when the spectral data are examined, the goal of this effort is to quantify this response utilizing MWIR camera hardware. Hence, by integrating the area underneath the MODTRAN^{TM} spectrum relative to the bandpass transmission of the infrared imager, it is possible to calculate a total flux, or total collected energy per pixel in the FOV. For the case shown in Figure 4.15, a 3.2

to 3.4 μm bandpass filter has been used to calculate the response to a plume expected in the FOV of the imager.

To demonstrate the importance of the surface albedo and solar scatter in the detection performance, a MODTRAN^{TM} simulation of a nighttime case has been prepared. The results of this simulation, shown in Figure 4.16, were processed using the same 3.2 to 3.4 μm filter. The result confirms that performance is greatly enhanced for daytime measurement conditions. In addition to the increased signature in the daytime case, the percentage of absorption is roughly 10 times that of the nighttime case. The large amount of solar scatter by the atmosphere and ground increases the infrared energy that is available in the band and thus increases the signal of the absorption; the solar scatter must be exploited to enhance detection performance to a useful level for MWIR applications.

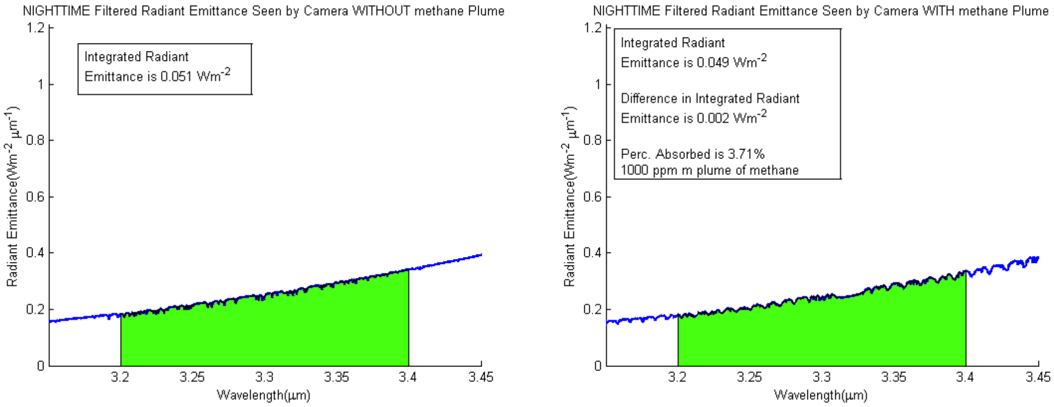

(a) **(b)**

Figure 4.16: MODTRAN^{TM} spectral radiance model result with (b) and without (a) a 1000 ppm·m plume of methane at ground level for a nighttime measurement case at 150 m.

4.8 Filter Selection for Methane

Using the MODTRAN^{TM} simulation of down-looking radiance at 150 m for atmospheric methane concentrations, we plot the expected energy calculated for a single pixel in the FOV as a function of filter bandwidth and center wavelength in Figure 4.17a. The previously calculated detection benchmark parameter of 0.005 pJ is plotted as a contour on the figure. Without an increased target plume present in the far field, we must select a filter that allows the system to operate above this limit, or the image will not be distinguishable in the FOV of the imager. Quite simply, this leads to selection of a filter with both a center wavelength (y-axis) and bandwidth (x-axis) that is located above the upper solid black line (benchmark limit of camera) in Figure 4.17a. The lower solid black line corresponds to another case of filtering that could be used to create a similar imaging device centered at 2.3 μm to capitalize on a different set of methane absorption bands. The present work, however, focuses on the absorption bands near 3.3 μm; this region is also interesting because there are other hydrocarbons with absorption features there.

When the concentration of the absorbing species is increased, the simulation can be re-run for a case containing a 1000 ppm·m plume using the appropriate MODTRAN^{TM} geometry and atmospheric conditions (see Figure 4.17b). Again, the benchmark radiance limit is annotated on the plot, and the total integrated radiance is plotted as a function of bandwidth and center wavelength. When a species measurement is planned, the contrast is best when the affected pixels to appear dark gray in the camera field of view. This condition translates to filter choices below the benchmark limit shown.

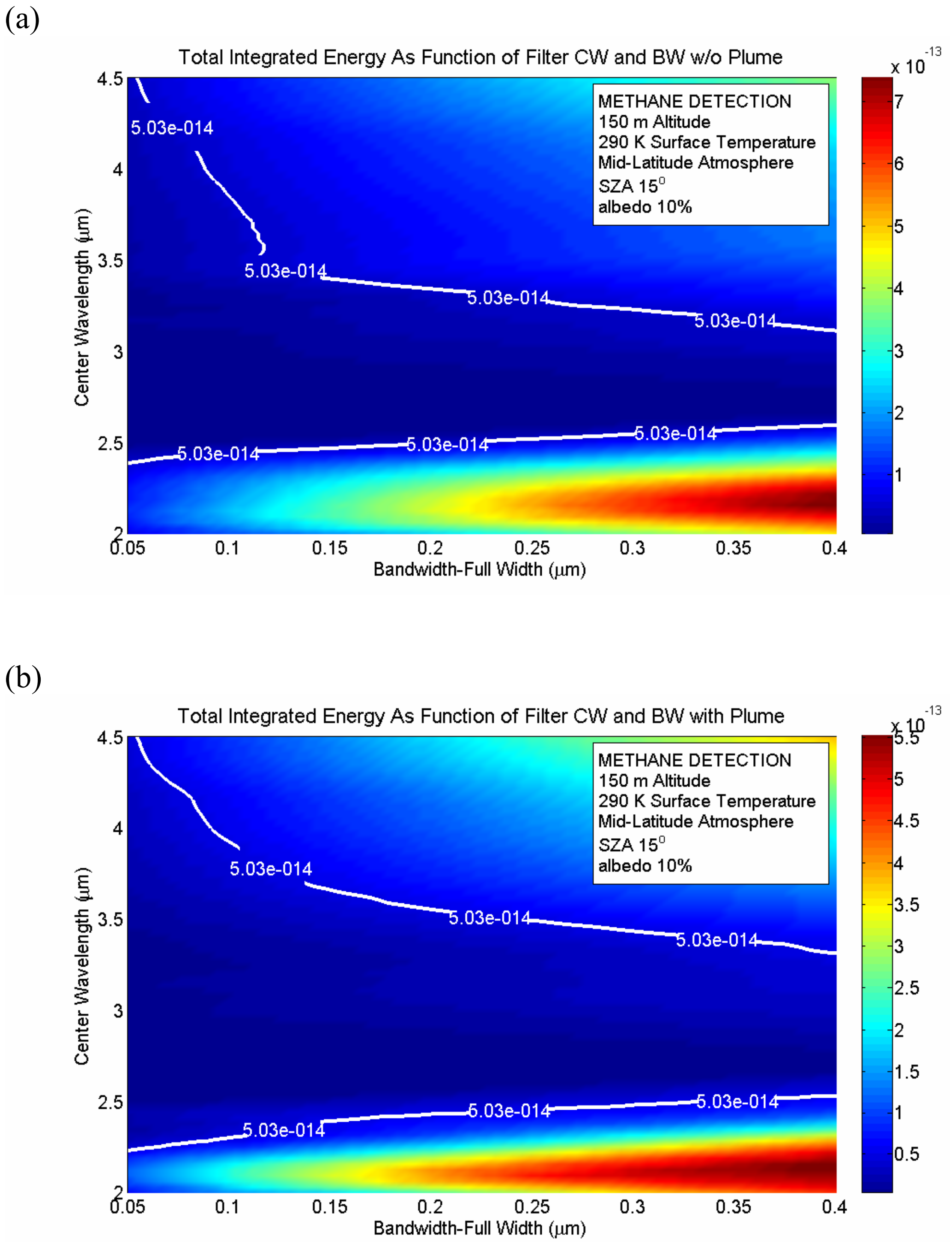

Figure 4.17: Integrated absorption as a function of filter center wavelength and bandwidth without (a) and with (b) a 1000 ppm·m plume of methane at ground level (surface albedo 10%).

An additional tradeoff considers the total difference between the collected energy or total contrast for conditions with and without the plume present. This parameter is plotted with the same rationale as the previous plots, and allows selection of the filter choice. A good rule of thumb is to be near or above the benchmark limit of the camera for the typical atmospheric case to maximize the total contrast, as shown in Figure 4.18a. Lastly, we must ensure that the sensitivity or contrast limit imposed by the chosen filter is above that needed by the camera. Figure 4.18b plots the difference in energy collected by a pixel in the FPA, and its magnitude can be observed by the color scale. In the worst case, the difference in collected energy for a pixel is 8.47×10^{-15} J, and this difference is 188 times greater than the 4.5×10^{-17} J energy detection threshold of the camera.

Figure 4.19 is a summation of the results from Figures 4.17 and 4.18. The dark blue line in Figure 4.19 shows the bottom rail sensitivity limit of the camera. Pixels that are at or below this limit will begin to darken and quickly appear as solid black beneath this value. Filter choices correspond to all those that are within the two blue lines. The black lines on the figure signify the same guidelines for the case when the species of interest is present. The light blue oval to the right side of the figure displays the region of filter choices that provide the maximum difference in received energy, while the light blue oval to the left side of the figure displays this difference in terms of a percentage of collected energy. The area bounded by the lines indicates the optimum filter choices.

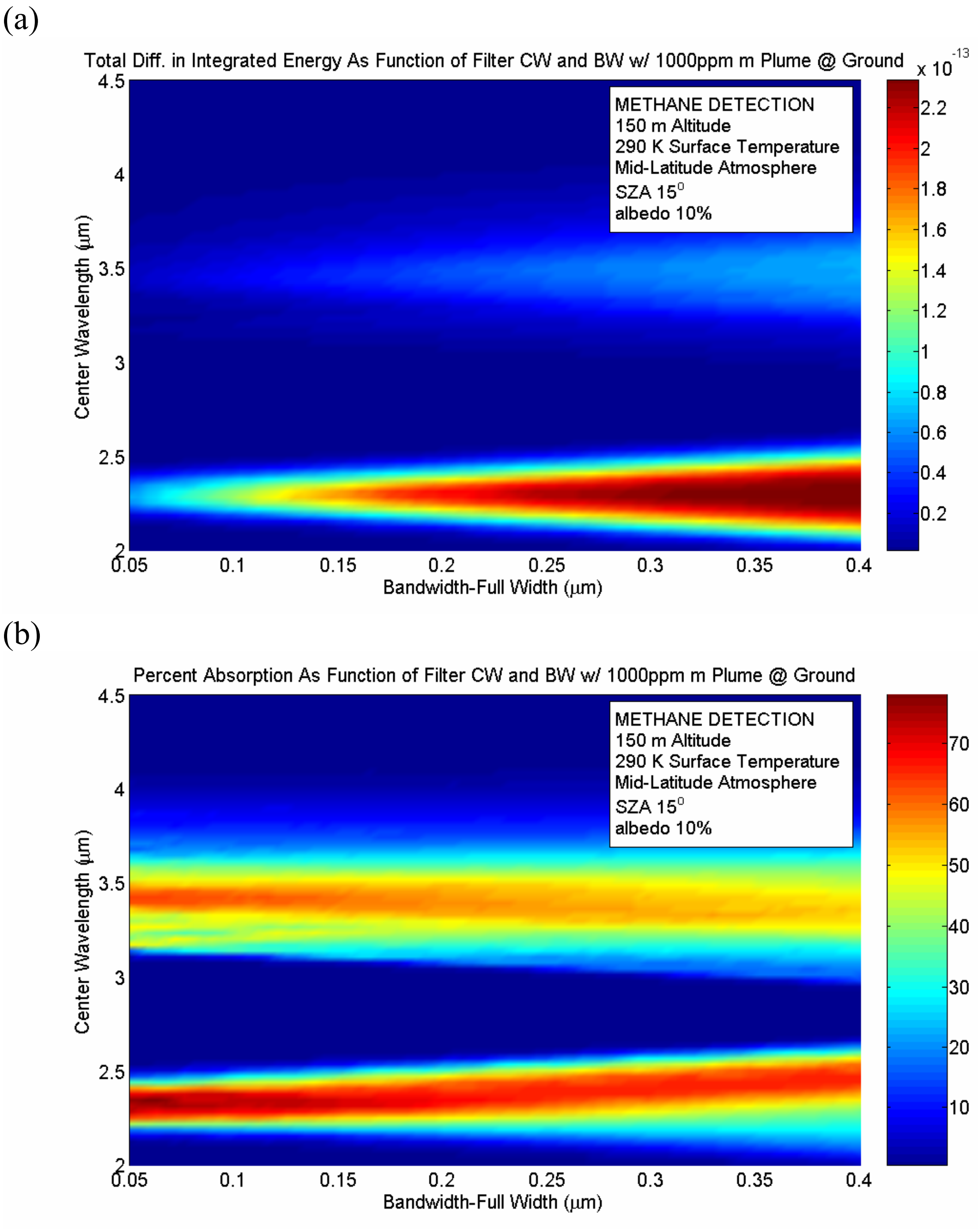

Figure 4.18: Percent difference (a) and total difference (b) in integrated absorption as a function of filter center wavelength and bandwidth due to a 1000 ppm·m plume of methane at ground level (surface albedo 10 %).

Choices farther to the right side will demonstrate greater differences in energy between the plume present and plume absent cases, while those to the left will observe greater percent differences. Choices that maximize percent difference will benefit from carefully adjusting the dynamic range of the camera to tightly bound the region of best performance under typical radiance conditions. Alternatively, choices that seek to maximize raw energy difference are more likely to be useful under a variety of conditions, although they may suffer due to lower contrast. A general purpose filter was selected with a bandwidth of 200 nm at a center wavelength of 3.375 µm. The location of this filter is marked by a gray star on Figure 4.19, and imaging results using this filter to image plumes are shown in Chapter 5.

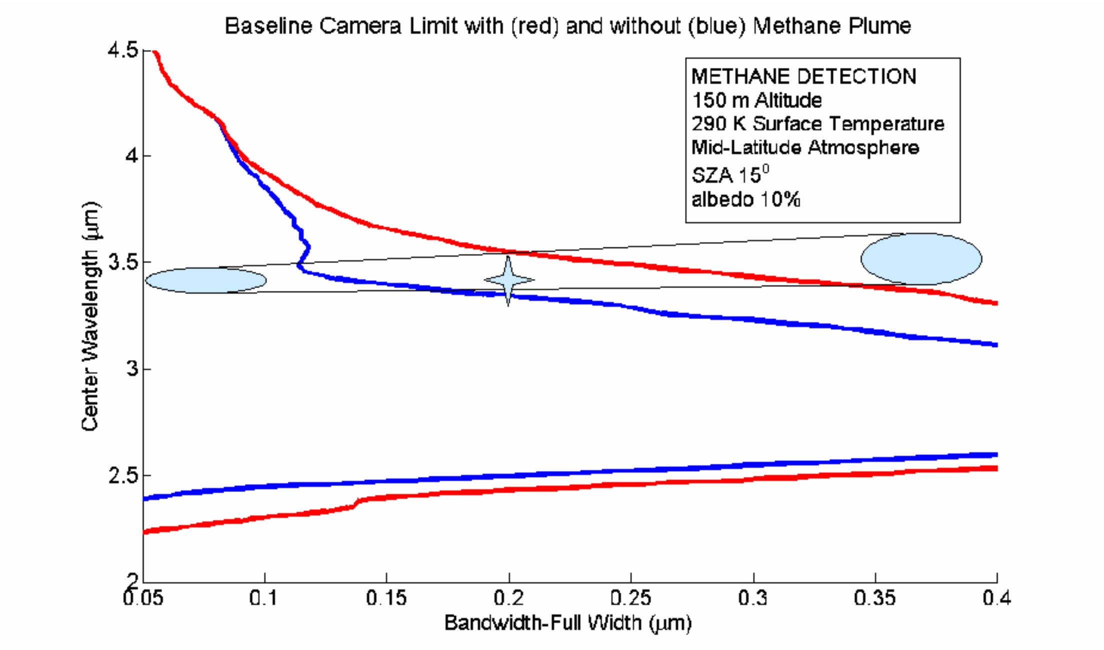

Figure 4.19: Summation of the results for the methane target case.

4.9 Final Filter Recommendations and Summary

A similar process to the one developed above was used to select optimal filters for the qualitative detection of propane, diesel and gasoline vapor. This analysis can be found in Appendix E. Based on our analysis, the best choices are summarized in Table 4.2 by the four infrared filters indicated. If the exact filter center wavelength and bandwidth are not available from suppliers, then slight adjustments to these specifications can be made. Actually, the filter centered at 3.375 μm with a 0.2 μm bandwidth should prove to be satisfactory for all of the hydrocarbons when using a single general-purpose filter.

Additionally, we conclude that useful results are not likely to be obtained at nighttime or at low solar zenith angles in winter, due to the reduced contributions of solar background, and reduced thermal emission available to the instrument. Best cases for observation will be during daylight, summer, and dry atmospheric conditions. However, emergency situations where fire or other sources of heat or light are present should significantly enhance the detection due to the added infrared emission in the source region.

Table 4.2: Recommended filters for initial testing

Target	Center Wavelength (μm)	Bandwidth (μm)	comment
Methane, Propane and Fuels	3.375	0.200	general purpose filter choice
Propane	3.300	0.280	selected for propane
Gasoline Vapor	3.300	0.250	selected for gasoline but can be used for all others
Diesel Vapor	3.430	0.130	selected for diesel but can be used for all others

CHAPTER 5
Validation of Multi-wavelength Infrared Imaging of Chemical Species

Earlier research defined the background theory of operation for the hydrocarbon leak detection using the Merlin MWIR camera.† The filters selected to enhance the detection of hazardous hydrocarbons in real-time were determined during this background study. The analysis presented here is a follow-on that describes the experimental verification of the previous development, and includes an example of propane detection using the general purpose filter at ranges from 30 to 180 m. The additional data analysis technique provides a way to quickly observe and characterize plumes in the FOV of the camera.

5.1 Calibration Tests

An initial set of tests was completed, and these results demonstrate the importance of solar scatter for hydrocarbon vapor imaging. Figure 5.1 shows some examples of the blackbody source being imaged at a distance of 15 m for temperature of 30 °C, 28 °C, 26 °C and 24 °C with the general purpose filter installed on the camera. For this particular test, the source was increased to a higher temperature and allowed to cool. The camera settings were not modified as the calibration took place. Note how the signature of the background light changes, i.e. the wall, is not observable at the final temperature. As the experiment was performed the Sun was setting, and thus less ambient light illuminated the outer room during this seven-minute period. This demonstrates, at least in a crude manner, the importance of the solar background for measurements through an MWIR bandpass filter. Furthermore,

---

† This research is broken up into theory and simulation (Chapter 4) of MWIR filtering techniques for the passive imaging of hydrocarbon plumes.

it shows that the dynamic range needs adjustments depending on the atmospheric radiance conditions present at the time of the experiment. Appendix F contains simulations of the total collected radiance when using the general purpose filter on the imager. These simulations are intended to help a designer determine the magnitude of contribution from thermal background and solar radiance to the total radiance.

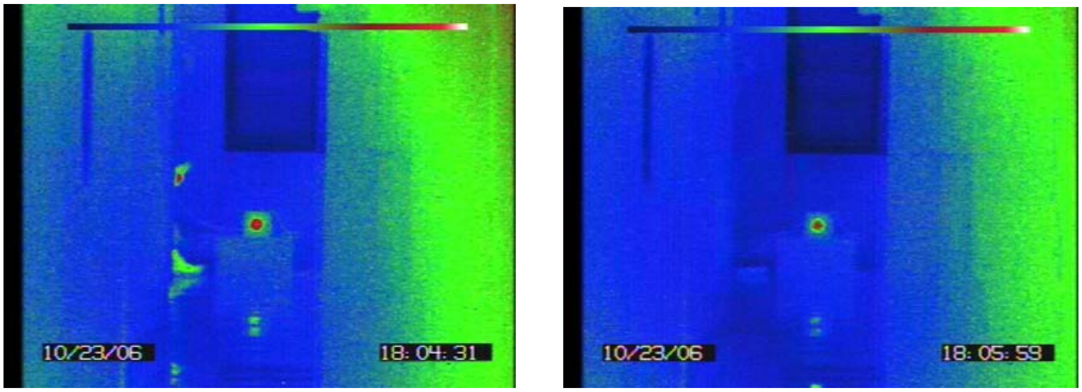

30 °C blackbody source 28 °C blackbody source

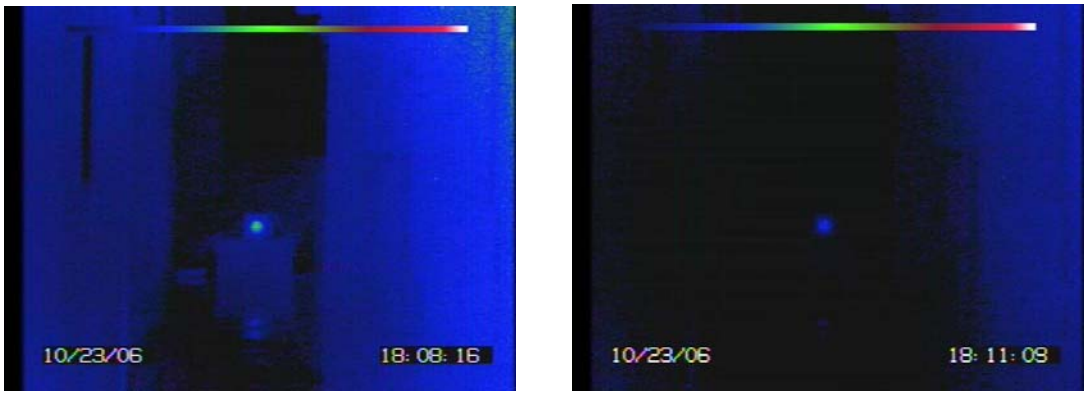

26 °C blackbody source 24 °C blackbody source

Figure 5.1: Initial calibration figures show the calibration source (center of frame) as it cooled over a period of seven minutes. The radiance from the source itself decreases as the source cools; furthermore, the radiance from the window decreases over the period of seven minutes as the Sun was setting.

5.2 General Camera Operation

Many possible settings are included within the firmware of the camera that can be modified to enhance the operation for detection of hydrocarbon leaks. We found during the experiments that four key parameters must be adjusted in order to properly image and detect hydrocarbon leaks in the far field.

1. Integration Time: Ideally this integration should be as long as possible in order that small differences in temperature are detected. However, there is a limit when the integration time becomes too large, the FPA becomes saturated.
2. Non-uniformity correction (NUC): The non-uniformity correction is used to correct any adjacent pixel deviation that may occur when the field of view of the camera is illuminated with a strong homogenous (single-temperature) source. This correction is critical to obtain proper images when operating with a filter. The filter function can be removed from the camera field of view. Thus, it will correct and smooth out any ‘ring’ or ‘kidney’ shapes that occur due to the non-uniform distortion from the combined filter and camera.
3. Brightness: The dynamic range of the camera is centered so it is neither zeroed nor saturated, and allows the user to observe and interpret the result from the FPA.
4. Contrast: Sets the display dynamics of the camera to make energy differences easier to observe; thereby, improving the sensitivity for lower concentrations of species in the plume.

Adjustment of these parameter values prior to a test is necessary when utilizing the Merlin camera for detection of hydrocarbon vapors. These adjustments can also be made via an attached control keypad. For flight operations however, remote camera control via a computer communications port would be necessary to make needed adjustments and observe during a measurement sequence.

5.3 Propane Detection Example

A single hydrocarbon (propane) was selected to confirm the filter selection and imaging approach. Multiple sequences of images were collected during propane tripod tests at several ranges from the source between 10:00 AM and 2:00 PM local time in State College, PA from October 25th to October 30th, 2006. Average ambient air temperatures ranged from 8 °C to 14 °C during the tripod tests. Throughout the data collection, the steps in setting up the Merlin imager were developed into a test plan that would allow repeatability in the measurement technique, and future operations by other researchers. This procedure is described in Appendix G. All measurements during this proof-of-concept study were made using the general purpose filter.

When the camera is properly configured, the absorption due to propane can be clearly observed at close range and at distances of 180 m, as shown by Figures 5.2 through 5.5 for both large (500 SCFH) and small (100 SCFH) propane leaks. Although it is difficult to see the propane plume in the images shown here for the 180 m case, the recorded video clearly shows the leak. An objective lens with a narrower

FOV would enhance long-range performance. A zoom lens system would be able to confirm leaks of this magnitude at several hundreds of meters.

Figure 5.2: Observation using general purpose filter (without plume – top and with 500 SCFH plume – bottom) for propane release at 30 m range.

Image subtraction can be used to dramatically enhance the imaging of hydrocarbon plumes. A background image can be created by taking an average over the first 100 frames of a collected movie and subsequently used to normalize the rest of the movie frames. This simple data processing technique was found to only show marginal success. If the approach is coupled with a Hamming window that averages the frames in the movie before the subtraction process however, then the success is greatly increased. Some examples of this image subtraction process are shown in Figures 5.6 and 5.7.

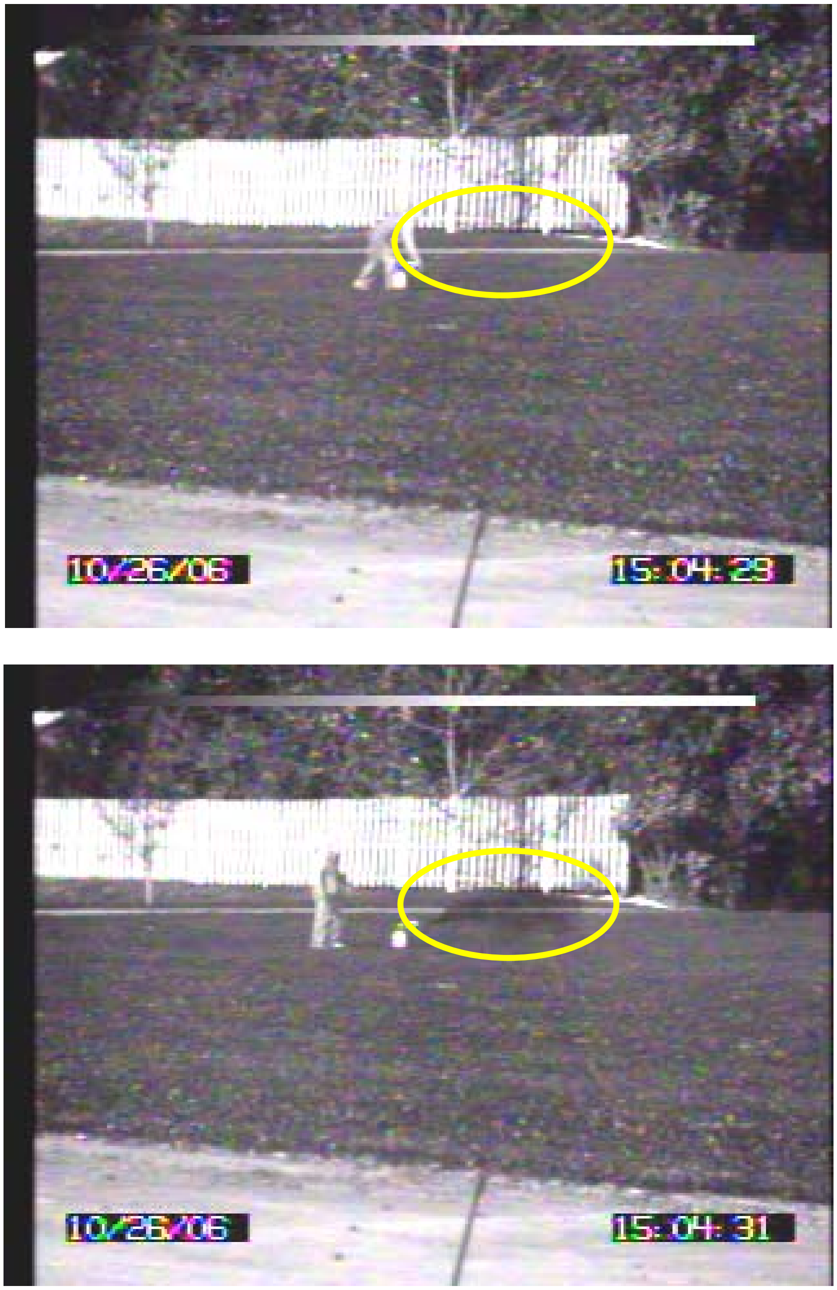

Figure 5.3: Observation using general purpose filter (without plume – top and with 500 SCFH plume – bottom) for propane release at 60 m range.

Figure 5.4: Observation using general purpose filter (without plume – top and with 500 SCFH plume – bottom) for propane release at 100 m range.

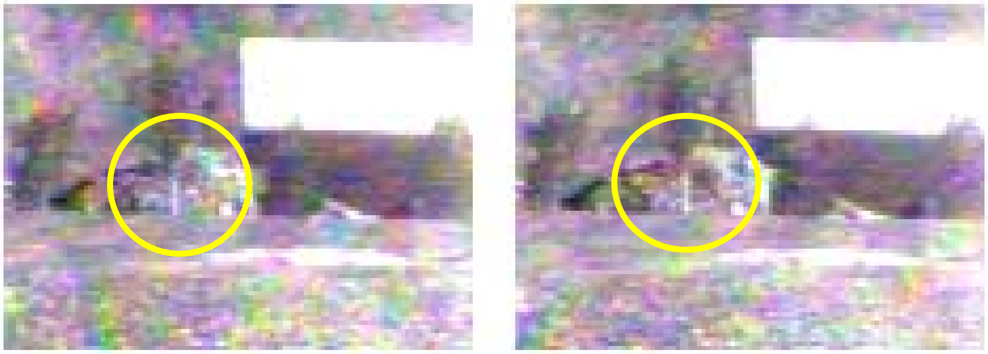

Figure 5.5: Observation using general purpose filter (without plume – left and with 500 SCFH plume – right) for propane release at 180 m range.

Figure 5.6: Before (top) and after (bottom) data processing technique is applied to data taken from 60 m range.

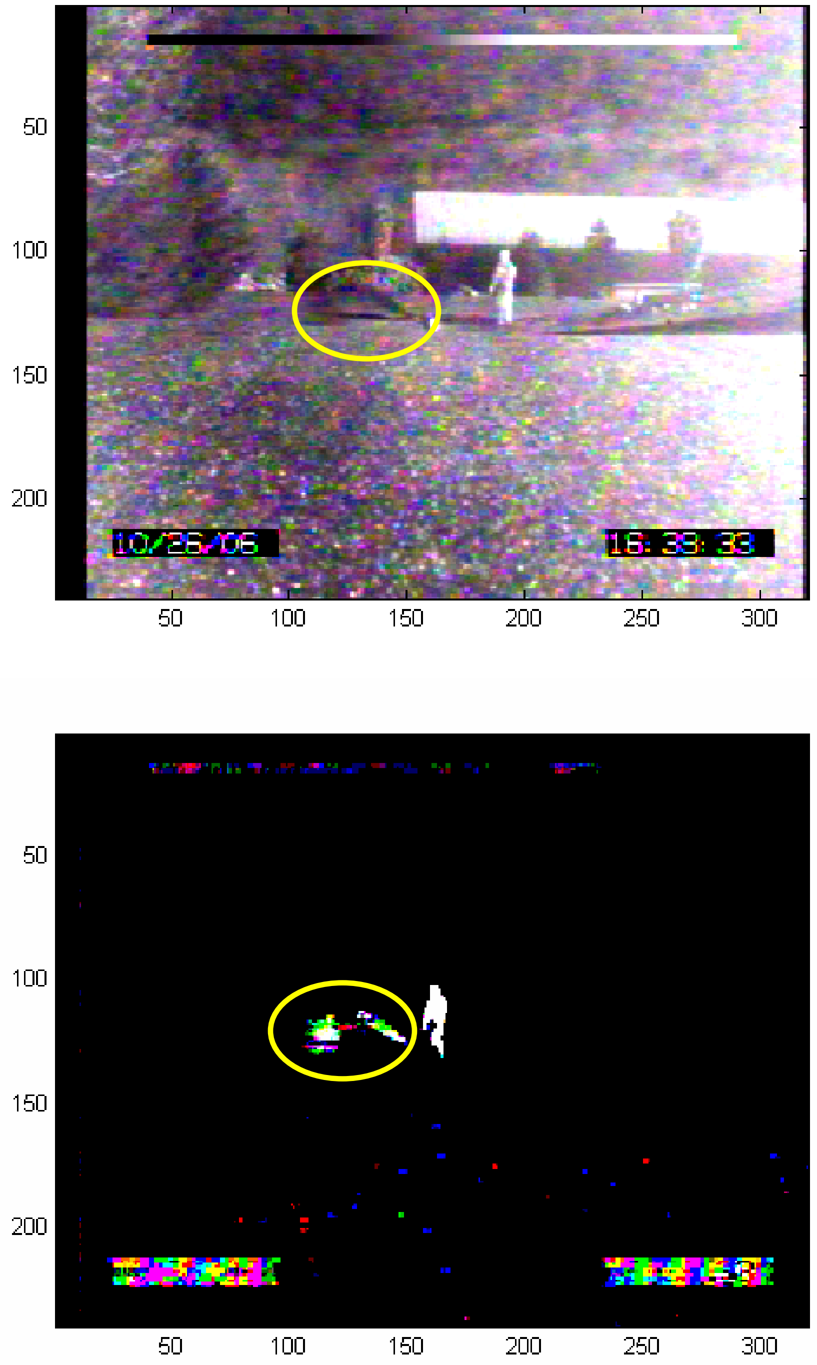

Figure 5.7: Before (top) and after (bottom) data processing technique is applied to data taken from 100 m range.

5.4 Advanced Processing Approaches

The discrete Fourier transform is an excellent tool for separating signal from noise. The Fourier transform is typically performed on a dataset to extract periodic signals or ensemble motions that are typically lost in noise, and it operates on a specific characteristic in the frequency spectrum. The inverse Fourier transform is then used to bring the data back to the time domain, where it is then presented as an improved data set.

When applying a similar approach to the detection of vapor plumes in the field-of-view of the MWIR imager, bandpass filtering in the frequency domain proves to be difficult, because there is not one target frequency of interest. Instead, the target frequency is a range of frequencies that represents the movement of the target gas. To test this theory, we have selected two test cases of pixels from the IR camera movie data when a large propane release was present. The first region, shown by the lower red square in Figure 5.8, encompasses an array of 10 x 10 pixels that are outside of the region affected by the absorption of the propane plume. The second region, shown by the upper red square in Figure 5.8, represents a second array of 10 x 10 pixels that lie within the region of the propane absorption.

A discrete 500-point Fourier transform is then performed on each of the 100 pixels in each of the arrays, and then averaged. For the region in which the plume is present, the averaged Fourier transform is shown as the dark blue line in Figure 5.9, while the plume-absent region corresponds to the light purple line in the figure. Both of the regions have a large DC component that is off scale; the plume region also has multiple small features present in the frequency spectrum from 0.5 to 3 Hz, corresponding to the actual data as subsecond variations due to turbulence motions in the background wind.

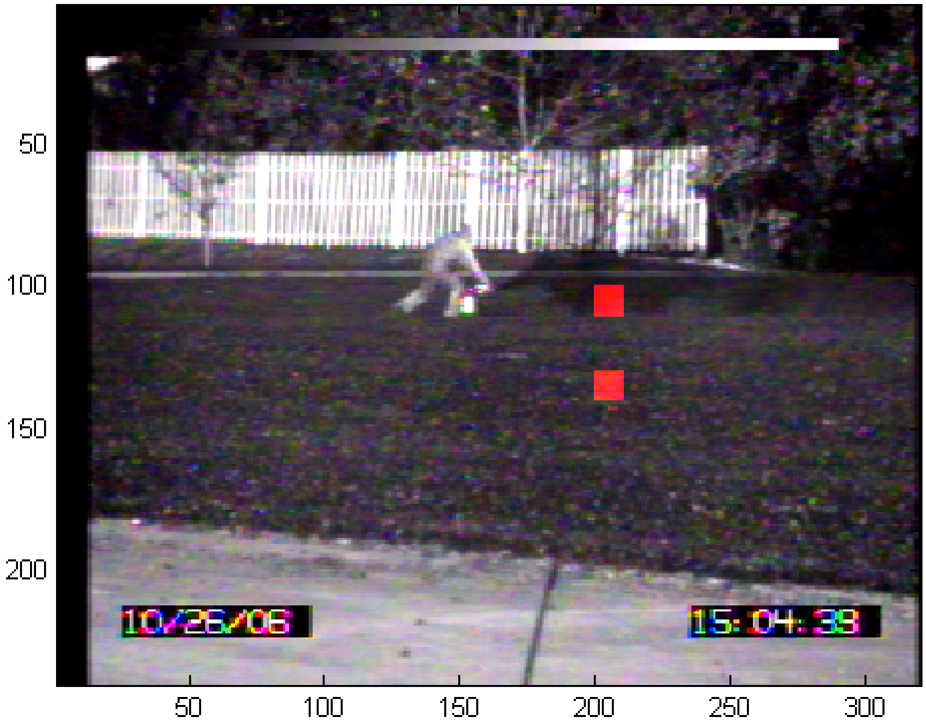

Figure 5.8: Plume (top square) and non-plume (bottom square) regions examined for Fourier analysis

The frequency variation across the FOV in the actual resolution of the imager is examined by performing the Fourier analysis for all pixels, and plotting the sum of the intensities for the frequency response range between 0.5 and 3 Hz (Figure 5.10). The same approach was performed for a measurement of a small propane release (100 SCFH) at 60 m, and a large propane release (500 SCFH) at 100 m. The results of these analyses can be found in Appendix H. In Figure 5.10, notice that the motions of the operator between his start and stop locations exceeds the frequency spectrum included in the analysis. The figure shows regions of increased change being primarily in the region of the plume, and in the area where the operator moves towards the tank to activate the release valve.

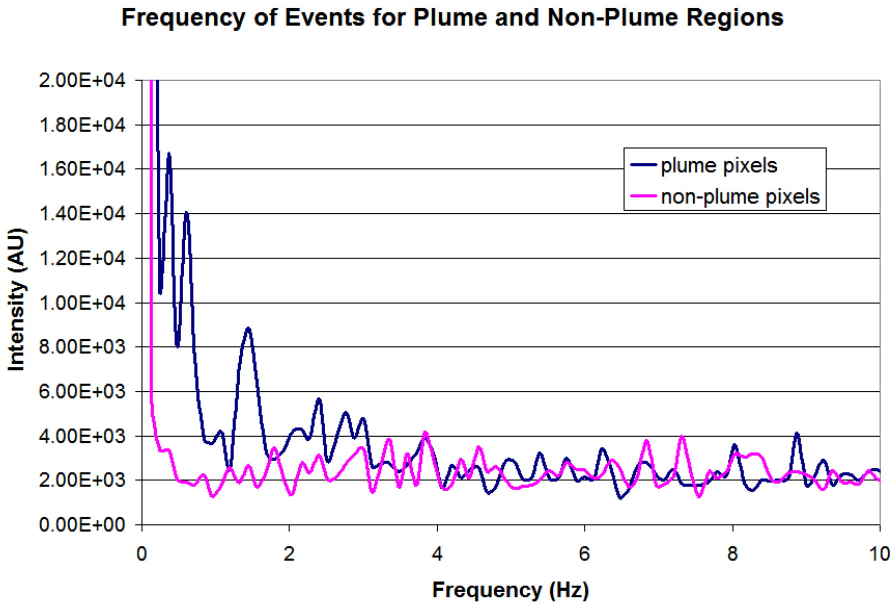

Figure 5.9: Frequency of events for plume and non-plume regions shown in Figure 5.8.

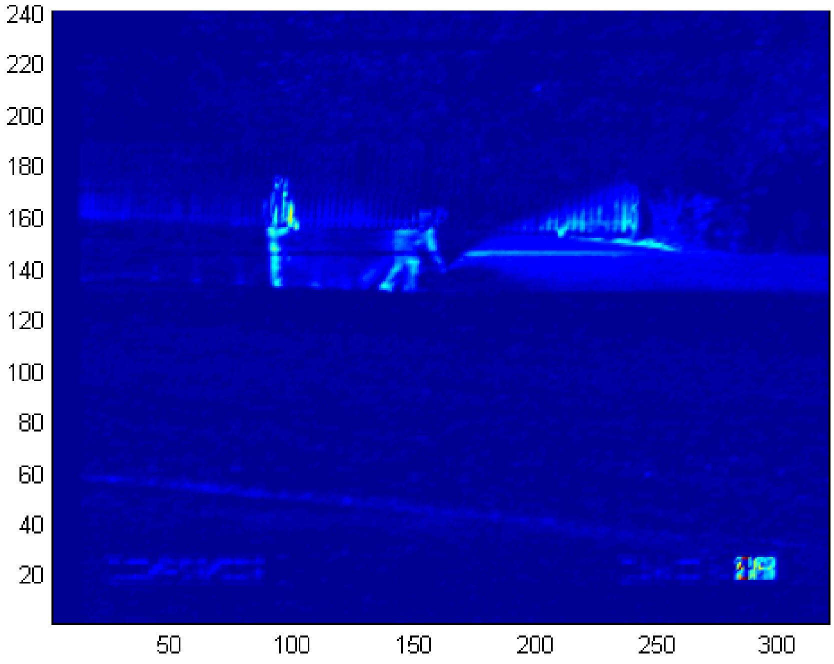

Figure 5.10: Sum of Fourier response for frequencies ranging from 0.5 to 3 Hz on a per-pixel basis for a 60 m range, and a 500 SCFH propane release.

Additional bright regions are due to the trees in the background, which are probably lightly tossing in the wind. To reduce the effects of the background variations, a second matrix is created using the Fourier analysis approach for a 10 frame set from the beginning of the dataset before the leak was active. This matrix was then subtracted from the total movie matrix to arrive at a difference matrix. A floor and ceiling filter that saturates the top and bottom ten percent of the data is used to accentuate the gain regions. The result of this process is shown in Figure 5.11.

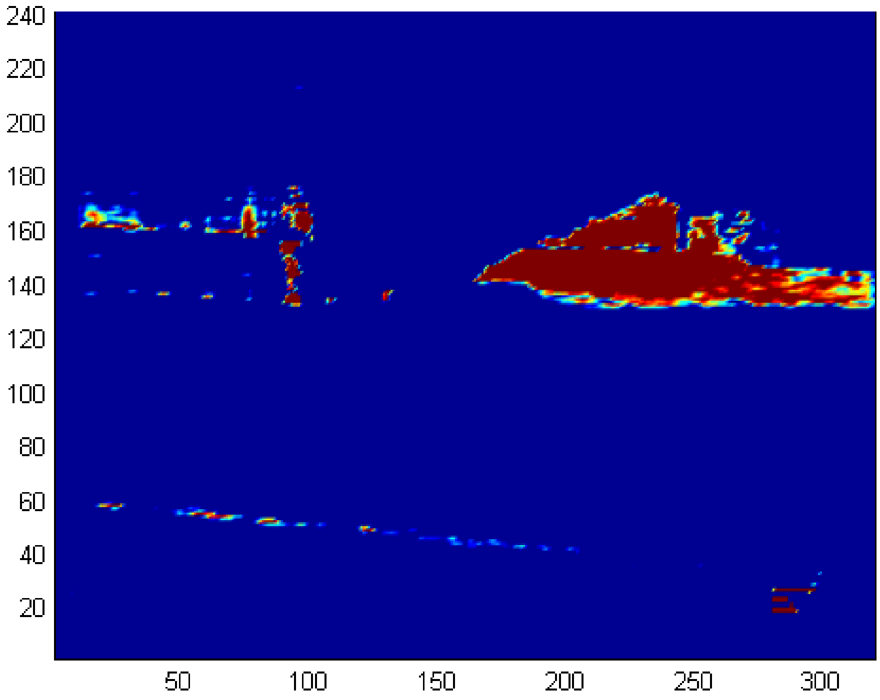

Figure 5.11: Plot of gain matrix. The gain matrix is then multiplied to background subtracted frames of the movie to accentuate the plume region.

The dark red regions correspond to regions of the largest change in the collected dataset, and they appropriately show the region of the plume and the region where the person is walking in the FOV of the camera. We denote this matrix as the "gain matrix." The result of reprocessing the movie using the previously discussed background image subtraction in addition to multiplying the "gain matrix" by each frame in the dataset is shown through a snap shot of frames in Figure 5.12. The region of the plume experiences increased pixel intensities via multiplication of the gain in targeted regions of the FOV.

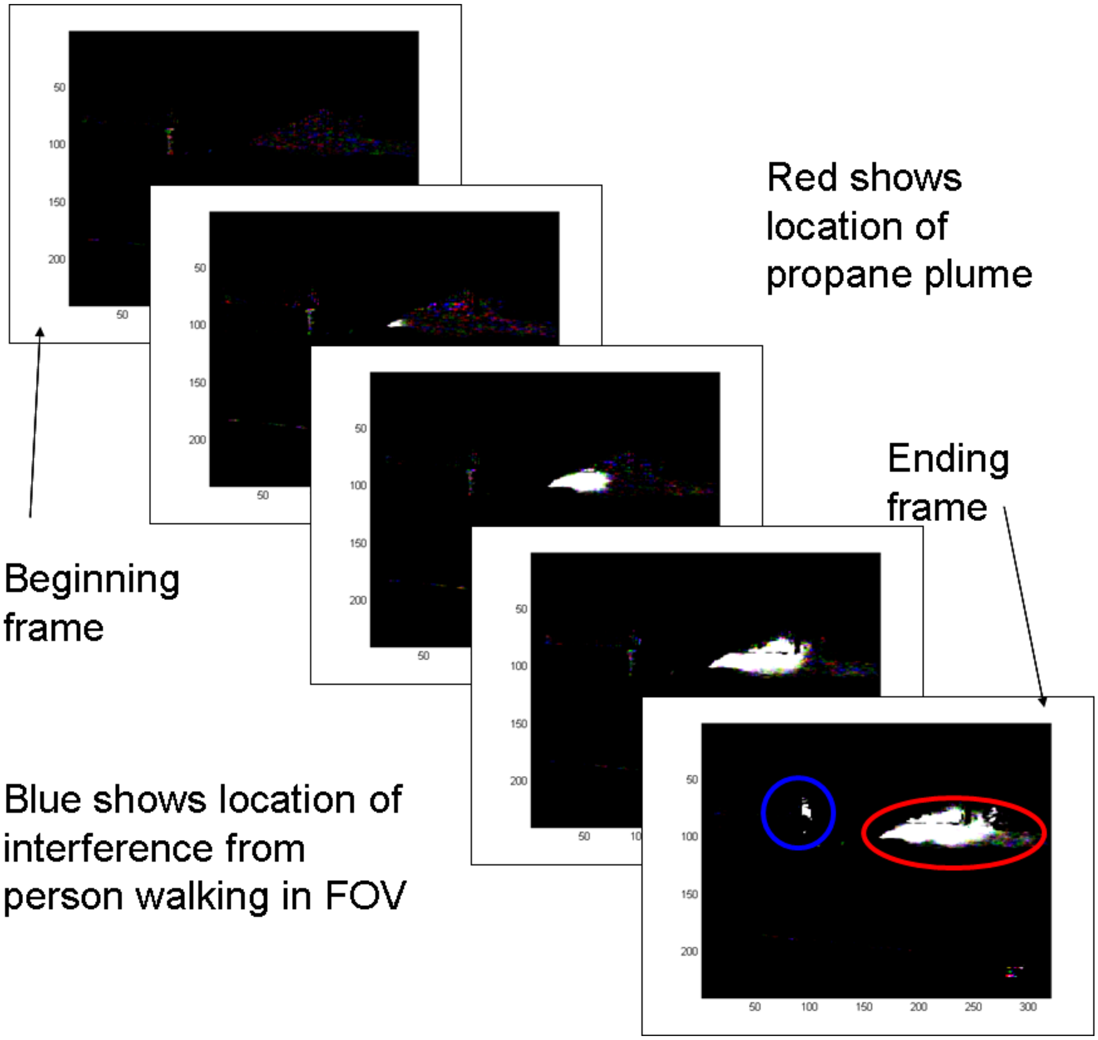

Red shows location of propane plume

Ending frame

Beginning frame

Blue shows location of interference from person walking in FOV

Figure 5.12: Frames captured from the final post-processed movie of a staged 500 SCFH propane release at 60 m. The top left frame shows the response just after the staged leak was activated. Subsequent frames (moving to the bottom right of the figure) show the increase in the extent of the plume as time progresses with the staged leak still active.

In the airborne measurement case, the system would be surveying pipelines or other remote areas from an airborne platform, and would have minimum human interference. Under this type of operation, a “gain matrix” could be created on the fly for regions of the ground observed by the imager through knowledge of the ground speed and of data segmented along the flight path. Small variations due to blur and movement of the terrain in the FOV would be straightforward to remove using the approach under the assumption that the aircraft is flying at a constant speed. This movement would generate a peak in the Fourier spectrum that could be analyzed before summation and creation of the difference and gain matrices. Sample calculations of pixel blur for the Merlin infrared camera are provided in Appendix I.

5.5 Summary

The hydrocarbon imaging capability of the system is demonstrated using a staged propane release. A Fourier analysis approach is adopted for analysis of target regions of a propane release to enhance the post processing of the images. Similar approaches can be implemented for the down-looking airborne measurement case if these considerations are incorporated into the design.

CHAPTER 6

Theory, Simulation, and Proof-of-Concept Studies for Supercontinuum Absorption Spectroscopy (SAS)

The combination of two-wavelength DAS with multi-wavelength differential absorption generates a detection and quantification scheme that extends the advantages of both techniques. Through the study of error in classical DIAL and DAS measurement (Chapter 3 of this work), we found that absorption wavelength choice, beam overlap percentage, and near simultaneous online and offline measurements are important factors in reducing error in the measured species concentration. When examining broadband multi-wavelength imaging approaches (Chapter 4 and 5 of this work), we found that many wavelengths can be used in a passive sensor to detect and qualitatively image hydrocarbon plumes. A supercontinuum source DAS approach provides many wavelengths that can be used for individual DIAL comparisons or a broadband analysis that is similar to multi-wavelength differential absorption and hyperspectral imaging. Furthermore, supercontinuum DAS removes the effects introduced in two wavelength DAS measurements that are due to poor beam match with the absorption feature, and space-time overlap of the online and offline wavelengths. These factors are usually the major source of error when using topographic target returns.

This chapter develops the theoretical background for Supercontinuum Absorption Spectroscopy (SAS), which is drawn from a combination of concepts and techniques examined in this work (Chapters 3 through 5).

6.1 Supercontinuum Absorption Spectroscopy (SAS) Background

Supercontinuum Absorption Spectroscopy (SAS) presents an alternative solution for spectroscopic mapping of atmospheric species that can provide advantages in terms of fabrication, operation, power requirements, and cost effectiveness. Photonic crystal fibers and sub-nanosecond pulses are used to generate a supercontinuum spectrum as a laser transmitter. The technique can be used at ranges of 10 m to 10 km with minimum system modification, while transmitting much less power than typical DIAL instruments. Improved designs have simplified the optical alignment by arranging the transmitter and receiver in a monostatic manner.

The developed system adopts a variant of the DOAS design presented by Platt [1994] where the transmitter and receiver of the SAS system are placed at the same location in a collinear configuration. The implementation of this geometry allows our experiments to be conducted by transmitting a supercontinuum beam from a roof laboratory to adjacent buildings where retroreflector targets are positioned. The retroreflector targets direct the beam back to the receiving telescope, where the optical signals are transferred to a spectrometer for analysis. This approach allows the collection of a large percentage of the transmitted signal, and when combined with a sensitive spectrograph, the absorption spectra has sufficient signal to use sub-second integration times.

With these advantages, the SAS system is capable of answering the research needs for highly accurate spectroscopic measurements in areas where laser visibility and/or eye-safety issues could impose restrictions, as well as providing a new capability for many applications in monitoring chemical species concentrations. Details of the design and sample datasets are discussed in this chapter. Additionally, data analysis algorithms developed for multiple wavelength DIAL lidar systems are discussed. An algorithmic approach has been selected, improved upon, and applied to analyze indoor and outdoor SAS spectra of water vapor and oxygen to demonstrate the validity of the measurement technique. Papers describing our efforts have been recently published [Brown, *et al.*, 2008a; Brown, *et al.*, 2008b].

6.2 Supercontinuum Source

A variety of nonlinear optical interactions within air silica microstructure fibers (photonic crystal fibers) allow the creation of supercontinuum coherent radiation, or "white light." The highly nonlinear properties of air-silica PCF fibers provide significant wavelength broadening as high-energy laser pulses are launched down the fiber. The most significant contributor of the several nonlinear effects present is self-phase modulation from using femtosecond laser pulses to generate supercontinuum laser light. Raman scattering, Brillouin scattering, and phase matching (four-wave mixing) are also contributors to the spectral broadening of the continuum, but these processes contribute to a far lesser extent when utilizing femtosecond pulses [Dudley, *et al.*, 2002]. These effects, along with the soliton self-frequency shift, become more critical for the generation of supercontinuum light in pulses that are broadened in time (i.e. picosecond or nanosecond pulses) [Dudley, *et al.*, 2002].

The SAS transmitter in our instrument uses a low power, relatively low cost supercontinuum source. By coupling sub-nanosecond laser pulses from a passively Q-switched microchip laser (JDSU NP-10620-100, wavelength at 1064 nm, average power ~ 70 mW) into an 18 m length of photonic crystal fiber (Blaze Photonics SC-5.0-1040), we are able to generate supercontinuum white light [Alfano, 1989; Wadsworth, *et al.*, 2002].

When using 40X microscope objectives to focus and re-collimate the light into the PCF, the typical supercontinuum output average power is 16 to 18 mW. The pump laser has a repetition rate of 8 kHz with a peak energy per pulse of about 8.75 μJ, which lends to four-wave mixing as the primary mechanism responsible for the creation of broadband laser light. A typical spectrum of the supercontinuum source used for the absorption investigations described in this work begins near 500 nm and extends into the near infrared beyond 1600 nm as shown in Figure 6.1(a).

To measure the full range of the supercontinuum source, the spectrum was collected by collimating the supercontinuum output and focusing the light down via a 20X microscope objective into a multimode fiber. This fiber was then connected to an Ando (now Yokogawa) optical spectrum analyzer (AQ6315E) input, and the wavelength region was scanned in approximately five seconds. Figure 6.1(b) shows an image of the raw supercontinuum output from the photonic crystal fiber, and Figure 6.1(c) shows the rainbow formed from the collimated supercontinuum passing through a 1100 lines/mm grating.

6.3 Laboratory Path Measurement

Our first experiments used the supercontinuum source to measure atmospheric water vapor content along a folded path in a laboratory environment [Begnoché, 2005]. This result was then compared with the MODTRAN™ [Berk, *et al.*, 2004] simulation result for the water vapor absorption band in the 1.3 to 1.5 µm region.

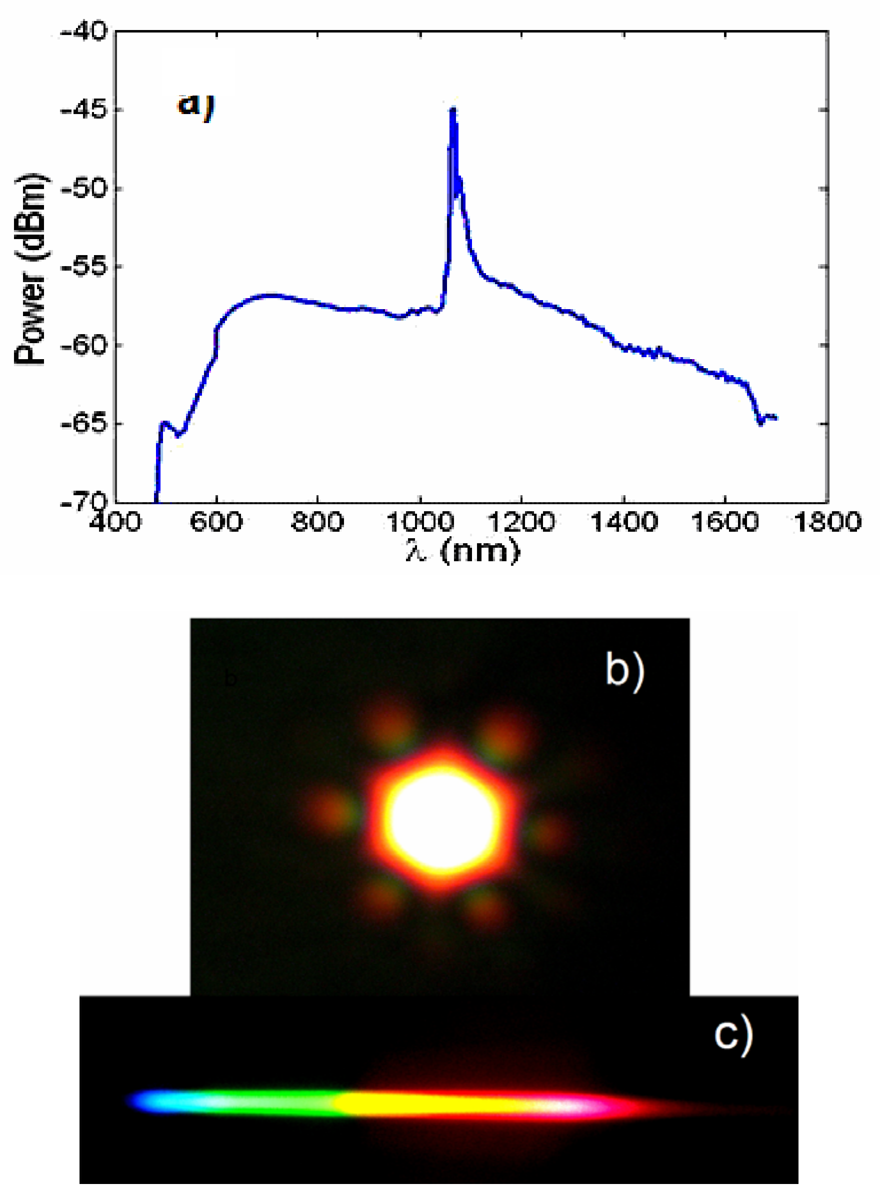

Figure 6.1: (a) Supercontinuum source spectrum; (b) The far field pattern of the supercontinuum spectrum generated from a photonic crystal fiber; and (c) Rainbow observed after collimated light passes through a prism.

6.3.1 Experimental Setup and Selection of Wavelength Region

The indoor laboratory supercontinuum absorption measurement traversed a 20 m path before being coupled into the Ando spectrometer for data collection. The aerosol scattering was minimized because the beam traversed a relatively short path length through filtered laboratory air. A simple experimental setup, shown in Figure 6.2, was employed to allow the collimated beam to traverse the absorption path and then be coupled into the Ando optical spectrometer via a 20X microscope objective, and a 3 m multimode fiber optic connection. Typically, subsecond scan times on the spectrometer were sufficient to capture the wavelength range of interest in low resolution for the indoor measurements of water vapor absorption spectra. When operated in this mode, the Ando spectrometer has a data collection range of roughly 200 nm; therefore, a spectral region of interest is specified prior to carrying out the experiment. The wavelength range for the Ando spectrum analyzer is set by examining the horizontal transmission for a 20 m path using an atmospheric transmission model. The MODTRAN^{TM} model is convenient for determining the approximate transmission profiles for typical cases of atmospheric conditions (temperature, pressure, constituent concentration, aerosol distributions, path length, etc.). Based on our examination of the MODTRAN^{TM} model output, the Ando spectrometer was configured to examine the water vapor absorption band in the near infrared between 1300 and 1500 nm (~7700 and 6700 cm^{-1}) because of the spectral features of the water vapor absorption overtone expected here.

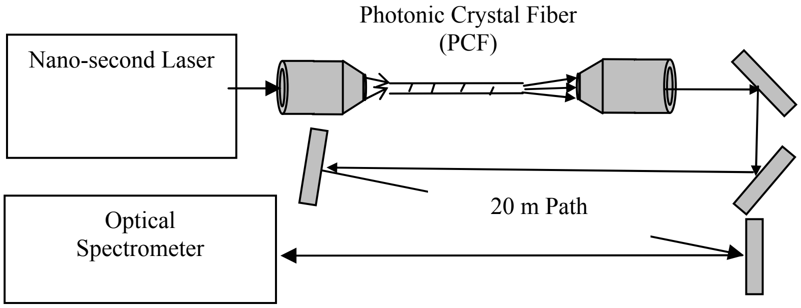

Figure 6.2: Experimental setup used to measure water vapor spectrum with a supercontinuum source.

6.3.2 Experimental Data Compared with MODTRAN^{TM} Result

A MODTRAN^{TM} simulation of the transmission on a 20 m experimental path under typical atmospheric conditions at a 1 cm^{-1} resolution selected for the spectrometer measurements is shown in Figure 6.3 as the pink line. The raw spectrum captured with the spectrometer during the experiment is shown in the same figure as the dark blue line. A significant deviation between the measurement and the simulated result is observed toward the ends of the chosen region of interest. Outside of the band of strong water vapor absorption, the experimental data were compared with the power spectrum of the supercontinuum source to examine the low-frequency attenuation experienced in these regions. By examining the power spectrum, Figure 6.3, we conclude that the poor correlation is not as a result of the spectrum of transmitted supercontinuum light, but instead due to an additional optical "instrument function," which is most likely associated with the optics used to couple the output into the optical spectrometer, as well as with the detector performance. To perform a general normalization of the measured spectrum for a comparison with the simulated MODTRAN^{TM} response, the wings of the absorption band are used to determine an approximate instrument function shown by Figure 6.4. The collected data are normalized for further analysis using the instrument function.

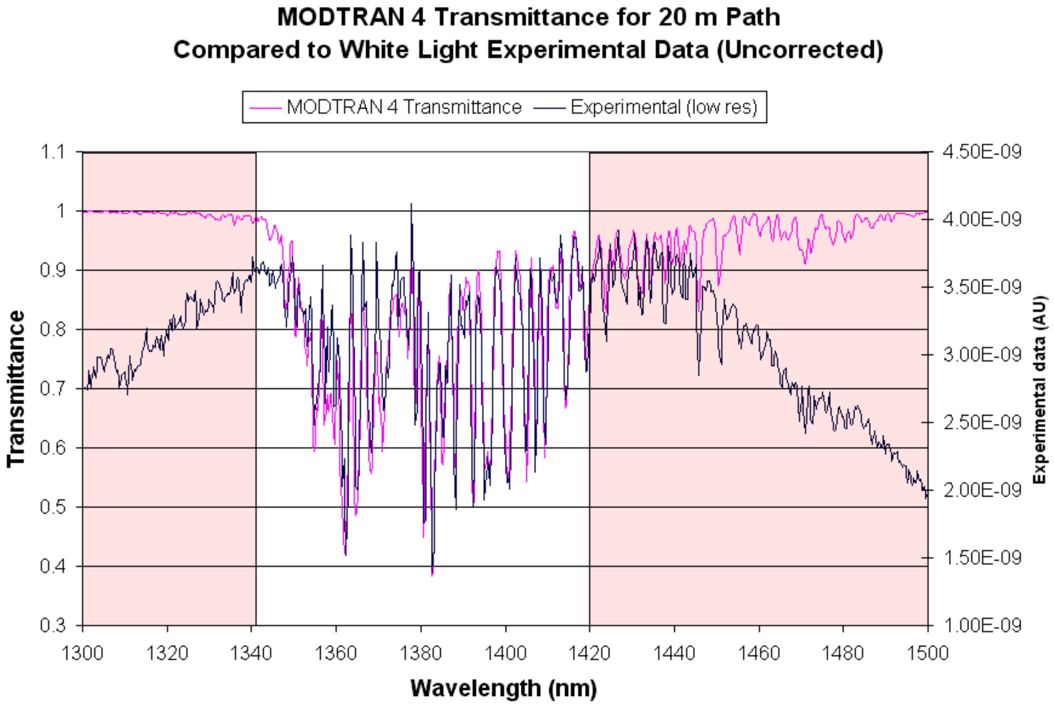

Figure 6.3: Water vapor transmittance 1300 -1500 nm raw experimental (blue) compared to MODTRAN^{TM}4 (pink).

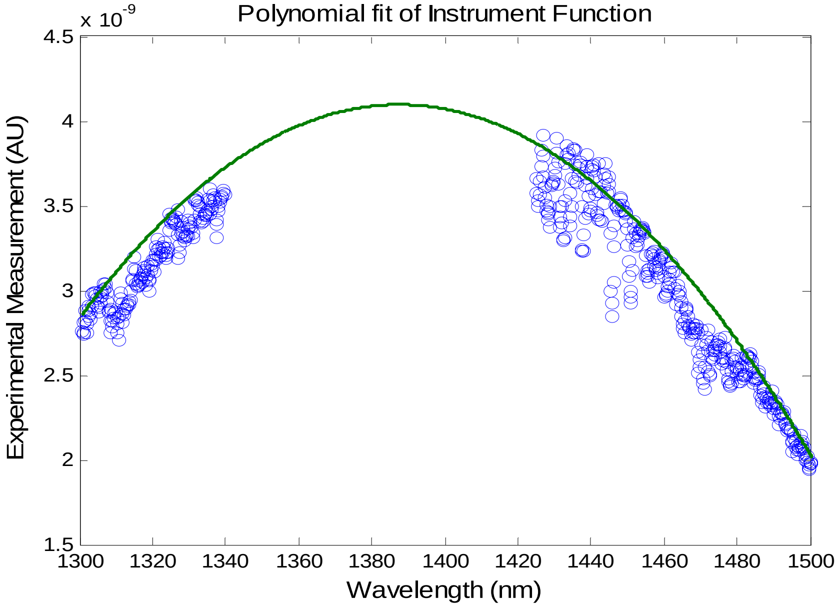

Figure 6.4: Normalization of experimental data utilizing polynomial fitting of non-absorbing wavelength ranges.

The results from normalized experimental data are compared with the model output of the MODTRAN™ 4 in Figure 6.5. The experimental data were captured with a resolution of 0.2 nm set in the Ando spectrometer, with a sampling increment of 0.05 nm. In the vicinity of 1.4 µm, these settings correspond to an equivalent MODTRAN^{TM} 4 resolution of 1 cm^{-1} with a sampling increment of 0.25 cm^{-1}.

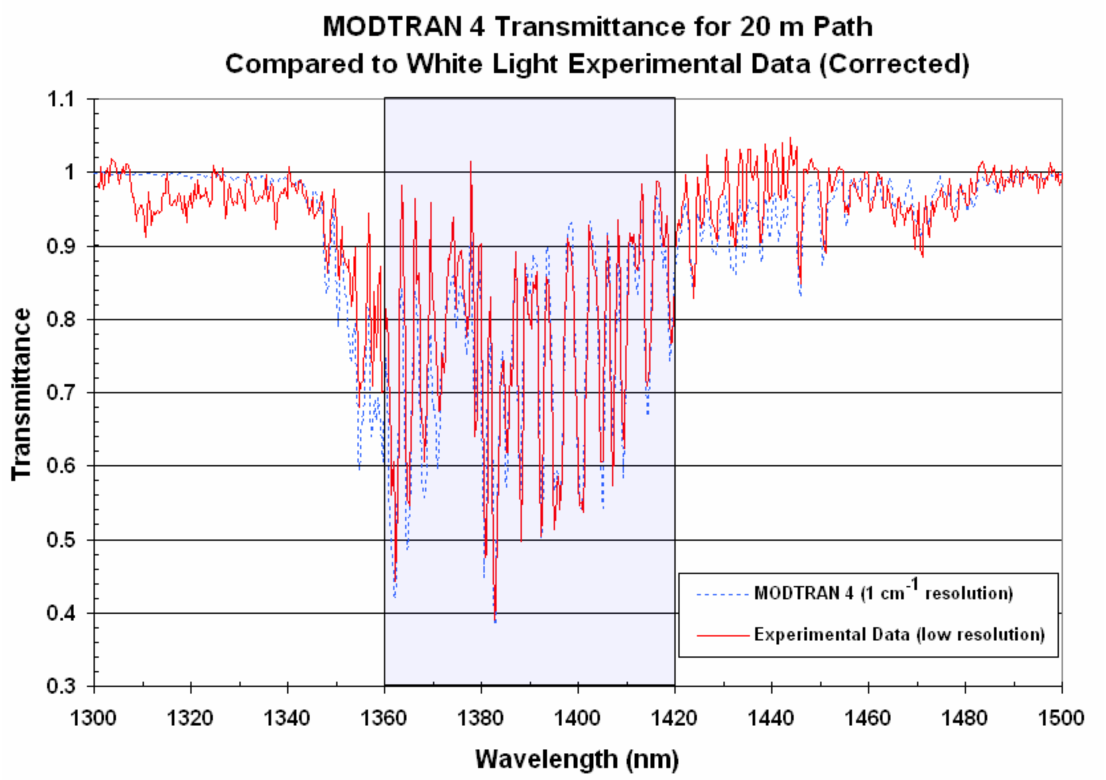

Figure 6.5: Normalized water vapor transmittance 1300-1500 nm measurements using the supercontinuum laser (red) are compared when the spectrometer slit is set for the 1 cm^{-1} resolution corresponding with MODTRAN™ 4 (blue).

Figures 6.5 through 6.7 show MODTRAN™ 4 and 5 results compared with normalized experimental spectra. Higher resolution experiment measurements are compared with the results from the beta test version of MODTRAN™ 5, which has a resolution capability of 0.1 cm^{-1}. In this case, the resolution of the spectrometer is configured to be 0.08 nm, with a sampling increment of 0.02 nm. In the vicinity of 1.4 µm, these settings correspond to an equivalent MODTRAN^{TM} 5 resolution of 0.4 cm^{-1} with a sampling increment of 0.1 cm^{-1}.

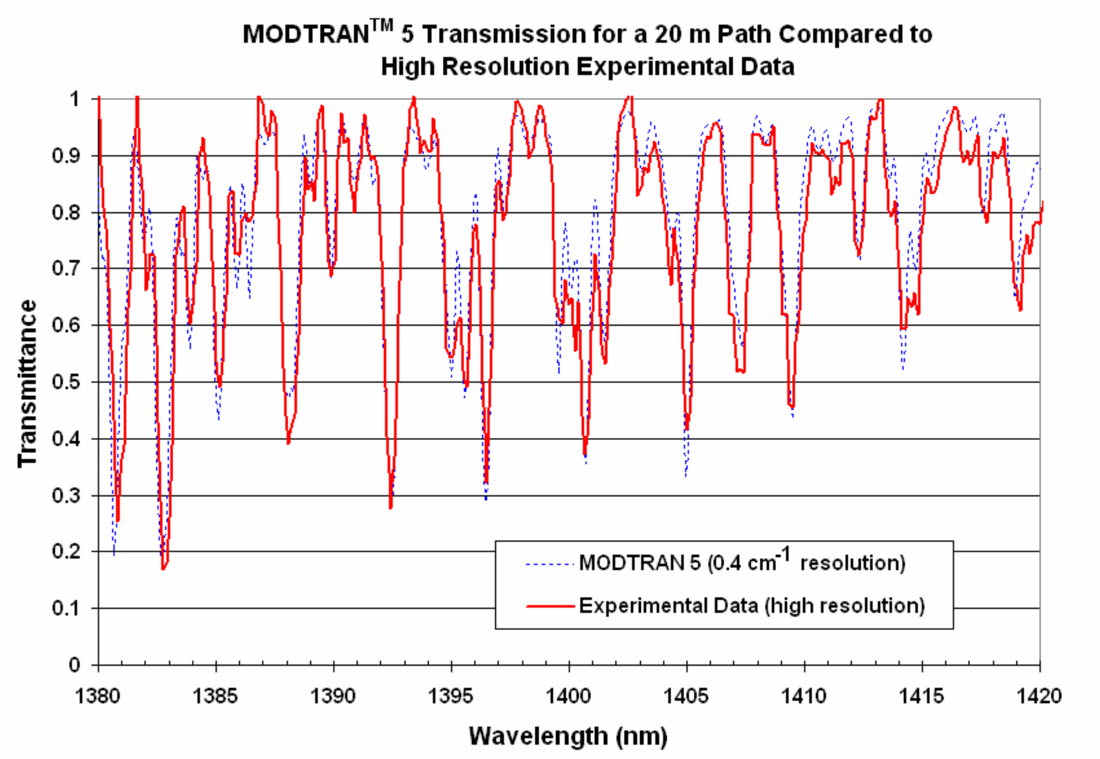

Figure 6.6: Water vapor transmittance 1380-1420 nm experimental measurements (red) compared with MODTRAN^{TM} 5 simulation (blue), with resolution matched to the instrument 0.4 cm^{-1} parameter.

The MODTRAN^{TM} results shown in the figures throughout this section are created using the point measurements of the laboratory air (relative humidity from a sling psychrometer, 37 +/- 1 %). The difference in measurement geometry can account for some of the observed differences, since the experiment is a path averaged measurement and it is being compared to a simulation created from a point measurement of water vapor concentration. The value of the water vapor concentration can also be obtained by data analysis of the experimental spectrum, and is done so in subsequent sections of this work. The effects due to pressure and temperature variations on the analysis procedure were not explored in this study; however, finer-resolution experiments would increase the influences of pressure and temperature effects on the magnitude and shape of the absorption features under investigation.

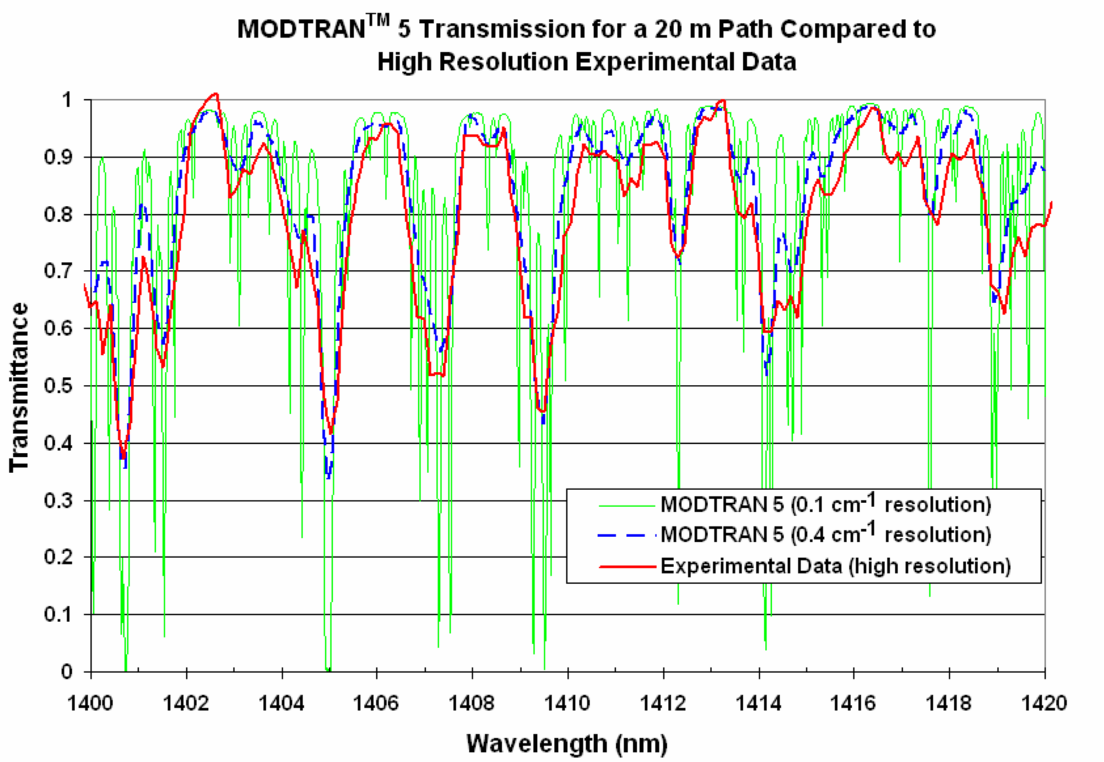

Figure 6.7: Water vapor transmittance 1400-1420 nm experimental measurement (red) compared to MODTRAN^{TM} 5 simulation with parameters selected to match the sensor (blue). The highest resolution available (0.1 cm^{-1}) for MODTRAN^{TM} 5 simulations (green) is also shown for reference.

6.4 Calculation of the Absorption Spectra

Later in this work, absorption path measurements are used to determine the concentration of the species along the path, and to create MODTRAN^{TM} simulations for comparison of the spectral match in an experiment data. The measured number density of an absorbing species depends heavily on accurate calculation of the absorption spectra for the species under investigation. A Matlab routine was designed to perform this calculation for any species with laboratory grade absorption spectra, or when the HITRAN [Rothman, *et al.*, 2001] spectral cross sections are available. In the case of the species of interest for this research, HITRAN cross sections are available. The routine calculates absorption spectra from HITRAN cross sections at a resolution that is 10 times finer than the experimental slit width used. The absorption spectra are then calculated using the following approach for temperature and pressure broadening of absorption lines.

The absorption spectra used for calculation of concentration path length begins by adjusting the spectral line intensity provided by the HITRAN database relative to the ambient air temperature. The following Equation 6.1 provides the mechanism to perform this calculation [Herzberg, 1962; Gamache, *et al.*, 1990],

$$S_{\eta\eta'}(T) = S_{\eta\eta'}(T_{ref})\left(\frac{T_{ref}}{T}\right)^{n} e^{\frac{1}{T}-\frac{1}{T_{ref}}} \frac{\left(1-e^{-\frac{c_2\nu_{\eta\eta'}}{T}}\right)}{\left(1-e^{-\frac{c_2\nu_{\eta\eta'}}{T_{ref}}}\right)} \quad \left[\mathrm{cm\ atm^{-1}molecule^{-1}}\right] \qquad [6.1]$$

where,

T is the ambient temperature in $[\mathrm{K}]$,

T_{ref} is the HITRAN reference temperature, 290 $[\mathrm{K}]$,

c_2 is the second radiation constant in units of $[\mathrm{cm\,K}]$,

$\nu_{\eta\eta'}$ is the HITRAN-provided line transition frequency in units of $[\mathrm{cm^{-1}}]$,

n is the HITRAN-provided coefficient of temperature dependence of the air-broadened halfwidth [unitless], and

$S_{\eta\eta'}(T_{ref})$ is the HITRAN-provided spectral line intensity at the reference temperature in units of $\left[\text{cm atm}^{-1}\text{molecule}^{-1}\right]$.

HITRAN also provides the air-broadened and self-broadened line halfwidths, which are used in the calculation of the actual pressure and temperature broadened line halfwidth,

$$\gamma(p,T)=\left(\frac{T_{ref}}{T}\right)^{n}\left[\gamma_{air}\left(p_{ref},T_{ref}\right)\left(p-p_{s}\right)+\gamma_{self}\left(p_{ref},T_{ref}\right)\left(p_{s}\right)\right]\ \left[\text{cm}^{-1}\ \text{atm}^{-1}\right] \quad [6.2]$$

where,

p is the ambient pressure in units of $[\text{atm}]$,

p_s is the HITRAN reference pressure, 1 $[\text{atm}]$,

$\gamma_{air}\left(p_{ref},T_{ref}\right)$ is the HITRAN-provided air-broadened line halfwidth at the reference temperature and pressure in $\left[\text{cm}^{-1}\ \text{atm}^{-1}\right]$, and

$\gamma_{self}\left(p_{ref},T_{ref}\right)$ is the HITRAN-provided self-broadened line halfwidth at the reference temperature and pressure in $\left[\text{cm}^{-1}\ \text{atm}^{-1}\right]$ [Herzberg, 1962; Gamache, *et al.*, 1990].

The pressure-shifted line transition frequency is then calculated through the following Equation 6.3 [Herzberg, 1962; Gamache, *et al.*, 1990],

$$\nu^{*}_{\eta\eta'}=\nu_{\eta\eta'}+\delta\, p\ \left[\text{cm}^{-1}\right] \quad [6.3]$$

where,

δ is the HITRAN-provided air-broadened pressure shift in units of $\left[\mathrm{cm}^{-1}\,\mathrm{atm}^{-1}\right]$.

Equations 6.1 through 6.3 are then used to create Equation 6.4, which calculates the pressure-shifted and temperature-broadened absorption spectra at ambient temperature and pressure using a standard Lorentzian lineshape function [Herzberg, 1962; Gamache, *et al.*, 1990].

$$\sigma(\nu, p, T) = S_{\eta\eta'}(T)\left(\frac{\gamma(p,T)}{\pi\left[\gamma(p,T)^2 + \left(\nu - \nu^*_{\eta\eta'}\, p\right)^2\right]}\right)\left[\mathrm{cm}^2\mathrm{molecule}^{-1}\right] \qquad [6.4]$$

The high resolution absorption data calculated using the above procedure are then convolved with the resolution of the spectrometer used for the experiment. The first step of the analysis approach performs the absorption spectra calculations for a range of slit widths near the expected match. The process then takes the inverse of these calculated absorption spectra, and tracks the correlation with the experimental data set. The slit width that corresponds to the correlation maximum is then selected as the optimum solution for the experiment. The selected slit width is then used to create the appropriate MODTRAN$^{\mathrm{TM}}$ simulation result. Alternatively, if the experimental spectrum is examined in a coarser resolution than when it was originally collected, then both the experimental spectra and the absorption cross section are convolved with the appropriate slit width. These spectra are then used for data analysis.

6.5 Data Analysis Algorithms

Although MODTRAN^{TM} provides us with the toolset required to quickly simulate a set of reference spectra for various concentrations of water vapor and other species, a real-time instrument requires a rapid processing scheme to determine a total concentration path length (CPL). A CPL algorithm needed for use with SAS experimental data should calculate the concentration of a species of interest using many features in the spectral region, rather than just the two wavelengths traditionally used in DIAL analysis. The data processing algorithm implemented should also provide the framework for detection and measurement of several mixed vapors in a composite spectrum.

Unlike typical frequency-agile lidar systems, where the composite response would consist of a number of carefully chosen laser lines used in a DIAL analysis, implementation of a supercontinuum source provides an opportunity to measure several species simultaneously. Furthermore, the supercontinuum source absorption measurement is performed without any time delay for tuning various wavelengths and uses a mixture of many online and offline features in the analysis. The spectral steps in the supercontinuum are much smaller than the absorption line width, thus removing the errors associated with matching the DIAL laser online peak with the absorption line of interest. These distinct advantages allow the SAS approach to be used for atmospheric species detection, and provides the ability to perform simultaneous detection of multiple vapors with strong spectral overlap, i.e. Spectral Pattern Recognition DIAL (SPR-DIAL) [Philbrick, *et al.*, 2006; Brown, *et al.*, 2006].

The algorithm approach developed has the capability to estimate the atmospheric concentration of multiple spectrally overlapping features. Although current experimental datasets that we have studied thus far do not possess absorption structures from multiple overlapping species, we have chosen to simulate such a case, and to test the performance of the algorithm prior to its application on experimental data. Theoretical absorption spectra are calculated as discussed above, and provide the basis for the calculation of atmospheric species concentrations. Atmospheric pressure and temperature affect these calculations, and hence are typically measured remotely using Raman lidar [Philbrick, 2005] and DIAL lidar techniques. The present research, however, uses local meteorological data for these atmospheric parameter values. The resolution of the absorption spectra and the experimental data are then matched before the algorithm is executed. Following the calculation of the appropriate absorption spectrum, the concentration of each possible target is calculated using many wavelengths to invert the spectrum into its several individual components representing the several species at their respective concentrations. For a detailed explanation of the core algorithm, we refer the reader to the work of Warren [1996] or Yin and Wang [2006], as the approach is built on the fundamentals developed in these works. The final concentration for each target is derived from a weighted average of multiple algorithmic results from this core process.

6.5.1 SAS Multi-wavelength Algorithm

Warren’s work generalizes a two-wavelength single-target methodology and evolves it to include multiple wavelengths and multiple targets [Warren, 1996]. The approach, however, is still tied to the paradigm of computing the ratio of wavelength pairs in the return signal. Later work of Warren derives an alternative method for detection and measurement based on a likelihood ratio test methodology, which directly utilizes the return signal of each wavelength. The lack of many DIAL pairs available sometimes forces this approach to arrive at CPLs that grow without bound as the algorithm is iterated. As stated by Warren, the iterative algorithm for the calculation of target species CPL is performed for each wavelength pair in his work, and it thus produces an estimate for CPL that is very sensitive to noise details [Warren, 1996]. The sensitivity to noise details is particularly enhanced for vapors whose spectra are highly structured, and unfortunately this sensitivity is typical of many targets of interest. Later changes made to the maximum likelihood estimator (MLE) algorithm by Yin and Wang [2006] forego the iterative procedures for each wavelength pair. Starting with an initial CPL guess, they simultaneously solve the noise covariance matrix, $\hat{\Lambda}$, and determine the CPL of multiple vapors [Yin and Wang, 2006]. Following this procedure, the SAS algorithm approach uses a complete array of wavelength-specific target vapor absorption parameters, α, simulated signal, $\hat{H}$, and average SAS integrated measurements, $\overline{Q}(j)$, to solve for the main bracketed component in Equation 6.5.

$$CPL_l = \frac{1}{n-1} \sum_{M=n-x}^{n} \left\{ \frac{\sum_{j=1}^{M} \left[\alpha_{jl} \hat{\Lambda}_1^{-1}(j,j) \left[\hat{H}_1 - \overline{Q}(j) - \sum_{l=1,l \neq 1}^{L} \alpha_{jl} CPL_l \right] \right]}{\sum_{j=1}^{M} \left[\alpha_{jl} \hat{\Lambda}_1^{-1}(j,j) \alpha_{jl} \right]} \right\} [ppm \cdot m] \qquad [6.5]$$

This modification is equivalent to looking at wavelength pairs concurrently, as a weighted sum of the entire set instead of as a set of individual estimations.

After sampling the input data (both absorption spectra and composite experimental measurement) at the appropriate wavelengths, the algorithm performs an iterative procedure on CPL. After a number of iterations, the result approaches an estimated CPL for each species, *l*, if that species is present in the collected dataset.

The final value for CPL in the SAS algorithm is calculated using many different wavelength selections to increase its robustness in analyzing real-world data collections. Because we have many wavelengths containing information of the species, we improve the accuracy of the calculated CPL by using a linearly spaced wavelength sampling scheme and then follow the convergence of the concentration calculation to a stable value. By picking a wavelength range of interest, and incrementing the number of laser wavelengths, *M*, from *n-x* to *n*, our CPL result is quite robust because it is an average of the results for these cases.

6.5.2 SAS Algorithm Performance Examination

A region in the near infrared that has spectrally overlapping absorption structure due to CO_2, CH_4, and H_2O has been selected for examination to test the performance of the developed data analysis approach. The program simulates a broadband SAS spectral return, and then analyzes the result as if it were an actual dataset of experimental spectra. Figure 6.8 shows the calculation result after including temperature and pressure broadening of the HITRAN line intensity datasets for the spectral region of interest. These absorption spectra are one of the main inputs to the MLE data processing step.

After the absorption spectra have been calculated, we simulate a SAS return using MODTRAN^{TM} 4 [Berk, *et al.*, 2004] with a signal-to-noise ratio (SNR) equation before differential absorption analysis. The simulated return corresponds to a one kilometer length path length with typical atmospheric concentrations of each of the atmospheric species.

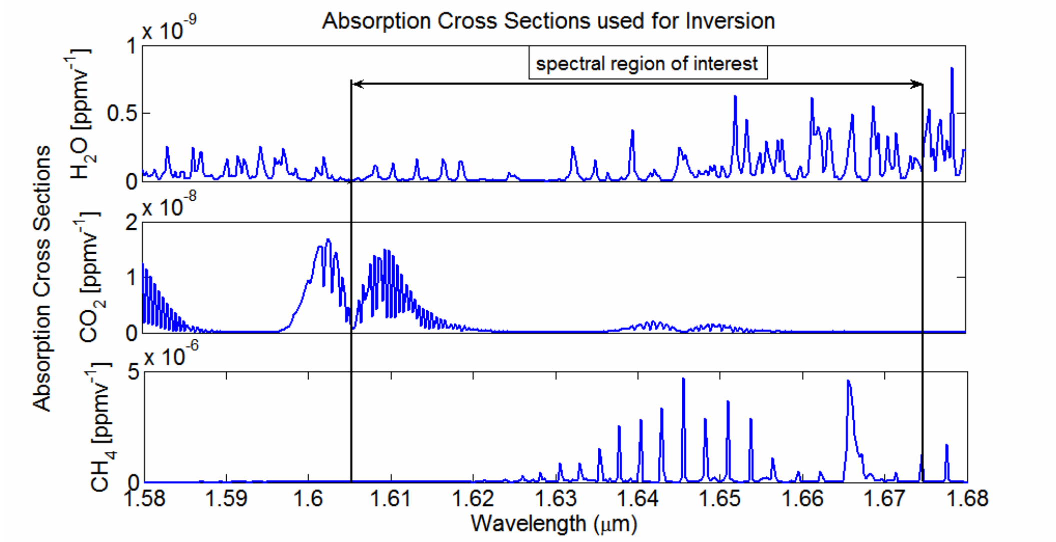

Figure 6.8: Cross section data of H_2O (upper), CO_2 (mid) and CH_4 (lower).

The signal-to-noise ratio equation allows us to introduce random fluctuations as a function of wavelength that approximates those fluctuations observed in our initial atmospheric path measurements. The typical equation for DIAL SNR [Measures, 1984] is normalized and modified for multiple species in terms of the spectral return power,

$$SNR_{total} = \left[2\left[\left(\frac{\sigma_{P_{off}^{T1}}}{< P_{off}^{T1} >} \right)^2 + \left(\frac{\sigma_{P_{on}^{T1}}}{< P_{off}^{T1} > - P_{\Delta}^{T1}} \right)^2 \right]^{-1} + 2\left[\left(\frac{\sigma_{P_{off}^{T2}}}{< P_{off}^{T2} >} \right)^2 + \left(\frac{\sigma_{P_{on}^{T2}}}{< P_{off}^{T2} > - P_{\Delta}^{T2}} \right)^2 \right]^{-1} + \ldots \right]^{1/2} . \qquad [6.6]$$

Here, $< P_{off}^{T1} > - P_{\Delta}^{T1} = < P_{on}^{T1} >$, and $< P_{off}^{T1} >$ is denoted as the average optimal offline return for species #1 with variance $\sigma_{P_{off}^{T1}}$, $< P_{on}^{T1} >$ is denoted as the average optimal online return for species #1 with variance $\sigma_{P_{on}^{T1}}$, and P_{Δ}^{T1} is denoted as the peak-to-peak differential power received for species #1 specified by the appropriate DIAL wavelengths. Because we are deriving a total signal-to-noise classifier for multiple targets using many wavelengths in a specified inversion band, we use the largest peak-to-peak differential power in the band for each target to specify P_{Δ}^{T1}. Although this value will change for different spectral ranges due to absorption strength and concentration of each species, it generally provides a way to track the performance of the MLE analysis algorithm as the SNR of the spectrum is reduced and the random fluctuations approach the peak-to-peak differences in the noiseless spectral return. We then add the normalized SNRs for each of the species present in quadrature to determine a total SNR. Figure 6.9 shows the normalized simulated SAS returns with different SNR cases.

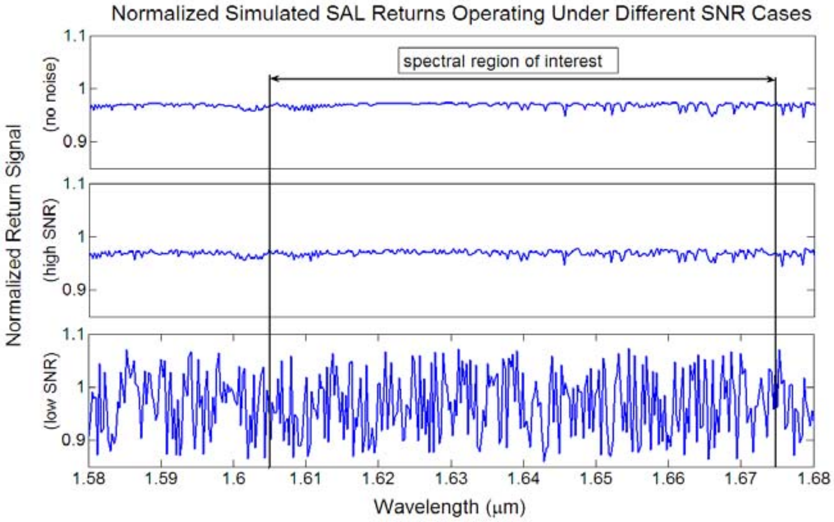

Figure 6.9: Simulated return calculation in 23km visibility for a 1 km path length under different SNR cases. Low SNR=4 and high SNR=10.

The top plot corresponds to a case where there is no noise, while the middle and lower plots correspond to high and low SNR cases respectively.

The performance of the MLE algorithm can be evaluated using the level of improvement in the standard deviation of the CPL result as the number of wavelengths used for comparisons is increased. The normalization of performance parameters is used to show this deviation from the ideal case in a manner that is easy to understand and compare for different levels of noise and signal while comparing the response of different species. Figure 6.10 shows the normalized percent difference from the exact concentration, and the normalized percent variation in this concentration for the concluded CPL for each of the three target gases.

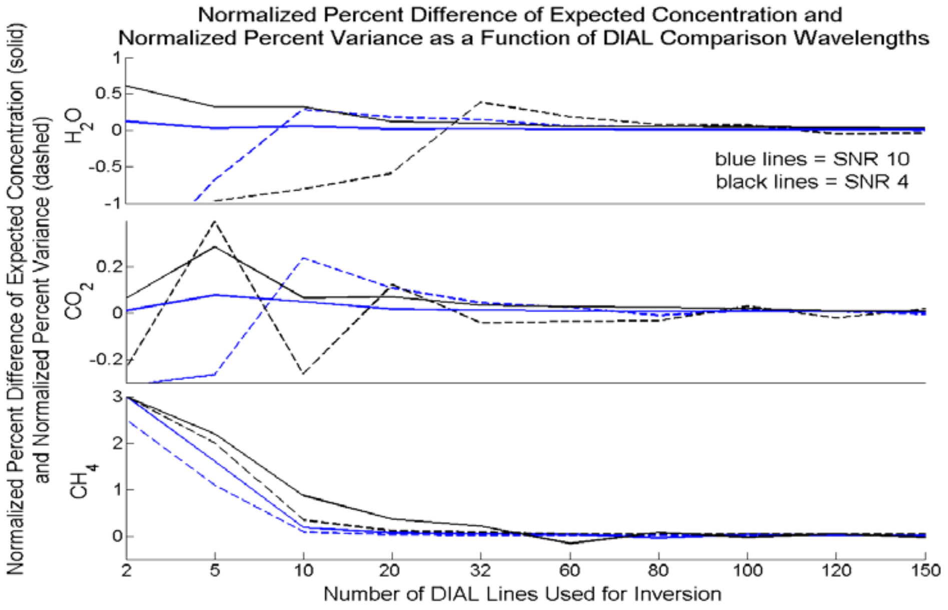

Figure 6.10: The normalized percent difference from the expected concentration (blue lines) and normalized percent variation (black lines) as a function of the number of DIAL lines used for comparison under a signal-to-noise ratio case of 4 (dashed line) and 10(solid line).

The analysis has been performed for two different signal to noise ratio cases, one with a SNR=4 and one with a SNR=10 using Equation 6.6. As the number of wavelengths used is increased, it can be observed that the accuracy of detection for H_2O and CH_4 using few lines is low due to the low absorption signal of these species in this spectral region. Furthermore, the inversion result of CO_2 is not highly accurate due to the noise interference and spectral bias for widely spaced wavelengths. As the number of wavelengths is increased however, the detection performance improves dramatically for each of the target species. From these results, it is clear that species detection from SAS return data using the MLE inversion with enough lines demonstrates good performance, even with low signal-to-noise ratio.

6.5.3 SAS Multi-wavelength Algorithm Applied to Experimental Data

The data from the initial 20 m path experiments described in Sect. 6.3.2 are processed to determine water vapor CPL using the absorption spectrum and the MLE algorithm. Figure 6.11 shows a schematic representation of the initial testing of the MLE algorithm. The figure shows a case where 50 linearly spaced wavelengths (red vertical lines) are used to sample the calculated absorption spectra and the collected experimental dataset between 1380 and 1420 nm. The result of the MLE algorithmic iteration is also shown in Figure 6.11. For this specific example, the procedure approximates the water vapor concentration to be approximately 10000 ppm for the 20 m path averaged measurement. A ground truth measurement at the time of the experiment arrived at a relative humidity 37 % for the air in the laboratory environment. This measurement was made at a temperature of 296 K, and leads to an equivalent concentration in ppm that can be calculated from [Lowe, 1977],

$$
\begin{aligned}
C_{H_2O}[ppm] &= 10^4(RH)\frac{Saturation\ Water\ Vapor\ Pressure}{Partial\ Pressure\ of\ Water} = 10^4(RH)\frac{P^o_{H_20}}{p_{H_2O}} \\
&= 10^4(RH)\left[\exp 13.3185\left(1-\frac{373.15}{T}\right) - 1.976\left(1-\frac{373.15}{T}\right)^2\right. \qquad .[6.7] \\
&\qquad \left. - 0.6445\left(1-\frac{373.15}{T}\right)^3 - 0.1299\left(1-\frac{373.15}{T}\right)^4\right].
\end{aligned}
$$

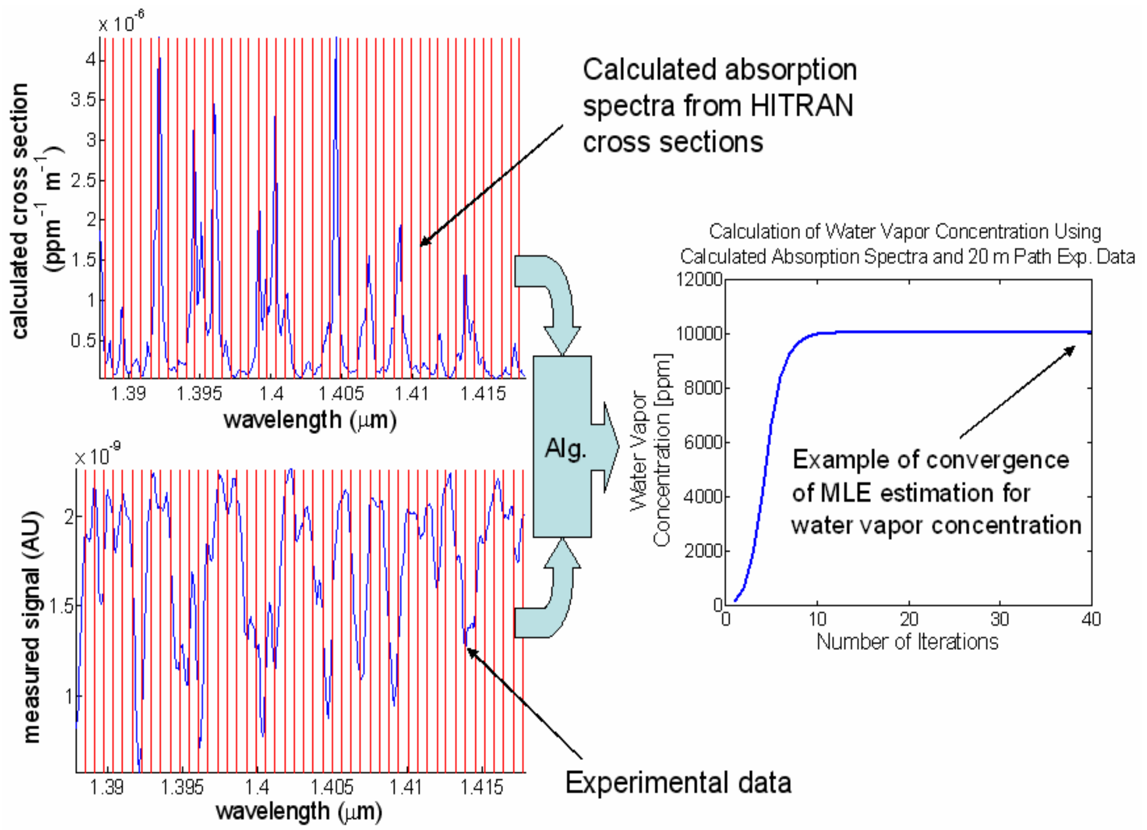

Figure 6.11: Shown on the left is the calculated water vapor absorption spectrum (top) and experimental data (bottom). The red vertical lines utilize a linearly spaced wavelength sampling scheme to feed spectral absorption information into the MLE algorithm. The algorithm iterates until it converges upon a best fit CPL (right), given the set of experimental data and absorption spectra of water vapor in a predetermined wavelength region.

The result is a concentration of water vapor of 10300 ppm and agrees well with the initial result from the MLE algorithm. This analysis is based on a single set of wavelengths. When multiple wavelength sets are used however, the MLE analysis provides a far more stable and confident result. The measured concentration is a path averaged value, and thus does not necessarily reflect the local variations along the path, or agree with a point measurement near the path.

Subsequent analysis uses an array of cases employing linearly spaced selected wavelengths within the measurement region starting with a guess of 10000 ppm. A case study using up to 500 wavelengths is shown in Figure 6.12.

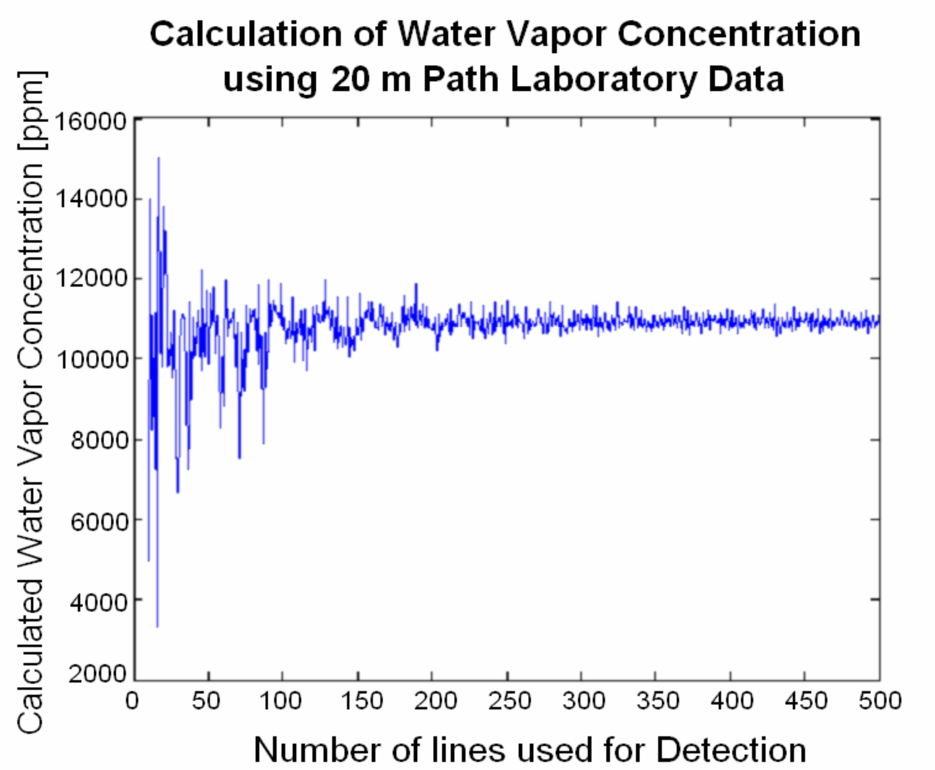

Figure 6.12: Calculation of water vapor concentration showing the convergence using 10 to 500 laser lines for comparison to 10900 +/- 75 ppm.

Beyond 200 linearly spaced wavelengths, the variation in the CPL result decreases and roughly varies between 2 and 5%. This analysis yields a concentration of water vapor of 10900 +/- 75 ppm, which is 2 % different from the value of relative humidity determined from the point measurements within the laboratory. This difference is larger than desired, but it is important to note that a one degree temperature change over the length of the path can result in a difference of this magnitude. Additionally, we note that the measurement volume is very different. The optical absorption measurement over a 20 m path compared with a laboratory point measurement of relative humidity should result in some difference.

6.6 Conclusions

Supercontinuum Absorption Spectroscopy (SAS) is demonstrated in the laboratory environment to detect, spectrally map, and quantify the concentration of water vapor. Hundreds of wavelengths combined with a multi-wavelength maximum likelihood analysis is used analyze the collected laboratory spectra after the supercontinuum beam traversed a 20 m path. The experimental measurement was validated by a sling psychrometer and a digital humidity meter present in the laboratory at the time of experimental data collection.

CHAPTER 7

Atmospheric Path Measurements using Supercontinuum Absorption Spectroscopy (SAS)

Following the laboratory proof-of-concept SAS measurements, a transceiver was built to perform atmospheric path measurements over the Penn State University Park campus. Water vapor and oxygen concentrations were both measured over several hundred meter paths during the measurement campaign. Two separate system topologies were tested using the approach. The results from these measurements are compared to MODTRAN^{TM} simulations and local meteorological data.

7.1 Initial Hardware Configuration

An outdoor SAS measurement was demonstrated by transmitting 16 to 18 mW of average power, which is sufficient to make highly accurate measurements of water vapor concentration along 300 m paths between building rooftops. Figure 7.1(a) shows the setup of the supercontinuum transceiver inside the door of the rooftop laboratory located on the EE East Building. The system utilizes a 114 mm diameter Newtonian telescope with a focal length of 450 mm. The fiber used to collect the reference and signal spectra was standard multimode telecom fiber with a 0.22 numerical aperture. The scanning rate and integration setting of the spectrometer was changed throughout outdoor experiment due to variations in the supercontinuum output power, and atmospheric conditions. Typically, the time required to capture one scan of the spectral region of interest was on the order of 1 to 5 seconds. A subset of this collected dataset was then later used for analysis of water vapor concentration along the path. Figures 7.1(b) and 7.1(c) are images taken during the operation of the instrument. Figure 7.1(b) shows the scattered component of the supercontinuum return from a retroreflector observed from 150 m away, and Figure 7.1 (c) shows the PCF under optimum coupling and hence peak output power conditions. The highly nonlinear PCF spreads the 1064 nm pump wavelength over a range of wavelengths in the visible and near infrared parts of the spectrum by the nonlinear optical processes discussed above.

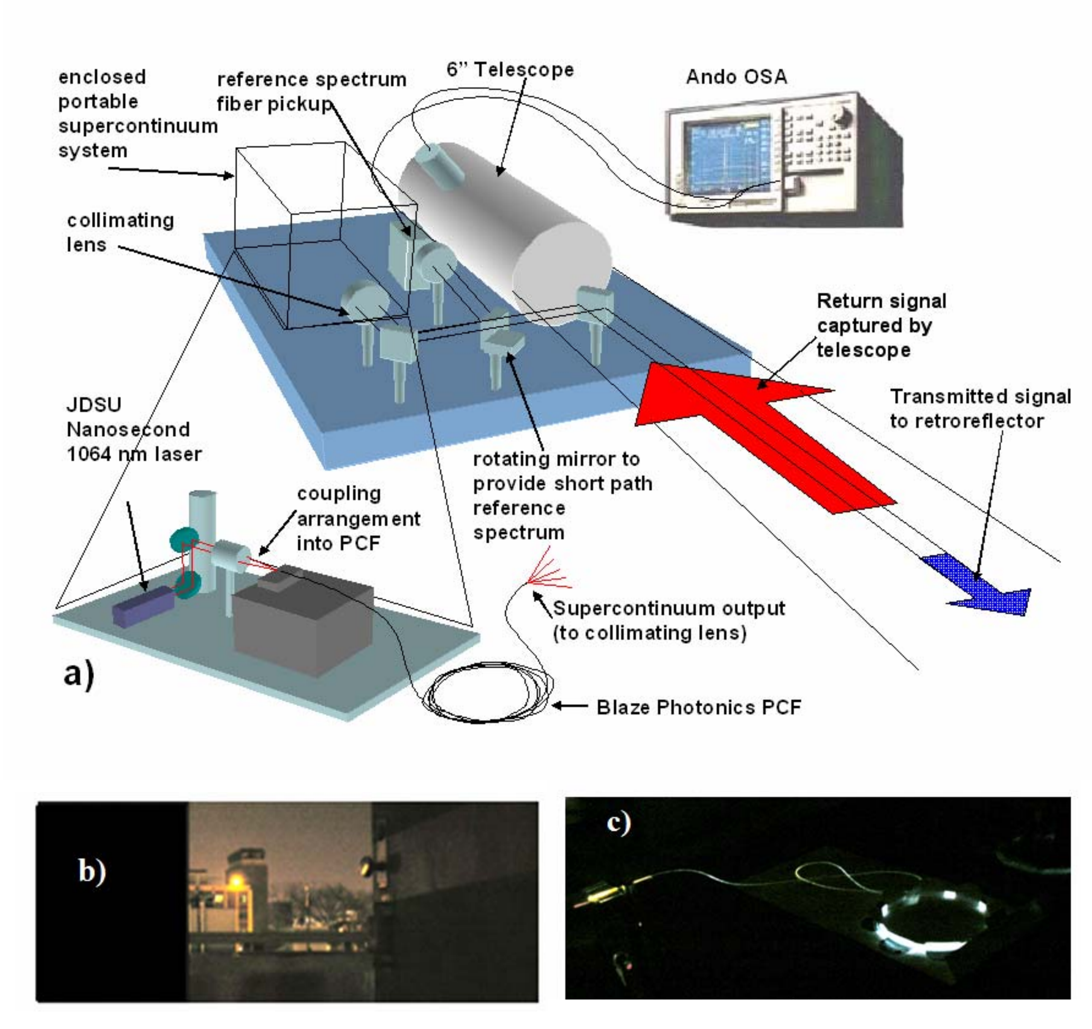

Figure 7.1: (a) Experimental setup for long path SAS measurements; (b) view through the laboratory door shows the reflection of UV-NIR supercontinuum source from a 6" retroreflector located ~150 m away; (c) the wavelength spread of the supercontinuum light can be observed in the PCF; when it is properly tuned for maximum output power, it is spread in wavelengths through the visible and near IR due to self-phase modulation.

7.2 Water Vapor Measurements

The spectral mapping and concentration calculation for water vapor along a 300 m path between buildings was obtained. These measurements generally agreed with the local meteorological measurements of relative humidity conducted within about 0.5 km of the test site and the results are examined in the following figures. The water vapor absorption features in the vicinity of 1.4 µm are clearly observed in both the experimental data and a MODTRAN^{TM} simulation shown in Figure 7.2.

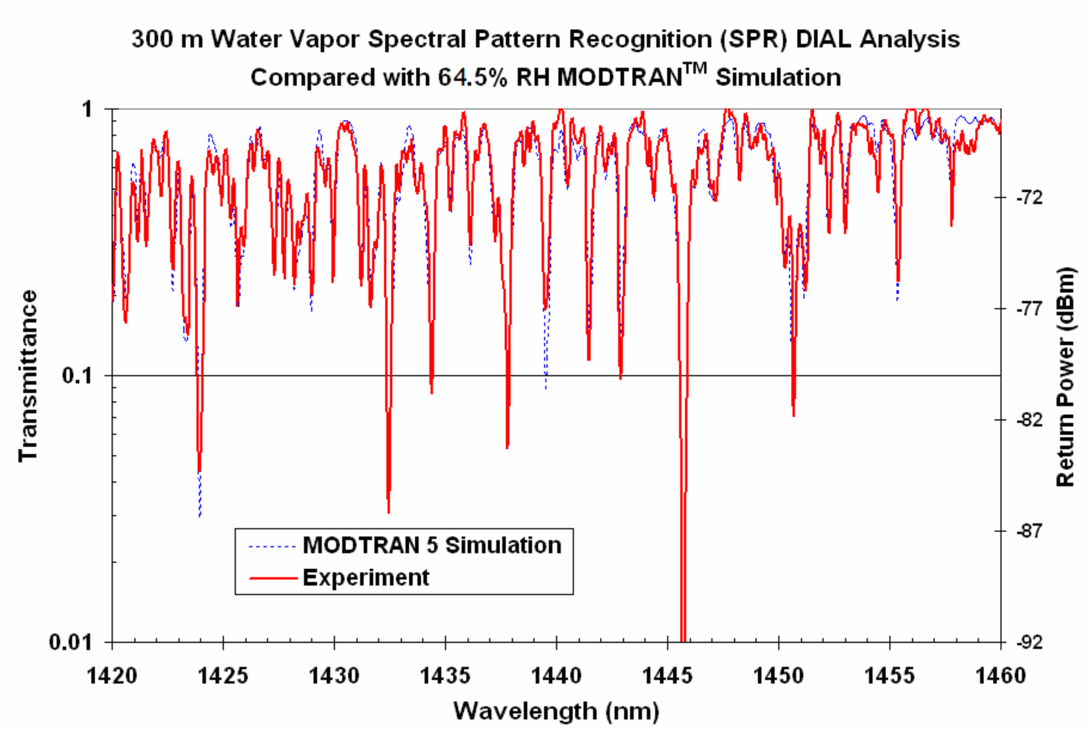

Figure 7.2: Spectral measurement in the 1420 to 1460 nm infrared region with strong water vapor absorption features.

The spectral features shown in Figure 7.2 were selected for CPL calculations because absorption was too strong in the original wavelength range examined during the short path indoor experiments. The absorption was so strong in the original range that no signal was detectable at the centers of several absorption lines in the supercontinuum beam between 1.380 and 1.420 μm. To reduce the absorption for our concentration path length calculations, measurements were performed on absorption features selected from a range of lower absorption in the region from 1.434 to 1.439 μm. The same spectral region was examined during two different experiments separated by a ten-hour period. The MLE results are shown in Figure 7.3. By taking the average concentration and standard deviation for MLE results using 100 to 120 wavelengths, we conclude that the first data set provides a concentration of water vapor of 9582 +/- 20 ppm, and the second data set provides 10793 +/- 32 ppm. Figure 7.4 compares this result with water vapor concentration recorded by the meteorological station nearby. As shown by the figure, the two supercontinuum absorption measurements of water vapor concentration generally agree with the 20 minute averaged meteorological station measurements. The percent difference for these cases is at a maximum of 4%. Throughout the measurement campaign, remote supercontinuum absorption measurements compared with nearby ground truth measurements generally agreed within 3 to 5%.

A least-square-fitting approach was examined as an alternative to the MLE approach for a set of SAS experimental data. The least-square-fitting algorithm used attempted to fit the data to various MODTRAN^{TM} simulations with different relative humidities. As shown by Figure 7.5, the best fit was obtained for a relative humidity of 62.5%, which agreed well with the 64.5% relative humidity measured by a meteorological station deployed nearby (~500 meters).

(a)

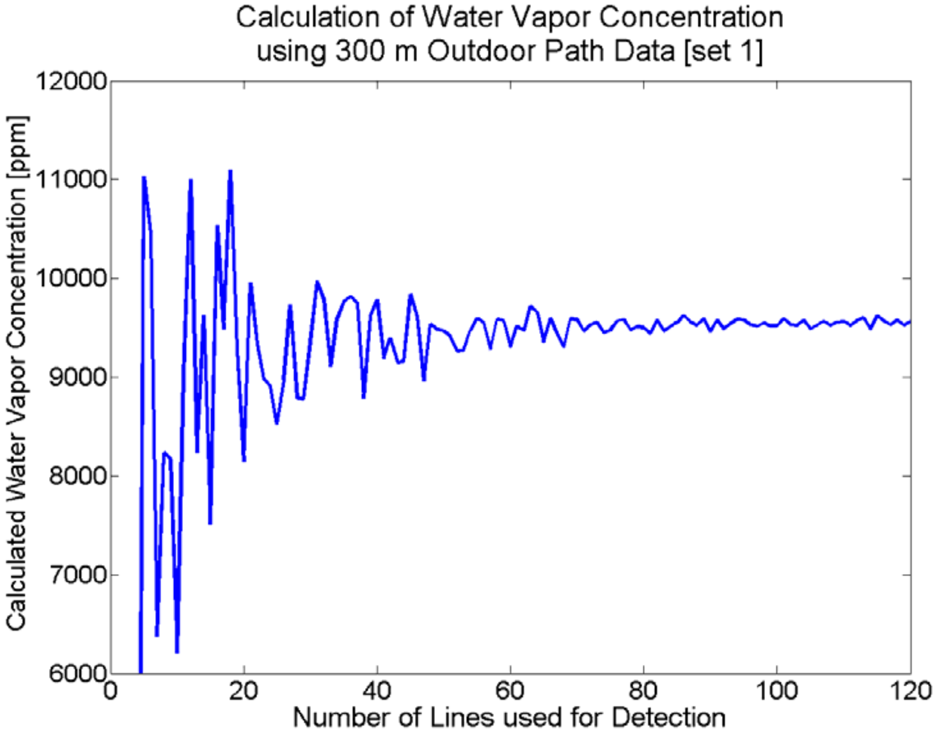

(b)

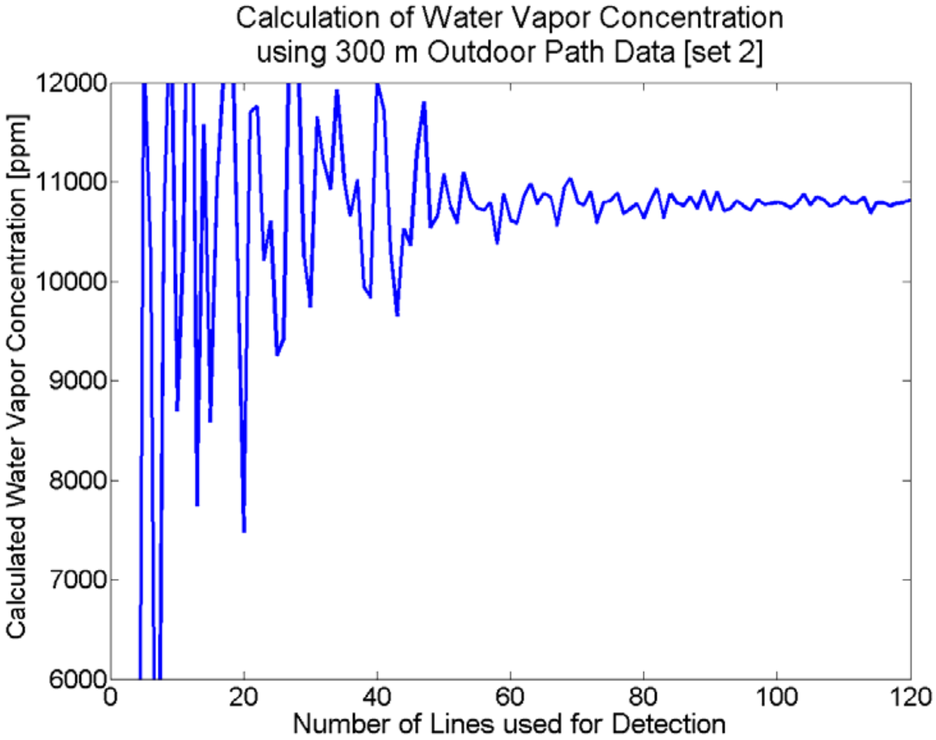

Figure 7.3: Result of MLE algorithm for two 300 m path averaged measurements of water vapor.

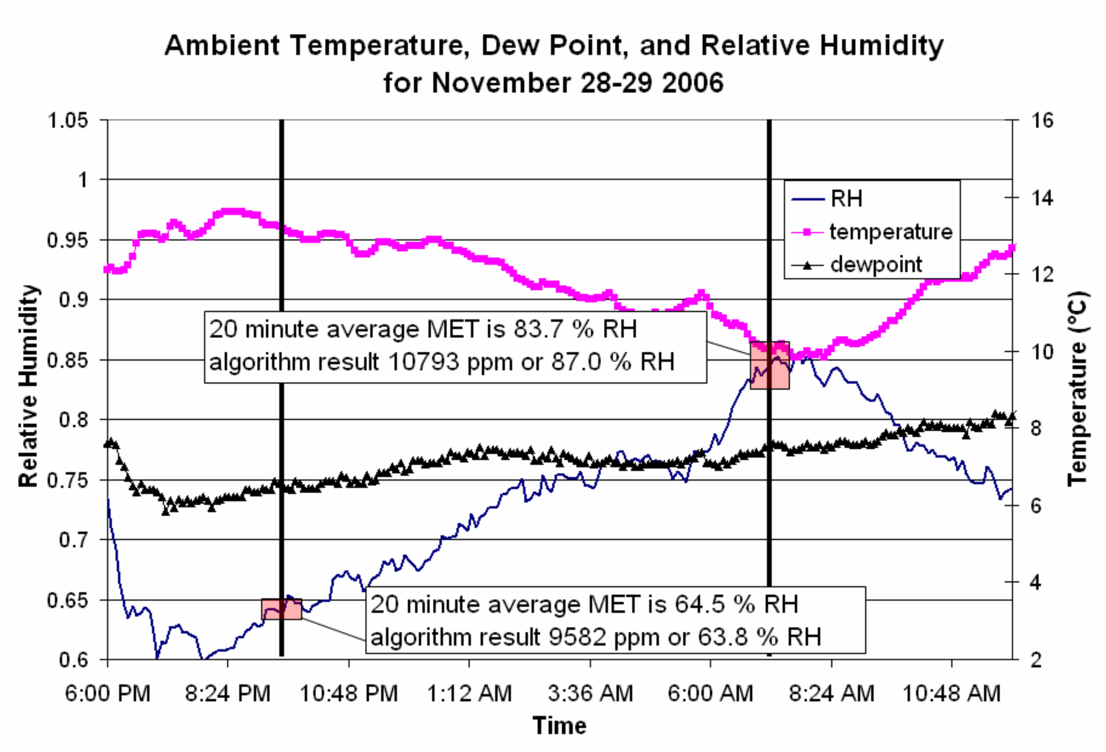

Figure 7.4: Comparison of averaged MLE results to local MET data from the Davis weather station located on the Walker Building.

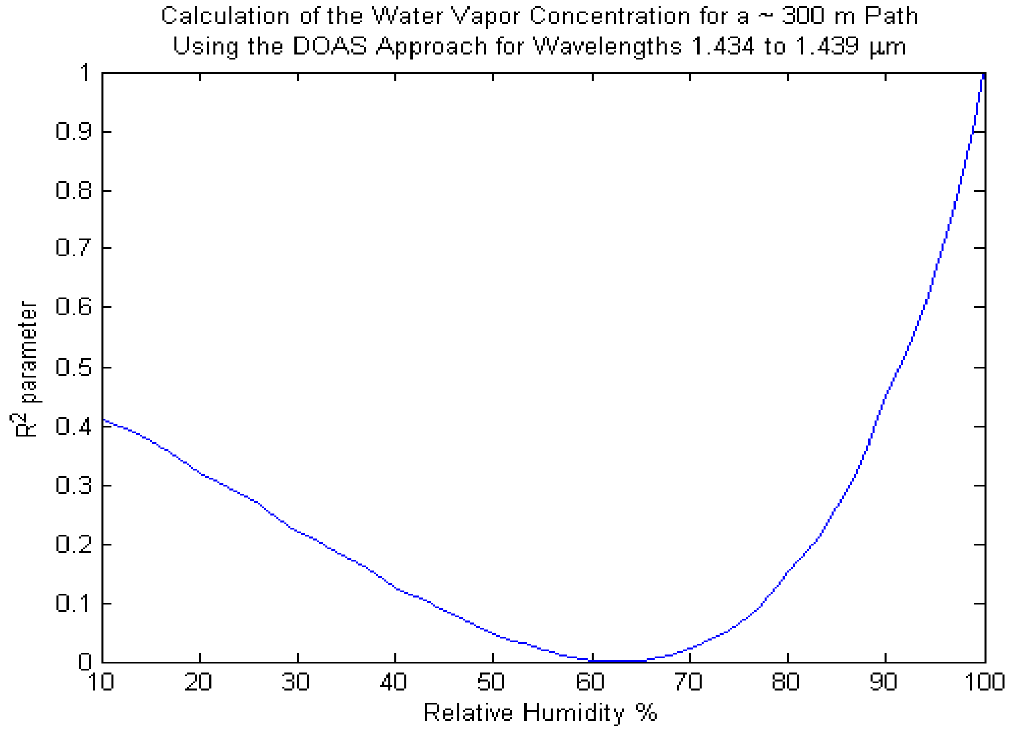

Figure 7.5: Least-square fitting of raw data to determine relative humidity concentration throughout path.

7.3 Oxygen Measurements

Various factors influence the strength of the SAS return signal. These include atmospheric turbulence, laser stability, and aerosol size, shape, and concentration, to name a few. The second-generation SAS sensor data was improved by using the liquid nitrogen cooled spectrograph. The high-sensitivity spectrograph provided a capability to collect the supercontinuum signals under a variety of environmental conditions that would usually limit long-path differential absorption measurements due to near complete extinction from scattering and absorption. Additionally, by remotely locating the supercontinuum source in a temperature stabilized laboratory, many of the low frequency wavelength fluctuations in the transmitted beam were reduced. By moving the supercontinuum source and the analysis equipment to the basement of the EE East building and using fiber coupling to the roof, it was possible to capture many datasets for each absorption measurement without much concern for sources of wavelength instability. A diagram of the second generation SAS system configuration is shown in Figure 7.6. The system makes use of various quick disconnects for alignment, in addition to tightly wound fiber coils before and after the 50 m fiber transfer between the roof and basement laboratories, to "filter" the transmitted and received supercontinuum spectra. An initial problem with the technique that was not earlier noted stemmed from the propagation of supercontinuum light down the optical fiber. Early laboratory based supercontinuum measurements (Chapter 6) focused on broadband absorption features observed in low resolution using the Ando spectrometer. When observing the same regions in high resolution, such as that required to observe the sharp oxygen features, relatively large fluctuations were observed in the spectrum. These fluctuations were created by nonlinear processes occurring as the short laser pulses traversed the optical fibers installed in the building between the roof and basement laboratories. Large “spikes” in the collected spectra occurred due to the variation in the efficiency of different high-order modes propagating in the fibers. The high order mode propagation in fibers, or any waveguide, is highly dependent on the wavelength of light and the small-scale nonlinear effects. Although the efficiency as a function of wavelength can be calculated from specific fiber parameters, this effort would prove to be extremely time consuming given that the supercontinuum spectrum is continuous across the entire absorbing region of interest. Even the fastest computers would require extensive computation time for the fiber lengths of interest (50 m). Therefore, filters were employed to provide a simple and easy way to allow the higher order modes to “leak” from the core-cladding interface. The transmission spectrum for the fiber is nearly constant when the higher order mode propagation is inhibited; this allows detection of species with fine structure when examining the collected spectrum in high resolution.

Further difficulties with the measurement approach were found when attempting to match the SAS experimental data with the spectra generated using HITRAN cross sections, or high resolution MODTRAN^{TM} simulation results. Initially, all of the MODTRAN^{TM} simulations for the SAS study were found to be offset from experimental results by roughly 0.2 to 0.3 nm for example, see Figure 7.7a. During the atmospheric water vapor absorption studies, this deviation had gone unnoticed because the spectral match was examined at a far coarser resolution and the initial tests with MODTRAN^{TM} 4 were limited to 1 cm^{-1} resolution. At the 2007 AFRL Transmission Meeting, it was suggested that this deviation could be due to the lack of the conversion of MODTRAN^{TM} output wavelengths from vacuum conditions to those expected in air. When then applying the standard equation [Bonsch and Potulski, 1998; Elden, 1966] for conversion (Equation 7.1) to the MODTRAN^{TM} outputs, excellent agreement is realized between normalized SAS return spectra containing oxygen absorption (Fig. 7.7). Note that the Equation 7.1 units for λ are in nanometers

$$\lambda_{air} = \frac{\lambda_{vac}}{1.0 + 2.735182\times10^{-4} + \frac{13.14182}{\lambda_{vac}^2} + \frac{2.76249\times10^5}{\lambda_{vac}^4}} \qquad [7.1]$$

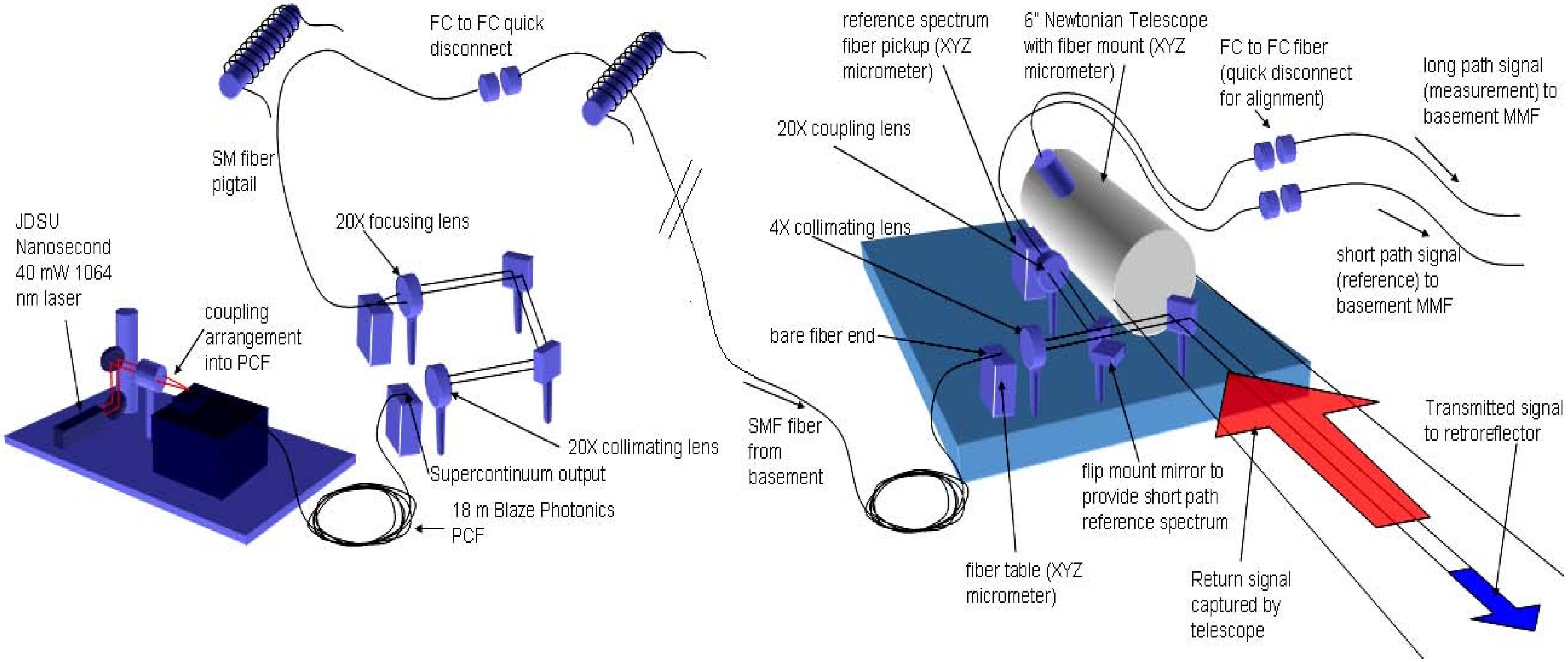

Figure 7.6: Supercontinuum absorption spectroscopy using a low power supercontinuum source and detector that are fiber optically coupled to rooftop mounted transceiver system.

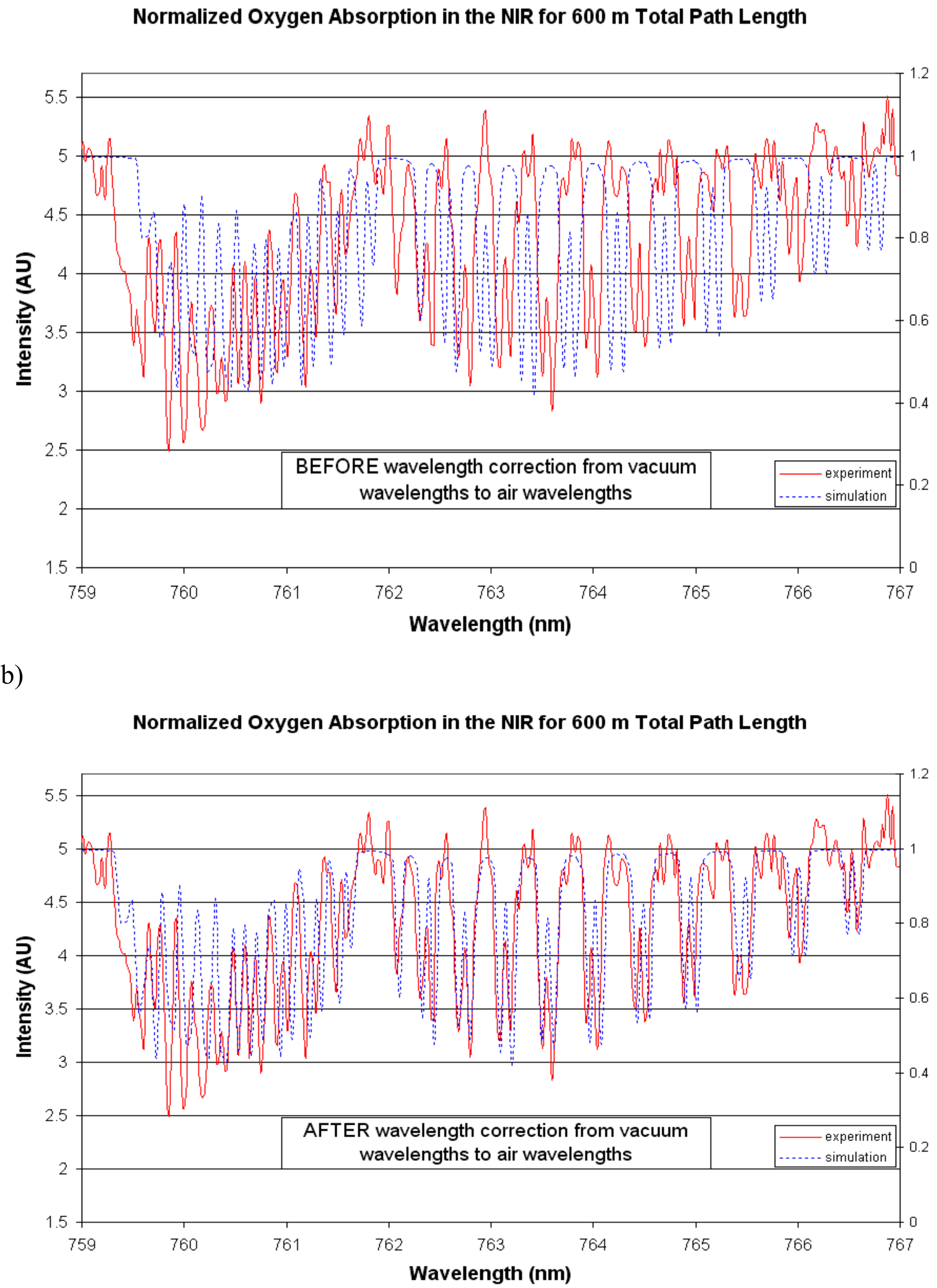

Figure 7.7: Uncorrected (a) and corrected (b) MODTRAN^{TM} simulation results compared with raw experimental data.

Additional experiments with oxygen absorption led to testing our MLE algorithm on normalized raw and spectrally smoothed SAS data. The MLE algorithm result using normalized raw data converged to a mean CPL that was reasonably accurate, however, the error bars on measurement were relatively large. The SAS normalized raw spectral return datasets and calculated HITRAN cross sections were then convolved with a coarser 6.42 cm^{-1} effective slit width to reduce some of the measurement uncertainties. The algorithm initially developed to determine the best effective slit width for calculating spectra was used to confirm the functionality of the cross section calculation and smoothing procedures. The result of this analysis is shown in Figure 7.8. As shown, the best match, or highest correlation coefficient, occurs when the inverted HITRAN cross section is compared with the smoothed data for all datasets with a 6.42 cm^{-1} effective slit width.

When the smoothed SAS spectral data are used in the analysis, the mean atmospheric oxygen concentration is 209180 ppm ± 47 ppm, compared with the standard atmospheric value of 20.95 %. The small standard deviation in the experimental result required that hundreds of wavelengths are used in the data processing. It is expected that the reason for the deviation from the standard atmospheric concentration of oxygen is due to an error in the path length, which was determined with a low-resolution laser range finder. With only a one meter resolution, the range finder can introduce hundreds of ppm error into the result calculated for atmospheric oxygen concentration. When the resolution, concentration, and range are properly entered in the MODTRAN^{TM} simulation, striking agreement is observed between the simulated and normalized experimental datasets as shown by Figures 7.9 and 7.10.

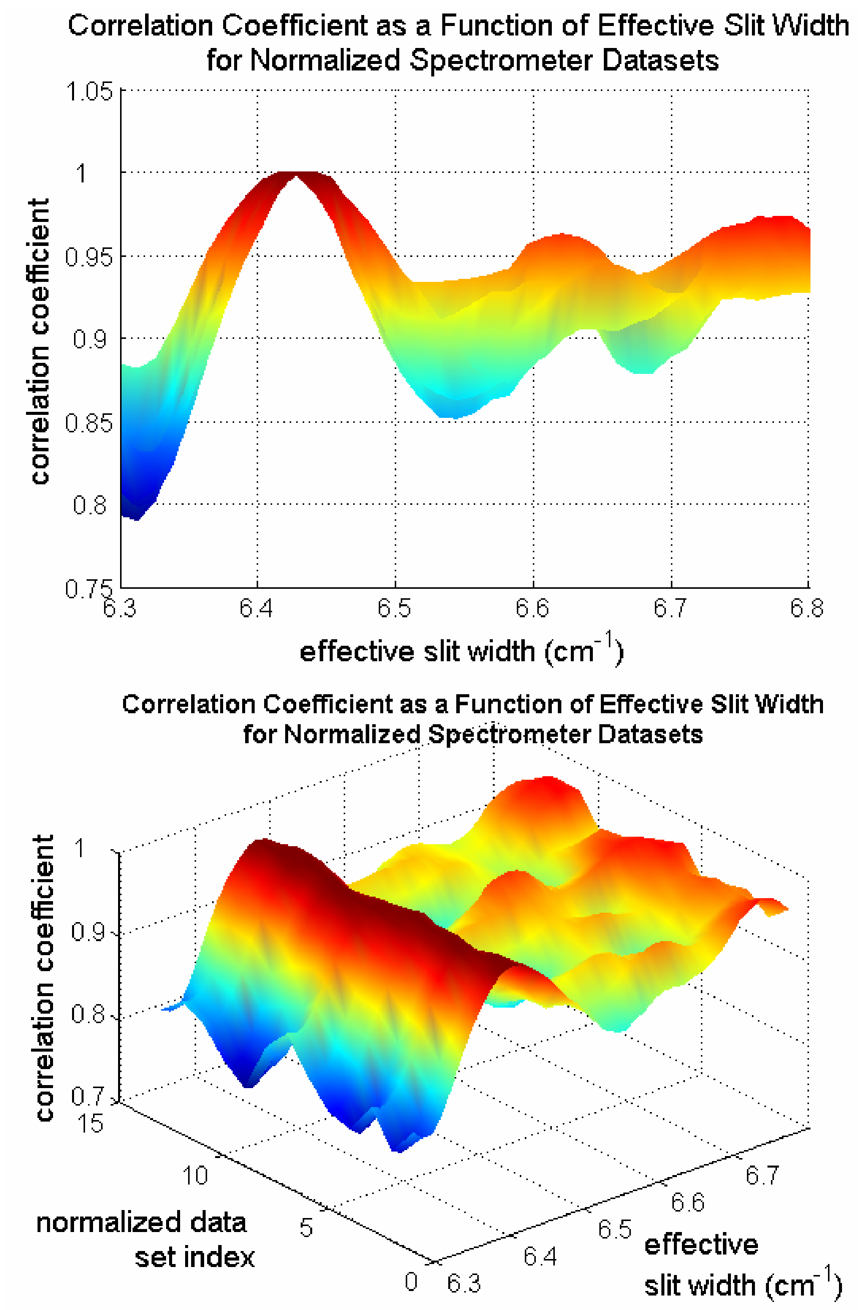

Figure 7.8: Calculation of correlation coefficient between smoothed SAS spectral return data and inverted HITRAN cross section as the effective slit width is varied for all datasets captured for a single atmospheric oxygen measurement. The red regions of the plot correspond to the regions of highest correlation coefficient, while the blue regions exhibit very low correlation.

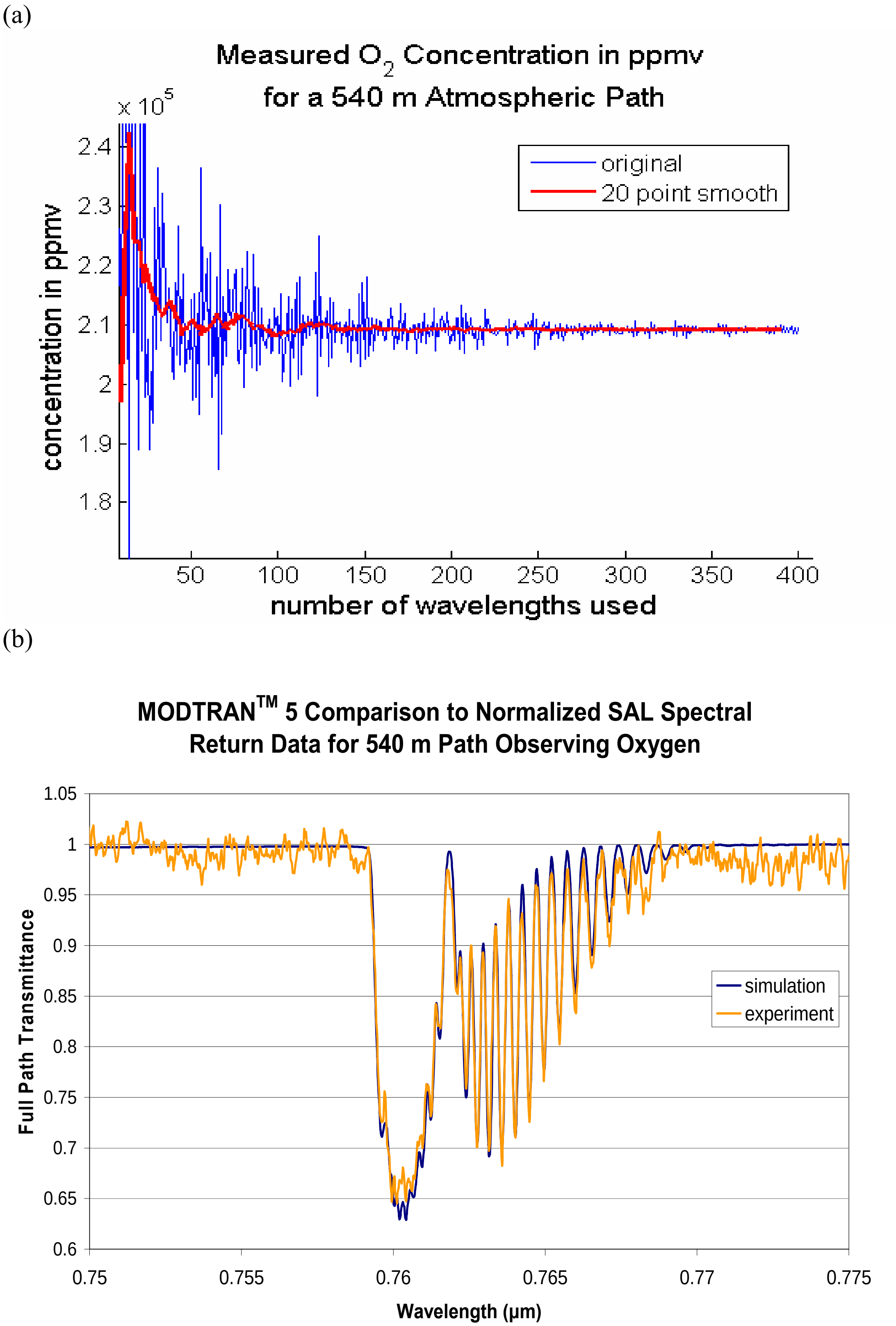

Figure 7.9: MLE algorithm result for concentration of oxygen (a), and comparison between experimental and simulated SAS data (b).

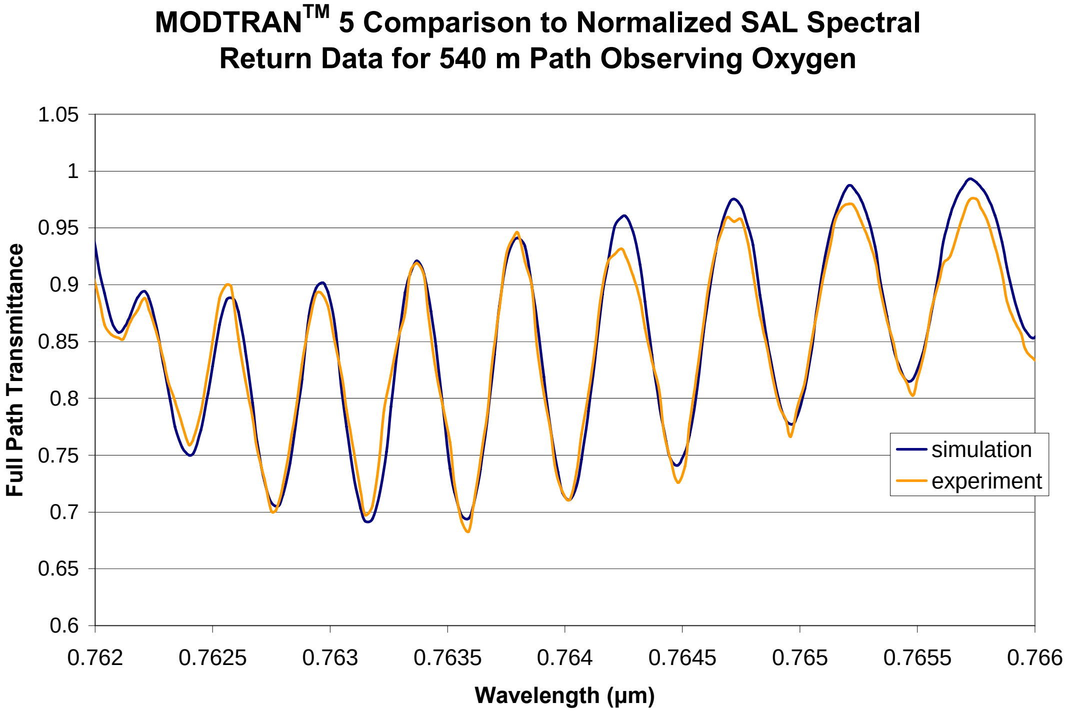

Figure 7.10: Zoom of spectral comparison between experimental and simulated SAS spectral return data for oxygen measurement.

7.4 Conclusions and Outlook

Rearranging the system measurement geometry and employing a long-path absorption technique has allowed development of a system that minimizes transmitted power, and is still capable of urban pollution monitoring and/or emergency response mapping of chemical species. Although supercontinuum sources are not included specifically in the ANSI eye-safe rating for this broad spectral region, the low transmitted power required for supercontinuum absorption measurements is an advantage for many applications. Additionally, we suggest that highly accurate trace species measurements can be achieved with a long-path geometry between ground and space. By employing longer integration times (tens to hundreds of seconds), we expect to reduce the requirements for the retroreflector target, and provide an even more robust system.

When employing the long-path absorption technique, the major limitation is the loss of range resolution. Several groups have shown that tomographic techniques can be used to unwrap the range resolution information when multiple long-path absorption measurements are taken as paths throughout the scanned volume. This unwrapping can be accomplished using an algorithm to interpret multiple path measurements based upon the Smooth Basis Function Method (SBFM) described by the work of Dresher, *et al.* [1996], Price [1999], and Hashomonay, *et.al.* [1999a]. Published approaches use a large number of long-path absorption measurements from a series of paths to retroreflector targets or detectors surrounding the measurement scene of interest. An alternative geometry that favors a real-world urban environment, where perimeter-based retroreflector arrays are not convenient, was evaluated by [Price 1998]. A similar technique using the SAS approach can be implemented by rapidly performing SAS measurements using a number of prepositioned retroreflector targets at different ranges. Several different scan geometries have been considered, and the approaches are described in the literature for prior DOAS work (a good background is available [Price, 1999; Price, *et al.*, 2001; Hashmonay *et al.*, 1999b; Wolfe and Byer, 1982]). Although some configurations are more time consuming for setup and alignment, they provide more accurate tomographic mapping capability and hence are particularly useful when attempting to quantify plume extent, source location, and magnitude.

The future system will utilize a newly developed supercontinuum source capable of extending the operational wavelength range into the midwave infrared. Ground-level differential absorption measurements with a midwave supercontinuum source transmitter will greatly expand supercontinuum absorption spectroscopy. Improved discrimination of target species, reduced false positive identification, and measurements at lower concentrations are expected with operations of a system operating in the midwave infrared; the high potential for use of this technique in the MWIR is primarily due to the rich absorption spectra of many interesting species present there. The measurements are expected to expand the capability of detection techniques available for hydrocarbon compounds, which are of interest to the Departments of Energy (DoE) and Transportation (DoT) because of concerns regarding natural gas and other pipeline leaks. The Departments of Defense (DoD) and Homeland Security (DHS) are seeking solutions, which can be answered by this technique, for detection of toxic chemicals, explosives, and chem-bio agents. Additionally, because the human eye is blind to midwave radiation, and the Earth-Sun radiance is a minimum in this region, such a system is ideally suited for many environmental applications that monitor air quality in cities and in industrial complexes.

CHAPTER 8

Summary, Conclusions, and Future Work

8.1 Summary

The errors and noise analyses for differential absorption lidar (DIAL), and differential absorption spectroscopy (DAS) have been reported in this work for geometries where the return is acquired from topographical scattering. These analyses are particularly useful in developing new performance estimates for down-looking airborne systems that must meet eye-safety standards.

Other approaches that are completely passive in nature provide another set of advantages for the remote sensing community. A system design using a new approach for passive remote imaging of hydrocarbons is described and tested using a prototype unit. The techniques presented describe the filter selection, which is of importance for the optimum performance of a system using this passive imaging approach. The work presents an analysis that optimizes the design approach for detection of four hydrocarbons. A proof-of-concept study is then performed that successfully images propane vapors to demonstrate the capability.

Lidar applications using supercontinuum laser sources have very broadband spectral characteristics while still retaining many of the benefits of lasers – easy to focus, collimate, direct, etc. A supercontinuum source was used to make indoor and outdoor measurements of oxygen and water vapor at atmospheric background levels. Data processing approaches were developed that allow the rapid extraction of concentration through multi-wavelength "DIAL-like" analyses. The DIAL and DAS lidar approaches are very robust, and the species concentration results they present are accurately derived from nearly continuous wavelength sampling of absorption spectra to uniquely identify and measure the species present.

8.2 Conclusions

1. The error analysis and simulation capability developed for airborne down-looking DIAL lidar systems can be used for conceptual designs and proof-of-concept studies in next-generation systems. The error analysis approach was tested with a sample of ANGEL DIAL lidar data, and showed substantial improvements in characterizing error assignments for the measurements. Additionally, the analysis and simulation can be used to develop various algorithms for real-time processing of DIAL lidar data acquired from an airborne platform.

2. The system is developed and tested to image hydrocarbon plumes at the mid-infrared wavelengths under typical atmospheric conditions, and it has been optimized using the MODTRAN^{TM} model for simulations of the transmission, absorption, and background radiance. The 3 to 5 μm region of the infrared is emphasized in the design of this system because the hydrocarbon species all have well-defined absorption spectra present in the region. Variations in the performance of the imager system, such as sensitivity, field of view, and minimal contrast, are modeled using the theory of radiative transfer to optimize the filter selection. The approach devised for selecting a filter allows a researcher to quickly and effectively select an optimum filter wavelength

and bandwidth for detection and imaging of a designated hydrocarbon. Optimum filter selection was determined for imaging of methane, propane, and diesel and gasoline vapors. If a number of different hydrocarbon species are expected to be present, a general purpose filter can be selected based upon the results presented. Demonstration of a prototype system operation is presented for the standoff detection of propane at ranges of 30 to 180 m using the general purpose filter. Data processing algorithms are proposed that examine the imaged scene as a function of time, and these demonstrated additional capability for identifying and selecting the regions of hydrocarbon vapor plumes.

3. A supercontinuum laser source was used as the transmitter for a differential absorption spectroscopy instrument. The technique was demonstrated on laboratory and atmospheric paths for measurements of ambient water vapor and oxygen concentration. The system tested two topologies, one with the transmitter and detector at the location of the transceiver optics, and another with the transmitter and receiver at separate locations. Broadband spectral measurements of the oxygen absorption region from 750 to 800 nm were used to obtain a path averaged calculation of oxygen concentration, which was found to be within 1% of the known atmospheric concentration. Measurements of water vapor in the NIR, from 1350 to 1470 nm, were compared with ground truth point source measurements, and the path averaged values are found to be within 3 to 4 %. The algorithm developed for

the calculation of oxygen and water vapor concentration is capable of handling multi-species concentration path length analysis, and it was tested using simulations to have less than 1% error in the retrieved compared with actual values.

8.3 Future work

1. The simulation program developed has already been utilized for initial calculations and simulations, and it will guide the development of the next generation ANGEL system for ITT Space Systems Division. The error approach developed in this work allows Penn State and ITT researchers to gauge the expected quality of airborne DIAL lidar datasets prior to collection, and provides the framework to create simulated ANGEL detection limits given anticipated experimental collection conditions. Simulated conditions that closely resemble actual flight data have been used and have been shown to be critically important for developing real-time data processing algorithms. These algorithms were developed in conjunction with the error calculation approach presented for simulations; the algorithms are not available for public release at this time however. Future work will expand the performance of these algorithms and continue to utilize the simulation to weigh the pros and cons of system modifications prior to implementation.

2. The midwave infrared hydrocarbon imaging studies will be expanded to experimentally measure additional species using filters designed in this study.

Data processing algorithms will be refined and further examined to find the relationship between plume-present and plume-absent areas as a function of time. As the data processing approach presented here suggests, applying a Fourier analysis on a per-pixel basis will allow the enhanced detection and rapid analysis of areas where hydrocarbon plumes are present. These analysis techniques will be further explored, for the case of even longer-range measurements using a longer focal length midwave infrared objective lens with the Merlin camera.

3. The Supercontinuum Absorption Spectroscopy future investigations will seek to confirm the performance of the approach with campaigns to study other atmospheric species in addition to improving the oxygen and water vapor that are currently monitored. The approaches taken have demonstrated that the current hardware is sufficient for measurements up to 600 m for the wavelengths between the mid-visible and the near infrared regions. Experimental observations and simulations show that this path length can be doubled or tripled with existing hardware. Although some results have exhibited an intermittent small offset from ground-truth measurements, future work will refine the CPL calculations and verify them with a campaign study, which will seek to determine any system biases. A study should undertake absorption and scattering experiments to investigate aerosol properties. The supercontinuum source can be imaged with CCD multi-static imagers to provide a fast and reliable way of determining aerosol size distribution and

concentration based upon knowledge developed in prior research [Novitsky, 2005; Park, 2008]. Demonstration of the supercontinuum absorption approach for a spectral measurement in the MWIR is also a major future goal of this work. A project to develop a MWIR supercontinuum source is underway. This source will be used to demonstrate absorption measurements for the detection of methane, propane, gasoline, or diesel vapor as well as many other chemical species in the 3 to 5 μm wavelength region.

REFERENCES

Agema Infrared Systems. 1981. Thermovision 400 Series Operating Manual. Danderyd, Sweden.

Alfano, R.R. 1989. *Supercontinuum Laser Source*, 2nd edn, Springer, New York, NY.

Asner, G. P. and Heidebrecht, K. 2003. "Imaging spectroscopy for desertification studies: Comparing AVIRIS and EO-1 Hyperion in Argentina Drylands," *IEEE Transactions on Geoscience and Remote Sensing*, Volume 41, Issue 6, pp. 1283-1297

Althouse, M.L. and Chang, C. 1995. "Chemical Vapor Detection and Mapping with a Multispectral FLIR," *SPIE,* vol. 2366, pp. 108-112.

Atkins, P.W. 1990. *Physical Chemistry*, 4th edn, W.H. Freeman and Company, New York, NY.

Barton, I.J. and Marshall, J.F. 1979. "Differential-absorption lidar measurements in the oxygen A band using a ruby lidar and stimulated Raman scattering," *Optics Letters*, vol. 4, pp. 78-80.

Baumgartner, R.A. and Byer, R.L. 1978. "Continuously tunable IR lidar with applications to remote measurements of SO_2 and CH_4," *Applied Optics*, vol. 17, pp. 3555-3561.

Begnoché, J. 2005. *Analytical Techniques for Laser Remote Sensing with a Supercontinuum White Light Laser*, Masters Thesis, The Pennsylvania State University, University Park, viewed July, 2008, <http://lidar1.ee.psu.edu/thesissite_eee.htm>.

Berk, A., Cooley, T.W., Anderson, G.P., Acharya, P.K., Bernstein, L.S., Muratov, L., Lee, J., Fox, M.J., Adler-Golden, S.M., Chetwynd, J.H., Hoke, M.L., Lockwood, R.B., Gardner, J.A. and Lewis, P.E. 2004. "MODTRAN5: A reformulated atmospheric band model with auxiliary species and practical multiple scattering options," *Proc. of the SPIE Algorithms and Technologies for Multispectral, Hyperspectral, and Ultraspectral Imagery XI,*, vol. 425, pp. 341-347.

Berk, A., Bernsten, L.S., and Robertson, D.C. 1989. *MODTRAN^{TM}: A Moderate Resolution Model for LOWTRAN7.* Air Force Geophysics Laboratory, Hanscom AFB, MA, GL-TR-89-0122, pp. 38.

Birch, K. P. and Downs M. J. 1993. "An updated Edlen equation for the refractive index of air," *Metrologia,* vol. 30**,** pp. 155-162

Bonsch, G. and Potulski, E. 1998. "Measurement of the refractive index of air and comparison with modified Edlen's formula," *Metrologia,* vol. 35**,** pp. 133 - 139.

Bourayou R., Méjean, G., Kasparian, J., Rodriguez, M., Salmon, E., Yu, J., Lehmann, H., Stecklum, B., Laux, U., Eislöffel, J., Scholz, A., Hatzes, A.P., Sauerbrey, R., Wöste, L. and Wolf, J. 2005. "White-light filaments for multiparameter analysis of cloud microphysics," *JOSA B*, vol. 22, p. 369.

Bohren, C.F. and Huffman, D.R. 1983. *Absorption and Scattering of Light by Small Particles*, John Wiley and sons, New York, NY.

Brown, D.M. 2005. *Remote Sensing Techniques in the Infrared Region of the Electromagnetic Spectrum*, Masters Thesis, The Pennsylvania State

University, University Park. , viewed July, 2008, <http://lidar1.ee.psu.edu/thesissite_eee.htm>.

Brown, D.M., Shi, K., Liu, Z. and Philbrick, C.R. 2008a. "Long-path supercontinuum absorption spectroscopy for measurement of atmospheric constituents," *Optics Express*, vol. 16, pp. 8457-8471.

Brown, D.M., Liu, Z. and Philbrick, C.R. 2008b. "Supercontinuum lidar applications for measurements of atmospheric constituents," *Proc. of the SPIE Laser Radar Technology and Applications XII*, vol. 6950, pp. 69500B-69500B-11.

Brown, D.M., Willitsford, A., Shi, K., Liu, Z. and Philbrick, C.R. 2006. "Advanced optical techniques for measurements of atmospheric constituents," *Proc. of the 28th Annual Review of Atmospheric Transmission Models*, Lexington, MA, , viewed July, 2008, <http://lidar1.ee.psu.edu/ppsite_eee.htm>.

Carlisle, C.B., Van Der Laan, J.E., Carr, L.W., Adam, P. and Chiaroni, J.P. 1995. "CO2 laser-based differential absorption lidar system for range-resolved and long-range detection of chemical vapor plumes," *Applied Optics*, vol. 34, pp. 6187- 6200

Chu, P.M. 2003. "Advances in optical methods for trace gas analysis" *Analytical and Bioanalytical Chemistry*, vol. 376, pp. 305–307.

Cosofret, B.R., Marinelli, W.J., Ustun, T., Gittins, C.M., Boies, M.T., Hinds, M.F., Rossi, D.C., Coxe, R. and Chang, S. 2004. "Passive infrared imaging sensor for standoff detection of methane leaks," Presented at SPIE Optics East Chemical and Biological Standoff Detection II (Philadelphia, PA).

Drescher, A.C., Gadgil, A.J., Price, P.N. and Nazaro, W.W. 1996. “Novel approaches for tomographic reconstruction of gas concentration and distributions in air: use of smooth basis functions and simulated annealing,” *Atmospheric Enviroment*, vol. 30, pp. 929-940.

Dudley, J., Gu, X., Xu, L., Kimmel, M., Zeek, E., O’Shea, P., Trebino, R., Coen, S. and Windeler, R. 2002. “Cross-correlation frequency resolved optical gating analysis of broadband continuum generation in photonic crystal fiber: simulations and experiments,” *Optics Express*, vol. 10, pp. 1215-1221.

Edlen, B. 1966. "The Refractive Index of Air", *Metrologia*, vol. 2, pp. 71-80.

European Space Agency. 2004. *ESA Earthnet: Scanning Imaging Absorption SpectroMeter for Atmospheric ChartographY, SCIAMACHY Design,* viewed July, 2008, <http://envisat.esa.int/object/index.cfm?fobjectid=1671&contentid=3832>.

Furry, D., Richards, A., Lucier, R. and Madding, R. 2005. “Detection of volatile organic compounds (VOC”s) with a spectrally filtered cooled mid-wave infrared camera,” viewed December, 2007, <http://www.flirthermography.com/media/2005-011%20Furry.pdf>.

FLIR Systems. 2008., *Thermal Imaging and Infrared Cameras*, viewed June, 2007, <http://www.flir.com>.

Fischer, M.L., Price, P.N., Thatcher, T.L., Schwalbe, C.A., Craig, M.J., Wood, E.E., Sextro, R.G., and Gadgil, A.J. 2001. ”Rapid measurements and mapping of tracer gas concentrations in a large indoor space,” *Atmospheric Environment*, vol. 35, pp. 2837-2844.

Galvez, M.C., Fujita, M., Inoue, N., Moriki, R., Izawa, Y. andYamanaka, C. 2002. "Three-wavelength backscatter measurement of clouds and aerosols using a white light lidar system," *Japanese Journal of Applied Physics*, vol. 41, pp. L284-L286.

Gamache, R.R., Hawkins R.L. and Rothman, L.S. 1990. "Total internal partition sums in the temperature range 70-3000k: Atmospheric linear molecules," *J. Mol. Spectrosc.*, vol.142, pp. 205-219.

Gordon, J.P. 1986. "Theory of the soliton self-frequency shift," *Optics Letters*, vol. 11, pp. 662-664.

Grund, C.J., Shald, S., Stearns, S.V. 2004. "Airborne three-line mid-IR DIAL for rapid chemical species plume mapping," *Proc. of the SPIE*, vol. 5412, pp.1-9.

Han, S., Kim, H., Kim, D., Ryu, G., Choi, H., Lee, D., and Bae, H. 2005. "A new method for analysis of differential optical absorption spectra using wavelet transform and independent component analysis," *Proc. of the IEEE Instrumentation and Measurement Technology Conference,* vol. 2, pp. 1579-1584.

Hashmonay, R.A., Yost, M.G. and Wu, C.F. 1999a. "Computed tomography of air pollutants using radial scanning path-integrated optical remote sensing," *Atmospheric Environment*, vol. 33, p 267-274.

Hashmonay, R.A. and Yost, M.G. 1999b. "Localizing gaseous fugitive emission sources by combining real time optical remote sensing and wind data," *J. Air Waste Manage. Assoc.*, vol. 49, pp. 1374-1379.

Hashmonay, R.A. and Yost, M.G. 1999c. “Innovative approach for estimating gaseous fugitive fluxes using computed tomography and remote optical sensing techniques,” *J. Air Waste Manage. Assoc.*, vol. 49, pp. 966-972.

Herzberg, G. 1962, *Molecular Spectra and Molecular Structure Vol. II, Infrared and Raman Spectra of Polyatomic Molecules*, D. Van Nostrand, New York, NY.

Hoelter, T.R., Petronio, S.M., Carralejo, R.J., Frank, J.D. and Graff, J.H. 1999. “Flexible high performance IR camera systems,” *Proceedings of SPIE The International Society for Optical Engineering*, vol. 3698, pp. 837-846.

Honninger, G., von Friedeburg, C. and Platt, U. 2004. “Multi axis Differential Optical Absorption Spectroscopy,” *Atmos. Chem Phys.*, vol. 4, pp. 231-254.

Hydea, P., Nelson, R., Kimes, D. and Levine, E. 2007. “Exploring LIDAR–RADAR synergy - predicting aboveground biomass in a southwestern ponderosa pine forest using LiDAR, SAR and InSAR,” *Remote Sensing of Environment*, vol. 106, pp. 28-38.

Inaba, H. 1976*, Laser Monitoring of the Atmosphere*, Hinkley, E.D. ed., Springer-Verlag, Berlin.

Inaba, H., Kobayasi, T., Ichimura, T. and Morihisa, M. 1966. “Laser radar application in atmospheric physics research”, *IEEE J. Quantum Electron*., vol. 2, p. 148.

Indigo Systems. 2002. Merlin Mid InSb MWIR Camera Users Manual, viewed July 18, 2008, < http://www.corebyindigo.com/usermanuals/MerlinMID120.pdf>.

Jin, M. and Dickinson, R.E.1999. “Interpolation of surface radiative temperature measured from polar orbiting satellites to a diurnal cycle,” Journal *of Geophysical Research*, vol. 104, pp. 2105-2116.

Kasparian, J., Bourayou, R., Boutou, V., Favre, C., Méjean, G., Mondelain, D., Mysyrowicz, A., Rodriguez, M., Salmon, E., Sauerbrey, R. A., Wille, H., Wolf, J-P., Wöste, L., Yu, J., Klingbeil, L., Rethmeier, K., Kalkner, W., Hartzes, A., Lehman, H., Eislöffel, J., Stecklum, B., Winkler, J., Laux, U., Hönger, S., Pan, Y-L., Chang, R. K., Hill, S. C.. 2003. "Ultrashort laser applications in lidar and atmospheric sciences," *Proceedings of the SPIE 12th International School on Quantum Electronics: Laser Physics and Applications*, vol. 5226, pp. 238-248.

Koch, G.J., Beyon, J.Y., Gibert, F., Barnes, B.W., Ismail, S., Petros, M., Petzar, P.J., Yu, J., Modlin, E.A., Davis, K.J. and Singh,U.N. 2008. "Side-line tunable laser transmitter for differential absorption lidar measurements of CO_2: design and application to atmospheric measurements," *Applied Optics*, vol. 47, pp. 944-956.

Knight, J.C., Birks, T.A., Russell, P.S. and Atkin, D.M. 1996. "All-silica single-mode optical fiber with photonic crystal cladding," *Optics Letters*, vol. 21, pp. 1547-1549.

Kuhnemann, F., Schneider, K., Hecker, A., Martis, A.E., Urban, W., Schiller, S. and Mlynek, J. 1998. "Photoacoustic trace-gas detection using a CW single-frequency parametric oscillator" *Applied Physics B*, vol. 66, pp. 741-745.

Li, G. 2004. *Atmospheric Aerosols and Particle Properties using Lidar*, Ph.D. Dissertation, The Pennsylvania State University, University Park, , viewed July, 2008, <http://lidar1.ee.psu.edu/thesissite_eee.htm>.

Li, P., Shi, K. and Liu, Z. 2005. “Manipulation and spectroscopy of a single particle using white light optical tweezers,” *Optics Letters*, vol. 30, pp. 156-158.

Lippert, J. 2005. “Spectral Collection,” excerpt from *Technology/Commercialization Roadmap for Optimized Sensor, Hazardous Liquids Airborne Lidar Observation Study (HALOS).* Technical Report. Department of Transportation Submission

Lowe, P.R. 1977. “An approximating polynomial for the computation of saturation vapor pressure,” *Journal of Applied Meteorology*, vol. 16, pp. 100-102.

McRae, T.G. and Kulp, T.J. 1993. “Backscatter absorption gas imaging: a new technique for gas visualization,” *Applied Optics*, Vol. 32, pp. 4037-4050.

Measures, R.M. 1984, *Laser Remote Sensing*,Wiley-Interscience, New York, NY.

Méjean, G., Kasparian, J., Salmon, E., Yu, J., Wolf, J.P., Bourayou, R., Sauerbrey, R., Rodriguez, M., Wöste, L., Lehmann, H., Stecklum, B., Laux, U., Eislöffel, J., Scholz, A. and Hatzes, A.P. 2003. “Towards a supercontinuum- based infrared lidar,” *Applied Physics B Lasers and Optics*, vol. 77, pp. 357- 359.

Mie, G. 1908. “Beitraege zur Opitek trueber Medien, speziell kolloidaler Metalosungen,” *Ann. Phys.*, vol.25, pp. 377-445.

Mishchenko, M.I., Travis, L.D., Kahn, R.A., and West, R.A. 1997. “Modeling phase functions for dustlike topospheric aerosols using a shape mixture of randomly oriented polydispersed spheroids,” *J. Geophys. Res.* vol 415, pp. 16831-16847.

Mooney, J.M, Shepherd, F.D., Ewing, W.S., Murguia, J.E. and Silverman, J. 1989. “Responsitivity nonuniformity limited performance of infrared staring cameras" in *Selected Papers on Radiometry*, I.J. Spiro, ed., SPIE Milestone Series, vol MS14, pp. 431-441.

Murdock, D.G., Brown, D.M., Gigliotti, T, Lines, R, Stoogenke, M. and Stearns, S. 2006. "GIS analysis of airborne lidar data for leak detection," *ESRI User Conference Proceedings*, viewed July, 2008, ,http://gis.esri.com/library/userconf/pug06/papers/lidar.pdf>.

Murdock, D.G., Stearns, S.V., Lines, R.T., Lenz, D., Brown, D.M. and Philbrick, C.R. 2008. "Applications of real-world gas detection: Airborne Natural Gas Emission Lidar (ANGEL) system," *J. Appl. Remote Sens.*, vol. 2, pp. 1-18.

Novitsky, E.J. 2002. *Multistatic Lidar Profile Measurements of Lower Tropospheric Aerosol and Particulate Matter*, PhD dissertation, The Pennsylvania State University, University Park, viewed July, 2008, <http://lidar1.ee.psu.edu/thesissite_eee.htm>.

Patty, R. R., Russwurm, G. M., McClenny, W. A. and Morgan, D. R. 1974. "CO_2 Laser Absorption Coefficients for Determining Ambient Levels of O_3, NH_3, and C_2H_4," *Appl. Opt.* **13**, 2850-2854.

Park, J. 2008. *Multiple Scattering Measurements Using Multi-static Lidar*, PhD dissertation, The Pennsylvania State University, University Park, viewed July, 2008, <http://lidar1.ee.psu.edu/thesissite_eee.htm>.

Philbrick, C.R., Liu, Z., Hallen, H., Brown, D., Willitsford, A. 2006. "Lidar techniques applied to remote detection of chemical species in the atmosphere," Proceedings of the International Symposium on Spectral

Sensing Research (ISSSR), viewed July, 2008, <http://lidar1.ee.psu.edu/ppsite_eee.htm>.

Philbrick, C.R. 2003. “Remote sensing of atmospheric properties using lidar,” viewed April, 2008, <http://lidar1.ee.psu.edu/neopsWeb/publicSite/papersandpresentations/ISSSR2003Philbrick.pdf>.

Philbrick, C.R. 2005. “Raman lidar characterization of the meteorological, electromagnetic, and electro-optical environment,” *Proc. of SPIE Lidar Remote Sensing for Environmental Monitoring VI*, vol. 5887, pp. 85-99.

Platt, U., Pemer, D. and Patz, H.W. 1979. “Simultaneous measurement of atmospheric CH_2O, O_3 , and NO_2 by differential optical absorption,” *J. Geophys. Res.*, vol. 84, pp. 6329-6335.

Platt, U. and Perner, D. 1983. “Measurements of atmospheric trace gases by long path differential UV/visible absorption spectroscopy,” *Springer Ser. Opt. Sci.*, vol. 39, pp. 95-105.

Platt, U. 2004. “Differential optical absorption spectroscopy (DOAS)” in *Air Monitoring by Spectroscopic Techniques*, M.W. Sigrist, ed., John Wiley and Sons, pp. 27-84.

Povey, I.M., South, A.M., T’Kint de Roodenbeke, A., Hill, C., Freshwater, R.A. and Jones, R.L. 1998. “A broadband lidar for the measurement of tropospheric constituent profiles from the ground,” *J. Geophys. Res.*, vol. 103, pp. 3369-3380.

Powers, P.E., Kulp, T.J. and Kennedy, R. 2000. “Demonstration of differential backscatter absorption gas imaging,” *Appl. Opt.*, vol. 39, pp. 1440-1448.

Price, P.N. 1999. “Pollutant tomography using integrated concentration data from non-intersecting optical paths,” *Atmos. Environ*, vol. 33, pp. 275-280.

Price, P.N., Fischer, M.L., Gadgil, A.J. and Sextro, R.G. 2001. “An algorithm for real-time tomography of gas concentrations using prior information about spatial derivatives,” *Atmos. Environ.*, vol. 35, pp. 2827-2835.

Rairoux, P., Schillinger, H., Niedermeier, S., Rodriguez, M., Ronneberger, F., Sauerbrey, R., Stein, B.,Waite, D., Wedekind, C., Wille, H. and Wöste, L. 2000. “Remote sensing of the atmosphere using ultrashort laser pulses,” *Appl. Phys. B*, vol. 71, pp. 573-580.

Ranka, J.K., Windeler, R.S. and Stentz, A.J. 2000. “Visible continuum generation in air-silica microstructure optical fibers with anomalous dispersion at 800 nm,” *Opt. Lett.*, vol. 25, pp. 25-27.

Rodriguez, M., Bourayou, R., Kasparian, J., Méjean, G., Mysyrowicz, A., Salmon, E., Sauerbrey, R.A., Wille, H., Wöste, L., Wolf, J-P., Yu, J., and Zimmer. 2003. “Femtosecond LIDAR: new perspectives of atmospheric remote sensing,” *Proceedings of the SPIE*, vol. **5149**, pp. 135-143.

Rothman L.S., Barbe A., Benner D.C., Brown L.R., Camy-Peyret C., Carleer M.R., Chance K.V., Clerbaux C., Dana V., Devi V.M., Fayt A., Flaud J-M., Gamache R.R., Goldman A., Jacquemart D., Jucks K.W., Lafferty W.J., Mandin J-Y, Massie ST, Nemtchinov V., Newnham D.A., Perrin A., Rinsland C.P., Schroeder J., Smith K.M., Smith M.A.H., Tang K., Toth R.A., Vander-Auwera J., Varanasi P., Yoshino K. The HITRAN molecular spectroscopic database: edition of 2000 including updates through 2001.

Sandsten J., Edner, H. and Svanberg, S. 2004. “Gas visualization of industrial hydrocarbon emissions,” *Opt. Express*, vol. 12, pp. 1443-1451.

Sandsten J., Weibring, P., Edner, H. and Svanberg, S. 2000. “Real-time gas-correlation imaging employing thermal background radiation,” *Opt. Express*, vol. 6, pp. 92-103.

Schotland, R. M. 1965. "The Determination of the Vertical Profile of Atmospheric Gases by Means of a Ground Based Optical Radar," *in Proceedings of the Third Symposium on Remote Sensing of Environment, October 1964* (U. Michigan, Ann Arbor,).

Sharpe, S.W., Johnson, T.J., Sams, R.L., Chu, P.M., Rhoderick, G.C. and Johnson, P.A. 2004. “Gas-phase databases for quantitative infrared spectroscopy,” *Applied Spectroscopy*, vol. 58, pp. 1452-1461.

South, A.M., Povey, I.M. and Jones, R.L. 1998. “Broadband lidar measurements of Tropospheric water vapor profiles” *Journal of Geophysical Research*, vol. 103, pg 191 – 231.

Sreenivasan, G. and Majumdar, T.J. 2006. “Mapping of Antarctic sea ice in the depletion phase: an indicator of climatic change?,” *CURRENT SCIENCE*, vol. 90, pp. 851-857.

Stearns, S., Lines, R., Murdock, D., Severski, M., Lenz, D., Brown, D. and Philbrick, C.R. 2005. “Airborne Natural Gas Emission Lidar (ANGEL) System,” *Proc. International Symposium on Spectral Sensing Research (ISSSR),* viewed July 18, 2008, <http://www.isssr2006.com/TALK_UPLOADS/Presentations-All.html>.

Stearns, S.V. 2005. “Airborne Assessment of Pipeline Integrity,” *GeoIntelligence*, viewed July 18, 2008, <http://www.ssd.itt.com/angel/literature/GEO_4-05_e.pdf>

Stearns, S.V., Lines, R.T., Grund, C.J. and Philbrick, C.R. 2005. “Active remote detection of natural gas pipeline leaks,” U.S. Department of Energy National Energy Technology Laboratory Technology Status Report, viewed July 18, 2008, <http://www.netl.doe.gov/scngo/Natural%20Gas/index.html>.

Stearns, S.V., Gigliotti, T.J. and Murdock, D.J. 2006. “Airborne DIAL (Differential Absorption Lidar) for broad area hazardous liquid leak detection,” *Proceedings of IPC2006: 6th International Pipeline Conference*, ICP2006-10460, September 25 - 29, Calgary, Alberta.

Stryland, E.W.V., Williams, D.R. and Wolfe, W.L. 1995, *Handbook of Optics, Vol.I, Fundamentals, Techniques, and Design.* 1st ed., McGraw-Hill Inc New York, NY.

Stothard, D.J.M., Dunn, M.H. and Rae, C.F. 2004. “Hyperspectral imaging of gases with a continuous-wave pump-enhanced optical parametric oscillator” *Optics Express*, vol. 12, pp. 947-953.

Tamura, K., Ippen, E.P., Haus, H.A. and Nelson, L.E. 1993. “77-fs pulse generation from a stretched-pulse mode-locked all-fiber ring laser,” *Optics Letters*, vol. 18, pp.1080-1082.

Tassou, M., Przygodzki, C., Delbarre, H. and Boucher, D. 2002. “Atmospheric gas detection with broadband sources,” *International Journal of Infrared and Millimeter Waves*, vol. 23, pp. 1227-1239.

Ulaby, F.T., Moore, R.K. and Fung, A.K. 1986, *Microwave Remote Sensing: Active and Passive, Vol. II -- Radar Remote Sensing and Surface Scattering and Emission Theory*, Addison-Wesley, Reading, MA.

U.S. Committee on Extension to the Standard Atmosphere (COESA), *U.S. Standard Atmosphere, 1976*, U.S. Government Printing Office, Washington, D.C.

Wadsworth W., Joly, N., Knight, J., Birks, T., Biancalana, F. and Russell, P. 2004. "Supercontinuum and four-wave mixing with Q-switched pulses in endlessly single-mode photonic crystal fibres," *Optics Express*, Vol. 12, pp. 299-309.

Wainner, R.T., Green, B.D., Allen, M.G., White, M.A., Stafford-Evans, J. and Naper, R. 2002. "Handheld, battery-powered near-IR TDL sensor for stand-off detection of gas and vapor plumes," *Applied Physics B*, Vol. 75, pp. 249-254.

Walmsley, H.L. and O'Connor, S.J. 1998. "The accuracy and sensitivity of infrared differential absorption lidar measurements of hydrocarbon emissions from process units," *Pure Appl. Opt.*, vol. 7**,** pp. 907–925.

Warren, R.E. 1996. "Optimum detection of multiple vapor materials with frequency-agile lidar," *Appl. Opt.*, vol. 35, pp. 4180-4193.

Warren, R.E. 1985a. "Detection and discrimination using multiple-wavelength differential absorption lidar," *Appl. Opt.*, vol. 24, pp. 3541-3545.

Warren R.E. 1985b. "Effect of pulse-pair correlation on differential absorption lidar," *Appl. Opt.*, vol. 24, pp. 3472-3475.

Warren R.E. and Vanderbeek, R.G. 2007. “Online estimation of vapor path-integrated concentration and absorptivity using multiwavelength differential absorption lidar,” *Appl. Opt.*, vol. 46, pp. 7579-7586.

Weast, R.C., Astle, M.J. and Beyer, W.H. 1986. *Handbook of Chemistry and Physics. 61 ed.*, CRC Press, Inc., Boca Raton, FL.

Weber, M., Bracher, A., Noel, S., Burrows, J.P., “Validation of SCIAMACHY in-flight measured irradiances, radiances and selected ENVISAT trace gas products by comparison with measurements from independent satellite instruments,” viewed December, 2007, <http://www.iup.uni-bremen.de/gome/paper/bracher2001.pdf>

Weibring P., Abrahamsson, C., Sjöholm, M., Smith, J.N., Edner, H. and Svanber, S. 2004. “Multi-component chemical analysis of gas mixtures using a continuously-tuneable lidar system,” *Appl. Phys. B*, vol. 79, pp. 525-530.

Wille, H., Rodriguez, M., Kasparian, J., Mondelain, D., Yu, J., Mysyrowicz, A., Sauerbrey, R., Wolf, J.P. and Woste, L. 2002. “Teramobile: a mobile femtosecond-terawatt laser and detection system,” *The European Physical Journal Applied Physics*, vol. 20, pp. 183-190.

Wolfe, D. C., Byer, R. L., 1982. “Model studies of laser absorption computed tomography for remote air pollution measurement,” *Applied Optics*, Vol. **21**, Issue 7, pp. 1165-1178.

Wolfe, W.L. 1996, *Introduction to Infrared System Design*, SPIE Publications, Bellingham, WA

Wöste, L., Wedekind, C., Wille, H., Rairoux, P., Stein, B., Nikolov, S.,Werner, C., Niedermeier, S., Schillinger, H. and Sauerbrey, R. 1997. "Femtosecond atmospheric lamp," *Laser und Optoelektronik*, vol. 29, pp. 51-53.

Wu, M., Ray, M., Fung, K.H., Ruckman, M.W., Harder, D. and Sedlacek, A.J. 2000. "Stand-off detection of chemicals by UV Raman spectroscopy," *Applied Spectroscopy*, vol. 54, pp. 800-806.

Xia, C., Kumar, M., Kulkarni, O.P., Islam, M.N., Terry, F.L., Freeman, M.J., Poulain, M. and Maze, G. 2006. "Mid-infrared supercontinuum generation to 4.5 μm in ZBLAN fluoride fibers by nanosecond diode pumping," *Opt. Letters*, vol. 31, pp. 2553-2555.

Yin S. and Wang, W. 2006. "Novel algorithm for simultaneously detecting multiple vapor materials with multiple-wavelength differential absorption lidar," *Chin. Opt. Lett.*, vol. 4, pp. 360-362.

Young, A. T. 1981. "Rayleigh scattering," *Applied Optics*, vol. **20**, pp. 533-535.

APPENDIX A

Explanation of Terms within Error Analysis for DAS

The CPL error for DAS presented in Chapter 3 of this work invokes various parameters that include variations or uncertainties encountered when operating a system in real-world conditions. The explanation of error propagation due to each of the parameters outlined in Chapter 3 (page 34) and Equation 3.11 is described in the following.

A.1 Uncertainty in Energy Measurements (Item #1)

The uncertainty in the shot-to-shot normalized return energy, exclusive of atmospheric variations and ground reflectivity variations, still contains Poisson error and electronic noise error. Therefore, the uncertainty in the normalized returned energy can be expressed as the quadrature sum of Poisson and electronic noise effects,

$$\delta E_j^{total} = \sqrt{\left(\delta E_j^{Poisson}\right)^2 + \left(\delta E_j^{electronic}\right)^2} \, . \tag{A.1}$$

The method outlined by Measures [1984], the fluctuation in energy from Poisson statistics, can be calculated from the total received energy, number of laser shots used for the measurement, detector efficiency, and integration time. Poisson statistics describe the error intrinsic in any photon measurements, while fluctuations due to system hardware electronic noise are dependent on the specific design and parts actually used in the system. For example, noise in the sensor monitoring the laser transmitted energy, and the other electronic noise sources can be minimized by using low noise detectors and sensor electronics. Errors due to Poisson statistics are only improved by taking larger numbers of measurements of the same parameter, or by increasing the signal intensity by increasing the transmitted photon flux.

The fluctuation in the total received energy due electronic noise is defined as a percent stability represented by the ensemble of typical tolerance values associated with the electrical subsystem and components. The energy received in the signal is weighted by its component noise to arrive at the uncertainty due to electronic noise, $\delta E_j^{electronic}$. This error primarily describes the fluctuation of the normalized return energy due to electronic noise in the system introduced by the transmitter and receiver. It is independent of photon signal noise and hence should be added in quadrature to Poisson contributions to arrive at the total amplitude. Knowledge of both sources of measurement error is used to describe the error in the normalized return energy,

$$\begin{aligned}\delta E_j^{total} &= \sqrt{\left(\delta E_j^{Poisson}\right)^2 + \left(\delta E_j^{electronic}\right)^2} \\ &= \sqrt{\left(\rho_\lambda \sqrt{\frac{n_j}{m_j}} \tau_d\right)^2 + \left(E_j^{total}\left(\frac{\varepsilon_{\%}^{elec}}{100}\right)\right)^2}, \\ &= \sqrt{\frac{\rho_\lambda \tau_d}{m_j} E_j^{total} + \left(E_j^{total}\left(\frac{\varepsilon_{\%}^{elec}}{100}\right)\right)^2}\end{aligned} \qquad [A.2]$$

where,

$\varepsilon_{\%}^{elec}$	is the percent fluctuation of signals due to electronic measurement error,
m_j	is the number of laser shots used for the calculation for wavelength j at the range of the topographical scatterer,
n_j	is the quantum efficiency at wavelength j of the detector, and

τ_d	is the detector integration time in seconds.

Therefore, the first term in the equation for CPL error fraction (Eq. 3.11) can be fully expressed in terms of known or calculated values with the parameter ρ_λ defined by Measures [1984] as,

$$\rho_\lambda = \frac{hc}{\lambda\eta(\lambda)\left(\frac{2\Delta R}{c}\right)} = \frac{hc}{\lambda\eta(\lambda)\tau_d}, \tag{A.3}$$

where,

ΔR	is the range to target in meters,
λ	is the wavelength of interest in meters,
$\eta(\lambda)$	is the detector efficiency of the detector at the wavelength of interest,
c	is the speed of light in meters per second, and
h	is Planck's constant.

The first term in the equation for target gas CPL error fraction (Eq. 3.11) can be rewritten using the combination of Poisson and electronics errors and sum expansion for both the online and offline wavelengths as,

$$\sum_{j=1}^{lasers}\left\{\left(\frac{\delta E_j^{total}}{E_j^{signal}}\right)^2\right\} = \frac{\frac{\rho_\lambda \tau_d}{m_{on}} E_{on}^{total} + \left(E_{on}^{total}\left(\frac{\varepsilon_{\%}^{elec}}{100}\right)\right)^2}{\left(E_{on}^{signal}\right)^2} + \frac{\frac{\rho_\lambda \tau_d}{m_{off}} E_{off}^{total} + \left(E_{off}^{total}\left(\frac{\varepsilon_{\%}^{elec}}{100}\right)\right)^2}{\left(E_{off}^{signal}\right)^2}. \tag{A.4}$$

A.2 Effects of Ground Reflectivity Variations (Item #2)

The overlap percentage of measurement and reference beams is a critical parameter in determining the system sensitivity and errors. Overlap percentage is defined by the overlapping area of the beams divided by the area of the larger beam size. Two examples of this parameter are shown in Figure A.1, where the overlap percentage would be the area of the shaded region divided by the area of the larger of the two circles. The variables shown in the figure, r_1, r_2, and c correspond to the radii of the two beams at operational range, and the center to center distance, respectively. These parameters can be entered in the simulation program, and are specified in meters. Clearly, the optimum 100% overlap condition can only be achieved with two beams identical in size and power distribution, and are also share a perfect center alignment. Although the analysis includes only a single input parameter for spatial overlap, a more robust calculation would entail weighting this parameter to reflect the similarity in the far field power distributions. These effects can be as important in error calculations, and they are encountered when optical misalignments are present in the far field distributions of the transmitted beams.

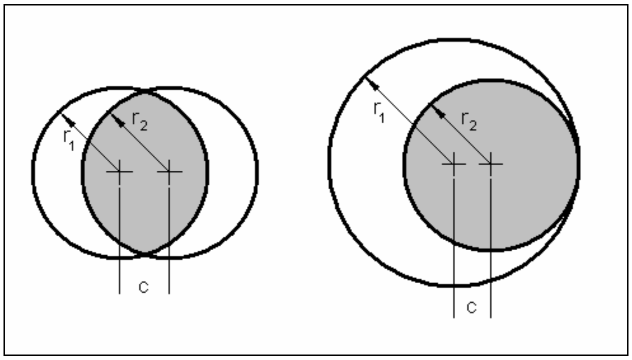

Figure A.1: Parameters used for determination of overlap percentage; r_1, r_2, and c correspond to the radii (which are defined by the $1/e^2$ point of intensity) of the two beams at operational range, and the center to center distance, respectively. All units are in meters, and can be input into the simulation program where they are used to calculate overlap percentage.

In the case of a fully overlapped system, the ground reflectivity variations would have no affect on return signature because both beams would be imaging the exact same spot on the ground. Therefore, the ground reflection term would drop out of the equation for CPL error fraction. If the overlap is less than perfect, the errors introduced are added in quadrature with the overall system error to describe the error of the measured CPL.

A.3 Uncertainty in the Atmospheric Optical Depth (Item #3)

The uncertainty in the atmospheric differential extinction optical depth refers to the magnitude of absorption of an interfering species. The typical DIAL analysis problem assumes that such additional absorption from interfering species is negligible. The non-typical case that considers this absorption is included as an uncertainty in the differential-extinction optical depth by Measures [1984]. This uncertainty is introduced in the equation for CPL error as an uncertainty in the species of interest using the propagation-of-errors method as shown in Equations 3.10 and 3.11. The CPL error in the species of interest due to the variations in the differential-extinction optical depth is calculated using one of the two correction methods:

1. Preliminary estimation of the absorption contribution from background interferents with an error range for this estimate (e.g. 2 +/- 0.5 ppm methane background).
2. Measurement of background absorption by the system when conditions are representative of the case with ‘no target plume present.’

The magnitude of the assigned error in these calculations is highly dependent on the correction method used. Unless the system is operating with poor overlap, it is typically better to use the system measurement of the background atmospheric absorption to find a value and its error for correcting the CPL for the species of interest. The disadvantage to this approach is that the atmospheric background error calculations invoke contributions from undesired absorption of each of the laser wavelengths transmitted. The errors introduced in the correction of the CPL reading depend on the method used and hence are explained as follows.

When it is desired to compensate for atmospheric background through a preliminary estimate of the spectral interference, the approximate background concentration and error (both in ppm) must be specified. In addition, the range error to topographical target must be specified, because its value affects the differential extinction optical depth; in some cases, the system is able to adjust dynamically using its own measurement of range to target. If we assume that errors in the differential absorption cross sections of the interfering species are negligible, then we can write the uncertainty in the differential-extinction optical depth as,

$$\delta\xi_e = \int_{R_1}^{R_2} \delta N_{bckg.interferent} * \delta R * \sigma^{A}_{diff,interferent} \ , \qquad [A5]$$

where,

$\delta N_{bckg.interferent}$ is the uncertainty in the background concentration of the interfering species [# / m^3],

δR is the uncertainty in the range to target [m],

$\sigma^{A}_{diff,interferent}$ is the differential absorption cross section of the interfering species [m^2].

If we assume that the errors introduced in the differential-extinction optical depth associated with range to target and background interference errors are independent, then the effects are added in quadrature. Therefore, the total differential-extinction error fraction can thus be calculated using the following relationship,

$$\begin{aligned}\frac{\delta\xi_e}{\xi_e} &= \sqrt{\left(\left(\frac{\delta\xi_e}{\xi_e}\right)_{altitude\ variation}\right)^2 + \left(\left(\frac{\delta\xi_e}{\xi_e}\right)_{bckg.\ variation}\right)^2} \\ &= \sqrt{\left(\frac{N_{bckg.interferent} * \delta R * \sigma^{A}_{diff,interferent}}{N_{bckg.interferent} * R * \sigma^{A}_{diff,interferent}}\right)^2 + \left(\frac{\delta N_{bckg.interferent} * R * \sigma^{A}_{diff,interferent}}{N_{bckg.interferent} * R * \sigma^{A}_{diff,interferent}}\right)^2} \\ &= \sqrt{\left(\frac{\delta R}{R}\right)^2 + \left(\frac{\delta N_{bckg.interferent}}{N_{bckg.interferent}}\right)^2}.\end{aligned} \qquad [A.6]$$

Note that this quadrature sum involves the uncertainty in each parameter divided by its average value because non-fluctuating variables cancel out. The final term in the equation for the species-of-interest CPL error fraction (Equation 3.11) can now be written in terms of known or measured parameters,

$$\begin{aligned}\xi_e^2\left(\frac{\delta\xi_e}{\xi_e}\right)^2 &= \left(N_{bckg.interferent} * R * \sigma^{A}_{diff,interferent}\right)^2 * \left[\left(\frac{\delta R}{R}\right)^2 + \left(\frac{\delta N_{bckg.interferent}}{N_{bckg.interferent}}\right)^2\right] \\ &= \left(CPL_{bckg.interferent} * \sigma^{A}_{diff,interferent}\right)^2 * \left[\left(\frac{\delta R}{R}\right)^2 + \left(\frac{\delta N_{bckg.interferent}}{N_{bckg.interferent}}\right)^2\right].\end{aligned} \qquad [A.7]$$

Alternatively, the background concentration of the atmospheric interferent species could be calculated on-the-fly by the instrument, assuming it is known a priori that the species of interest is not in the measurement path during calibration. Instrument calibration using this technique is useful when the spectrally interfering species can vary between measurement campaigns, or where the confidence in the preliminary estimation of their concentrations is low. When this method is used, the calculation of the uncertainty in the differential-extinction optical depth appropriately invokes the CPL error fraction algorithm. This causes us to once again redefine the final term in the equation for CPL error fraction of the species of interest (Equation 3.11) as,

$$\begin{aligned}\xi_e^2\left(\frac{\delta\xi_e}{\xi_e}\right)^2 &= \left(CPL_{bckg.interferent} * \sigma^A_{diff,interferent}\right)^2 * \left(\frac{\delta CPL_{bckg.interferent} * \sigma^A_{diff,interferent}}{CPL_{bckg.interferent} * \sigma^A_{diff,interferent}}\right)^2 \\ &= \left(CPL_{bckg.interferent} * \sigma^A_{diff,interferent}\right)^2 * \left(\varepsilon^{interferent}_{CPL}\right)^2.\end{aligned} \qquad \text{[A.8]}$$

In this case, the CPL error fraction of the background interferent, $\varepsilon^{interferent}_{CPL}$, is calculated in the classical manner using Equation 3.11, as if the interferent is the species of interest. As one may expect, this calculation is performed under the assumption that the contribution of the differential extinction, exclusive of interferent species, is negligible. The result of this calculation is then introduced into Equation A.8 that is used with Equation 3.11 to calculate CPL error fraction of the actual species of interest. Although this technique sounds cumbersome, it is the method that is typically applied where one or more lines are used, because the error will propagate from the first DIAL comparison, and it will compound as the layers of analysis are increased.

A.4 Match of the On-line Laser to the Selected Absorption Feature (Item #4)

The absorption spectra of the species of interest, as well as any other known contributors to absorption in the selected spectral region are calculated for the system parameters, or they are measured by the transceiver system during data acquisition. Although the methodology utilizing the laboratory measured absorption coefficient is a precise one, real-world testing can exhibit slightly different absorption spectra due to temperature or pressure variations. The most accurate CPL measurements will be acquired when the absorption coefficient is measured on a per sample basis using a known concentration in a calibration gas cell. When this method is used, the error introduced into the final CPL is only due to the errors in measuring this parameter and can be accounted for using the same methodology outlined above (item #1). Ideally, the absorption spectra for the species at a specific on-line wavelength should not change for the duration of the measurement, however, the linewidth and stability of the laser can introduce fluctuations in the absorption coefficient.

A.5 Additional Atmospheric Interference (Item #5)

Additional atmospheric interference from solar radiance, thermal radiance, and optical scattering along the path are additional sources of error, which are well known contributors to errors in lidar systems. Thermal infrared radiance from the Earth’s surface is minimized for systems looking skyward. Although this thermal radiance component from the Earth’s surface may contribute additional errors, the effect can be included in the contribution from variations in ground reflectivity and beam overlap.

APPENDIX B
DIAL Performance Simulations

The DIAL simulations developed by Penn State are designed to aid in the design of DIAL lidar systems at the earliest of stages. Our DAS simulation has been tailored to examine the limitations of specific designs, and to evaluate sensors that are being tested and operated. The DAS performance simulations are similar to the DIAL simulations in predicting performance and evaluating capability. The DIAL simulation is primarily used to evaluate performance as a function of range, and transceiver size. The transceiver parameter values are varied, along with the range to target, to determine the minimum detectable concentration limit for a set of possible system designs. Without the added benefit of topographical scatter, the system limitations imposed by the SNR depend upon the background atmospheric scattering, which is usually dominated by aerosol scatter. Therefore, given the approximate system sizes and detector detectivity (sensitivity) it is feasible to plot general performance curves for DIAL systems after choosing the desired wavelengths, which determine the absorption cross section at these wavelengths. The DIAL simulations developed depend upon the MODTRAN^{TM} 5 transmission and radiance models to accurately model the performance and the interference properties of suggested systems. As an example, we describe the simulation of a system designed to operate under standard atmospheric conditions and detect methane gas plumes using wavelengths in the MWIR. We have assumed a standard solid state detector detectivity of 10^{10} cm Hz$^{0.5}$ W^{-1}, which is in the range of commercial-off-the-shelf (COTS) available MWIR detectors. Using MODTRAN^{TM} 5 along with the standard DIAL equations and the wavelengths shown in Table 3.1, we have simulated the minimal detectable concentration limit as a function of range to target, transmitter energy, and receiving telescope size. This example includes the performance evaluation for daytime and nighttime operation shown by Figure B.1.

The "performance parameter," which consists of the product of the transmitter energy (J) and receiving telescope size (m^2), is the y-axis variable, and this parameter can be related to system size and cost. By choosing an approximate transmitter power and receiver size, one can move horizontally on the plot and quickly determine the minimum detectable limit as a function of range for the given system design, and chosen atmospheric conditions (standard summer atmosphere at mid-latitudes in this case with 23 km visibility). One interesting point to note in this specific simulation is that although the sun-earth emission background is at a minimum in the midwave infrared (where this simulation was evaluated), slight interference for daytime measurements does degrade performance. Subtleties similar to these are often missed in system design processes and hence it is our goal to simulate such features using DIALSIM and DASSIM to reduce the influence of such problems.

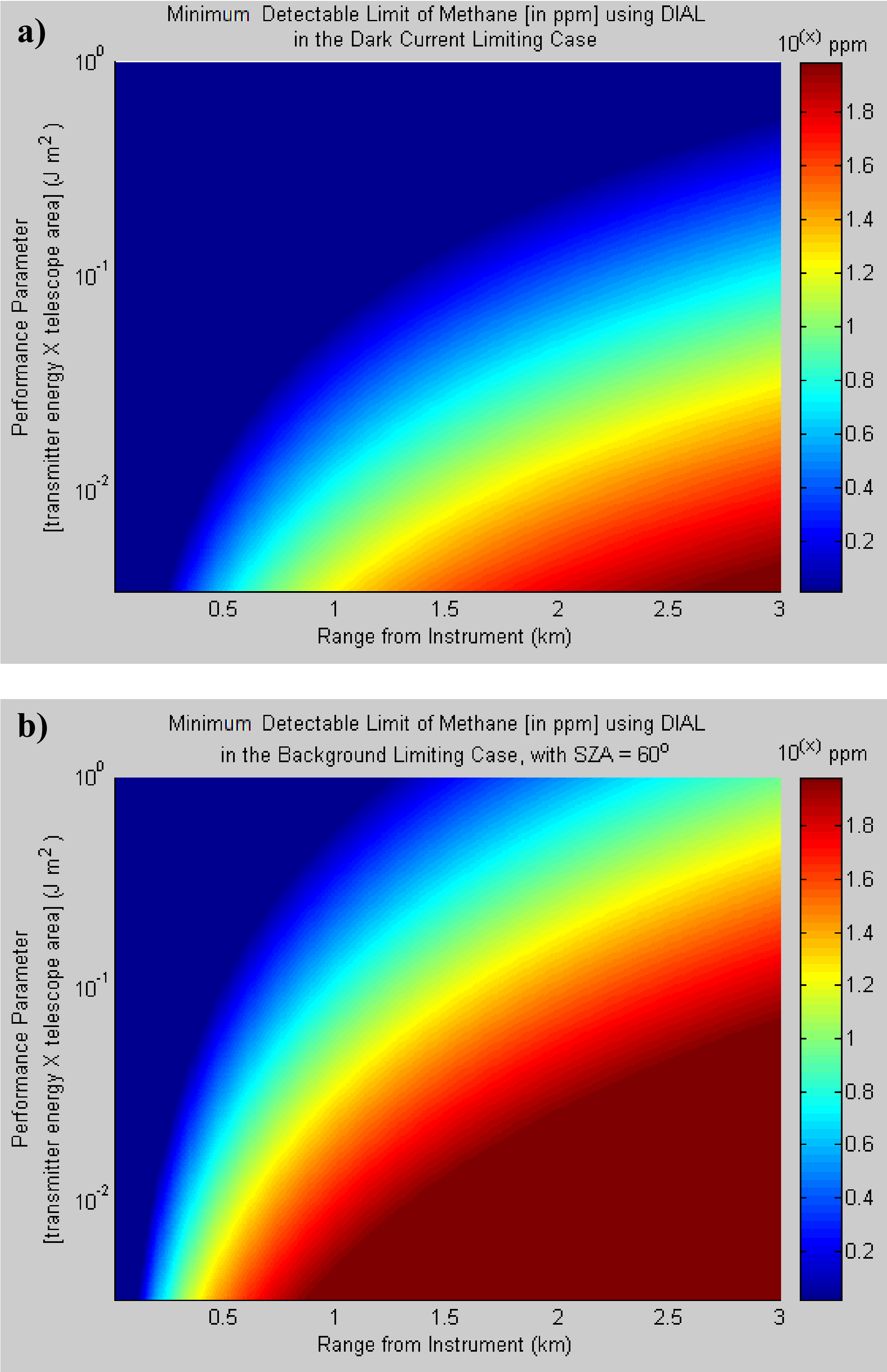

Minimum Detectable Limit of Methane [in ppm] using DIAL in the Dark Current Limiting Case

Minimum Detectable Limit of Methane [in ppm] using DIAL in the Background Limiting Case, with SZA = 60°

Figure B.1: DIAL performance simulation output for comparing dark (a) and light (b) (χ=60°) limiting case of methane detection in the MWIR.

APPENDIX C
DAS Performance Simulations Supplement

The return energy for both the on-line and off-line wavelengths is calculated along with percent error as a function of target plume size. As the plot in Figure C.1a suggests, the increase in the species (methane) CPL causes the return energy to decrease rather drastically for the online wavelength. The fluctuation in these return energies governs the percent error of measurements obtained by the system. Assuming that we have a case of 100% beam overlap and perfect electronics thus creating a transmitted and return energy measurement error of zero, our only error in the sample comes from the Poisson error that is intrinsic to any type of photon collection process. Figure C.1b shows this error as a percentage of plume magnitude. At very large concentrations, the system (particularly the online wavelength channel) is starved for return energy and hence causes the Poisson error to quickly become significant.

For the same system considered above, we introduce a 5% error due to variations in the transmitted and received energy measurements combined in quadrature, and in addition we reduce the beam overlap percentage to 80%. The plots of return energy and percentage error as a function of target plume size for this case are shown in Figure C.2.

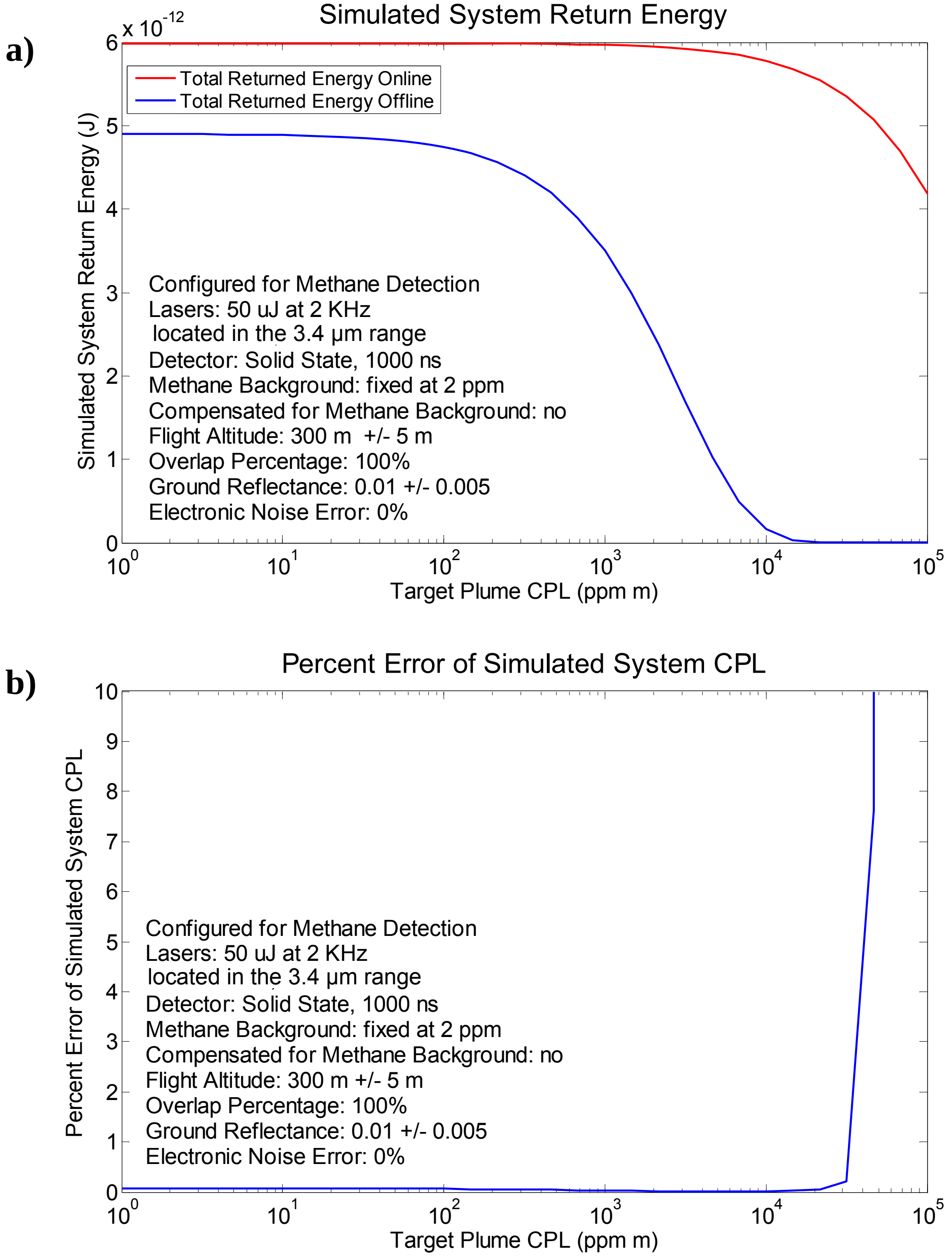

Figure C.1: Simulation results for methane detection for the system summarized in Table 3.1, with no transceiver measurement error and 100% overlapping beams. (a) Online and offline energy return as a function of plume concentration and (b) Percentage error as a function of plume concentration.

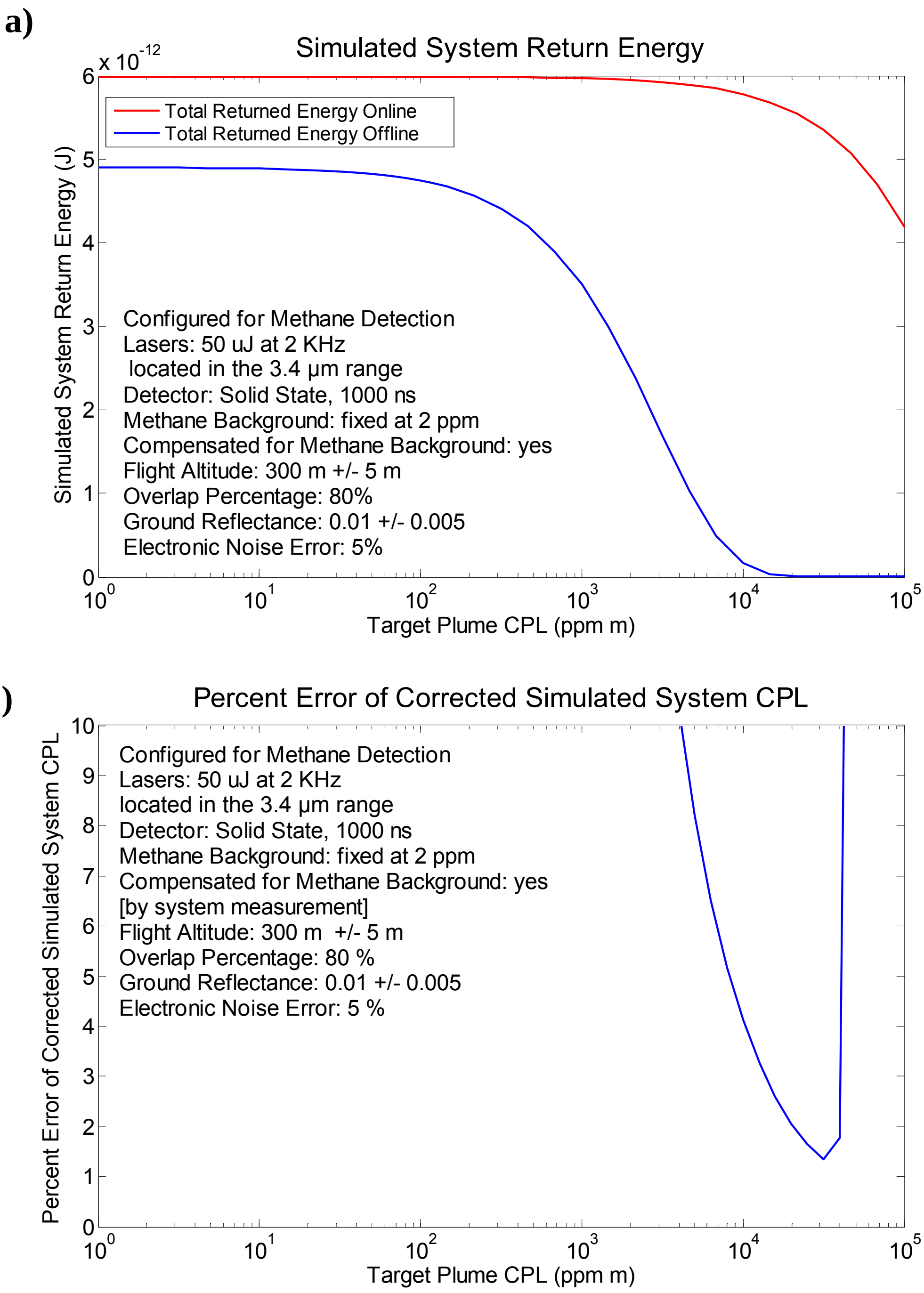

Figure C.2: Simulation result for methane detection with atmospheric methane background compensation where transceiver measurement error and overlap error are introduced. (a) Online and offline energy return as a function of plume concentration and (b) Percentage error as a function of plume concentration.

APPENDIX D
Absorption Calculations from Ideal Blackbody Radiators

The observation of hydrocarbon plumes by imaging the absorption in a passive manner depends on the concentration of the hydrocarbon species, and ultimately the amount of radiance being absorbed. The calculations presented in this section describe the importance of a significant source of radiance in the field of view of an imager by showing the absorption as a function of wavelength and blackbody radiator temperature. Figure D.1 shows the absorption due to a 1000 ppm·m diesel plume for different ideal blackbody radiator temperatures as a function of wavelength. Figures D.2 and D.3 show similar plots for a 1000 ppm·m plume of gasoline and methane vapor, respectively. Note on all the figures that the absorption magnitude is much greater for all wavelengths as the temperature of the ideal blackbody radiation source is increased. Large absorption magnitudes generate larger differences in photon counts per pixel when comparing plume-present and plume-absent cases, and therefore absorption is easier to observe under these conditions.

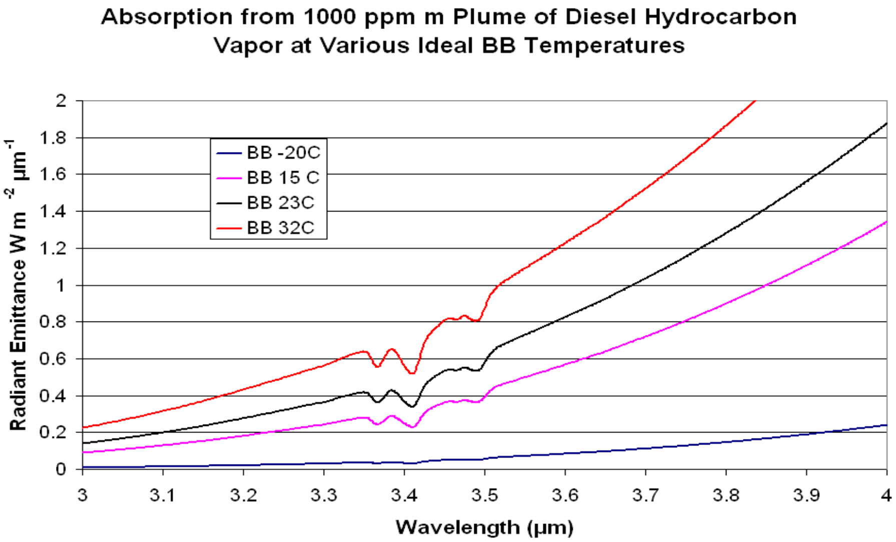

Figure D.1: Absorption from a 1000 ppm·m diesel plume at various ideal blackbody radiator temperatures.

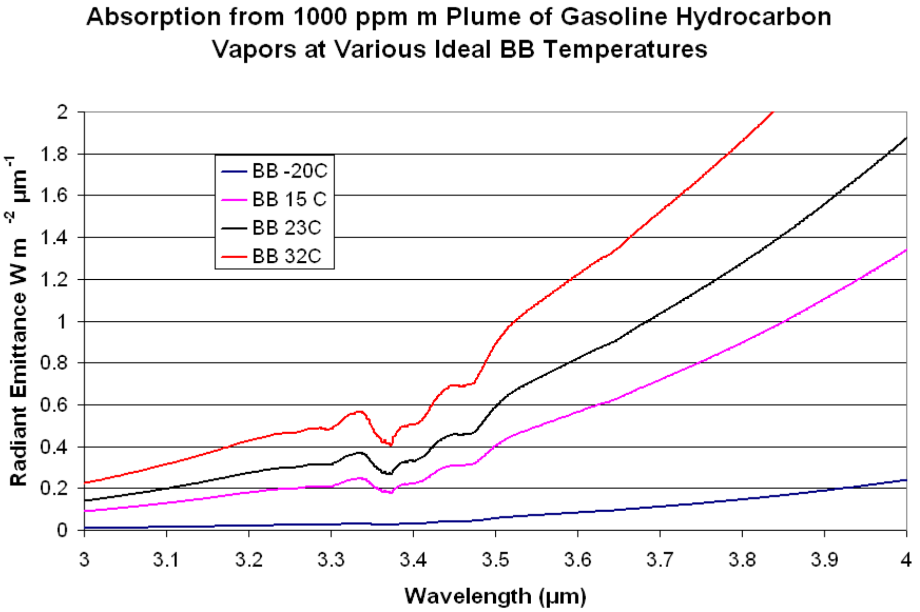

Figure D.2: Absorption from a 1000 ppm·m gasoline plume at various ideal blackbody radiator temperatures.

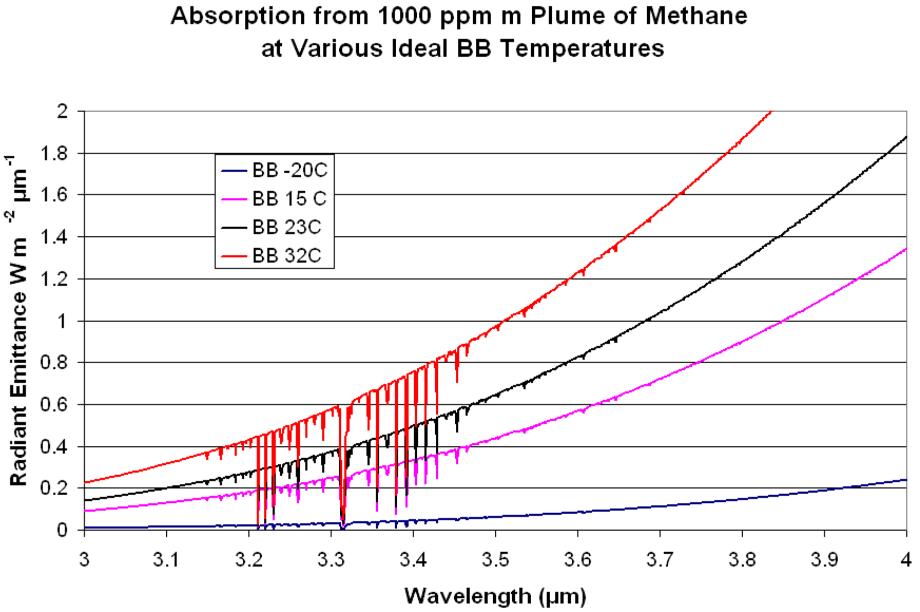

Figure D.3: Absorption from a 1000 ppm·m methane plume at various ideal blackbody radiator temperatures.

APPENDIX E
Filter Selection for Propane, Gasoline and Diesel Vapors

Detection for additional species that are not included in the MODTRAN^{TM} spectral model is investigated by treating the MODTRAN^{TM} result without a plume as an infrared source of blackbody radiation. Then, the absorption due to a 1000 ppm·m size plume of propane, diesel, or gasoline vapors, is calculated and convolved with the MODTRAN^{TM} result. Although this does not allow us to include absorption and re-radiation of infrared energy through the atmosphere, as the MODTRAN^{TM} model does for the case of a 1000 ppm·m ground level methane plume, it provides a useful alternative method. Figure E.1 shows the modification of a MODTRAN^{TM} simulation output and the expected detection in the passband of the 3.2 to 3.4 μm fior a 1000 ppm·m plume of propane. Like the previous method, the response is simulated as a function of filter center wavelength and bandwidth for propane, gasoline, and diesel vapors. The results of this analysis are shown in Figures E.2 through E.10.

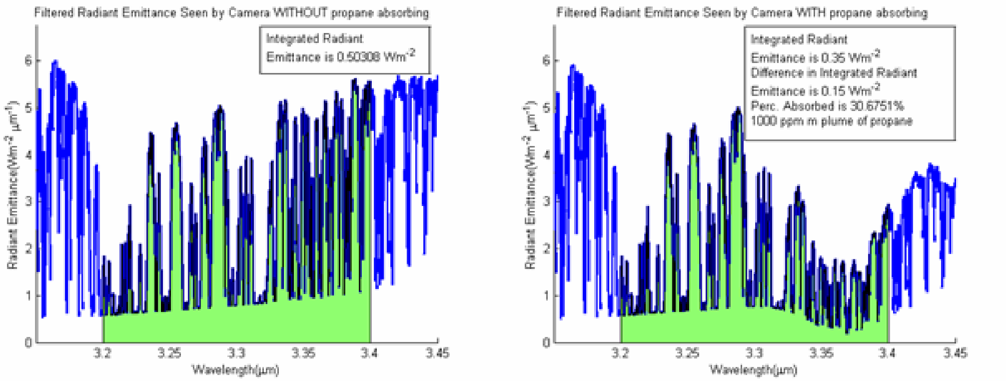

(a) (b)

Figure E.1: Expected modification (b) to MODTRAN^{TM} spectral model result (a) when imaging a 1000 ppm·m plume of propane. Note: Does not include radiative transfer.

Figures E.8 through E.10 show the results for each of the target hydrocarbon species. The gray star on each of these plots represents the location of the general purpose filter, while the red star represents the filter choice that enhances performance for the given target, and a summary of these results is listed in Table 3.2.

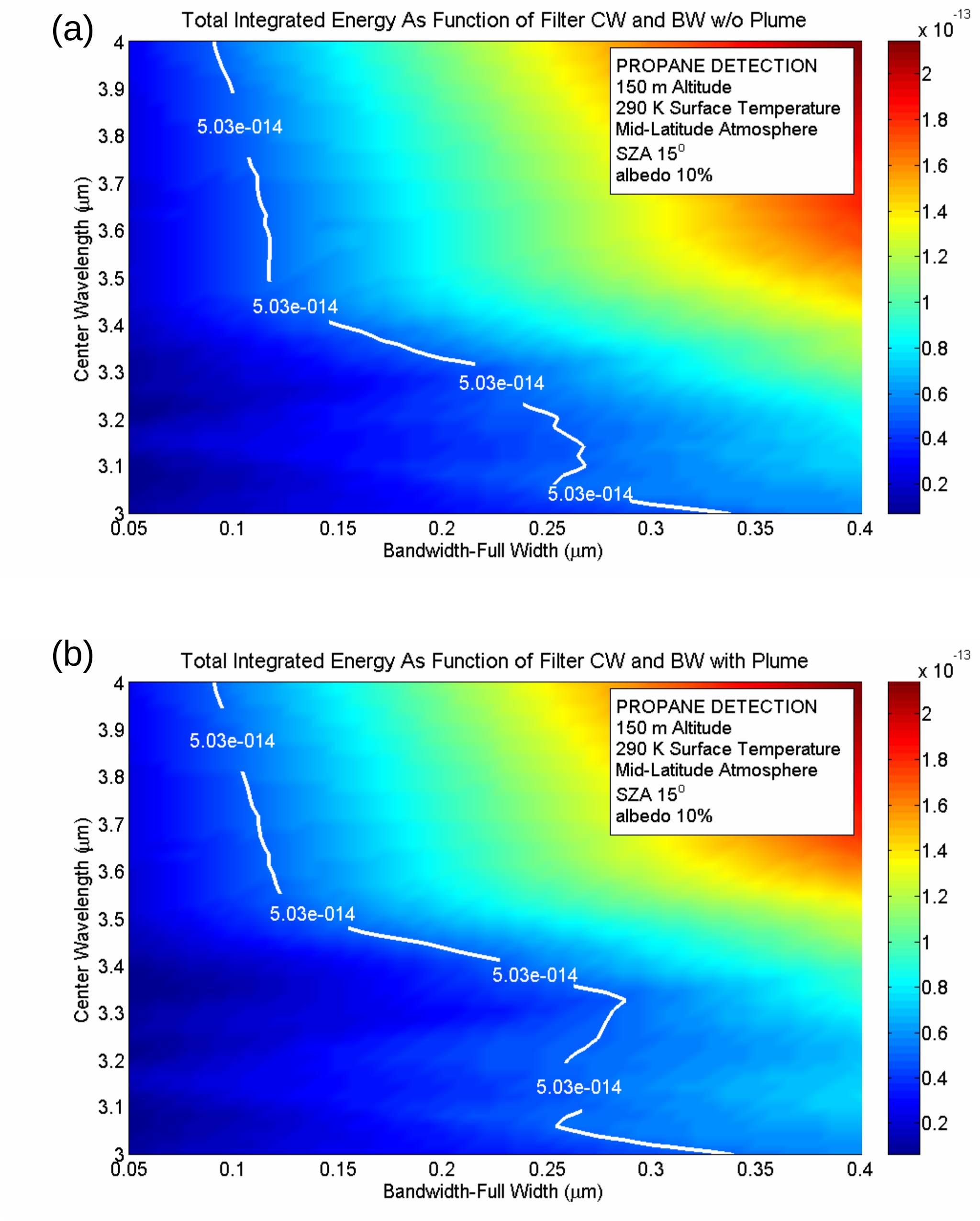

Figure E.2: Result of integrated radiant energy for propane simulation without a plume (a) and with (b) 1000 ppm·m plume.

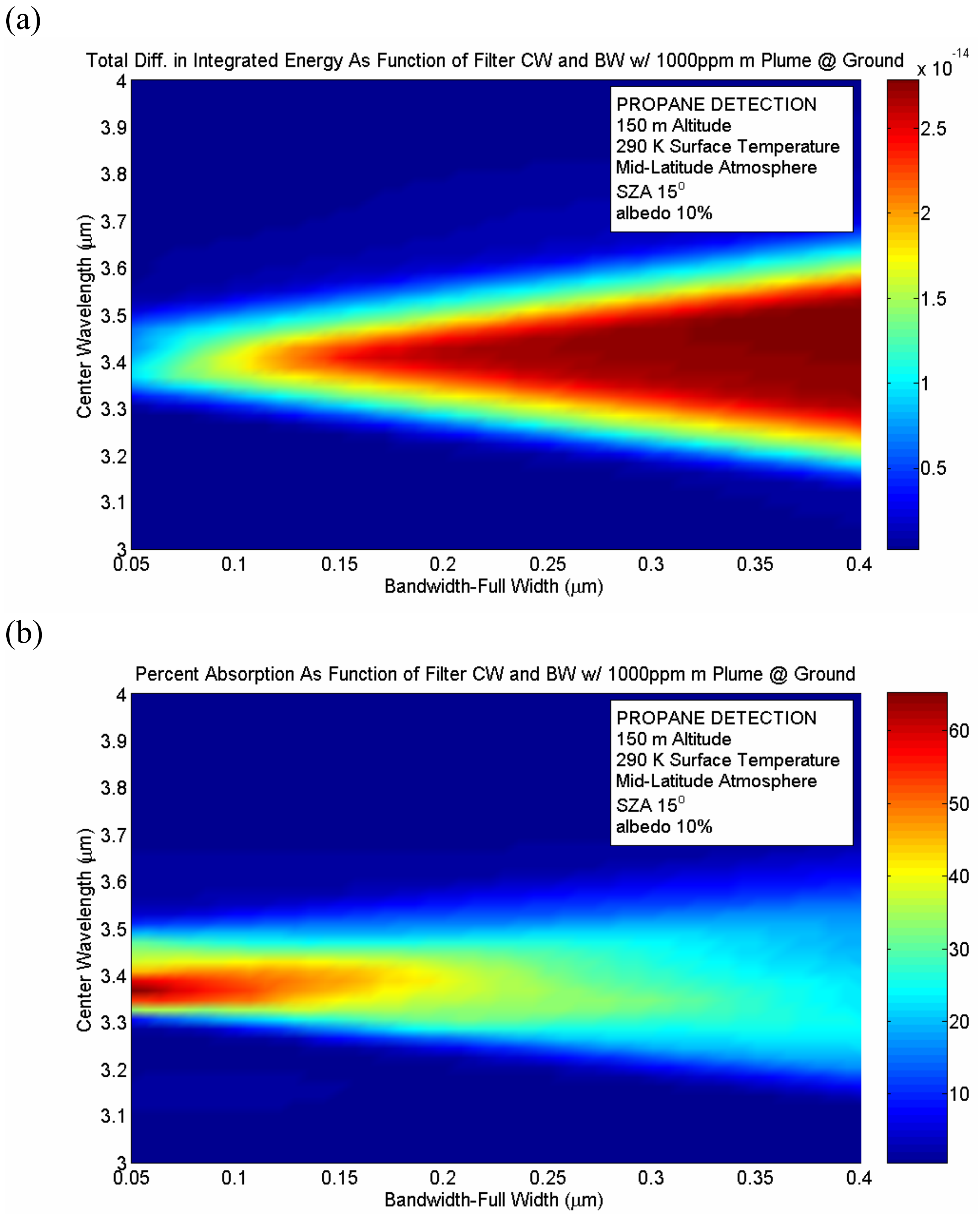

Figure E.3: (a) Percentage of absorption, and (b) difference in integrated radiant energy for propane.

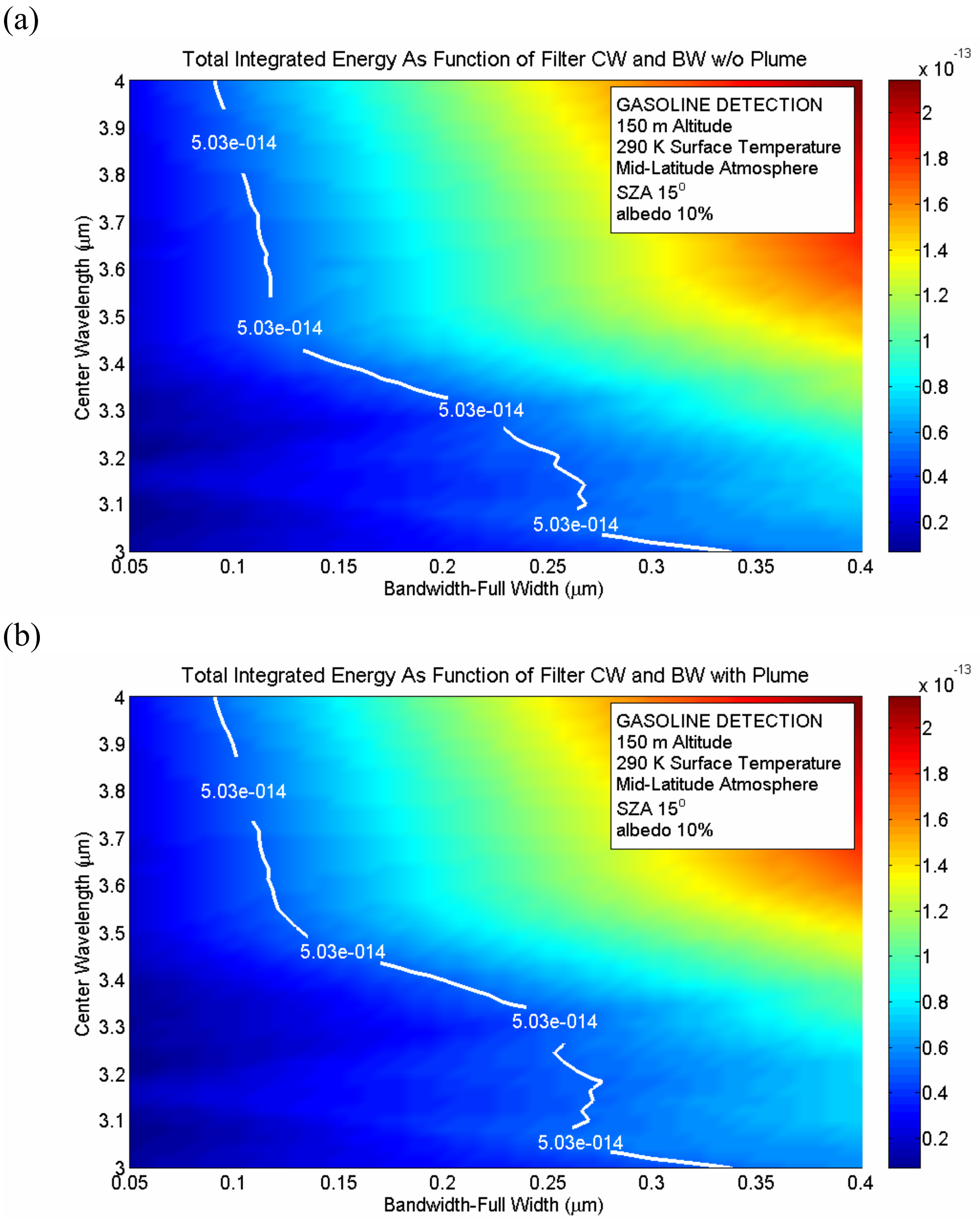

Figure E.4: Result of integrated radiant energy for gasoline vapor simulation without a plume (a) and with (b) 1000 ppm·m plume.

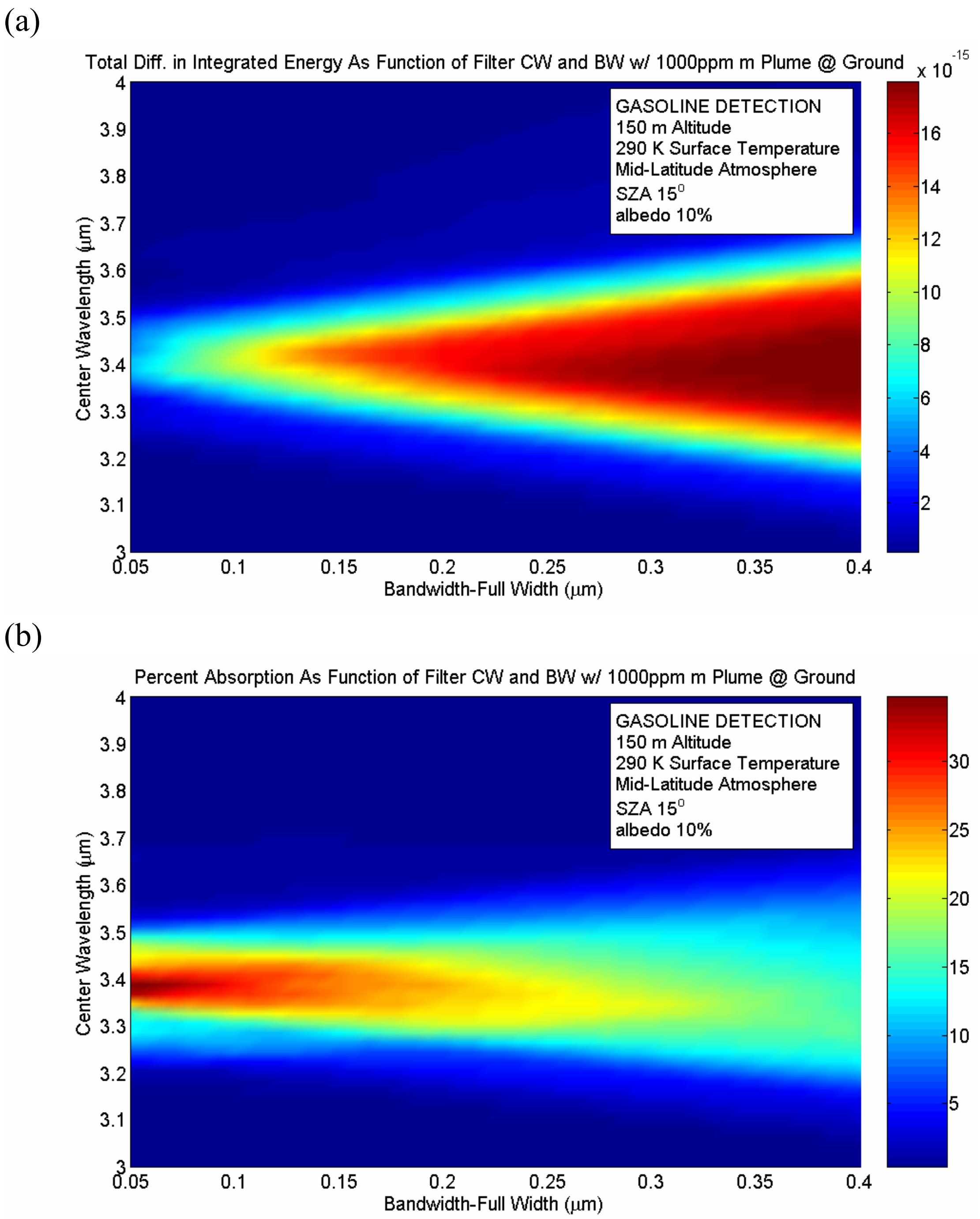

Figure E.5: (a) Percentage of absorption, and (b) difference in integrated radiant energy for gasoline vapor.

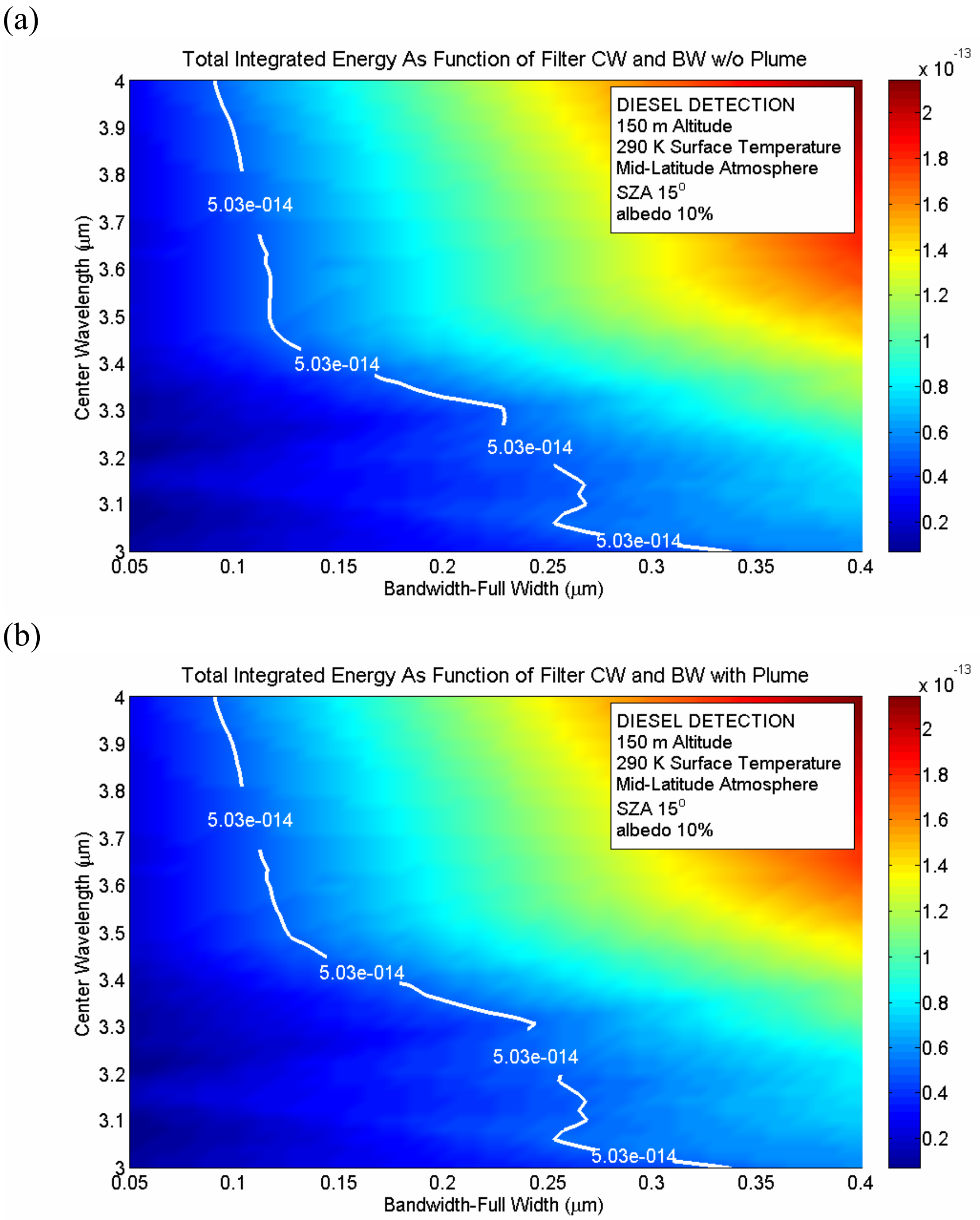

Figure E.6: Result of integrated radiant energy for diesel vapor simulation without a plume (a) and with (b) 1000 ppm·m plume.

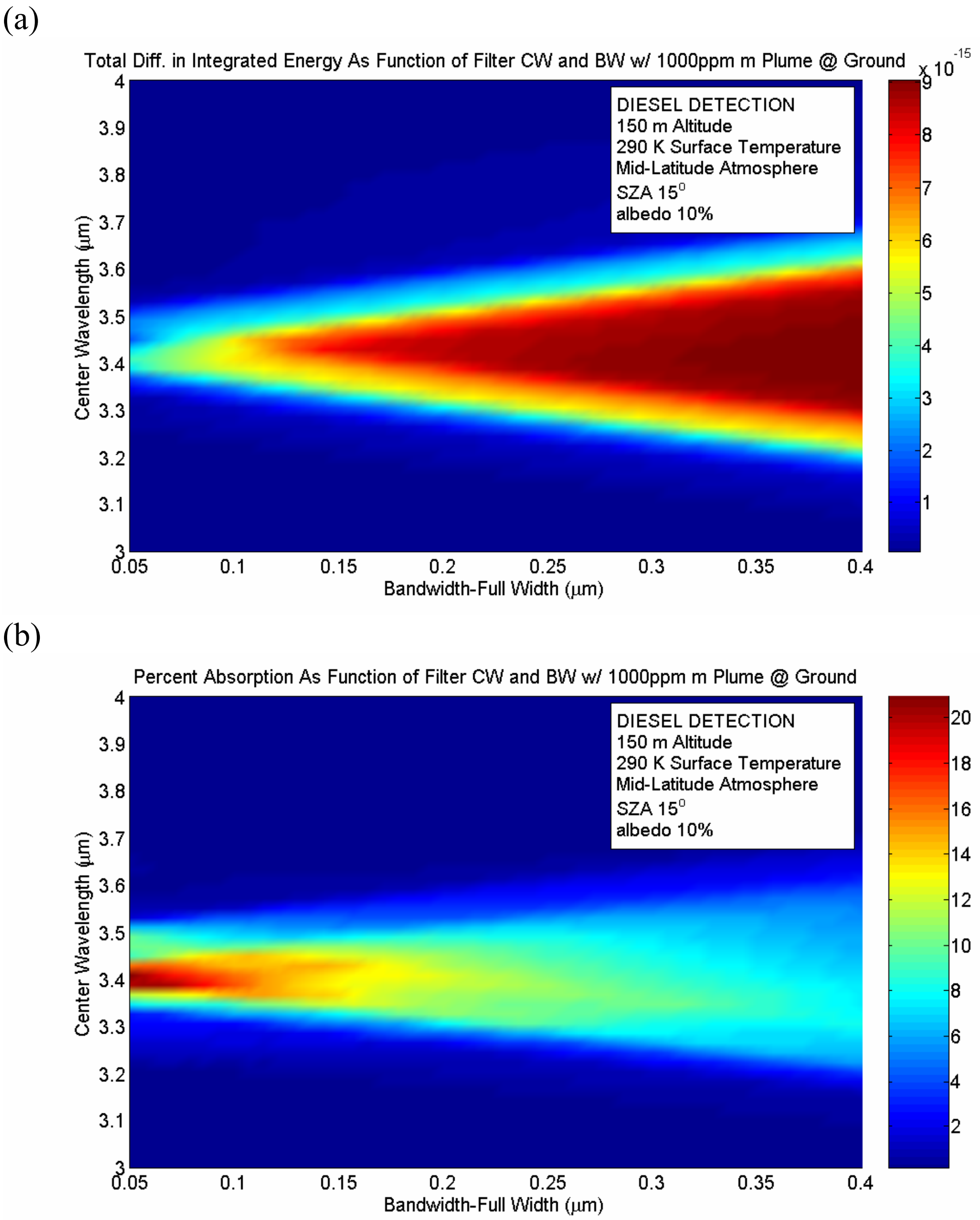

Figure E.7: (a) Percentage of absorption, and (b) difference in integrated radiant energy for diesel vapor.

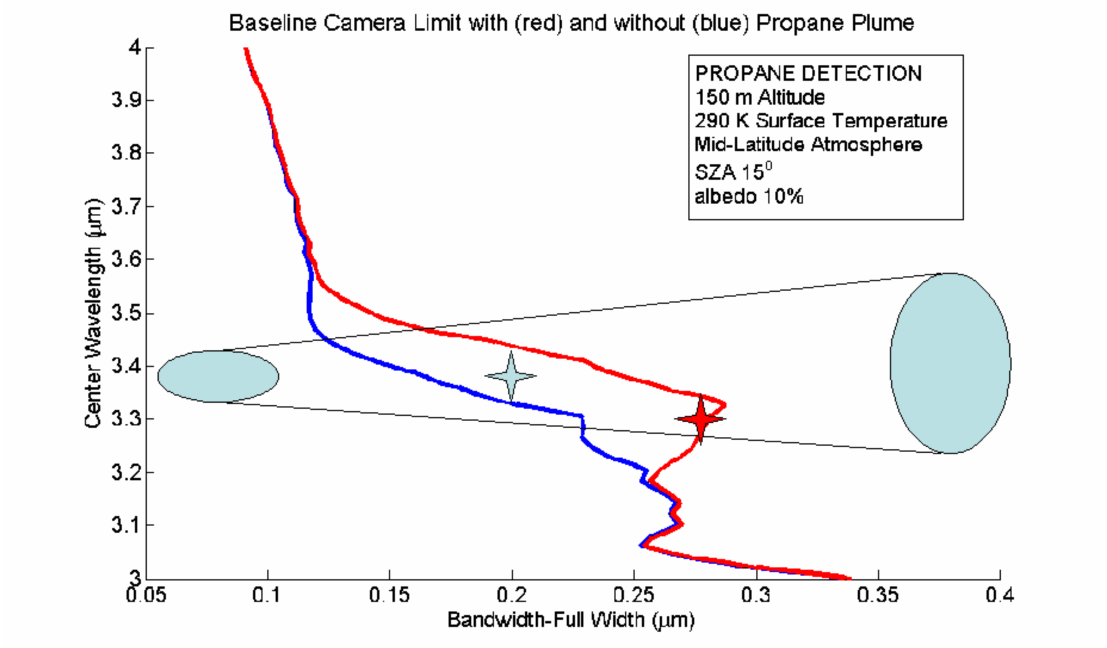

Figure E.8: Summation of the results for the propane target case.

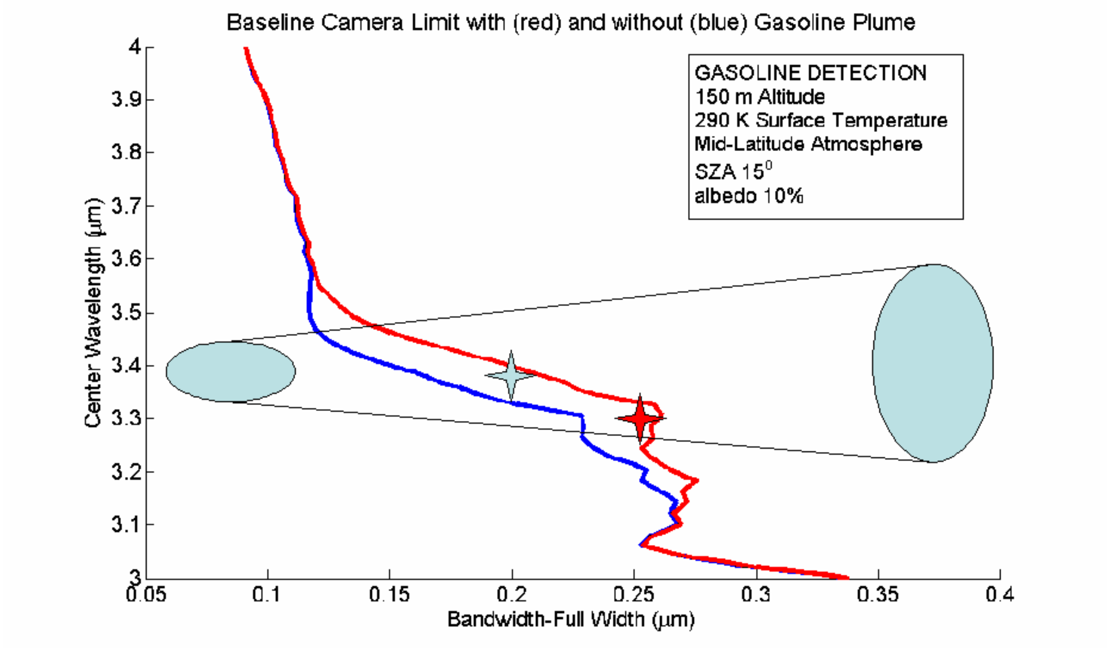

Figure E.9: Summation of the results for the gasoline target case.

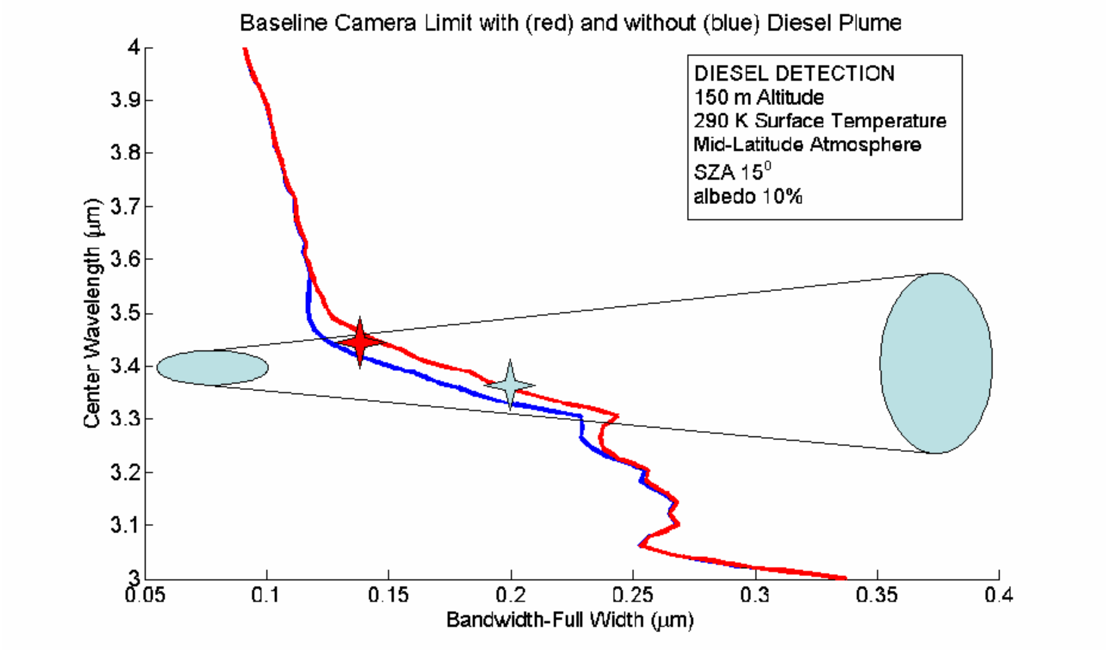

Figure E.10: Summation of the results for the diesel target case.

APPENDIX F

Radiant Flux Calculations through the General Purpose Filter

The radiant flux through the general purpose filter can be calculated by multiplying the band-pass region of the filter by the radiance source spectrum. The simulations contained below in Figure F.1 show total collected flux by the imager when it is operated at a 150 m altitude in a down-looking configuration. Each of the figures show the total collected flux in Wm^{-2} using the colorscale shown to the right, while the axes correspond to different cases of radiance.

As an example, a case of methane detection is examined. Using the software, similar figures can be created for other hydrocarbon species absorbing in the region. The x-axis varies the contribution from the Earth (background thermal radiance corresponding to the surface temperature). The y-axis varies the contribution from the Sun (reflected solar radiance as a function of solar zenith angle). The three rows correspond to different cases of surface albedo. The first column corresponds to the case when there is no plume present at the ground, while the second column corresponds to a case of a methane plume present at the ground. The third column plots the difference between the first two columns to determine the total difference in radiant flux captured at the imager.

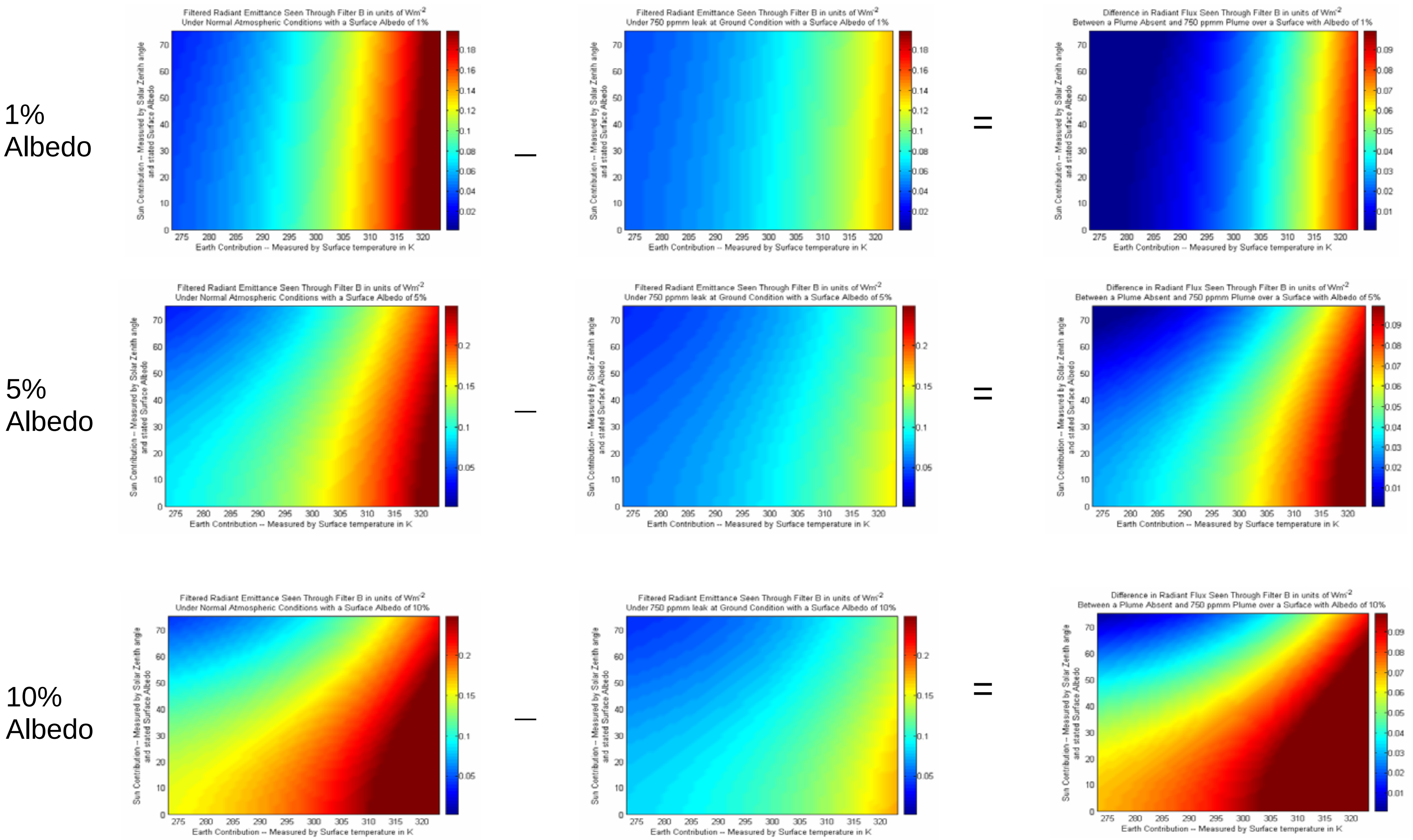

Figure F.1: Upwelling radiance observed through the general purpose filter under normal atmospheric conditions (left) and for the case of a 750 ppm·m plume of methane at ground level (middle). Difference between the plume present and plume absent cases (right).

APPENDIX G

Detailed Operation of the MWIR Imager

The following details the proper setup procedure for the imaging detection of hydrocarbon gas leaks:

1. Insert general purpose filter.
2. Turn camera on.
3. Change camera to NUC 11.
4. Change display to grayscale.
5. Allow camera to stabilize ~30 minutes.
6. Change/check that integration time is greater than or equal to 2000 microseconds.
7. Perform 2 point NUC correction
    a. Typically a cold source could be as simple as the lens cap.
    b. A hot source could be the surface of the palm of your hand (held in the field of view until completion (15-30 seconds).
8. Focus camera at proper range.
9. Activate AutoGain Control (AGC) and wait 5 seconds while the contrast and brightness are adjusted.
10. Deactivate AGC by pressing up or down on the contrast one time.

If the AGC is left active, then the camera will choose (and continue to choose) the optimized settings of contrast and brightness to most efficiently image the surface in the field of view. Under good solar radiation conditions (high noon), the AGC will produce a useful result allowing the operator to view the absorption effect due to the target gas. If this is the case, then simply deactivating the AGC by pressing either of the contrast buttons one time while observing the target will fix the contrast and brightness such that the radiation background will not force the system into an automatic adjustment mode, which makes it impossible to describe anything about the magnitude of the leak. With the AGC deactivated, the ‘shadowing’ effect of the target will remain in the field of view when these settings are fixed. Under poor contrast conditions (cold surface temperature and low solar contribution, i.e. cold day and overcast or nighttime conditions) the autogain control operation struggles with selecting the proper settings to most effectively image the scene. If this is the case, then the slight tandem adjustment of the camera brightness and contrast settings via the commands from a laptop computer, or keypad, can further help to enhance the imaging scene. Through the brief experiments conducted by us, the best approach to accomplish this task is to:

11. Increase the contrast 5 settings.
12. Decrease the brightness 5 settings.
13. Repeat steps 11 and 12 as necessary.

When adjusting the contrast and brightness, however, it is important to note that there are 40 levels of brightness and 40 levels of contrast in between the values posted to the output screen. Although the settings have been adjusted via 5 single-button presses on the keypad, the brightness and contrast values on the screen may not change. At this point, hydrocarbon leaks of significant size should be detectable.

The automatic and manual adjustments can make it possible to detect a hydrocarbon plume and determine its location, size, and movement. However, making these adjustments negates any opportunity to provide information on the magnitude of the leak. Preliminary testing of the camera indicates that it may be possible to estimate the magnitude of the plume through proper calibration using reference sources and controlling the Merlin camera through a computer which records and controls the brightness and contrast setting.

APPENDIX H

Additional Infrared Imaging Cases of Propane Detection

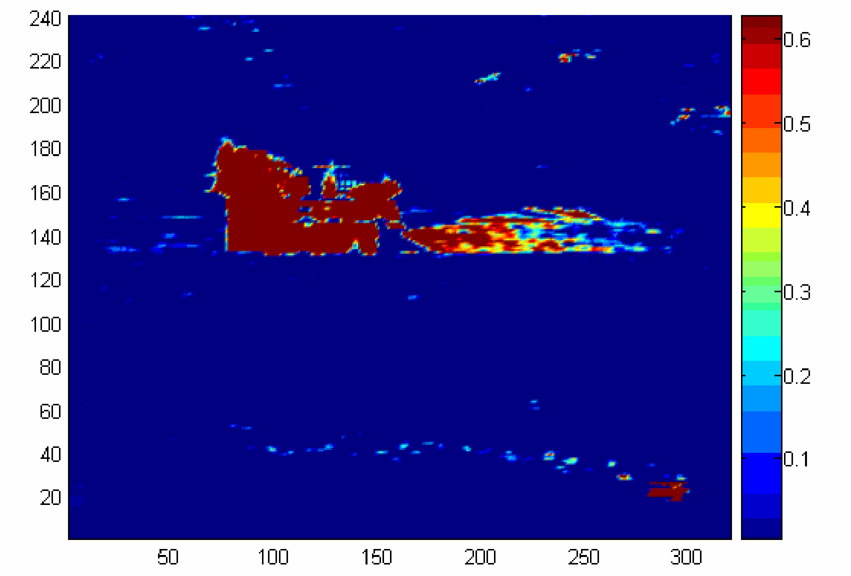

Figure H.1: Sum of Fourier response for frequencies ranging from 0.5 to 3 Hz on a per-pixel basis for a 60 m range using a staged 100 SCFH release. The red corresponds to the region in the figure where the most temporal variation occurs during the movie. The blue regions exhibit regions that are unchanging throughout the length of the movie.

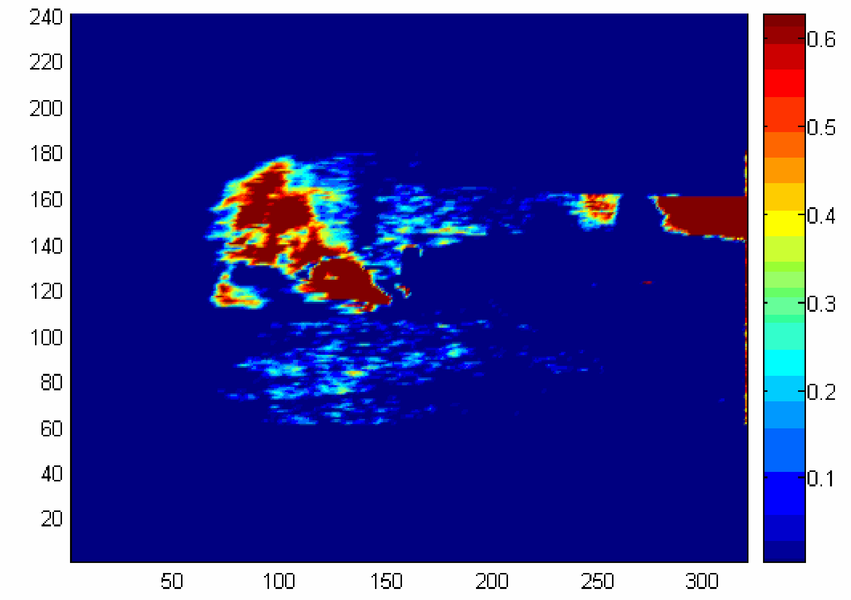

Figure H.2: Sum of Fourier response for frequencies ranging from 0.5 to 3 Hz on a per-pixel basis for a 100 m range using a staged 500 SCFH release. The red corresponds to the region in the figure where the most temporal variation occurs during the movie. The blue regions exhibit regions that are unchanging throughout the length of the movie.

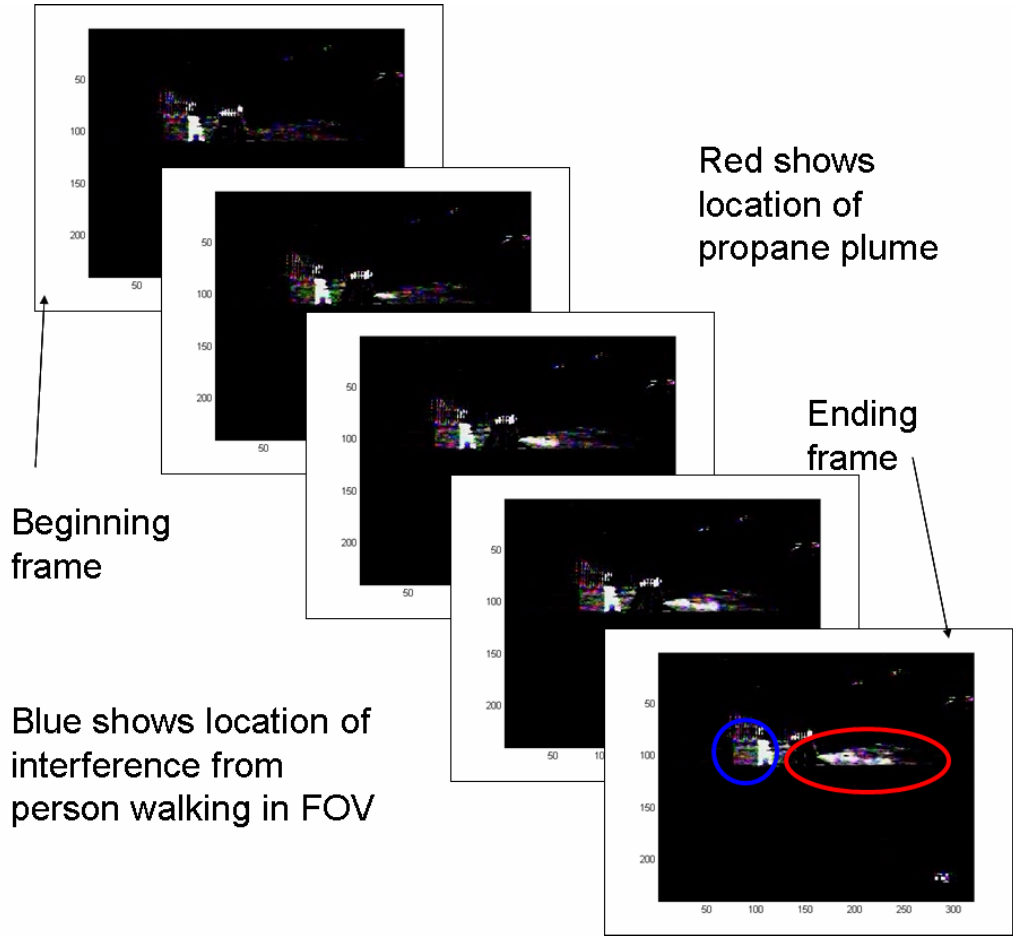
Red shows location of propane plume

Ending frame

Beginning frame

Blue shows location of interference from person walking in FOV

Figure H.3: Frames captured from the final post processed movie of a staged 100 SCFH propane release at 60 m.


Red shows location of propane plume

Beginning frame

Ending frame

Figure H.4: Frames captured from the final post processed movie of a staged 500 SCFH propane release at 100 m.

APPENDIX I
Infrared Camera Mounting Analysis and Solutions

Spatial location of the hydrocarbon absorption plumes from flight altitude via the MWIR camera system requires overlapping frames and selecting the refresh rate of the imaging system. A refresh rate that is too slow will cause blurring in the imagers, and poor performance in detecting plumes.

The specifications for the Merlin MWIR camera describes the field-of-view of the camera as 31° by 41°, and it images onto a 256 by 320 pixel focal plane array. At altitudes of 300 m and 150 m, this field of view translates into a 166 by 225 m (83 m by 112 m for 150 m altitude) rectangle delineated upon the land surface as shown by Figure I.1. The surface area resolution corresponds to the resolution on the focal plane array and renders a pixel resolution at the ground of 0.648 m by 0.7 m, also depicted by Figure I.2. This resolution is clearly adequate to determine approximate location of absorption due to hydrocarbon plumes.

With an assumption that the Cessna Grand Caravan is flying at an average speed of 180 mi hr^{-1} (80 m s^{-1}), the magnitude of camera blurring can be computed. The worst case integration time (digital refresh rate) of 16.67 ms at a speed of 80 meters-per-second results in a blur interval of 1.33 m. When comparing this to the resolution of roughly 0.7 m by 0.65 m (0.35 m by 0.32 m) at range, a blur between two adjacent pixels will exist when viewed from 300 m, and the blur will cover four pixels when observed from 150 m.

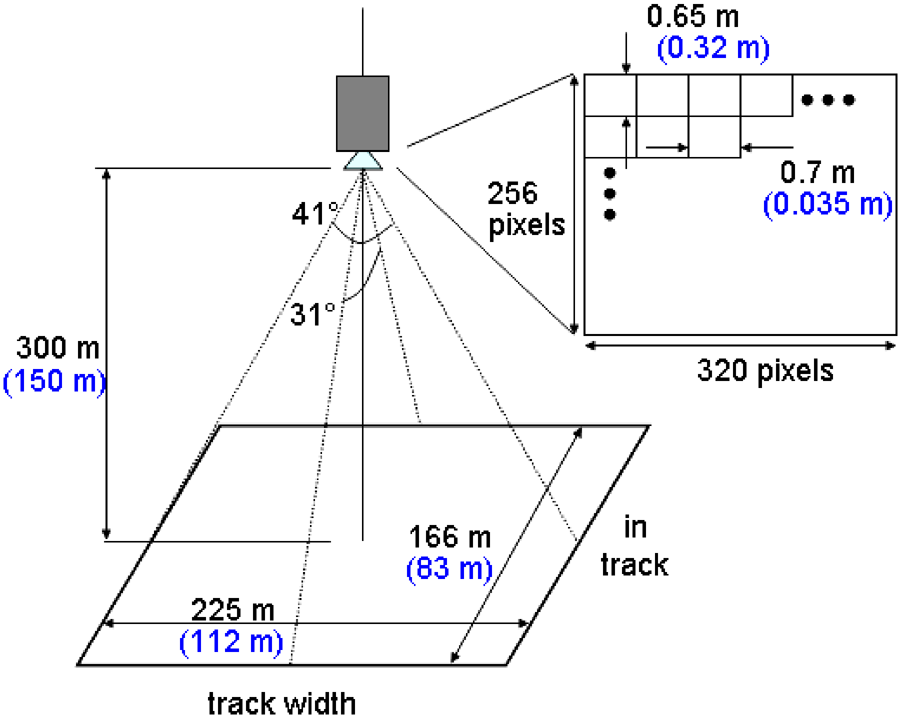

Figure I.1: Resolution of MWIR camera operating at a flight altitude of 300 m and 150 m.

The pixel smear area will have quite a significant influence on the image quality when the camera is nadir-pointed from the aircraft. Also, when the camera is mounted on the aircraft, pitch or roll motion can slightly magnify the effect. Based upon a review of images, we estimate that real-time images should be viewed with a blur less than a half-pixel width to maintain reasonable image quality.

Further analysis of the pixel blur in the image at the flight altitudes of interest (150 m and 300 m) is necessary to determine a cost-effective, proportional solution. A useful improvement in performance is gained by pivoting the camera to a backward-look direction shown in Figure I.2 (configuration B). The average 80 m s^{-1} flight speed for a Cessna Grand Caravan is faster than the current average data collection flight speeds on the ANGEL system, typically about 55 to 60 m s^{-1}. The slower flight speed corresponds to less pixel blur, and with the same camera refresh rate, a distance covered per refresh interval of 0.97 m.

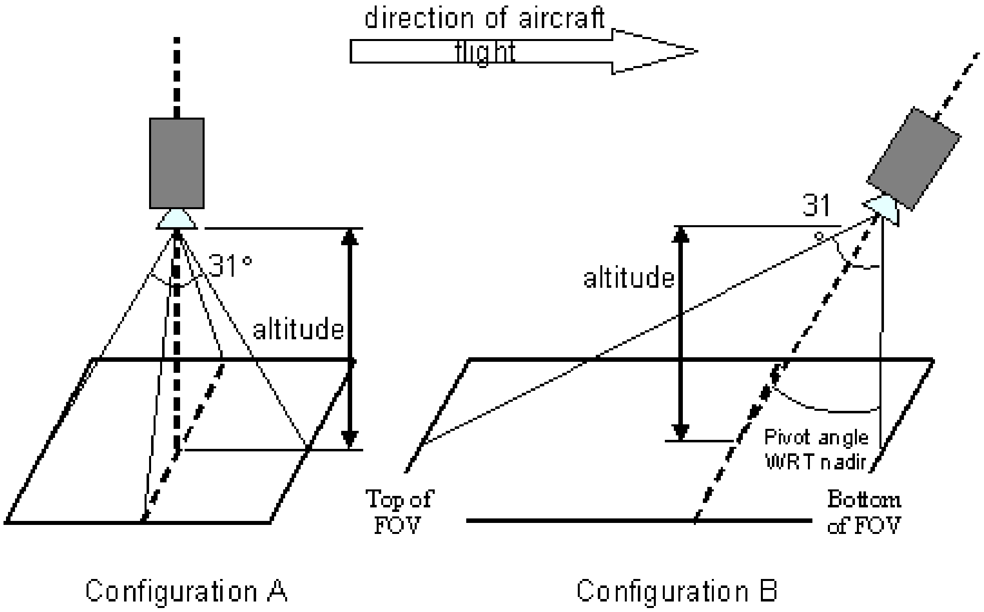

Figure I.2: Potential flight configurations of the MWIR camera on-board the aircraft. B will reduce pixel blur at the cost of resolution at top of the field-of-view (FOV).

For the case with a pivoted camera view angle, the resolution is calculated at the top, centerline, and bottom of the field of view. These in track resolution calculations are presented in Figure I.3 where they are plotted versus the camera centerline with respect to nadir. For example, if we review the example for a 300 m flight altitude, the dotted dark blue line corresponds to deterioration of the resolution at the top of the field of view denoted in Figure I.3 as the camera images a location on the ground farther from the aircraft. The light blue dotted line represents the center of the field of view exhibiting similar degradation in the resolution as the camera is rotated in a backward direction.

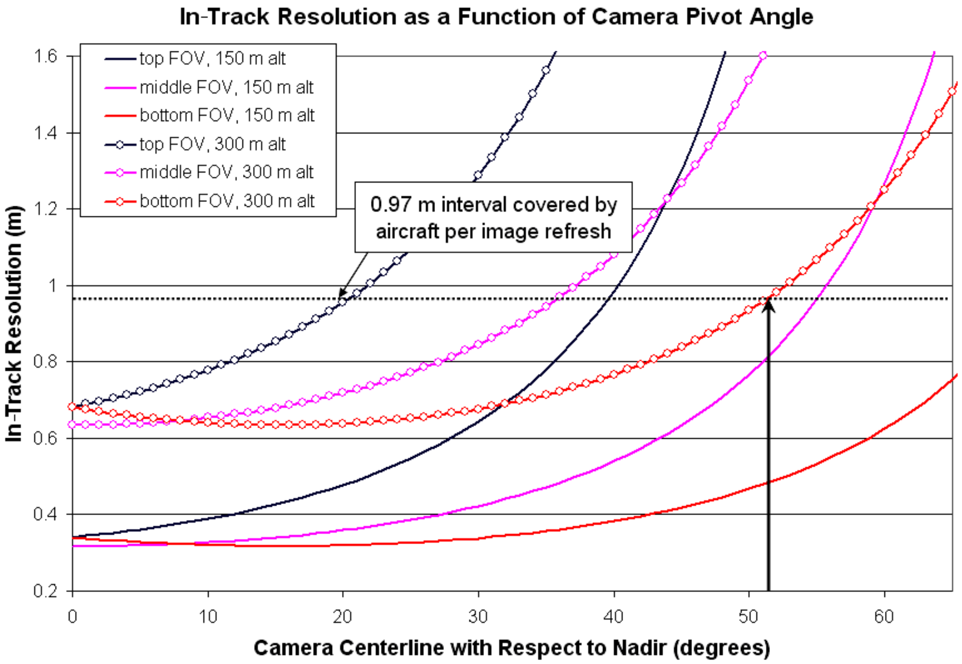

Figure I.3: In-track resolution as a function of camera centerline with respect to nadir for two different flight altitudes, 300 m and 150 m.

When examining the bottom bound of the field of view (red dotted line), we notice a better resolution with optimum at 15.5° before worsening, and showing similar behavior at the other reference locations. This improvement in resolution occurs as the bottom end of the field of view passes through the nadir point and the distance between the aircraft and the point of interest is at a minimum. A similar effect can be noted for the 150 m altitude, described by the solid lines in Figure I.3. The distance traveled between refresh rates calculated previously as 0.97 m is also noted on the graph as a point of reference for the ratio of pixel blur. Configurations (in altitude and pivot angle) that reside below the black horizontal dotted line will result in a pixel blur being less than one adjacent pixel along the in-track direction, due to the resolvable pixel area of the camera being greater. Those above the line can be classified as configurations yielding greater than a single pixel blur. For example, at an altitude of 300 m pivot angles greater than 51° (arrow, Figure I.3) will result in a single pixel blur or less over the entire image. The same configuration flown at an altitude of 150 m will cause more than one pixel blur in roughly the bottom half of the image, but the pixel area has increased notably. Figure I.4 describes the pixel blur as a function of camera pivot angle. Here, we have accounted for 1 pixel blur being equivalent to the amount of distance the aircraft travels per refresh, and this plot can be used to examine the relationship between multiple pixel blur and pivot angle.

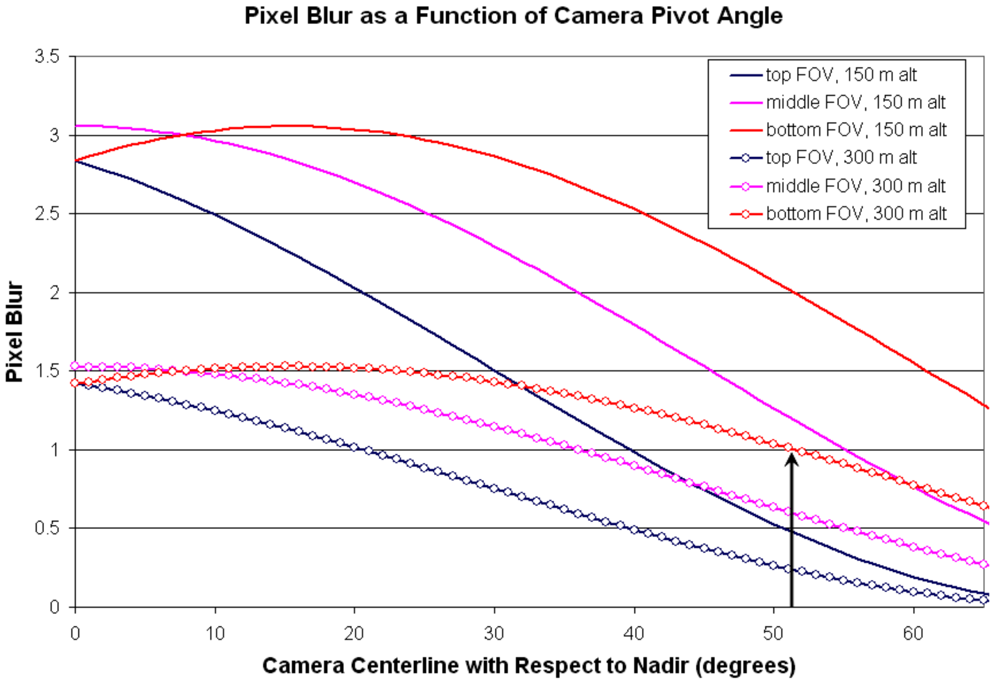

Figure I.4: Pixel blur as a function of camera centerline with respect to nadir for two different flight altitudes, 300 m and 150 m.

From the above analysis, it can be concluded that flight at typical 130 mph will result in blurring of image by about 3 pixels from altitude of 150 m (1.5 pixels from 300 m). The effect can be reduced by pointing at an angle (probably backward) relative to flight path. At a 45° angle, the blur can be reduced to 1.6 pixels at 150 m altitude (0.8 pixels at 300 m), with reduced image spatial resolution.

VITA

David Michael Brown was born in Baltimore, Maryland in October of 1981. He attended Dulaney High School in Timonium, Maryland, and graduated in 1999. He obtained a Bachelor of Science degree in Electrical Engineering from The Pennsylvania State University in August of 2003, and earned a Master of Science degree in Electrical Engineering from The Pennsylvania State University in May of 2005. While in graduate school at Penn State he served as a teaching assistant and lab instructor for courses in the Department of Electrical Engineering. Concurrently, he served as a research assistant for the lidar laboratory in the Department of Electrical Engineering. He received a Doctorate of Philosophy in Electrical Engineering from The Pennsylvania State University in August of 2008. His primary research interests are in electromagnetics, optical properties of the atmosphere, and remote sensing. He is a registered EIT (FE) in the state of Maryland, and is a member of IEEE, SPIE, and OSA.